Imperial College London
Department of Physics

Deep laser cooling and coherent control of molecules

Luke Caldwell

Submitted in part fulfilment of the requirements
for the degree of Doctor of Philosophy at
Imperial College London, February 2020

Abstract

Ultracold molecules can be used for a diverse set of exciting applications including controlled quantum chemistry, probes of physics beyond the standard model, simulation of many-body quantum systems and quantum information processing. However their rich internal structure makes the required control of their motional and internal states difficult. In the last decade, the field has made rapid progress on developing techniques for producing, cooling and trapping molecules and, whilst challenges remain, many of these applications are now being realised.

This thesis presents my work on laser cooling and coherent control of calcium monofluoride (CaF) molecules. We load molecules into a three-dimensional magneto-optical trap (MOT), the first such trap for CaF and the second for any molecule. The MOT contains around 2×10^4 molecules with an initial temperature of 12 mK. Lowering the laser intensity brings the temperature of the MOT down to 960 µK. To further cool the molecules we load them into a blue-detuned optical molasses, cooling them to 5.4(7) µK. This temperature is ~ 40 times below the Doppler limit and corresponds to a typical molecule moving at only a few times the single-photon recoil velocity. We optically pump the molecules into a single Zeeman sub-level and coherently transfer them between rotational states using microwave radiation. We load the molecules into a magnetic trap where they remain confined for about 5 s, the lifetime being limited by vibrational excitation due to room-temperature blackbody radiation. We show how to prepare the trapped molecules in a coherent superposition of two rotational states, and how to maintain this coherence for long periods, up to 6.4(8) ms. Detailed simulations of the remaining decoherence mechanisms suggest that it is possible to extend this to more than a second by compressing the sample to a smaller size, and using a magnetic trap geometry where the direction of the field is nearly uniform across the trapping volume. Finally we explore theoretically how Raman sideband cooling can be applied to molecules in optical tweezer traps, potentially providing a route to full quantum control.

Acknowledgements

I have truly enjoyed my PhD and have many people to thank.

My first contact with the Centre for Cold Matter (CCM) was a cold email I sent after browsing the Imperial College website. Thank you to Sanja who, in hindsight, almost certainly flagged that email to Ed as worth him reading and without whom the last four years would have been very different. You have been nothing but helpful, friendly and generally lovely since I arrived. Thank you to Ed for taking a punt on someone who hadn't done any physics for more than two years and giving me my first start in the group. Thank you to Dylan, Xiaxi and Jimmy in the level 1 lab who were so welcoming and generous with their time when I first arrived, teaching me the basics of UHV and laser systems. Thank you to Hannah for getting me up and running on the CaF experiment, putting up with my early ineptitudes, teaching me all manner of lab skills and setting the best possible example of how to write your thesis. We worked an awful lot of hours on the experiment together, diagnosing lost MOTs, tracking down dodgy power supplies and generally coercing the experiment into doing our bidding. I think we made a pretty good team! Thanks also to Sarunas, Jonas and Arijit who joined me at the CaF control desk at various points. Thank you to Noah, Stefan and Jack, postdocs who contributed so much to the project. It has been a pleasure to work with all of you and I have appreciated your varied approaches to physics and life.

I have been very fortunate to have two excellent PhD supervisors—Mike and Ben. I have learnt a huge amount from you both and am very grateful for the support and encouragement you have given me over the last three and a half years. The group is testament to your efforts to foster a friendly, collaborative and hard-working atmosphere whilst encouraging a sensible work-life balance that is so often absent in academia. Thank you to Ben for your encyclopaedic knowledge of lab phenomena and your willingness to come and lend a hand solving the knottiest of technical problems. Thank you to Mike for almost always obliging my requests for a quick chat about physics, even after you learnt that they very often turn into a rather long chat... Your careful consideration and clear physical pictures mean that I always come away from your office feeling like I understand the problem better.

Thank you to Eric and Jun for hosting me at JILA for two months in my third year and to Tanya, Yuval, Will, Tanner, Maddie and Jutta for making me feel so welcome there.

Thank you to Emma without whom I would never have finished, or indeed started, this PhD. You are a constant source of kindness, support and patience. Thank you for being my biggest fan, my harshest critic, my best friend and now, for marrying me.

Thank you to Dad, an ever-present source of practical and emotional guidance. Thank you for looking after us all, even in the last year and a half when you needed looking after yourself. Thank you for always supporting your children and helping us as we find our own paths through life.

To Mum. Your belief in me gave me the confidence to return to physics after taking time out and you always went far beyond the call of duty in trying to learn enough physics to understand what it was your son did everyday in a basement in South Kensington. I miss you terribly.

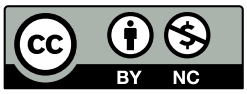

I declare that this thesis is my own work. Information derived from the published and unpublished work of others has been acknowledged in the text and references are given.

Luke Caldwell (2020)

Parts of the work described in this thesis have been published in the following articles:

[1] S. Truppe, H. J. Williams, M. Hambach, L. Caldwell, N. J. Fitch, E. A. Hinds, B. E. Sauer, and M. R. Tarbutt. "Molecules cooled below the Doppler limit". *Nat. Phys.* 13.12 (2017), pp. 1173–1176.

[2] H. J. Williams, S. Truppe, M. Hambach, L. Caldwell, N. J. Fitch, E. A. Hinds, B. E. Sauer, and M. R. Tarbutt. "Characteristics of a magneto-optical trap of molecules". *New J. Phys.* 19.11 (2017), p. 113035.

[3] H. J. Williams, L. Caldwell, N. J. Fitch, S. Truppe, J. Rodewald, E. A. Hinds, B. E. Sauer, and M. R. Tarbutt. "Magnetic Trapping and Coherent Control of Laser-Cooled Molecules". *Phys. Rev. Lett.* 120.16 (2018), p. 163201.

[4] J. A. Blackmore, L. Caldwell, P. D. Gregory, E. M. Bridge, R. Sawant, J. Aldegunde, J. Mur-Petit, D. Jaksch, J. M. Hutson, B. E. Sauer, M. R. Tarbutt, and S. L. Cornish. "Ultracold molecules for quantum simulation: rotational coherences in CaF and RbCs". *Quantum Sci. Technol.* 4.1 (2018), p. 014010.

[5] L. Caldwell, J. A. Devlin, H. J. Williams, N. J. Fitch, E. A. Hinds, B. E. Sauer, and M. R. Tarbutt. "Deep Laser Cooling and Efficient Magnetic Compression of Molecules". *Phys. Rev. Lett.* 123.3 (2019), p. 033202.

[6] L. Caldwell, H. J. Williams, N. J. Fitch, J. Aldegunde, J. M. Hutson, B. E. Sauer, and M. R. Tarbutt. "Long Rotational Coherence Times of Molecules in a Magnetic Trap". *Phys. Rev. Lett.* 124.6 (2020), p. 063001.

[7] L. Caldwell and M. R. Tarbutt. "Sideband cooling of molecules in optical traps". *Phys. Rev. Res.* 2.1 (2020), p. 013251.

Contents

Abstract **2**

Acknowledgements **3**

List of Tables **10**

List of Figures **11**

1 Introduction **13**
1.1 Why ultracold molecules? . . . 13
1.1.1 Ultracold chemistry . . . 13
1.1.2 Strongly correlated quantum systems . . . 14
1.1.3 Precision Measurement . . . 14
1.1.4 Quantum Information . . . 15
1.2 Progress in production of ultracold molecules . . . 15
1.2.1 Assembly from ultracold atoms . . . 15
1.2.2 Direct cooling . . . 16
1.3 This thesis . . . 18

2 Structure of CaF **20**
2.1 Introduction . . . 20
2.2 Molecular equations of motion . . . 20
2.2.1 Non-relativistic molecular Hamiltonian . . . 20
2.2.2 Born-Oppenheimer approximation . . . 22
2.2.3 The radial equation . . . 23
2.2.4 Energy scales in molecules . . . 24
2.2.5 Higher order effects . . . 25
2.3 Labelling states . . . 25
2.3.1 Hund's cases . . . 25
2.3.2 Spectroscopic notation . . . 26
2.3.3 Application to CaF . . . 27
2.4 Ground state effective Hamiltonians . . . 28
2.4.1 Field free . . . 28
2.4.2 Magnetic field . . . 30
2.4.3 Electric field . . . 30
2.5 Electric dipole transitions . . . 30
2.5.1 Transition dipole moment . . . 30
2.5.2 Selection rules . . . 31
2.5.3 Spontaneous emission . . . 32
2.5.4 Vibrational branching . . . 32

3 Laser cooling of molecules: theory **34**
3.1 Introduction . . . 34
3.2 Doppler cooling . . . 34
3.2.1 Two-level atom . . . 34
3.2.2 Doppler limit . . . 36
3.2.3 Application to molecules . . . 37
3.3 Magneto-optical trap . . . 38
3.3.1 Basic principles . . . 38
3.3.2 Application to molecules . . . 39
3.4 Below the Doppler limit . . . 39
3.4.1 Introduction . . . 39
3.4.2 Sisyphus cooling . . . 40
3.4.3 2-level system in lin$\|$lin field . . . 41
3.4.4 Polarisation gradients – $F' = F + 1$ system in lin$\perp$lin field . . . 46
3.4.5 Application to molecules . . . 49
3.4.6 Velocity selective coherent population trapping . . . 51

4 Setup of the experiment **53**
4.1 Introduction . . . 53
4.2 Source . . . 53
4.3 Lasers . . . 55
4.3.1 Preparation of light . . . 55
4.3.2 Delivery to chamber . . . 59
4.3.3 Locking . . . 59
4.4 Magnetic field . . . 59
4.4.1 Slowing coils . . . 59
4.4.2 MOT coils . . . 60
4.4.3 Shim coils . . . 60
4.5 Imaging . . . 61
4.6 Microwaves . . . 62
4.7 Computer control . . . 62

5 Sub-Doppler cooling **63**
5.1 Slowing and the MOT . . . 63
5.1.1 Introduction . . . 63
5.1.2 Molecule number . . . 63
5.1.3 Lifetime . . . 65
5.1.4 Capture velocity . . . 66
5.1.5 Temperature . . . 67
5.1.6 Compressed MOT . . . 68
5.2 Multi-frequency molasses . . . 69
5.2.1 Introduction . . . 69
5.2.2 Cooling time . . . 70
5.2.3 Magnetic field . . . 70
5.2.4 Intensity . . . 72
5.2.5 Beam alignment . . . 73
5.2.6 Systematic error in ballistic expansion temperature measurements . . . 73
5.3 Single-frequency molasses . . . 74
5.3.1 Motivation . . . 74
5.3.2 Simulations . . . 75
5.3.3 Experiment . . . 77

5.3.4 Temperature measurement by ballistic expansion . . . 77
5.3.5 Temperature measurement by phase-space rotation . . . 78
5.3.6 Systematic shifts and uncertainties in phase-space rotation method . . . 83
5.3.7 Dependence of temperature on cooling parameters . . . 85
5.3.8 Magnetic compression . . . 86

6 Coherent control and magnetic trapping 88
6.1 Introduction . . . 88
6.2 Optical pumping . . . 88
6.2.1 Sideband extinction . . . 90
6.2.2 Intensity . . . 90
6.2.3 Duration . . . 91
6.2.4 Total efficiency and limitations . . . 91
6.2.5 Alternative approach . . . 91
6.3 Coherent microwave control . . . 92
6.4 Single-pulse spectroscopy . . . 93
6.4.1 $|1,0,0\rangle \rightarrow |0,1,0\rangle$ transition . . . 93
6.4.2 $|1,0,0\rangle \rightarrow |0,1,1\rangle$ transition . . . 94
6.4.3 Understanding experimental imperfections . . . 96
6.5 Blow away . . . 97
6.6 Magnetic trapping . . . 98
6.6.1 Lifetime . . . 99
6.6.2 Heating rate . . . 101
6.7 Ramsey spectroscopy . . . 101
6.7.1 Ramsey spectroscopy in free space . . . 102
6.7.2 Ramsey spectroscopy in a trap . . . 104

7 Extending rotational coherence times in a magnetic trap 107
7.1 Introduction . . . 107
7.2 Theory . . . 108
7.3 Measurements of g_l and g_r . . . 108
7.3.1 Calibrating the $\mathcal{B}$ field . . . 110
7.3.2 Ramsey spectroscopy . . . 113
7.4 Coherence times . . . 114
7.4.1 Decoherence in magnetic trap . . . 114
7.4.2 Understanding decoherence in the trap . . . 114
7.4.3 Decoherence in free space . . . 119
7.5 Vibrational state dependence . . . 121
7.6 Conclusions . . . 121

8 Sideband cooling of molecules 122
8.1 Introduction . . . 122
8.2 Theory of sideband cooling in state-dependent potentials . . . 124
8.2.1 Raman step . . . 124
8.2.2 Optical pumping step . . . 125
8.3 Stark shift . . . 128
8.4 Simple molecule . . . 129
8.4.1 Linearly polarised light . . . 129
8.4.2 Elliptically polarised light . . . 130
8.4.3 Sideband cooling of simple molecule . . . 131
8.4.4 Heating during optical pumping . . . 132

8.5 Real molecule . . . 134
8.5.1 Reduction to the simplified molecule . . . 134
8.5.2 Residual state mixing . . . 135
8.5.3 Tensor Stark shifts . . . 137
8.6 Real light: a tweezer trap . . . 138
8.6.1 Anharmonicity . . . 139
8.6.2 Polarisation gradients . . . 139
8.7 Cooling recipe and conclusions . . . 141

A Stark shift operator and its matrix elements **143**
A.1 Operator . . . 143
A.2 Matrix elements for $^1\Sigma$ states . . . 145
A.3 Matrix elements for $^2\Sigma$ states . . . 147

Bibliography **150**

List of Tables

2.1 Parameters in effective Hamiltonian for CaF $X^2\Sigma^+$ state. 29
2.2 Selection rules governing electric-dipole transitions between electronic states in molecules. 32
2.3 Branching ratios for decays from the $A^2\Pi_{1/2}$ and $B^2\Sigma^+$ states in CaF. 32

4.1 Laser frequencies and powers used in the experiment. Frequencies are determined from a wavemeter and are accurate to $\sim 600\,\mathrm{MHz}$. 57

5.1 Range of parameters used for capture velocity simulations. 67

7.1 Results of electronic structure calculations for g_l and g_r for a variety of potentially laser-coolable molecules at their equilibrium bond lengths R_e. Calculations by Jeremy Hutson and Jesús Aldegunde [6]. 109

List of Figures

2.1 Schematic of the energy level structure of the $X^2\Sigma^+$, $A^2\Pi$ and $B^2\Sigma^+$ states of CaF. . 27
2.2 The $N = 0$ and $N = 1$ levels of the $X^2\Sigma^+(v = 0)$ state of CaF in magnetic and electric fields . . . 29

3.1 Scattering forces on a two-level atom . . . 35
3.2 Schematics for magneto-optical trapping (a) $F' = F + 1$, (b) $F' \geq F$. . . . 38
3.3 Energy levels of the combined atom–field system. . . . 41
3.4 Cooling of a two-level atom moving in a 1D, blue detuned, standing light wave. . . . 45
3.5 Level diagram for $F = \frac{1}{2} \rightarrow F' = \frac{3}{2}$. . . . 46
3.6 Illustration of Sisyphus mechanism for $F = 1/2 \rightarrow F' = 3/2$ system in a red detuned standing wave composed of two counter propagating laser beams linearly polarised at 90 degrees to each other. . . . 47
3.7 Illustration of Sisyphus mechanism for $F = 1 \rightarrow F' = 1$ system in a blue detuned standing wave composed of two counter-propagating laser beams, linearly polarised at 45 degrees to each other. . . . 50
3.8 Steady-state force along x in an $F = F' = 1$ system moving in a 3D $\sigma^+\sigma^-$ light field as a function of velocity in x direction. . . . 50

4.1 Schematic of the experiment . . . 53
4.2 Schematic of buffer gas cell . . . 54
4.3 Transitions driven in the experiment. . . . 55
4.4 Schematic showing experiment optics . . . 56
4.5 Frequency spectrum of each laser . . . 57
4.6 Schematic of MOT coils . . . 60
4.7 H-bridge circuit used to control the MOT coils. . . . 61

5.1 MOT fluorescence as a function of time after turning off $\mathcal{L}_{21}$ at $t = 55\,\mathrm{ms}$. . . . 64
5.2 Single shot fluorescence image of MOT. . . . 65
5.3 MOT capture velocity measurements. . . . 66
5.4 Temperature of the MOT versus I_{00}. . . . 68
5.5 Compressed MOT. . . . 69
5.6 Temperature measurement in the multi-frequency molasses. . . . 70
5.7 Temperature of molecules as a function of hold time in the multi-frequency molasses. . 71
5.8 Temperature of molecules following the multi-frequency molasses as a function of magnetic field. . . . 71
5.9 Temperature of molecules following the multi-frequency molasses as a function of intensity. 72
5.10 Schematic of molasses cooling schemes. . . . 74
5.11 Dark states in the Λ-enhanced and single-frequency molasses. . . . 76
5.12 Simulations of the three cooling schemes. . . . 77
5.13 Temperature measurements of the single -frequency molasses by ballistic expansion. . . 78
5.14 Temperature measurement by ballistic expansion, highlighting a difficulty of this method for large, cold clouds. . . . 79

5.15 Phase space rotation in a 1D magnetic trap. . . . 80
5.16 Molecule evolution in the 1D harmonic trap. . . . 81
5.17 Image analysis for phase space rotation temperature measurements. . . . 82
5.18 Temperature versus single-frequency molasses parameters. . . . 85
5.19 Sequence for reducing eddy-currents when switching off harmonic trap. . . . 87

6.1 Timing sequence of the coherent control experiments. . . . 89
6.2 Stick spectra showing $\mathcal{L}_{00}$ sideband structure used for optical pumping. . . . 89
6.3 Optimising sideband extinction for optical pumping. . . . 90
6.4 Effect of light intensity on optical pumping. . . . 91
6.5 Effect of optical pumping duration on efficiency. . . . 92
6.6 Single-pulse microwave spectroscopy – depletion of $N = 1$ population versus microwave frequency. . . . 93
6.7 Exploring eddy currents from MOT coil switch off. . . . 94
6.8 Shim coil calibration using microwave spectroscopy. . . . 95
6.9 Rabi flops on the $|1, 0, 0\rangle \rightarrow |0, 1, 1\rangle$ transition and Windfreak chirp. . . . 96
6.10 Blow away pulse. . . . 98
6.11 Rabi flops on the $|0, 1, 1\rangle \rightarrow |1, 2, 2\rangle$ transition. . . . 99
6.12 Magnetic trap loss rate versus helium flow rate for molecules in states $|0, 1, 1\rangle$ and $|1, 2, 2\rangle$. 100
6.13 Ramsey fringes for CaF molecules prepared in a coherent superposition of states $|0\rangle = |N = 0, F = 1, M_F = 1\rangle$ and $|1\rangle = |N = 1, F = 2, M_F = 2\rangle$. . . . 102
6.14 Ramsey data for CaF molecules prepared in a coherent superposition of states $|0\rangle = |N = 0, F = 1, M_F = 1\rangle$ and $|1\rangle = |N = 1, F = 2, M_F = 2\rangle$. . . . 105

7.1 Calculated magnetic sensitivities of transitions $|N\rangle_{\mathrm{str}} \leftrightarrow |N + 1\rangle_{\mathrm{str}}$ for a variety of alkaline-earth fluorides and hydroxides of interest for laser cooling. . . . 110
7.2 Calibration of current in MOT coils. . . . 111
7.3 Calibration of the $\mathcal{B}$ field produced at molecules by MOT coils as a function of current. 112
7.4 Magnetic sensitivity of the transitions $|0\rangle_{\mathrm{str}} \leftrightarrow |1\rangle_{\mathrm{str}}$ and $|1\rangle_{\mathrm{str}} \leftrightarrow |2\rangle_{\mathrm{str}}$. . . . 113
7.5 Ramsey fringes for molecules in the magnetic trap. . . . 114
7.6 Simulations of decoherence mechanisms for molecules in the trap. . . . 115
7.7 Simulation of Ramsey fringes in trap including all decoherence mechanisms. . . . 120
7.8 Ramsey fringes for molecules in free space. . . . 120

8.1 Schematic of the two steps of Raman sideband cooling. . . . 123
8.2 Schematic of the coordinate system used in this chapter. . . . 126
8.3 Energies of the $N = 1$ states of the model molecule as a function of $\alpha_2' I/w$, in the case where $\beta = \pi/24$. . . . 130
8.4 Ratio of tensor Stark shift to scalar Stark shift for the $N = 1$ states of the model molecule, as a function of polarisation angle β from the Z axis. . . . 131
8.5 Ratio of tensor Stark shift to scalar Stark shift for the $N = 1$ states of the model molecule, as a function of ellipticity parameter ξ. . . . 132
8.6 Mean change in n during optical pumping $\overline{\Delta n^{\mathrm{op}}}$ as a function of n and $\omega_{\mathrm{t}0}/\omega_{\mathrm{t}1}$ for $\eta_1 = 0.2$. 133
8.7 Branching ratio as a function of magnetic field for decay from each spin manifold of the $\mathrm{B}^2\Sigma^+(N = 0)$ states of CaF to a different spin manifold within $\mathrm{X}^2\Sigma^+(N = 1)$. . . . 136
8.8 Energy levels of CaF as a function of light intensity, in a magnetic field of 300 G. . . . 137
8.9 Ratio of tensor Stark shift to scalar Stark shift for the $N = 1$ states of CaF. . . . 138
8.10 Calculated elements of the $\mathcal{S}$ tensor, related to the polarisation tensor of the light. . . . 140

Chapter 1

Introduction

1.1 Why ultracold molecules?

The ability to cool atomic systems to ultracold temperatures and control their quantum state has yielded exciting advances across the physical sciences. They include atomic clocks [8–10], quantum degenerate gases [11–14], extraordinarily precise tests of fundamental physics [15–19], sensors for tiny forces [20, 21] and new platforms for quantum simulation and computing [22, 23]. Compared to atoms, molecules possess extra degrees of freedom (rotation and vibration – together ro-vibration) which lead to a more complex internal structure. Many proposals have been made to exploit this richer structure for exciting extensions to work carried out with atoms, as well as to open pathways to completely new fields of study. Some areas where ultracold molecules can provide key advantages over atomic systems are outlined below.

1.1.1 Ultracold chemistry

At temperatures accessible by conventional chemistry experiments, measurements are necessarily averages over a large number of internal states, speeds and orientations of the reactants. The de Broglie wavelength of particles is typically many orders of magnitude smaller than the characteristic range of the interactions between them. At ultracold temperatures—typically defined as less than one millikelvin—it is possible to restrict the reactants to single (or few) quantum states with de Broglie wavelengths comparable to, or even larger than, the interaction scale. Probing the intricate details of the interaction, in principle fully described by quantum mechanics, is possible [24, 25].

Theoretical studies have suggested interesting properties for reactions occurring at these energies. For example Balakrishnan and Dalgarno [26] found that at such low temperatures, reactants are able to tunnel through the reaction barrier leading to non-zero reaction rates in the limit of zero temperature. Chemical reactions occurring in the extreme limit of quantum degeneracy, where the de Broglie wavelength of the particles becomes comparable to the inter-particle spacing, may also be enhanced or suppressed due to many-body effects [27–29]. Although experiments at ultracold temperatures explore conditions well beyond any occurring in nature—sub-millikelivin temperatures are many orders of magnitude colder than even interstellar space—studies of chemical processes at these extreme temperatures are likely to ultimately provide greater understanding of thermally averaged dynamics at higher temperatures.

Ultracold polar molecules are of particular interest for these studies due to the way that interaction strengths between particles can be tuned across broad ranges, potentially providing the means to exert control over reaction rates and outcomes with external fields [30, 31].

1.1.2 Strongly correlated quantum systems

Since the first realisations of Bose-Einstein condensation (BEC) in 1995 [11, 12], ultracold atoms have provided an ideal platform for the study of degenerate many-body quantum systems and there are many excellent reviews on the topic—see for example Ref. [32]. Many-body phenomena rely on interactions between the constituents. Atoms produced in ultracold gases generally have only extremely short-range, or *contact* interactions; they interact only when they come into extremely close proximity with each other. Despite this, the interactions already play a crucial role in the properties of quantum degenerate gases and the study of these weakly interacting trapped quantum gases has been very rich.

In recent years there has been much interest [25, 33] in extending the available experimental platforms to enable exploration of the physics of strongly correlated quantum gases. As such, systems exhibiting long-range and anisotropic interactions—in particular those with dipole-dipole interactions, have attracted a lot of attention. Many experimental platforms are being explored including Rydberg atoms with large electric dipole moments [34, 35] and highly magnetic atoms [36–39]. Hetero-nuclear diatomic molecules are a promising candidate due to the potential for large permanent electric dipole moments and the ability to tune the strength of the inter-molecule interactions with external dc and microwave fields [40, 41]. Ultracold polar molecules produced at high phase-space densities would pave the way for realising a vast range of unique many-body systems with interesting properties [33, 42–47].

Trapping of ultracold polar and non-polar molecules in an optical lattice would enable quantum simulations of many condensed matter models [33, 48] and exploration of their phase diagrams [49]. Notable proposals include extensions of the Hubbard model [50, 51] and a variety of lattice spin models [52–57] which could provide insight into phenomena such as quantum magnetism [58], thought to be important in understanding high-temperature super-conductivity. Schemes to realise topological phases of matter in dipolar gases have also been described [59–61]. Of particular interest is the possibility of engineering a system with topological order which can support anyonic excitations [62, 63]. Such a system could provide a quantum platform resilient to perturbations with enormous opportunity for study in its own right as well as implications for quantum information processing.

1.1.3 Precision Measurement

Various precision measurement experiments which aim to search for evidence of physics beyond the standard model can be enhanced through use of ultracold molecules in place of atoms [64]. Diatomic molecules have been proposed as good candidates for studying parity violation [29, 65, 66] due to the enhanced sensitivity of rovibrational spectra to nuclear effects. In measurements of the electron electric dipole moment (eEDM), sensitivity is greatly enhanced by the enormous internal electric fields of polar molecules [67]. Indeed in this case the current most stringent limits are already set by experiments using molecules [68, 69], but the advent of suitable molecules at ultracold temperatures promises orders of magnitude improvements in coherence times and therefore measurement precision [70]. Molecules have also been used for testing the possibility of time varying fundamental constants [71–74]. Here

sensitivity to variations may be strongly enhanced by probing transitions between close-lying levels of different types (electronic and vibrational) [75–77].

1.1.4 Quantum Information

The coherence times of qubits in quantum information processing devices is typically limited by the coupling strength of the qubits to their environment. In contrast, the number of gate operations that can be performed in this time is determined by the coupling strength between qubits; the greater the coupling strength, the faster operations can be performed. The promise of a universal quantum computer combined with the challenge of balancing these dual requirements is inspiring research on many fronts.

The properties of ultracold molecules are ideally suited to overcoming the problem. Long coherence times, in common with atomic systems, and the ability to tune the electric dipole interaction between molecules with external fields allows for the same qubit to fulfil storage and computational responsibilities [78]. Various schemes have been proposed; molecules in an optical lattice with logic encoded in rotational [79] or vibrational [80, 81] states, optimal control based approaches [82] and proposals that make use of rotational transitions in molecules, conveniently located in the microwave region, to couple them to solid state devices [83, 84].

1.2 Progress in production of ultracold molecules

A broad range of techniques are being pursued to produce samples of cold and ultracold molecules. Some are suited only to certain species of molecule and others are more suited to particular types of experiment and so it is likely that many methods will be required to fully explore the diverse range of applications outlined above. In this section an overview is given of various methods, and their applicability discussed. Two broad approaches have emerged, direct cooling of molecules and assembly from already ultracold atoms.

1.2.1 Assembly from ultracold atoms

Undoubtedly the greatest progress to date towards some of the goals of the previous section has been made by assembling ultracold molecules from ultracold atoms. Clouds of ultracold atoms are overlapped and then weakly bound molecules created via photo- or magneto-association. These weakly bound molecules can then be coherently transferred to the ground state using stimulated Raman adiabatic passage (STIRAP). Magneto-association has had the most success with multiple groups succeeding in producing ensembles of ultracold, ground-state bialkali molecules with high phase space densities [85–90]. Coherent control over rotational and hyperfine states has been demonstrated [91–93] and a quantum degenerate gas of polar KRb molecules produced [94]. Experiments have set new model-independent limits on time variation of the electron-to-proton mass ratio [74] and even begun to investigate quantum effects on collisional properties of the molecules [95].

The technique is limited to producing molecules composed of atoms that can be separately laser cooled but this still results in a broad range of available properties. For example fermionic and bosonic molecules have been produced enabling investigation of the effects of quantum statistics. To date the

only ground-state molecules produced in this way are bialkali species whose ground electronic state has no electronic spin or magnetic moment, a limitation for many condensed matter applications. Long trap-lifetimes in excited triplet states, with associated magnetic moment, have been demonstrated [96] and work is underway to create alkaline-earth molecules with richer structure [97, 98]. However, there remain clear limits on the species that can be created in this way.

1.2.2 Direct cooling

The alternative approach is direct cooling of the molecular species themselves. A number of techniques are being actively pursued and are outlined below. Reaching the ultracold regime often necessitates multiple steps using different techniques to cross different temperature regimes. For each technique discussed we give the approximate temperatures that can be achieved.

1.2.2.1 Buffer gas cooling

One approach which had early success is to cool molecules by collisions with a buffer gas. An inert gas like Helium can be straight-forwardly cooled to very low temperatures in a cryostat and then used as a bath with which to thermalise a sample of molecules. Molecules with appreciable magnetic moments cooled by collisions in this way can easily be loaded into a deep magnetic trap. A wide variety of molecules can be cooled and trapped in this way [99, 100] with typical temperatures of around 1 K and densities of up to 10^9 cm^{-3}.

1.2.2.2 Deceleration from molecular beams

Molecular beams have been a focus of chemical physics for many years and a huge variety of molecular species can be produced in well-collimated beams. A common technique is supersonic expansion where the gas expands from a high-pressure cell through a small aperture into a low-pressure region. In this process particle collisions convert the thermal energy of the molecules to velocity along the direction of the beam and temperatures of a few kelvin can be readily achieved in the frame moving with the molecular beam. Interesting experiments at cold temperatures can be conducted in this moving frame [101] but increasing the experiment time requires increasing the apparatus size so there is a clear advantage to having the molecules stationary in the lab frame.

Various approaches to decelerate and cool the beam in the lab frame have emerged. One technique is to precool the molecules in the high-pressure cell with a buffer gas of cold atoms, created with a helium cryostat. This precooling can result in a beam of molecules that is much slower (a few hundred m s^{-1} or less compared with several hundred m s^{-1}) and has a narrower velocity distribution than a typical hot beam. The approach can be combined with other methods below to produce cold molecules in the lab frame.

Stark decelerators One method is to use electric field gradients to slow molecules in weak-field seeking states. This approach is applicable to any molecule with an electric dipole moment. To decelerate down to rest in the lab frame, hundreds (or thousands) of stages of electrodes can be arranged in an array, known as a 'Stark Decelerator'. This technique has produced well controlled beam sources [102–104] and been used for loading molecules into magnetic or electrostatic traps [105–107]. An

interesting variant loads molecules into a spinning electrostatic quadrupole guide and slows them with centrifugal forces [108]. Trapped molecules with temperatures in the hundreds of millikelvin range and densities of order 10^8 cm^{-3} have been demonstrated with these techniques.

Zeeman decelerators Another conservative decelerator for molecules with magnetic dipole moments makes use of magnetic fields. Here, considerable success has been had with tens of stages of magnetic traps pulsed on and off sequentially to slow a particular velocity group from the beam [109]. Loading into a static magnetic trap has been demonstrated [110] as well as co-trapping with atoms [111]. Temperatures and densities achieved are similar to those demonstrated with electric-field decelerators.

Other Various other methods that have been demonstrated for slowing molecules from beam sources including optical stark deceleration [112], photodissociation [113], kinematic collisions with atoms [114, 115], counter-rotating supersonic nozzles [116, 117] and reflection from a receding paddle [118].

1.2.2.3 Further cooling

The above techniques for deceleration use conservative fields and so conserve the phase-space density of the molecules from the original beam. Trapped samples produced in this way have typical temperatures of tens to hundreds of millikelvin, lower than the initial beam only at the expense of the number of molecules. To decrease the temperature further and increase the phase space density into the region required for many of the applications mentioned in Sec. 1.1, it is necessary to introduce a dissipative mechanism that provides further cooling.

Some approaches have been developed that rely on the electric or magnetic forces on a molecule being dependent on its internal state. A molecule in a conservative potential that climbs a potential hill, exchanging kinetic for potential energy, can then have that energy dissipated by being transferred irreversibly to another internal state that interacts differently with the field. An example is the optoelectronic cooling technique used in [119]. Here the authors were able to trap 3×10^5 formaldehyde molecules at 420 µK, well into the ultracold regime.

Another proposal of similar principles was presented in Ref. [120]. Molecules are prepared in a magnetic trap and an optical dipole trap is then placed high up the side of the trap potential such that the most energetic molecules are momentarily stationary there. A single excitation can then induce a transition to a different state that drops the molecules into the dipole trap with extremely low kinetic energy. Moving the dipole trap down the potential one can collect many molecules at low temperature.

A final example of this type of approach is evaporative cooling, commonly used in atomic physics to lower the final temperature of atoms towards quantum degeneracy [11]. An RF knife is used to selectively remove hot molecules from a conservative trap by transferring them to an untrapped internal state. If the sample is of sufficient density, the remaining molecules can rethermalise by collisions to lower their overall temperature. Applying this technique directly to warm molecules has proven difficult [121] but a recent experiment has observed bimolecular collisions for the first time [122] and it is likely, as with atoms, to be a key tool in bridging the gap between the ultracold regime and quantum degeneracy.

Another approach is to make use of well established techniques for producing ultracold atoms and then use them to sympathetically cool molecules by collisions. This technique has the advantage of

not requiring high initial densities of molecules—a high density of atoms is sufficient—and potentially allows for cooling without loss of molecules. The technique requires overlapping atoms and molecules in the same trap which has been demonstrated [111].

1.2.2.4 Laser cooling

Perhaps the most obvious solution is to try to extend the extraordinary success of laser cooling atoms to molecules. This has proven very challenging. The problem is that slowing a typical molecule to rest from a thermal beam requires scattering many thousands of photons. In general a single cycle of photon absorption followed by spontaneous emission can leave the molecule in a huge range of ro-vibrational states, thus ending the cooling cycle. Leaks to a few other levels can be managed by adding repump lasers—as is frequently done in atomic systems—but this approach quickly becomes impractical when faced with decay paths to tens or hundreds of other levels as in a typical molecule.

Fortunately, in 2004 [123], it was determined that for a few classes of molecules it is possible to find an excited state that decays back to a useful ground state. The key principle is that the electronic excitation associated with the absorption of the optical photon should not perturb the molecular bond. In this case, when the molecule decays from the excited state, it remains in the same vibrational state. The situation is realised in many alkaline-earth monohalides where one of the electrons in the outer shell of the alkaline-earth atom is involved in the bond with the halogen and the other is almost entirely localised around the alkaline-earth atom. This unpaired electron can—to a very good approximation—be freely excited without perturbing the molecular bond. In 2008, the combination of this principle with appropriate angular-momentum and parity selection rules led to the proposal of a (nearly) closed cycling transition in a molecule [124].

Experimental results soon followed. Many of the ground-breaking first experiments were done at Yale using SrF molecules. In 2009, they demonstrated the ability to cycle around 150 photons using only a single repump laser [125]. By adding a further repump laser, they showed laser cooling of a beam of molecules in 1D in 2010 [126], and slowing of the beam by radiation pressure in 2012 [127].

The workhorse of laser-cooled atom experiments is the magneto-optical trap (MOT) which both traps and cools atoms in three dimensions. The cold, dense samples created by the MOT serve as the starting point for almost all experiments with ultracold atoms and a molecular counterpart was the holy grail of molecule laser cooling experiments for many years. A 2D MOT of YO was demonstrated at JILA in 2013 [128] and in 2014, the Yale group demonstrated the first 3D MOT of molecules [129].

Since then, the field of laser-cooled molecules has expanded rapidly. In addition to the original MOT of SrF, 3D MOTs have now been demonstrated with CaF [2, 130] and YO [131]. Transverse cooling has been achieved for beams of both SrOH [132], the first polyatomic species, and YbF, a species of interest for eEDM searches [133]. The CaF experiment here at Imperial first demonstrated laser slowing in 2014 [134], with velocities suitable for capture in a MOT reached in 2017 [135].

1.3 This thesis

This thesis details our work on realising the world's second 3D MOT of molecules, cooling them below the Doppler limit for the first time in an optical molasses and developing the techniques required for coherent control over their internal state. The thesis is structured as follows: In Chapter 2 we give a

basic overview of molecular structure, which is then applied to the theory of laser cooling molecules in Chapter 3. In Chapter 4 we give details of the apparatus used in the experimental chapters of the thesis. Chapter 5 presents our experimental results on the MOT, and the implementation and improvement of an optical molasses. In Chapter 6 we present our results on coherent manipulation of the internal state of the molecules and loading them into a magnetic trap. In Chapter 7 we explore ways of using the internal structure of the molecule to extend the coherence time of rotational superpositions in the magnetic trap. Finally, in Chapter 8, we show theoretically how Raman sideband cooling could be applied to molecules in optical tweezer traps.

Chapter 2

Structure of CaF

2.1 Introduction

The tools of laser cooling are well established for atomic systems. To understand the complications in applying these to molecules, it is important to understand the additional complexity in the molecules' internal structure. In this chapter, we give a basic overview of the energy spectrum of a molecule. Much of the discussion is applicable to many diatomic molecules but we will ultimately focus specifically on CaF.

2.2 Molecular equations of motion

The full equations of motion for a diatomic molecule are highly complex but we can gain considerable insight by making some well-founded approximations. These approximations will allow us to separate the molecular dynamics into different types of motion that occur at different energy scales; electronic, vibrational and rotational motion.

2.2.1 Non-relativistic molecular Hamiltonian

The first approximation we will make is to start with the non-relativistic Hamiltonian for the molecule,

$$H = T_{\mathrm{n}} + T_{\mathrm{e}} + V_{\mathrm{nn}} + V_{\mathrm{en}} + V_{\mathrm{ee}}. \tag{2.1}$$

Here T_{n} is the kinetic energy operator for the nuclei, T_{e} the kinetic energy operator for the electrons and V_{nn}, V_{en}, V_{ee} characterise the nucleus–nucleus, electron–nucleus and electron–electron Coulomb

interactions respectively:

$$T_{\mathrm{n}} = -\frac{\hbar^2}{2M_A}\nabla_A^2 - \frac{\hbar^2}{2M_B}\nabla_B^2, \tag{2.2a}$$

$$T_{\mathrm{e}} = -\frac{\hbar^2}{2m_{\mathrm{e}}}\sum_{i=1}^{N_{\mathrm{e}}}\nabla_i^2, \tag{2.2b}$$

$$V_{\mathrm{nn}} = \frac{Z_A Z_B e^2}{4\pi\epsilon_0 |\vec{R}_{AB}|}, \tag{2.2c}$$

$$V_{\mathrm{en}} = -\frac{e^2}{4\pi\epsilon_0}\sum_{i=1}^{N_{\mathrm{e}}}\left(\frac{Z_A}{r_{iA}} + \frac{Z_B}{r_{iB}}\right), \tag{2.2d}$$

$$V_{\mathrm{ee}} = \frac{e^2}{4\pi\epsilon_0}\sum_{i<j=1}^{N_{\mathrm{e}}}\frac{1}{r_{ij}}. \tag{2.2e}$$

In Eqs. (2.2), we have labelled the two nuclei A and B. M_A and M_B are their respective masses, Z_A and Z_B their atomic numbers, and $\vec{R}_{AB}$ the displacement between them. We also introduce $\vec{R}_X$, the displacement of nucleus X from the origin and $\vec{\nabla}_X$ the gradient operator with respect to this displacement. The summations are over the N_{e} electrons of the molecule with r_{iX} the separation of i'th electron from nucleus X and r_{ij} the separation of the i'th and j'th electrons.

We can simplify the kinetic energy terms by switching to nuclear centre of mass coordinates,

$$\vec{R}_{CM} = \frac{M_A\vec{R}_A + M_B\vec{R}_B}{M_A + M_B}, \qquad \vec{R}_{AB} = \vec{R}_A - \vec{R}_B, \qquad \mu = \frac{M_A M_B}{M_A + M_B}. \tag{2.3}$$

Since we are interested in the internal state of the molecule rather than the translation of the centre of mass, we neglect the overall translation term and are left with

$$T_{\mathrm{n}} = -\frac{\hbar^2}{2\mu}\nabla_{AB}^2, \tag{2.4a}$$

$$T_{\mathrm{e}} = -\frac{\hbar^2}{2m_{\mathrm{e}}}\sum_{i=1}^{N}\nabla_i'^2 - \frac{\hbar^2}{2(M_A + M_B)}\sum_{i,j}\nabla_i'\cdot\nabla_j'. \tag{2.4b}$$

The primes on the gradient operators in the expression for T_{e} indicate that the derivatives are with respect to the nuclear centre of mass coordinates. The second term in the expression for T_{e} is called the mass polarisation term. It accounts for small fluctuations in the centre of mass of the whole molecule relative to the nuclear centre of mass as the electrons move around. The interaction terms are unaffected by the coordinate transform since they involve only relative coordinates.

The eigenstates of the molecule satisfy

$$H\psi(\vec{x}, \vec{R}_{AB}) = E\psi(\vec{x}, \vec{R}_{AB}), \tag{2.5}$$

where $\vec{x} = \{\vec{r}\}$ denotes the full set of electronic coordinates. We can choose to expand the eigenstates $\psi(\vec{x}, \vec{R}_{AB})$ as

$$\psi(\vec{x}, \vec{R}_{AB}) = \sum_q \phi_q^e(\vec{R}_{AB}; \vec{x})\chi_q(\vec{R}_{AB}), \tag{2.6}$$

where the $\phi_q^e(\vec{R}_{AB};\vec{x})$ satisfy

$$H_{\rm e}(\vec{R}_{AB};\vec{x})\phi_q^e(\vec{R}_{AB};\vec{x}) = \left(T_{\rm e}(\vec{x}) + V_{\rm ee}(\vec{x}) + V_{\rm en}(\vec{R}_{AB};\vec{x})\right)\phi_q^e(\vec{R}_{AB};\vec{x}) = E_q^e(R_{AB})\phi_q^e(\vec{R}_{AB};\vec{x}). \quad (2.7)$$

The notation $f(\lambda;\vec{x})$ means that f is a function of the coordinates $\vec{x}$ which depends on the parameter λ. Equation (2.7) is the Schrödinger equation for the electrons when the nuclei are fixed in place; the internuclear vector $\vec{R}_{AB}$ is demoted to a parameter of this modified Hamiltonian. The $\phi_q^e(\vec{R}_{AB};\vec{x})$ are the electronic wavefunctions and the corresponding energies $E_q^e(R_{AB})$ depend only on the magnitude of $\vec{R}_{AB}$. The simplifying assumptions used in the following sections will rely on these wavefunctions well approximating the true electronic wavefunctions. Qualitatively, this seems reasonable because the mass difference between the electrons and the nuclei means that the electronic motion is much faster than the nuclear motion; the $\phi_q^e(\vec{R}_{AB};\vec{x})$ can adiabatically follow the motion of the nuclei. Note that the $\phi_q^e(\vec{R}_{AB};\vec{x})$ can be chosen to be simultaneous eigenstates of L_λ, the total electronic orbital angular momentum along the internuclear axis, because $[L_\lambda, H_{\rm e}] = 0$,

$$L_\lambda\phi_q^e(\vec{R}_{AB};\vec{x}) = \Lambda\phi_q^e(\vec{R}_{AB};\vec{x}). \quad (2.8)$$

2.2.2 Born-Oppenheimer approximation

Substituting Eq. (2.6) into Eq. (2.5) gives

$$\sum_q (T_{\rm n} + V_{\rm nn} + H_{\rm e})\phi_q^e(\vec{R}_{AB};\vec{x})\chi_q(\vec{R}_{AB}) = E\sum_q \phi_q^e(\vec{R}_{AB};\vec{x})\chi_q(\vec{R}_{AB}). \quad (2.9)$$

Multiplying through from the left by $\phi_p^{e*}(\vec{R}_{AB};\vec{x})$, integrating over the electronic coordinates and using the orthogonality of the electronic wavefunctions we have

$$\sum_q \int {\rm d}\vec{x}\phi_p^{e*}(\vec{R}_{AB};\vec{x})T_N\phi_q^e(\vec{R}_{AB};\vec{x})\chi_q(\vec{R}_{AB}) + \left(\frac{Z_A Z_B e^2}{4\pi\epsilon_0 R_{AB}} + E_p^e(R_{AB})\right)\chi_p(\vec{R}_{AB}) = E\chi_p(\vec{R}_{AB}). \quad (2.10)$$

The first term on the left hand side can be expanded further,

$$\begin{aligned}
&\sum_q \int {\rm d}\vec{x}\phi_p^{e*}(\vec{R}_{AB};\vec{x})T_N\phi_q^e(\vec{R}_{AB};\vec{x})\chi_q(\vec{R}_{AB}) = \\
&\quad -\frac{\hbar^2}{2\mu}\nabla^2_{\vec{R}_{AB}}\chi_p(\vec{R}_{AB}) - \frac{\hbar^2}{2\mu}\sum_q\left(\int {\rm d}\vec{x}\phi_p^{e*}(\vec{R}_{AB};\vec{x})\nabla_{\vec{R}_{AB}}\phi_q^e(\vec{R}_{AB};\vec{x})\right)\nabla_{\vec{R}_{AB}}\chi_q(\vec{R}_{AB}) \\
&\quad -\frac{\hbar^2}{2\mu}\sum_q\left(\int {\rm d}\vec{x}\phi_p^{e*}(\vec{R}_{AB};\vec{x})\nabla^2_{\vec{R}_{AB}}\phi_q^e(\vec{R}_{AB};\vec{x})\right)\chi_q(\vec{R}_{AB}).
\end{aligned} \quad (2.11)$$

The second and third terms in Eq. (2.11) are those which couple the electronic and nuclear motion and involve gradients of the electronic wavefunctions with respect to the nuclear coordinates. Provided we are far from avoided crossings between the different potential energy curves corresponding to different electronic states, these quantities are very small and, for the present purposes, can be neglected. The dropping of these terms is known as the Born-Oppenheimer approximation. Returning to Eq. (2.10),

we now see that that the nuclear wavefunctions $\chi_p(\vec{R}_{AB})$ obey a nuclear Schrödinger equation,

$$\left(-\frac{\hbar^2}{2\mu}\nabla^2_{AB} + V_{\rm n}(R_{AB})\right)\chi_p(\vec{R}_{AB}) = E\chi_p(\vec{R}_{AB}). \tag{2.12}$$

The nuclei move in the central potential $V_{\rm n}(R_{AB}) = \frac{Z_A Z_B e^2}{4\pi\epsilon_0 R_{AB}} + E^e_p(R_{AB})$ formed from the combination of the mutual electrostatic repulsion of the nuclei and the potential created by the wavefunctions of the electrons. To solve Eq. (2.12), we express ∇^2_{AB} in polar coordinates,

$$\nabla^2_{AB} = \frac{1}{R^2_{AB}}\frac{\partial}{\partial R_{AB}}\left(R^2_{AB}\frac{\partial}{\partial R_{AB}}\right) + \frac{\vec{R}^2}{R^2_{AB}} \tag{2.13}$$

where we have introduced the nuclear angular momentum operator $\vec{R}$, not to be confused with the various position variables which all have subscripts. Equation (2.12) can now be solved using the ansatz

$$\chi_p(R_{AB}, \Theta, \Phi) = \frac{1}{R_{AB}} f_v(R_{AB}) g(\Theta, \Phi), \tag{2.14}$$

where Θ and Φ are the spherical polar angular coordinates of $\vec{R}_{AB}$. As always for a central potential, the angular eigenfunctions $g(\Theta, \Phi)$ are the spherical harmonics,

$$g(\Theta, \Phi) = Y_{R,m_R}(\Theta, \Phi). \tag{2.15}$$

The Y_{R,m_R} are eigenstates of both $\vec{R}^2$ and R_Z, the projection of $\vec{R}$ onto the laboratory Z axis:

$$\vec{R}^2 Y_{R,m_R} = R(R+1)Y_{R,m_R}, \tag{2.16a}$$

$$R_z Y_{R,m_R} = m_R Y_{R,m_R}. \tag{2.16b}$$

We are finally left with the radial equation,

$$\left(-\frac{\hbar^2}{2\mu}\frac{\mathrm{d}^2}{\mathrm{d}R^2_{AB}} + \frac{R(R+1)}{2\mu R^2_{AB}} + E^e_p(R_{AB}) + \frac{Z_A Z_B e^2}{4\pi\epsilon_0 R_{AB}} - E\right) f_v(R_{AB}) = 0. \tag{2.17}$$

2.2.3 The radial equation

Equation (2.17) can be solved numerically but to gain some physical insight we note that the low-lying nuclear wavefunctions for any stable molecule are usually well localised in a region of the potential which is harmonic. This is because of the strength of molecular bond and the large mass of the nuclei. The potential created by the electrons can be Taylor expanded about the equilibrium separation $R^{\rm eq}_{AB}$,

$$\begin{aligned} E_p(R_{AB}) &\simeq E_p(R^{\rm eq}_{AB}) + \frac{1}{2}\left(\frac{\mathrm{d}^2 E_p}{\mathrm{d}R^2_{AB}}\right)\Big|_{R_{AB}=R^{\rm eq}_{AB}}(R_{AB} - R^{\rm eq}_{AB})^2 + \ldots \\ &\simeq E_p(R^{\rm eq}_{AB}) + \frac{1}{2}k(R_{AB} - R^{\rm eq}_{AB})^2 + \ldots, \end{aligned} \tag{2.18}$$

where $k = \left(\frac{\mathrm{d}^2 E_p}{\mathrm{d}R_{AB}^2}\right)\Big|_{R_{AB}=R_{AB}^{\mathrm{eq}}}$. If we now define $E_r = \frac{R(R+1)}{2\mu {R_{AB}^{\mathrm{eq}}}^2}$ and $E_v = E - E_p(R_{AB}^{\mathrm{eq}}) - E_r$, we reduce Eq. (2.17) to the harmonic oscillator equation,

$$\left(-\frac{\hbar^2}{2\mu}\frac{\mathrm{d}^2}{\mathrm{d}R_{AB}^2} + \frac{1}{2}k(R_{AB} - R_{AB}^{\mathrm{eq}})^2 - E_v\right) f_v(R_{AB}) = 0. \tag{2.19}$$

The eigenenergies are $E_v = \hbar\omega(1/2 + v)$, where $\omega = \sqrt{k/\mu}$, and correspond to eigenstates involving the familiar Hermite polynomials.

Whilst this first order approximation works reasonably well for low lying vibrational states, of course as the internuclear separation deviates from R_{AB}^{eq}, the effective potential seen by the nuclei is no longer well approximated as harmonic. This anharmonicity becomes important as higher vibrational states are excited. The exact form of the electronic potential as a function of R_{AB} can be obtained from numerical solutions of Eq. (2.7) but various closed form approximations have been developed. A particularly successful one is the Morse potential,

$$E_p(R_{AB}) \simeq D_{\mathrm{e}}(1 - e^{\beta(R_{AB}-R_{AB}^{\mathrm{eq}})})^2, \tag{2.20}$$

where D_{e} is the well depth and β a parameter related to the width of the well. This potential has the required behaviour that it approaches that of free atoms in the limit of large R, while at small R ($R \ll R_{AB}^{\mathrm{eq}}$)), the potential is dominated by the electrostatic repulsion between the two nuclei. The Schrödinger equation for the Morse potential has exact analytical solutions with eigenvalues and eigenstates given by

$$E_v = 1 - \frac{1}{\lambda^2}\left(\lambda - v - \frac{1}{2}\right)^2, \tag{2.21}$$

$$f_v = A_v z^{\lambda - v - \frac{1}{2}} e^{-\frac{1}{2}z} L_v^{(2\lambda - 2v - 1)}(z), \tag{2.22}$$

where $\lambda = \frac{\sqrt{2\mu D_{\mathrm{e}}}}{\beta\hbar}$, $z = 2\lambda e^{-(R_{AB}-R_{AB}^{\mathrm{eq}})}$, $A_v = \left[\frac{v!(2\lambda-2v-1)}{\Gamma(2\lambda-v)}\right]^{\frac{1}{2}}$ is a normalisation factor,[1] and $L_v^{(\alpha)}(z)$ is a generalised Laguerre polynomial (see for example [136]).

2.2.4 Energy scales in molecules

The most important result from this treatment is that the total molecular wavefunction can be factored out into electronic, vibrational and rotational parts with their respective motion occurring at different energy scales,

$$\psi_{q,v,R,m_R}(\vec{R}_{AB}, \vec{x}) = \phi_q^e(\vec{R}_{AB}; \vec{x})\frac{1}{R_{AB}} f_v(R_{AB}) Y_{R,m_R}(\Theta, \Phi). \tag{2.23}$$

The highest energy scale in a molecule is E_{e}, the energy associated with transitions between the different electronic states which is of order $\alpha^2 m_{\mathrm{e}} c^2$ where α is the fine structure constant. Typically values of E_{e} are a few eV or a few hundred THz. The spacing between vibrational levels is E_v. For low lying vibration levels this is $\sim \hbar\omega$. We can make an order of magnitude estimate for how this energy compares with E_{e}. The confining forces on the nuclei are similar to those on the electrons but the masses are very different. Since $\omega = \sqrt{k/\mu}$, E_v is approximately $\sqrt{m/M}E_{el} \sim 10^{-2}E_{el} \sim 10^{-2}$ eV or a few THz. Finally, the

[1] For the avoidance of doubt, Γ here is the gamma function rather than Γ used later as a scattering rate!

smallest energy scale in our coarse structure is associated with rotational motion. In the rigid rotor approximation, the rotational energy of a given rotational level is $E_r = \hbar^2 \frac{R(R+1)}{2I} \equiv BR(R+1)$ where I is the moment of inertia $I \sim \mu {R_{AB}^{\text{eq}}}^2$. Typically $E_r \sim 10^{-4} E_{el} \sim 10^{-4}$ eV or a few tens of GHz.

2.2.5 Higher order effects

The treatment of Sec. 2.2 has allowed us to approximate the energies and wavefunctions of the molecular eigenstates. Further accuracy requires consideration of the effects of the terms we neglected in our approximations. These are terms such as the centrifugal distortion caused by rotation of the molecule and the magnetic interactions that arise from a full relativistic treatment—including those involving the spin degrees of freedom of the electrons and nuclei. Even our relatively simple treatment so far required calculation of the electronic wavefunctions. Such calculations are necessary to predict any of the properties accurately but are a formidable task for all but the simplest molecules. The usual approach is to formulate an effective Hamiltonian acting only within a single vibrational level. This effective Hamiltonian is derived from the full Hamiltonian by using perturbation theory to absorb the effects of matrix elements that couple to states outside this subspace into new parameters of the effective Hamiltonian. The values of these parameters will depend on the details of the electronic wavefunctions but can then be experimentally determined by fitting to spectroscopic data. A full derivation of such an effective Hamiltonian is given in, for example, Chapter 7 of Brown and Carrington [137]. In Sec. 2.4 we give the effective Hamiltonian for the ground state of CaF with and without static external fields. Appendix A develops an effective Hamiltonian for the ac Stark Shift produced by an off-resonant light field.

2.3 Labelling states

The spherical symmetry of an atom means that atomic Hamiltonians commute with both $\vec{J}^2$ and $\vec{L}^2$. Their associated quantum numbers J and L, along with the spin S are normally used to label states. In molecules, the additional nuclei breaks this symmetry and so J and L are no longer *good quantum numbers*.

The various possible ways that electronic and nuclear angular momenta couple to each other makes finding meaningful *good quantum numbers* in a generic molecule challenging. Fortunately, diatomic molecules retain cylindrical symmetry around their inter-nuclear axis—which we will call λ—and there are some relatively simple rules.

2.3.1 Hund's cases

Hund's coupling cases are idealised situations where specific terms which couple angular momenta in the molecular Hamiltonian dominate over other terms and provide a helpful starting point for understanding molecular spectra. There are five cases, denoted by the letters (a) through (e), but the relevant states of CaF are well described by cases (a) and (b) so we will discuss only those here.

2.3.1.1 Case (a)

In Hund's case (a), the interaction between the nuclear rotation $\vec{R}$ and the electronic motion is very weak. The electronic orbital angular momentum $\vec{L}$ and electronic spin angular momentum $\vec{S}$ are strongly coupled both to each other—through the spin-orbit interaction—and to the internuclear axis. Both $\vec{L}$ and $\vec{S}$ precess around the internuclear axis and so their projections along this axis Λ and Σ are well defined. The basis states are $|\Lambda\rangle\,|S,\Sigma\rangle\,|J,\Omega\rangle$, where the quantum numbers are defined by:

$$L_\lambda\,|\Lambda\rangle = \Lambda\,|\Lambda\rangle\,, \tag{2.24}$$
$$\vec{S}^2\,|S,\Sigma\rangle = S(S+1)\,|S,\Sigma\rangle\,, \tag{2.25}$$
$$S_\lambda\,|S,\Sigma\rangle = \Sigma\,|S,\Sigma\rangle\,, \tag{2.26}$$
$$\vec{J}^2\,|J,\Omega\rangle = J(J+1)\,|J,\Omega\rangle\,, \tag{2.27}$$
$$J_\lambda\,|J,\Omega\rangle = \Omega\,|J,\Omega\rangle\,. \tag{2.28}$$

Here $\vec{J}$ is the total angular momentum in the absence of nuclear spin $\vec{J} = \vec{R} + \vec{L} + \vec{S}$.

2.3.1.2 Case (b)

In Hund's case (b), the spin-orbit coupling is weak—or non-existent for molecules where either L or S is zero. In this case Ω is not well defined. The electronic orbital angular momentum $\vec{L}$ precesses around the internuclear axis. The rotational angular momentum $\vec{R}$ first couples to $\vec{L}$ to form a resultant $\vec{N}$ which then couples to $\vec{S}$ to form the total angular momentum $\vec{J}$. The basis states are $|\Lambda\rangle\,|(N,S)J\rangle$ where the quantum numbers are defined by:

$$L_\lambda\,|\Lambda\rangle = \Lambda\,|\Lambda\rangle\,, \tag{2.29}$$
$$\vec{N}^2\,|(N,S)J\rangle = N(N+1)\,|(N,S)J\rangle\,, \tag{2.30}$$
$$\vec{S}^2\,|(N,S)J\rangle = S(S+1)\,|(N,S)J\rangle\,, \tag{2.31}$$
$$\vec{J}^2\,|(N,S)J\rangle = J(J+1)\,|(N,S)J\rangle\,. \tag{2.32}$$

2.3.2 Spectroscopic notation

In a diatomic molecule, the different electronic states are labelled as

$$(\text{unique letter})^{2S+1}|\Lambda|^{+/-}_{|\Omega|}. \tag{2.33}$$

The spectroscopic label starts with a unique letter designating the electronic state. The ground state is labelled X and other letters used for higher lying levels (e.g. $A, B, C, \ldots$).[2] The superscript $(2S+1)$ is the spin multiplicity, followed by $|\Lambda|$, the magnitude of the projection of the electronic orbital angular momentum onto the internuclear axis. By analogy with atomic spectroscopic labels, the values of $|\Lambda| = 1, 2, 3, \ldots$ are denoted $\Sigma, \Pi, \Delta, \ldots$ etc.[3]. The subscript $|\Omega|$ is the magnitude of the projection of the total electronic angular momentum onto the internuclear axis. For states with $\Lambda = 0$, $|\Omega|$ is implied

[2]The labelling of the electronically excited states proceeds approximately alphabetically but sometimes breaks from this when new, lower lying states are discovered later.

[3]The Σ label is not to be confused with the quantum number for the projection of $\vec{S}$ onto the internuclear axis.

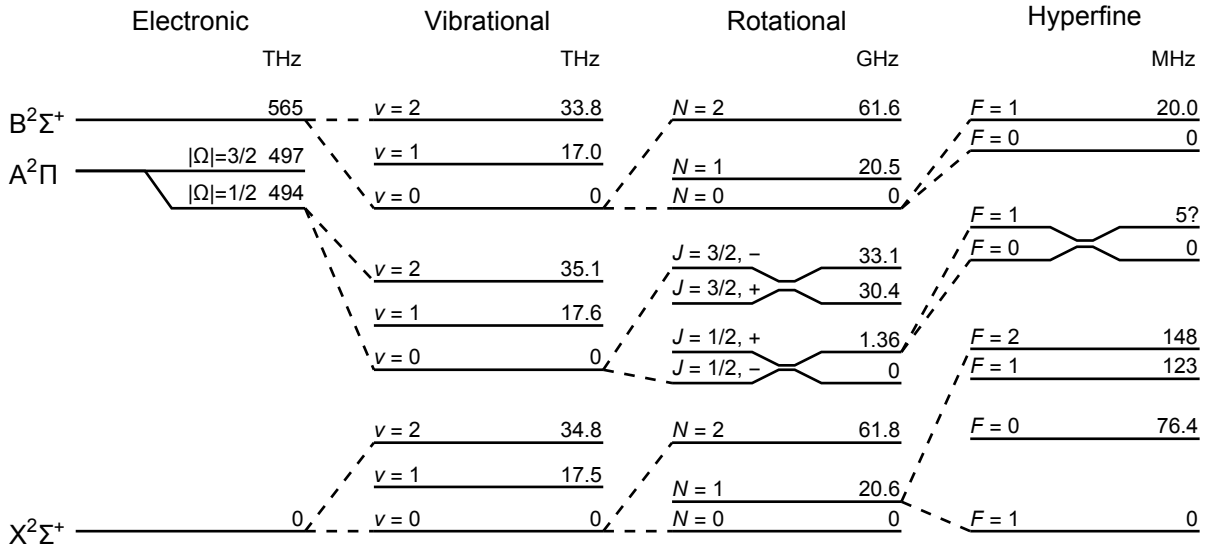

Figure 2.1: Schematic of the level structure of the $X^2\Sigma^+$, $A^2\Pi$ and $B^2\Sigma^+$ states of CaF. From left to right, the four panels show the electronic, vibrational, rotational and hyperfine structure of each of the states. In each we focus on the sub-level most relevant to the laser cooling experiments described in this thesis. All energies are given relative to the lowest energy state in sub-level shown, the units are given at the top right of each panel. The $+/-$ symbols labelling the rotational sub-levels of the $A^2\Pi_{1/2}(v = 0)$ state indicate their parity. The hyperfine splitting of the $A^2\Pi_{1/2}(v = 0, J = 1/2, +)$ state is unknown but estimated to be 5 MHz [138].

from the value of other quantum numbers and so this part is often omitted. Finally, the superscript $+/-$ is sometimes used to indicate the reflection symmetry of the wavefunction under reflection in a plane containing the internuclear axis.

2.3.3 Application to CaF

All work described in this thesis relates to $^{40}Ca^{19}F$, referred to throughout as CaF. The molecule has an ionic bond, with the calcium atom essentially donating an electron to the fluorine atom. This leaves a single unpaired electron, almost entirely localised around the Ca atom and almost independent of the molecular bond. This localisation means the electron can be excited without significantly affecting the potential seen by the nuclei. As we will see this is an important property of CaF for our purposes as it enables laser cooling. The calcium and fluorine nuclei have spins of 0 and 1/2 respectively. In this section, we describe the three electronic states relevant to this thesis, their sub-structure is shown in Fig. 2.1.

2.3.3.1 The $X^2\Sigma^+$ state

The ground electronic state of CaF is $X^2\Sigma^+$. The projection of the orbital angular momentum on the internuclear axis Λ is zero and the state has $S = 1/2$ from the single unpaired electron. The + super script indicates the even parity of the ground rotational state.

The state is best described in the case (b) basis. The spin-rotation interaction couples the electronic spin $S = 1/2$ to the rotational angular momentum, to form $\vec{J} = \vec{S} + \vec{N}$. Note that in this case $\vec{N} = \vec{R}$ because there is no electronic orbital angular momentum. Each rotational level is split by this

spin-rotation interaction into two levels with $J = N \pm 1/2$. These levels are then further split by the hyperfine interaction which couples $\vec{J}$ to the nuclear spin $\vec{I}$ to give $\vec{F} = \vec{I} + \vec{J}$. The hyperfine interaction is actually of similar size to the spin-rotation interaction in CaF and so the diagonalisation must be done simultaneously. Throughout this thesis, this structure will be referred to as hyperfine structure although strictly it is formed from a combination of the spin-rotation and hyperfine interactions. In the $N = 1$, first rotationally excited state—which forms the ground state of our cycling transition—this gives four states labelled by $F = 1^-, 0, 1^+, 2$ as shown on the right hand side of Fig. 2.1. Note that there are two states with $F = 1$ and, where necessary, we use the $\pm$ superscript to distinguish them; the $+$ state is higher in energy.

2.3.3.2 The $A^2\Pi$ state

The lowest-lying electronically excited level is the $A^2\Pi$ state with $|\Lambda| = 1$. The decay rate from this state is $2\pi \times 8.3\,\text{MHz}$ [138]. The spin-orbit interaction creates two states $A^2\Pi_{1/2}$ and $A^2\Pi_{3/2}$ with $|\Omega| = 1/2$ and $3/2$ respectively. The $A^2\Pi_{1/2}$ state lies 494.5 THz above the X state and the $A^2\Pi_{3/2}$ state a further 2.2 THz above that [139]. Both states are best described in the case (a) basis but neither the spin-orbit, nor rigid-body rotation terms are diagonal in this basis. The off-diagonal terms of these slightly mix the Π states with the nearby $B^2\Sigma$ state (described below). The mixing occurs only between states of the same parity and so lifts the degeneracy of the $\Omega = \pm 1/2$ and $\pm 3/2$ pairs of states. This effect is known as Λ-doubling and, for the $A^2\Pi_{1/2}$ state used in our cycling transition, results in a pair of states of opposite parity separated by 1.36 GHz [139]. In the experiment, we address the even parity component of the lowest rotational level within $A^2\Pi_{1/2}$ which has $J = 1/2$. Note that the even parity component lies above the negative parity component. This level is further split by the hyperfine interaction into two states with $F = 0$ and 1. The splitting of the levels is not resolved but is estimated to be $\sim 5\,\text{MHz}$ [138].

2.3.3.3 The $B^2\Sigma^+$ state

The next lowest-lying electronically excited level is the $B^2\Sigma^+$ state. The decay rate from this state is $2\pi \times 6.3\,\text{MHz}$ [140]. It lies 564.8 THz above the X state or some 70 THz above the A state. However it decays almost exclusively directly to the X state with an experimentally measured branching ratio to the A state below 1×10^{-6} [135]. Its character, despite the small mixing with the $A^2\Pi$ state described above, is very similar to that of the X state and also best described in the case (b) basis. The hyperfine interaction in the $N = 0$ rotational ground state—the only rotational level relevant for the work described in this thesis—gives rise to two states with $F = 0$ and 1, separated by 20 MHz.

2.4 Ground state effective Hamiltonians

2.4.1 Field free

The effective field-free Hamiltonian for a single vibrational level of a $^2\Sigma$ state molecule with a single nuclear spin, appropriate for the ground state of CaF, is

$$H_{\text{ff}} = B\vec{N}^2 - D\vec{N}^4 + \gamma\vec{S}\cdot\vec{N} + b\vec{I}\cdot\vec{S} + c(I\cdot\hat{\lambda})(S\cdot\hat{\lambda}) + C\vec{I}\cdot\vec{N}, \tag{2.34}$$

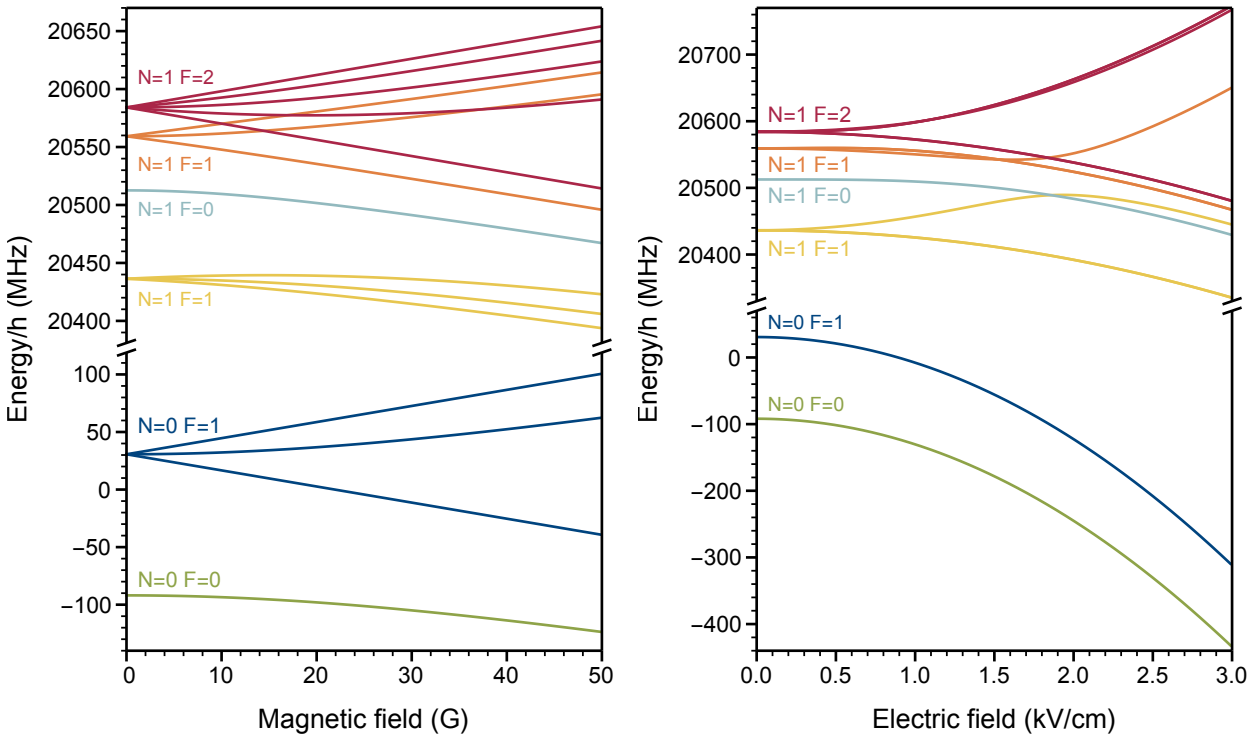

Figure 2.2: The $N = 0$ and $N = 1$ levels of the $X^2\Sigma^+(v = 0)$ state of CaF. (a) Energies as a function of magnetic field, at zero electric field. (b) Energies as a function of electric field, at zero magnetic field. Note the breaks in the vertical axes.

where we define $\hat{\lambda}$ as a unit vector along the internuclear axis in the direction from negative to positive charge (fluorine to calcium)[4]. The first term is the rotational kinetic energy, the second term is the correction to the first due to centrifugal distortion, the third is the spin–rotation coupling, the fourth and fifth are the hyperfine interaction and the sixth is the nuclear-spin–rotation interaction. The most accurate (at the time of writing) values of these parameters for the CaF $X^2\Sigma^+(v = 0)$ state are given in Table 2.1.

[4]The direction of the vector is only relevant for the interaction with an electric field as in Sec. 2.4.3.

Table 2.1: Parameters in effective Hamiltonian for CaF $X^2\Sigma^+$ state.

Parameter	Value (MHz)	Reference
B	10 267.5387(37)	[141]
D	0.014 060(24)	"
γ	35.658 91(2)	[142]
b	109.1839(5)	"
c	40.1190(26)	"
C	0.028 76(37)	"

2.4.2 Magnetic field

The effective Zeeman Hamiltonian for the interaction of CaF with a static magnetic field $\vec{\mathcal{B}}$ is (see, for example, pg. 351 of Brown and Carrington [137]),

$$\begin{aligned} H_{\mathrm{Z}} &= H_{\mathrm{e}} + H_{\mathrm{n}} + H_{\mathrm{r}} + H_{\mathrm{a}} \\ &= g_S \mu_{\mathrm{B}} \vec{S} \cdot \vec{\mathcal{B}} - g_{\mathrm{N}} \mu_{\mathrm{N}} \vec{I} \cdot \vec{\mathcal{B}} - g_{\mathrm{r}} \mu_{\mathrm{B}} \vec{N} \cdot \vec{\mathcal{B}} + g_l \mu_{\mathrm{B}} (\vec{S} \cdot \vec{\mathcal{B}} - (\vec{S} \cdot \hat{\lambda})(\vec{\mathcal{B}} \cdot \hat{\lambda})). \end{aligned} \tag{2.35}$$

H_{e} describes the interaction of the electron magnetic moment with $\vec{\mathcal{B}}$, H_{n} describes the contribution from the nuclear magnetic moment, H_{r} the rotational Zeeman interaction, and H_a the anisotropic correction to the electronic Zeeman interaction. The first term is by far the largest with $\mu_B/\mu_N \sim 1700$ and g_l and g_{r} several orders of magnitude smaller than the electron g-factor $g_S \simeq 2.002$. Figure 2.2(a) shows the energies of the $N = 0$ and $N = 1$ levels of CaF as a function of magnetic field, calculated by numerical diagonalisation of $H_{\mathrm{ff}} + H_{\mathrm{Z}}$.

2.4.3 Electric field

The effective Stark Hamiltonian for CaF in a dc electric field is

$$H_{\mathrm{St}} = -\mu_e \vec{E} \cdot \hat{\lambda}, \tag{2.36}$$

where $\vec{E}$ is the electric field and μ_e is the permanent electric dipole moment of the molecule, defined in Sec. 2.5.2. Figure 2.2(b) shows the energies of the $N = 0$ and $N = 1$ levels of CaF as a function of electric field, calculated by numerical diagonalisation of $H_{\mathrm{ff}} + H_{\mathrm{St}}$.

2.5 Electric dipole transitions

2.5.1 Transition dipole moment

The strength of an electric-dipole transition is proportional to the square of the matrix element

$$\vec{d}_{if} = \langle \psi_f | \, \vec{d} \, | \psi_i \rangle \, . \tag{2.37}$$

Here $\vec{d} = eZ_A\vec{R}_A + eZ_B\vec{R}_B - e\sum_i \vec{r}_i$ is the electric dipole operator of the molecule and $|\psi_i\rangle$, $|\psi_f\rangle$ are two different internal states of the molecule. In the Born-Oppenheimer approximation, where the total molecular wavefunction can be written as a product of electronic, vibrational and rotational wavefunctions, we have

$$\begin{aligned} \vec{d}_{if} &= \langle \psi_{q',v',R',m_{R'}} | \, \vec{d} \, | \psi_{q,v,R,m_R} \rangle \\ &= \int Y^*_{R',m_{R'}} \frac{1}{R_{AB}} f_{v'}{}^* \phi^{e*}_{q'} \vec{d} \phi^e_q \frac{1}{R_{AB}} f_v Y_{R,m_R} R^2_{AB} \, \mathrm{d}R_{AB} \sin\Theta \, \mathrm{d}\Theta \, \mathrm{d}\Phi \, \mathrm{d}\vec{x} \, . \end{aligned} \tag{2.38}$$

In order to factorise this, we rotate our coordinate system so that the Z axis lies along the internuclear axis $\hat{\lambda}$. Moving to spherical tensor notation allows us to do this elegantly. We define $\vec{\mu}$, the electric

dipole operator in this rotated frame and relate it to $\vec{d}$ by

$$d_j = \sum_{k=-1}^{1} D_{jk}(\Theta, \Phi)\mu_k, \tag{2.39}$$

where d_j and μ_k are the j'th and k'th spherical tensor components of $\vec{d}$ and $\vec{\mu}$ respectively and D_{jk} is the operator that rotates the coordinates from one frame to the other. This transformation allows us to express the integral of Eq. (2.38) as a product of two parts

$$\vec{d}_{if} = \sum_j \hat{e}_j \sum_k \int Y^*_{R',m_{R'}} D_{jk}(\Theta,\Phi) Y_{R,m_R} \sin\Theta \,\mathrm{d}\Theta \,\mathrm{d}\Phi \int f_{v'}{}^* \phi^{e}_{q'}{}^* \mu_k \phi^e_q f_v \,\mathrm{d}R_{AB}\,\mathrm{d}\vec{x}\,, \tag{2.40}$$

where $\hat{e}_j$ is the j'th spherical unit vector. We define the transition dipole moment,

$$\mu_k^{q',q}(R_{AB}) = \int \phi^{e}_{q'}{}^*(R_{AB};\vec{x})\mu_k \phi^e_q(R_{AB};\vec{x})\,\mathrm{d}\vec{x}\,. \tag{2.41}$$

The dependence of the dipole moment on the internuclear distance can be expanded in a Taylor series in the same way as we did for the vibrational potential in Eq. (2.18),

$$\mu_k^{q',q}(R_{AB}) \simeq \mu_k^{q',q}(R^{\mathrm{eq}}_{AB}) + \frac{\partial \mu_k^{q',q}}{\partial R_{AB}}\left(R_{AB} - R^{\mathrm{eq}}_{AB}\right) + \ldots. \tag{2.42}$$

If we take only the first term, a constant, we can finally express d_{if} as a simple product of three terms,

$$\begin{aligned}\vec{d}_{if} = &\sum_j \hat{e}_j \sum_k \int Y^*_{R',m_{R'}} D_{jk}(\Theta,\Phi) Y_{R,m_R} \sin\Theta \,\mathrm{d}\Theta \,\mathrm{d}\Phi \\ &\times \mu_k^{q',q}(R^{\mathrm{eq}}_{AB}) \\ &\times \int f_{v'}{}^* f_v \,\mathrm{d}R_{AB}\,.\end{aligned} \tag{2.43}$$

2.5.2 Selection rules

The first line in the product of Eq. (2.43) contains the angular dependence of the matrix element and determines the angular-momentum selection rules; namely $\Delta R = 0, \pm 1$, $\Delta m_R = 0, \pm 1$ but $R = 0 \nleftrightarrow R' = 0$.

The second line in the product, the transition dipole moment, depends on the character of the electronic states in question. Note that for transitions within an electronic state, $q' = q$, only the $k = 0$ term is non-zero; $\mu_k^{q,q}$ is just the expectation value of the electric dipole of the molecule in the molecular frame; this is μ_e, the permanent electric dipole moment of the molecule. For homo-nuclear molecules this expectation value is zero and so rotational and vibrational transitions within an electronic state are electric-dipole forbidden. For CaF in the $X^2\Sigma^+$ state, the permanent electric dipole is 3.1 D [143].

The final term describes the overlap of the vibrational wavefunctions; its square is called the Franck-Condon factor. When $q' = q$, the vibrational wavefunctions come from the same molecular potential and so are orthogonal to one another, implying the vibrational quantum number cannot change. For transitions which change electronic state, there are no selection rules for vibration—a

Table 2.2: Selection rules governing electric-dipole transitions between electronic states in molecules.

Quantity	Rule
Parity	$+ \leftrightarrow -$
Rotation	$\Delta R = 0, \pm 1$ $\Delta m_R = 0, \pm 1$ $R = 0 \nleftrightarrow R' = 0$
Vibration	None

Table 2.3: Branching ratios for decays from the $A^2\Pi_{1/2}$ and $B^2\Sigma^+$ states in CaF. For decays to $X^2\Sigma^+(v = 0)$ or $(v = 1)$ the branching ratios quoted are calculated [144, 145]. The other branching ratios were measured in our experiment [2, 135].

	$X^2\Sigma^+$			
	$v = 0$	$v = 1$	$v = 2$	$v = 3$
$A^2\Pi_{1/2}(v = 0)$	0.964	0.035	0.00084	0.000025
$B^2\Sigma^+(v = 0)$	0.998	0.002	0.000015	—

serious headache for application of laser cooling to molecules—but their transition probabilities are discussed in more detail in Sec. 2.5.4.

A final selection rule is evident from the form of Eq. (2.37), the operator $\vec{d}$ is anti-symmetric under parity inversion and so the initial and final states must have opposite parity to have a non-zero matrix element. All selection rules are summarised in Table 2.2.

2.5.3 Spontaneous emission

The spontaneous emission rate from an excited state $|\psi_e\rangle$ to $|\psi_g\rangle$ is given by

$$\Gamma_{eg} = \frac{\omega_{eg}^3}{3\pi\epsilon_0\hbar c^3}|\vec{d}_{eg}|^2, \tag{2.44}$$

where $\hbar\omega_{eg}$ is the energy separation between the two states. Typical values of $|\vec{d}_{eg}|$ for dipole-allowed transitions are on the order of $1\,\text{eÅ} \sim 10^{-29}\,\text{C m}$ and so typical decay rates are on the order of $10^{-40}\omega^3$ Hz. The ω^3 scaling combined with the radically different energy scales for the different degrees of freedom in molecules means that the decay rates for different transition types are very different. Using the typical energy separations from Sec. 2.2.4 we find typical decay rates of a few MHz for electronic transitions, a few Hz for vibrational transitions and a few µHz for rotational transitions. This decay rate for rotational transitions corresponds to a lifetime of several days, effectively infinite on the timescale of an atomic physics experiment.

2.5.4 Vibrational branching

The lack of selection rules for vibration-changing transitions means that the overlap integral in Eq. 2.43 provides the only protection against vibrational branching during spontaneous emission

from an electronically excited state. For CaF, the A and B states correspond to excitation of the unpaired electron which is localised around the Ca nucleus. As discussed in Sec. 2.3.3, to a very good approximation this electron makes no contribution to the potential experienced by the nuclei and so the excited states have very similar vibrational potentials to the ground state. The resultant vibrational wavefunctions are therefore nearly identical and the overlap integral in Eq. 2.43 extremely small for $v' \neq v$. In such cases the Frank-Condon factor alone provides a poor estimate of the vibrational branching ratio—often wrong by orders of magnitude—and it is important to consider the effect of the next term in the transition dipole moment expansion from Eq. (2.42). The vibrational branching ratios from the $A^2\Pi_{1/2}(v = 0)$ and $B^2\Sigma^+(v = 0)$ states are given in Table 2.3.

Chapter 3

Laser cooling of molecules: theory

3.1 Introduction

In this chapter we outline the key concepts of laser cooling and discuss the issues and challenges to be tackled in applying them to molecules.

3.2 Doppler cooling

3.2.1 Two-level atom

Consider a two-level atom with states $|e\rangle$ and $|g\rangle$ separated by energy $\hbar\omega_0$, interacting with the electromagnetic field of a laser beam $\hat{\epsilon}E_0\cos(\omega_0+\delta)t$. The optical Bloch equations for the system in the rotating wave approximation are

$$\frac{\partial\rho_{\mathrm{ee}}}{\partial t} = i\frac{\Omega}{2}(\tilde{\rho}_{\mathrm{eg}}-\tilde{\rho}_{\mathrm{ge}})-\Gamma\rho_{\mathrm{ee}}, \tag{3.1a}$$

$$\frac{\partial\rho_{\mathrm{gg}}}{\partial t} = -i\frac{\Omega}{2}(\tilde{\rho}_{\mathrm{eg}}-\tilde{\rho}_{\mathrm{ge}})+\Gamma\rho_{\mathrm{ee}}, \tag{3.1b}$$

$$\frac{\partial\tilde{\rho}_{\mathrm{ge}}}{\partial t} = -(\frac{\Gamma}{2}+i\delta)\tilde{\rho}_{\mathrm{ge}}-i\frac{\Omega}{2}(\rho_{\mathrm{ee}}-\rho_{\mathrm{gg}}), \tag{3.1c}$$

$$\frac{\partial\tilde{\rho}_{\mathrm{eg}}}{\partial t} = -(\frac{\Gamma}{2}-i\delta)\tilde{\rho}_{\mathrm{eg}}+i\frac{\Omega}{2}(\rho_{\mathrm{ee}}-\rho_{\mathrm{gg}}). \tag{3.1d}$$

Here $\rho_{ij} = \langle i|\,\rho\,|j\rangle$ are the matrix elements of the density operator with $\tilde{\rho}_{\mathrm{ge}} = \tilde{\rho}^*_{\mathrm{eg}} = \rho_{ge}e^{-i\omega_0 t}$, $\Omega = -\langle g|\,\vec{d}\cdot\hat{\epsilon}\,|e\rangle\,E_0/\hbar$ is the Rabi frequency and $\Gamma = \omega_0^3\left|\langle g|\,\vec{d}\,|e\rangle\right|^2/(\pi\epsilon_0\hbar c^3)$ is the rate of spontaneous emission from the excited state.

The system reaches steady state in a time on the order of $1/\Gamma$. The steady-state excited state population $\rho^{\mathrm{st}}_{\mathrm{ee}}$ can be found by setting all the time derivatives in Eqs. (3.1) equal to zero and solving for ρ_{ee}. In this steady state limit, we can write the scattering rate as $R_{\mathrm{sc}} = \Gamma\rho^{\mathrm{st}}_{\mathrm{ee}}$. We find

$$\begin{aligned} R_{\mathrm{sc}} &= \Gamma\frac{\frac{\Omega^2}{\Gamma^2}}{1+\frac{4\delta^2}{\Gamma^2}+\frac{\Omega^2}{2\Gamma^2}} \\ &= \frac{\Gamma}{2}\frac{I/I_{\mathrm{s}}}{1+\frac{4\delta^2}{\Gamma^2}+I/I_{\mathrm{s}}}, \end{aligned} \tag{3.2}$$

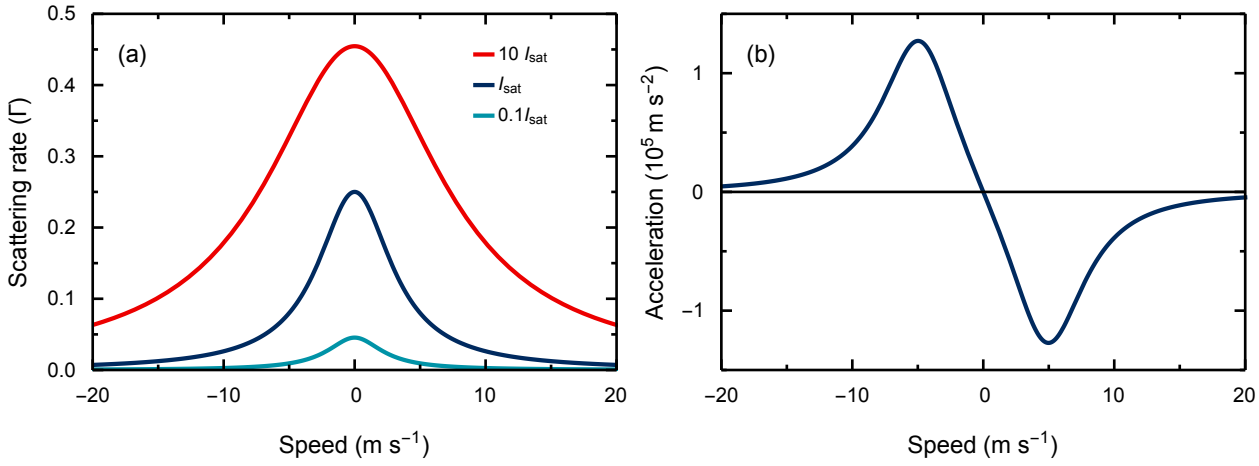

Figure 3.1: (a) Scattering rate as a function of velocity for laser on resonance with atoms at rest. (b) Acceleration as a function of velocity for counter-propagating laser beams with $I = I_s$. Parameters used throughout are $m = 59\,\mathrm{u}$ and $\Gamma = 2\pi \times 8.3\,\mathrm{MHz}$.

where in the second line we have substituted the intensity of the laser field, $I = \epsilon_0 c E_0^2/2$ and defined the saturation intensity,

$$I_s = \frac{c\epsilon_0 \Gamma^2 \hbar^2}{4\left|\langle g|\,\vec{d}\cdot\hat{\epsilon}\,|e\rangle\right|^2} = \frac{\pi c h \Gamma}{3\lambda^3}. \tag{3.3}$$

Figure 3.1(a) shows R_{sc} for three different intensities, plotted as a function of atomic velocity in the direction of the light which enters Eq. (3.2) via the Doppler shift of the light. The scattering rate is a Lorentzian centred on $\delta = 0$ with a full-width at half-maximum of $\Gamma\sqrt{1 + I/I_s}$. The maximum scattering rate, for $I \gg I_s$, is $\Gamma/2$. Each scattering event consists of absorption of a photon from the light field and then spontaneous emission in a random direction[1]. The average momentum change of the atom during this process is $\hbar k$ where k is the wavevector of the laser field. The force exerted by a laser beam with wavevector $\vec{k}$ parallel to the velocity v of the atom is then

$$\vec{F}_{rad} = \hbar\vec{k}R_{sc} = \hbar\vec{k}\frac{\Gamma}{2}\frac{I/I_s}{1 + \frac{4(\delta_0 - kv)^2}{\Gamma^2} + I/I_s}, \tag{3.4}$$

where we have explicitly included the dependence of the detuning on the velocity of the atom.

Now consider two counter-propagating laser beams, each with intensity I. Provided the intensities are low, to first approximation, the total force is just the sum of the force from each beam. The scattering forces are in opposite directions but do not cancel for non-zero velocity due to the Doppler shifts. Figure 3.1(b) shows the force as a function of velocity for $I = I_s$ and $\delta_0 = \Gamma$. For low velocities, $v \lesssim \delta_0/k$, we can expand the force about $v = 0$ to write $\vec{F}_{rad} = -\alpha v$ with

$$\alpha = -\frac{8\delta_0 \hbar k^2 I/I_s}{\Gamma(1 + 4\delta_0^2/\Gamma^2 + I/I_s)^2}. \tag{3.5}$$

[1]The emission direction in a real atom is not actually completely random but rather with probability determined by the dipole emission pattern $P(\theta, \phi)$. However this makes no difference to the argument because the emission pattern is always symmetric under reflection in any plane through the origin $P(\theta, \phi) = P(\pi - \theta, \phi + \pi)$.

The force damps the atom towards zero velocity. The friction coefficient α has a maximum value of $\hbar k^2/2$ for $I = 2I_s$ and $\delta_0 = -\Gamma/2$.

The arrangement is called an optical molasses and the approach generalises to three dimensions by using three pairs of counter-propagating laser beams with k-vectors having components along all three orthogonal axes.

3.2.2 Doppler limit

So far we have considered the average damping force but to understand the limit of this cooling mechanism we need to consider the heating that arises due to fluctuations in this force. In three dimensions, the temperature of the system is related to $\langle v^2 \rangle$, the variance of the velocity distribution by $(3/2)k_B T = (1/2)m\langle v^2 \rangle$. We first focus on the effect of the damping force on $\langle v^2 \rangle$,

$$\frac{\mathrm{d}\langle v^2 \rangle_{\mathrm{damp}}}{\mathrm{d}t} = 2\langle \vec{v} \cdot \frac{\mathrm{d}\vec{v}}{\mathrm{d}t} \rangle = \frac{2}{m}\langle \vec{v} \cdot \vec{F}_{\mathrm{rad}} \rangle. \tag{3.6}$$

Using our result for low intensities from Eq. (3.5) we have

$$\frac{\mathrm{d}\langle v^2 \rangle_{\mathrm{damp}}}{\mathrm{d}t} = \frac{16\delta_0 \hbar k^2 I/I_s}{m\Gamma(1 + 4\delta_0^2/\Gamma^2 + I/I_s)^2}\langle v^2 \rangle. \tag{3.7}$$

At very low velocities, the absorption and emission of photons are equally likely in any direction and each scattering event increases $\langle v^2 \rangle$ by $2(\hbar k/m)^2$. The scattering events occur at a rate

$$R_{\mathrm{sc}} = \frac{\Gamma}{2}\frac{6I/I_s}{1 + \frac{4\delta^2}{\Gamma^2} + I/I_s}, \tag{3.8}$$

where we have included all six beams. The heating rate is then

$$\frac{\mathrm{d}\langle v^2 \rangle_{\mathrm{fluc}}}{\mathrm{d}t} = 2R_{\mathrm{sc}}\left(\frac{\hbar k}{m}\right)^2. \tag{3.9}$$

Putting the terms for heating and cooling together gives

$$\frac{\mathrm{d}\langle v^2 \rangle}{\mathrm{d}t} = \frac{16\delta_0 \hbar k^2 I/I_s}{m\Gamma(1 + 4\delta_0^2/\Gamma^2 + I/I_s)^2}\langle v^2 \rangle + \frac{\Gamma}{2}\frac{12I/I_s}{1 + \frac{4\delta^2}{\Gamma^2} + I/I_s}\left(\frac{\hbar k}{m}\right)^2. \tag{3.10}$$

For $\delta_0 < 0$ the system reaches a steady state with $\langle v^2 \rangle = \langle v^2 \rangle^{\mathrm{st}}$ and temperature,

$$T_{\mathrm{D}} = \frac{m\langle v^2 \rangle^{\mathrm{st}}}{3} = -\frac{\hbar\Gamma^2}{8k_B\delta_0}(1 + 4\delta_0^2/\Gamma^2 + I/I_s). \tag{3.11}$$

This temperature, known as the Doppler temperature, depends on both the intensity and the detuning of the laser beams. The lowest temperature, known as the Doppler limit, is reached for $I \ll I_s$, $\delta_0 = -\Gamma/2$, and is $T_{\mathrm{D}} = \hbar\Gamma/2k_B$. For a decay rate from the excited state of $\Gamma = 2\pi \times 8.3\,\mathrm{MHz}$, as in the CaF A state, this temperature is 199 µK.

3.2.3 Application to molecules

The techniques discussed above can be extended to molecules, with a few substantial caveats. Consider a beam of CaF molecules having typical velocities of a few hundred $\mathrm{m\,s^{-1}}$. Bringing a molecule to rest using the scattering force on the $A \rightarrow X$ or $B \rightarrow X$ transitions requires scattering $\sim 10^4$ photons. For a generic diatomic molecule this is extremely challenging because branching to other rovibrational states during spontaneous emission means that a prohibitive number of repump lasers are required.

The first problem to tackle is vibrational branching. As discussed in Sec. 2.5.4, there are no selection rules for vibration and so the only way to prevent branching to is to find a molecule with very small branching ratios to other vibrational states. The branching ratios given for CaF in Table 2.3 mean that only a few vibrational repump lasers are required to scatter tens of thousands of photons.

Branching to other rotational states can be prevented by using the $X(v = 0, N = 1)$ first rotationally excited state as the ground state of our cycling transition. When exciting this state to the $A^2\Pi_{1/2}(J = 1/2)$ state, the angular momentum and parity selection rules discussed in Sec. 2.5.2 mean that the molecule can decay only back to $X(v = 0, N = 1)$.

Whilst this choice of ground state prevents rotational branching, it comes at a cost. Because the excited state has higher angular momentum than the ground state, there are no transitions where the excited state always decays back to the same hyperfine level of the ground state. To plug these leaks we need to account for the molecule decaying to any of the twelve Zeeman sub-levels within the hyperfine structure of $X(v = 0, N = 1)$ shown in Fig. 2.1. We must add frequency sidebands to our laser to address them all. The coupling of multiple ground states to the same excited state, exacerbated by any vibrational repump lasers which also connect to the excited state, reduces the maximum excited state population at high intensities and thus the maximum achievable scattering rates. We can quantify these effects with a simple rate model [70]. In this model, the modified equation for the scattering rate is

$$R_{\mathrm{sc}} = \Gamma \frac{n_{\mathrm{e}}}{(n_{\mathrm{g}} + n_{\mathrm{e}}) + 2\sum_{j=1}^{n_{\mathrm{g}}}(1 + 4\delta_j^2/\Gamma^2) I_{\mathrm{s},j}/I_j}, \tag{3.12}$$

where n_{e} and n_{g} are the number of excited and ground states respectively, I_j is the intensity of the light driving transition j, δ_j is its detuning and $I_{\mathrm{s},j}$ is the saturation intensity for the transition. If the light fields driving each of the transitions have equal detunings from resonance Δ and the total intensity I is split equally between them, we can recover an expression with a form very similar to Eq. 3.2,

$$R_{\mathrm{sc}} = \frac{\Gamma_{\mathrm{eff}}}{2} \frac{I/I_{\mathrm{s,eff}}}{1 + \frac{4\Delta^2}{\Gamma^2} + I/I_{\mathrm{s,eff}}}. \tag{3.13}$$

The maximum scattering rate is limited to $\Gamma_{\mathrm{eff}}/2 = \Gamma n_{\mathrm{e}}/(n_{\mathrm{e}} + n_{\mathrm{g}})$ which, for many ground states, can be much smaller than $\Gamma/2$ from the two-level case of Eq. 3.2. In addition, this maximum scattering rate requires an intensity $I \gg I_{\mathrm{s,eff}} = I_{\mathrm{s}} n_{\mathrm{g}}^2/2(n_{\mathrm{e}} + n_{\mathrm{g}})$, meaning potentially much higher laser powers than for a simple two-level (or quasi two-level) system.

Finally, for any given polarisation of the light field, transitions with $F' \leq F$ have a dark state; a superposition of m_F states which does not couple to the light field. To scatter a large number of photons we need to destabilise these dark states. This can be done using a magnetic field at an angle to the laser polarisation or by modulating the polarisation of the light.

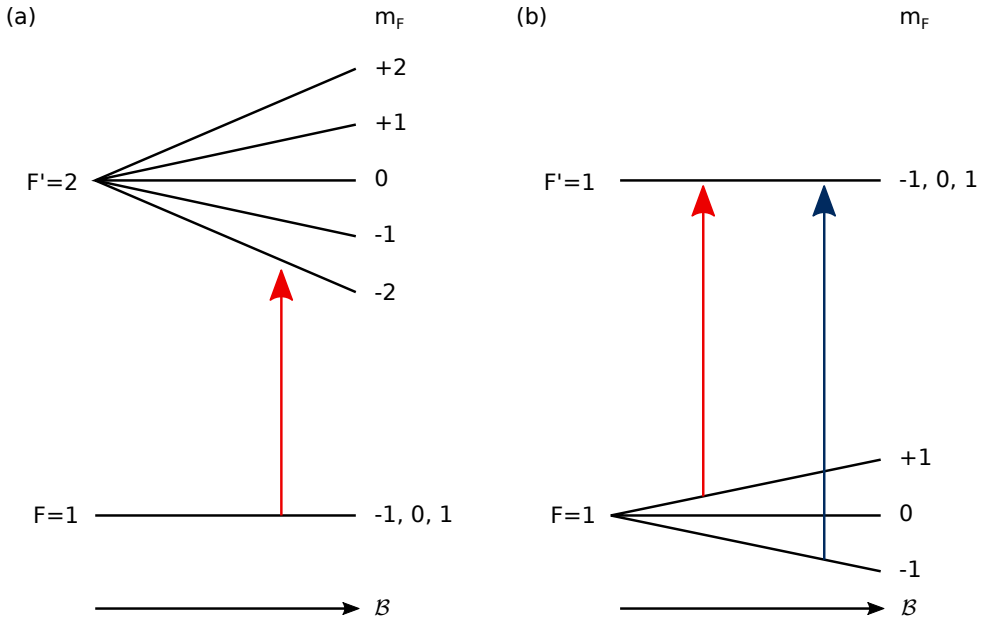

Figure 3.2: Schematics for magneto-optical trapping. (a) A conventional MOT with $F' = F + 1$ and a magnetic moment in the excited state that is larger than that in the ground state. Red arrow represents detuning of the light, the restoring beam has σ^- polarisation. (b) A dual-frequency MOT for a transition of the type $F' \geq F$. The two arrows represent detuning of the two components. The restoring beam has a red-detuned component with σ^- polarisation and a blue-detuned component with σ^+ polarisation.

3.3 Magneto-optical trap

3.3.1 Basic principles

The optical molasses discussed above provides cooling but no confinement; atoms or molecules subject to such a light field will eventually diffuse away. A magneto-optical trap (MOT) provides confinement by adding a quadrupole magnetic field gradient to the optical molasses. As explained below, for a particular choice of laser beam polarisations, this introduces a position-dependent force that confines particles close to the zero of the magnetic field. MOTs have proven to be extraordinarily useful in atomic physics and now serve as the starting point for a huge array of experiments with ultracold atoms.

The MOT is usually created by adding a pair of coils to an optical molasses. Each coil carries equal current, but flowing in opposite directions, producing a quadrupole $\mathcal{B}$ field; zero at the centre of the two coils with $|\mathcal{B}|$ increasing linearly for small displacements in any direction from this zero. Figure 3.2(a) illustrates the principles of the MOT in one dimension. An atom positioned near the field zero has a transition of the type $F' = F + 1$ where F' and F are the total angular momentum of the excited and ground states respectively and we assume that the excited state has a magnetic moment while the ground state does not. The transition is addressed by two circularly polarised, counter-propagating laser beams with the same handedness (σ^+ and σ^- relative to the positive x direction); absorption of a photon from the beam which propagates in the positive x direction increases the angular momentum by one whilst absorption of a photon from the beam which propagates in the negative x direction decreases the angular momentum by one. For red-detuned light, and displacements away from the field zero in

the positive x direction, the σ^- transition is closer to resonance than the σ^+ transition and so the atom absorbs preferentially from the beam propagating in the negative x direction. For displacements in the opposite direction, the reverse applies and the atom absorbs preferentially from the beam propagating in the positive x direction. In both cases there is a preferential scattering from the beam that pushes the atom back towards the field zero—we will refer to this as the restoring beam—and so the atom is confined.

3.3.2 Application to molecules

In molecules there are two principle complications. These are discussed in detail in Ref. [146] but summarised here. The first is that, in all molecules for which laser cooling has been demonstrated thus far, the ground state has a magnetic moment, whilst the excited state does not—or at least it is very small. For CaF the ground state has a large magnetic moment from the unpaired electron spin, whilst the $^2\Pi_{1/2}$ excited state also has a contribution from the orbital angular momentum which nearly cancels it. The Zeeman splitting of the ground state only, creates no preference for absorbing from one beam or the other and thus no restoring force.

The second complication is that, as discussed in Sec. 3.2.3, finding a cycling transition requires utilising transitions of the type $F' \leq F$. In this case, assuming we can arrange for a preference to scatter from the restoring beam, only a few photons can be scattered by that beam before the molecule is pumped to a state which is dark to it. Now, in order to scatter another photon from the restoring beam, the molecule must first scatter a photon from the anti-restoring beam and there is no net restoring force.

In the work described in this thesis, we solve these problems with what has become known as a dual-frequency MOT [147]. Figure 3.2(b) illustrates the principles. To each MOT beam, we add a second frequency of light which is blue detuned from the zero-field transition and has the opposite handedness. Now when the molecule reaches the state which is dark to the red-detuned restoring beam, it scatters preferentially from the blue-detuned restoring beam and a restoring force is recovered. However the presence of both blue- and red-detuned light creates competition between Doppler cooling and Doppler heating. It turns out that Doppler cooling dominates provided the blue-detuned component is further from resonance than the red-detuned component.

An alternative strategy is possible using what is known as an rf MOT. In this scheme, the polarisation and $\mathcal{B}$ field gradients are reversed at time intervals short compared to the optical pumping time. Now the dark state is continually transformed into a bright state and the detuning ensures molecules scatter more photons from the restoring beam than the anti-restoring one. This scheme has been used to create MOTs of SrF at Yale [129], CaF at Harvard [130] and YO at JILA [131].

3.4 Below the Doppler limit

3.4.1 Introduction

Soon after Doppler cooling was demonstrated in three-dimensions for atomic systems, it became apparent that the theory presented above did not capture the whole picture. In fact experiments with optical molasses cooled atoms to much lower temperatures than the limit of Eq. 3.11 [148]. To

understand the observed discrepancies we need to reconsider the approximations made in deriving the limit. There are two key assumptions, the first is that the force from multiple beams is simply the sum of the scattering forces expected from each of the beams individually. The second is that the atom can be treated as a two-level system. This section will outline how the breakdown of these two assumptions can lead to temperatures significantly below the Doppler limit and even below the single photon recoil limit. We will then discuss how the techniques can be adapted to molecules.

Two distinct mechanisms were identified to explain the lower than expected temperatures observed experimentally in atomic systems [149, 150]. They are often referred to as 'Sisyphus' and 'orientation-dependent' sub-Doppler cooling. The Sisyphus mechanism is most relevant to the techniques we will use to cool molecules and so we will focus on that here.

3.4.2 Sisyphus cooling

Estimating the total force by simply adding the forces from the individual beams misses the effect of interference. In reality this interference means that any three-dimensional molasses will have gradients of both polarisation and intensity[2]. An atom in a light field experiences a shift of its energy levels due to the interaction between the field and the optically induced dipole. These light shifts, also called ac-Stark shifts, depend on the strength of the coupling of the atom to the field. This coupling strength in turn depends on the intensity of the local field as well as the scalar product between the local polarisation and the orientation of the atom's polarisation. This means that, for many atoms, in many different standing light-wave configurations, the energies of various internal states are position dependent.

Consider an atom in an internal state which couples to a light field. As it moves through a periodic, spatially varying field such as that set up by counter propagating laser beams, it experiences potential peaks and troughs. When it moves into a region where the energy of its internal state increases (decreases), it must lose (gain) kinetic energy to compensate. The corresponding mechanical force on the atom is called the dipole force. This coherent, conservative force results from a redistribution of photons between the two beams. As the atom moves up a potential hill it absorbs photons from the counter-propagating beam and transfers them to the co-propagating beam by stimulated emission. In this way, momentum can be exchanged between the atom and the field and the kinetic energy of the atom changes as it moves through the field. This phenomenon has been observed experimentally [151].

To see how this conservative process of exchanging momentum with the field—which results in no net force when averaged over a wavelength of the field—can lead to cooling, we need to consider spontaneous emission. For a system with spontaneous emission and multiple ground states, there exists, for any local polarisation, a 'steady state' in to which the system is optically pumped in a characteristic time τ. It is this time delay that allows for the net force. An atom which moves a fraction of a wavelength through the spatially varying light field during τ will, in general, no longer be in the local 'steady state'. If, in addition to moving out of the local 'steady state', the atom also moves up a potential hill then it can convert a fraction of its kinetic energy to internal energy which can then be dissipated by spontaneous emission as it is optically pumped back to the local steady state.

To understand the mechanism in more detail we will look at some simple one-dimensional examples that capture the key physics.

[2] A uniform polarisation across space is possible only in two or fewer dimensions.

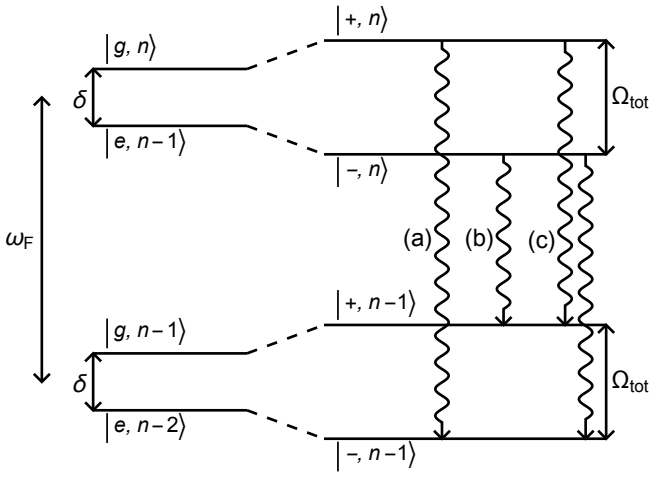

Figure 3.3: Energy levels of the combined atom–field system. On the left are the energy levels in the absence of coupling between the atom and the field while on the right are the energy levels for non-zero interaction. Wavy lines show the possible transition types as described in the text.

3.4.3 2-level system in lin‖lin field

Consider an atom with two states $|g\rangle$ and $|e\rangle$ separated by energy $\hbar\omega_0$, moving in the field of two counter-propagating plane waves with frequency ω_F detuned δ from the atomic transition; $\delta > 0$ is blue detuned. We choose a coordinate system where the plane waves propagate along $\pm z$ and are linearly polarised along y.

It is worth stating up front that, for reasons explained later, sub-Doppler temperatures are not possible in this configuration. However the simple model gives us a straightforward route to understanding the 'Sisyphus' mechanism, the physics of which is very similar, but more difficult to elucidate, in more complex multilevel systems.

The total Hamiltonian for the system is

$$H = H_{\mathrm{A}} + H_{\mathrm{F}} + H_{\mathrm{I}}, \tag{3.14}$$

where the atom Hamiltonian can be written as

$$H_{\mathrm{A}} = \hbar\omega_0 \left|e\right\rangle \left\langle e\right|, \tag{3.15}$$

and the field is described by

$$H_{\mathrm{F}} = \hbar\omega_F(a^\dagger a + \frac{1}{2}). \tag{3.16}$$

First consider the atom positioned at a point where the two waves interfere destructively and there is a field zero. The energy levels of the system are shown on the left hand side of Fig. 3.3. Here there is no coupling between the atom and the field ($H_{\mathrm{I}} = 0$) and the eigenstates of the combined system can be characterised by the eigenstates of the atom, $|e\rangle$ or $|g\rangle$, and the eigenstates of the field, Fock states labelled by the photon number n. They form a ladder of manifolds which we will label by n

separated by $\hbar\omega_F$, each containing two states of the form $|e, n-1\rangle$ and $|g, n\rangle$. If $\delta = 0$ the two-levels are degenerate, otherwise the state $|g, n\rangle$ has an energy $\hbar\delta$ greater than state $|e, n-1\rangle$. Note that this means $|e, n-1\rangle$ has higher energy than $|g, n\rangle$ for a field that is red detuned from the atomic transition.

When the atom is positioned in a region of non-zero intensity we must consider the atom–field interaction term. In the dipole and rotating wave approximations this can be written

$$H_{\mathrm{I}} = -\vec{d} \cdot \left(|e\rangle \langle g| \, \vec{E}^{+}(\vec{r}) + |g\rangle \langle e| \, \vec{E}^{-}(\vec{r}) \right), \tag{3.17}$$

where $\vec{d}$ is the atomic electric dipole moment and $\vec{E}^{+}(\vec{r})$ and $\vec{E}^{-}(\vec{r})$ are the positive and negative frequency components of the electric field operator taken for an atom at position $\vec{r}$,

$$\vec{E}^{+}(\vec{r}) = \mathcal{E}(\vec{r}) a, \tag{3.18}$$

$$\vec{E}^{-}(\vec{r}) = \mathcal{E}^{*}(\vec{r}) a^{\dagger}. \tag{3.19}$$

Here we have taken the semi-classical approximation by replacing $\vec{R}$, the atom position operator with $\langle \vec{R} \rangle = \vec{r}$, its average value[3]. $\mathcal{E}(\vec{r})$ is the electric field distribution relating to the particular mode of the light field which in this case, by an appropriate choice of coordinates, can be written as $\mathcal{E}(\vec{r}) = \mathcal{E}_0 \vec{e}_y \cos(kz)$ with $\vec{e}_y$ the unit vector in the y direction. H_{I} is zero on the diagonal—neither $|g\rangle$ or $|e\rangle$ has a space-fixed dipole moment—but non-zero off the diagonal. It couples states within the same manifold—transitions from g to e with absorption of one photon—with a matrix element

$$\langle e, n-1 | \, H_{\mathrm{I}} \, | g, n \rangle = -d_y \mathcal{E}_0 \cos(kz) \sqrt{n} = \frac{\hbar \Omega(z)}{2}, \tag{3.20}$$

where $\Omega(z) = -2 d_y \mathcal{E}_0 \cos(kz) \sqrt{n}/\hbar$ is the Rabi frequency. Note that $\Omega(z)$ depends on the number of photons n in the field. Here we will neglect this dependence by supposing that the laser beam is initially excited in some coherent state with a Poisson distribution for n, the width Δn of which is very small compared with the average number of photons. However, this dependence turns out to be important in the discussion of energy conservation (see footnote 5 for more details). The new eigenstates of the coupled system are shown on the right hand side of Fig. 3.3 and are given by

$$|+, n; z\rangle = \cos\theta(z) \, |e, n-1\rangle + \sin\theta(z) \, |g, n\rangle \,, \tag{3.21a}$$

$$|-, n; z\rangle = -\sin\theta(z) \, |e, n-1\rangle + \cos\theta(z) \, |g, n\rangle \,. \tag{3.21b}$$

These eigenstates, often called the dressed states of the system, are given by an effective rotation of the uncoupled states, with the rotation angle defined by $\tan 2\theta(z) = -\Omega(z)/\delta$ for $0 \leq \theta(z) \leq \pi/2$. The

[3]It can be shown that forces and diffusion coefficients calculated semi-classically in this way are identical to the full quantum treatment provided that $k\Delta v \ll \Gamma$ and $\Delta \vec{r} \ll \lambda$ [152]. Because of the uncertainty principle, these conditions are only compatible if $\frac{\hbar^2 k^2}{2m} \ll \hbar\Gamma$. For CaF on the $A^2\Pi_{1/2}(v=0, J=1/2, N=0) \leftarrow X^2\Sigma^{+}(v=0, N=1)$ transition, $\frac{\hbar^2 k^2}{2m}/(\hbar\Gamma) \sim 10^{-3}$.

energies of these states are

$$E_{+,n}(z) = n\hbar\omega_F + \hbar\omega_0 + \frac{\hbar\Omega_{\rm tot}(z)}{2} \tag{3.22a}$$

$$\text{and} \quad E_{-,n}(z) = n\hbar\omega_F + \hbar\omega_0 - \frac{\hbar\Omega_{\rm tot}(z)}{2}, \tag{3.22b}$$

where $\Omega_{\rm tot}(z) = \sqrt{\Omega(z)^2 + \delta^2}$. Since the number of photons in the field and the state of the atom are not well defined, we have labelled the states $|\pm, n; z\rangle$ where n is the manifold and the higher energy state in each manifold is labelled $+$ and the lower $-$. Which state corresponds to the unperturbed $|g, n\rangle$ or $|e, n-1\rangle$ states at the points of zero field depends on the detuning. The main point to note here is that the energies and eigenstates vary with the position of the atom along the standing wave.

As discussed above, if we neglect spontaneous emission[4], an atom moving through the field will experience a periodic array of potential hills and coherently exchange its kinetic and internal energy as it passes over them[5]. Now consider the effect of spontaneous emission which couples states from different manifolds $|\pm, n; z\rangle$ and $|\mp, n-1; z\rangle$. The matrix elements for transitions between these states are

$$\langle \pm, n-1; z|\, \vec{d}\,(|e\rangle\langle g| + |g\rangle\langle e|)\,|\mp, n; z\rangle\,. \tag{3.25}$$

Since the interaction with the field mixes the $|e\rangle$ and $|g\rangle$ states, there are three different types of allowed transition, shown by the wavy arrows in Fig. 3.3. Their transition frequencies are:

(a) $\omega_F + \Omega_{\rm tot}(z)$ for $|+, n; z\rangle \to |-, n-1; z\rangle$,

(b) $\omega_F - \Omega_{\rm tot}(z)$ for $|-, n; z\rangle \to |+, n-1; z\rangle$,

(c) ω_F for $|+, n; z\rangle \to |+, n-1; z\rangle$ and $|-, n; z\rangle \to |-, n-1; z\rangle$.

[4] An atom moving through the field can actually make non-adiabatic transitions between states even without spontaneous emission. It is possible to show that the rate of these transitions is negligible compared to spontaneous emission provided that $kv \ll \left(4\pi\Gamma\delta^4/\Omega_{\rm max}^2\right)^{\frac{1}{3}}$ where $\Omega_{\rm max} = \Omega(z)$ evaluated at an antinode [153]. These non-adiabatic transitions will turn out to be important for sub-Doppler cooling of real atoms.

[5] Armed with quantitative expressions for the energies of the dressed states, it is interesting to think about how energy conservation is maintained during this process. As the atom moves up a potential hill, it loses energy but at first glance it is unclear how we can account for this with cycles of stimulated absorption and emission. Since both counter propagating waves have the same frequency (and thus contain photons of the same energy), it seems any cycle of stimulated absorption followed by emission must leave the atom with the same amount of energy as it started with.

The crucial point here is that the light shift $\Omega_{\rm tot}$, depends on Ω which in turn depends on the photon number (see Eq. (3.20)). The energy corresponding to adding or removing a photon from the system is $\Delta E_n(z) = E_{+,n+1}(z) - E_{+,n}(z) = -(E_{-,n+1}(z) - E_{-,n}(z))$. We can compare this to the energy required in the absence of the atom-field interaction,

$$\Delta E_n(z) - \hbar\omega_F = \frac{1}{2}\left(\sqrt{(n+1)d_y^2\mathcal{E}_0^2\cos^2 kz + \hbar^2\delta^2} - \sqrt{nd_y^2\mathcal{E}_0^2\cos^2 kz + \hbar^2\delta^2}\right). \tag{3.23}$$

One interpretation of this difference is that the energy of the field photons has shifted due to the presence of the atom. The difference depends on the atoms position z and so, in this interpretation, there is a difference in energy between photons absorbed and emitted at different points in the field. As an atom moves into a region where the energy of a field photon is increasing, the energy of photons it absorbs is slightly less than the energy of the photons it emits. The reverse is true when its motion takes it through a region where the photon energy is decreasing. The argument becomes particularly straightforward in the limit of large detuning ($\delta \gg \Omega$). Now the photon energy shift is independent of n and given by

$$\Delta E_n(z) - \hbar\omega_F = \frac{d_y^2\mathcal{E}_0^2\cos^2 kz}{4\hbar\delta}. \tag{3.24}$$

Transitions of type (c) have no effect on the internal energy of the moving atom; they correspond to a photon from the laser mode being scattered from the atom into another mode. But types (a) and (b) change the internal energy and thus provide a means for irreversible loss or gain of energy from the field. Where they occur preferentially depends on the detuning. For $\delta > 0$, the higher energy $|+, n; z\rangle$ state in each manifold corresponds, in the zero field limit, to $|g, n\rangle$. In this case transitions of type (a) occur preferentially at antinodes of the field where the contaminations of $|+, n; z\rangle$ by $|e, n-1\rangle$ and $|-, n-1; z\rangle$ by $|g, n-1\rangle$ are largest. In contrast, transitions of the type (b), occur preferentially at the nodes where $|-, n; z\rangle$ and $|+, n-1; z\rangle$ coincide respectively with $|e, n-1\rangle$ and $|g, n-1\rangle$.

We can now see that for $\delta > 0$, type (a) transitions—where internal energy is lost from the atom to the field—occur preferentially where the light shift, and thus the amount of energy lost to the field, is maximum. Type (b) transitions—where internal energy is transferred from the field to the atom—occur preferentially at points where the light shift, and thus the energy gained from the field, is minimum. In this way, kinetic energy can be dissipated by the field. Figure 3.4 shows how the atom can continuously lose energy over many cycles. The rate at which momentum is lost to the field is directly proportional to the velocity of the atom[6]—the rate at which it passes over the potential hills—and so we have a friction force, $F = -\alpha v$, which cools the atom. The argument is exactly reversed for $\delta < 0$ and the atom is heated.

The size of the force on the molecule when climbing the potential hill is directly related to the height of the hill, or the modulation of the dressed levels Ω_{tot}. An order of magnitude estimate is helpful here: assuming a dipole matrix element of $1\, ea_0$ and a typical laser intensity of $50\,\text{mW}\,\text{cm}^{-2}$, the hill height is equivalent to $\sim 10^3$ photon recoils on a typical optical transition. When travelling at tens of centimetres per second—roughly the Doppler limit for most alkali atoms—this hill is climbed in $\sim 10^{-6}\,\text{s}$ giving a rate of momentum transfer equivalent to a scattering rate of 10^9 photons per second, roughly three orders of magnitude higher than typical optical cycling rates. The size of the hills also increases indefinitely with intensity, in contrast with the force from photon scattering discussed in Sec. 3.2 which saturates at $\hbar k\Gamma/2$.

At first glance, these large friction forces with very low photon scattering ought to lead to lower temperatures, however as alluded to in the introduction to this section, there is a slight problem. To understand, it is instructive to think about the relevant time scales. From Fig. 3.4 it is clear that for effective cooling, we require the time spent in the $|-; z\rangle$ levels to be comparable to time spent in the $|+; z\rangle$ levels or equivalently the decay rate out of each state be approximately equal. Since the decay is just spontaneous emission from $|e\rangle$ with rate Γ, the only control we, as experimentalists, have over it is the population of the $|e\rangle$ state. For a weak standing wave with blue detuning, the $|+, n; z\rangle$ state corresponds nearly to $|g\rangle$ with only a small amount of mixing from the $|e\rangle$ state in high field regions. In this case the atom's lifetime in $|+, n; z\rangle$ is long and, although decay events occur preferentially at the antinodes, they are mainly to $|+, n-1; z\rangle$ since that has the most ground state character. The very occasional decays to $|-; z\rangle$ states are quickly followed by another decay back to $|+; z\rangle$ states and net friction forces are almost non-existent. To make the populations more equal and realise the large friction forces discussed, high intensity fields must be used so that, at least at the antinodes, the states are well mixed. Unfortunately this increased excited state population is accompanied by a large scattering rate meaning, as we saw in Eq. (3.9), a large diffusion coefficient and so an equilibrium temperature higher

[6]This is only true for small velocities. It can be shown that the condition is $v \ll \Gamma\lambda$ [153].

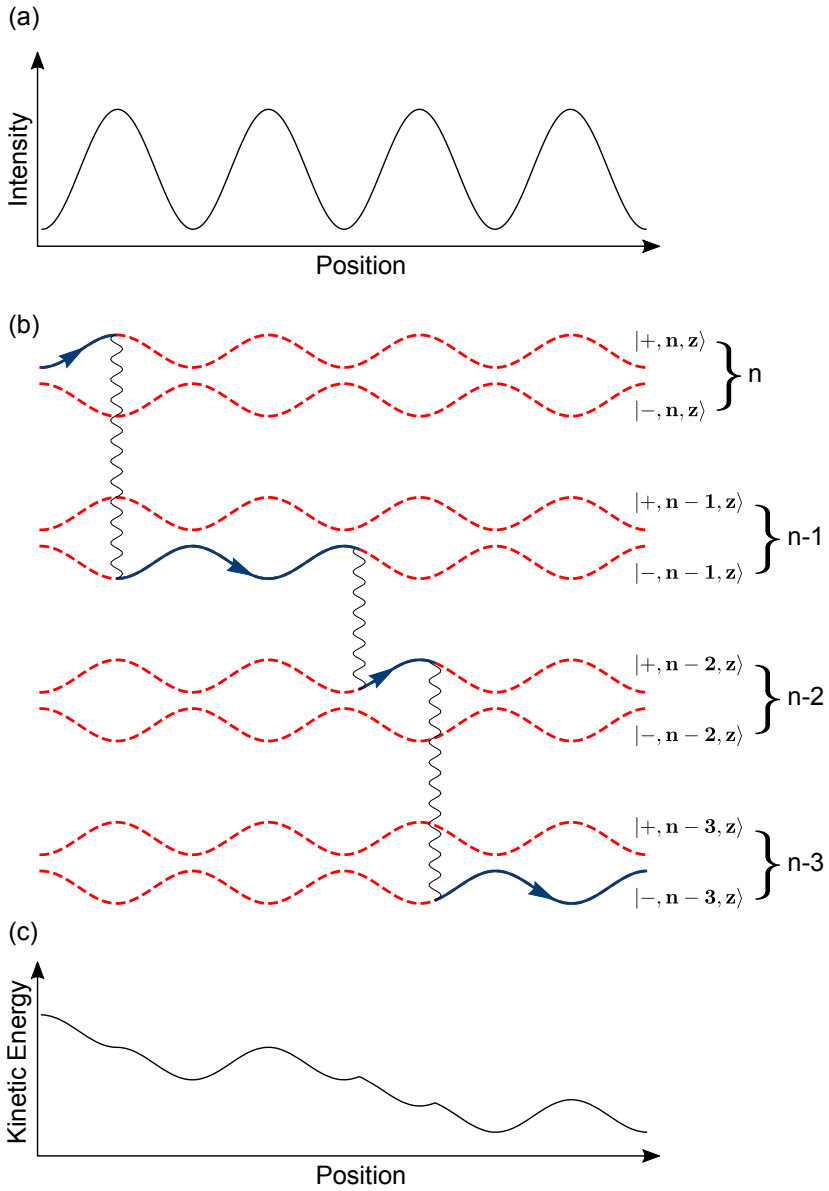

Figure 3.4: Cooling of a two-level atom moving in a 1D, blue detuned, standing light wave. (a) Intensity of light field formed by two counter-propagating, linearly polarised laser beams. (b) Trajectory of combined atom–field system in dressed state picture as the atom moves through light field for $\delta > 0$. (c) Change in kinetic energy of atom as it moves through light field.

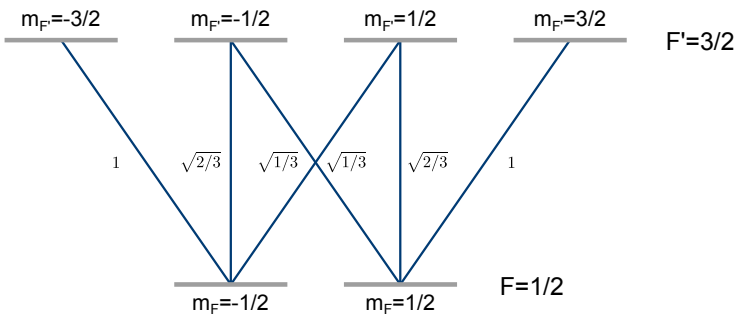

Figure 3.5: Level diagram for $F = \frac{1}{2} \rightarrow F' = \frac{3}{2}$. Clebsch-Gordon coefficients are labelled for each transition.

than for usual radiation pressure cooling [153]. Nevertheless, extremely rapid 1D cooling is possible using this technique and has been demonstrated by collimation of a beam of caesium atoms [154].

In the next section we will see how we can use the multi-level nature of atoms in combination with polarisation gradients to work around this problem and realise large friction forces at low intensities.

3.4.4 Polarisation gradients – $F' = F + 1$ system in lin⊥lin field

To study polarisation effects we must abandon our two-level atom and look at a more realistic system with multiple ground states. We take the simplest example that avoids the complication of dark states—covered in the next section—and consider a transition $F = \frac{1}{2} \rightarrow F' = \frac{3}{2}$ as shown in Fig. 3.5.

The light field is again composed of two laser beams, counter-propagating along the z axis, but this time one is linearly polarised along x and the other along y. Note that in this case, there are no intensity gradients—the polarisations of the two waves are perpendicular so there is no interference—and the intensity does not depend on z. However, now we have gradients in the ellipticity of the polarisation. As a result, as the atom moves along the z axis, the size of the matrix element coupling each of the ground states to excited levels varies. As in the two-level case, this coupling produces dressed states which are admixtures of the ground and excited states and accompanying shifts in the energies of the states.

Figure 3.6 shows how the polarisation of the light field, and the energies of the dressed ground states, vary with atom position for $\delta > 0$. The local polarisation is linear along $(\vec{e}_x + \vec{e}_y)/\sqrt{2}$ at $z = 0$, circular (σ^- defined along positive z direction) at $z = \lambda/8$, linear along $(\vec{e}_x - \vec{e}_y)/\sqrt{2}$ at $z = \lambda/4$ and then circular (σ^+) at $z = 3\lambda/4$ before repeating.

We can now again look at the effects of spontaneous emission which couple pairs of ground and excited states with transitions $\Delta m_F = -1, 0, 1$. We will concentrate on the low intensity regime, $\Omega_{\text{tot}} \ll \Gamma$. In this limit, the dressed states are nearly equal to the uncoupled states. We can neglect the populations of the excited dressed states—those that correspond to the bare excited states in the zero field limit—since the system will spend relatively little time there. We consider only the ground dressed states—those that correspond to the bare ground states in zero field limit. This is very similar to the low intensity regime in the two-level system except that now there are multiple ground states to consider.

For ease of notation, we will label the dressed states with the bare state that they correspond to

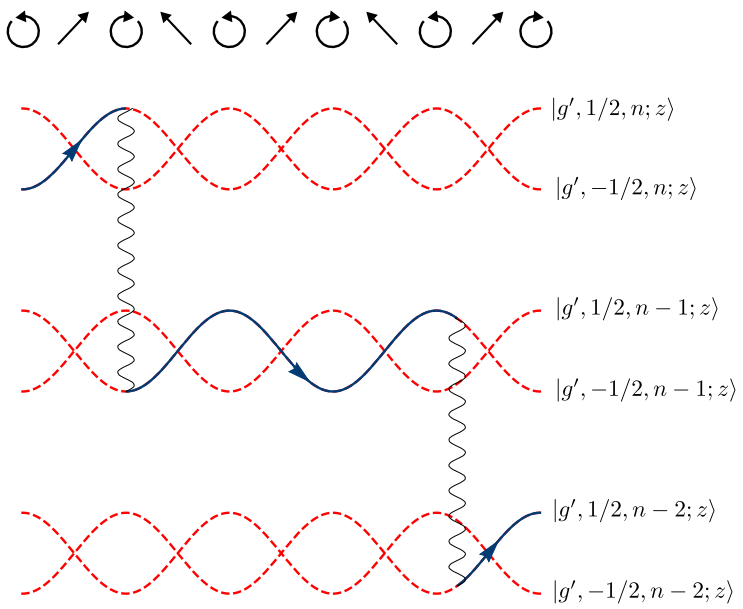

Figure 3.6: Illustration of Sisyphus mechanism for $F = 1/2 \rightarrow F' = 3/2$ system in a red detuned standing wave composed of two counter propagating laser beams linearly polarised at 90 degrees to each other. Top line shows how polarisation varies with position along standing wave. Red dashed lines indicate how energy of dressed atomic ground states varies with position and blue arrows show a sample trajectory of the system.

in zero field (with a prime to distinguish them) and the manifold, n. In a region of σ^+ polarisation, the $|g', -1/2, n; z\rangle$ state is a mixture of $|g, -1/2\rangle$ and $|e, 1/2\rangle$ and so is equally likely to decay back to either $|g', -1/2, n-1; z\rangle$ or $|g', 1/2, n-1; z\rangle$. This can happen directly or, more rarely, via a short lived excited state. The $|g', 1/2, n; z\rangle$ state is $|g, 1/2\rangle$ mixed with $|e, 3/2\rangle$ and so can only decay back to $|g', 1/2, n-1; z\rangle$. This imbalance leads to the population being optically pumped into $|g', 1/2, n-1; z\rangle$. Similar arguments show that, in regions of σ^- polarisation, the population accumulates in $|g', -1/2, n-1; z\rangle$. In the linearly polarised regions, symmetry considerations tell us that the two ground states are equally populated.

For $\delta > 0$, the state to which the system is optically pumped is also the state whose energy is maximum—the light shift is positive for positive δ and the Clebsch-Gordon coefficient is largest for the $m_F = 1/2 \rightarrow m'_F = 3/2$ transition. As a result atoms accumulate there and then gain kinetic energy as they move out of the region of circular polarisation and down the potential hill before being transferred back to the top of the potential hill in the next oppositely circularly polarised region by optical pumping. The atom continuously gains energy as it moves through the field. For $\delta < 0$ the argument is reversed and the atom may be cooled. This process is illustrated in Fig. 3.6.

Whereas in the two-level atom we had only one internal time, the excited state lifetime $\tau = 1/\Gamma$, the addition of extra levels has given us another internal time τ_{p}, the optical pumping time. Since both of the states we are transferring between are (nearly) ground states, their lifetimes can be equal and the cooling effective even in the low intensity regime.

We can make an order of magnitude estimate for the friction coefficient [149]. From Fig. 3.6 it is clear that the friction force is maximised when a photon is scattered at the top of each potential hill.

This corresponds to a velocity

$$v \sim \Gamma_p/k \tag{3.26}$$

where $\Gamma_\mathrm{p} \sim 1/\tau_\mathrm{p}$ is the optical pumping rate. For this particular velocity, the energy dissipated per unit time is

$$\frac{\mathrm{d}W}{\mathrm{d}t} \sim \hbar\Delta\Gamma_\mathrm{p}, \tag{3.27}$$

where Δ is the energy lost climbing a potential hill. But we can also write

$$\frac{\mathrm{d}W}{\mathrm{d}t} = -Fv \sim \alpha v^2. \tag{3.28}$$

Combining Eqs. (3.26), (3.27) and (3.28) gives an estimate for the friction coefficient,

$$\alpha = \hbar k^2 \frac{\Delta}{\Gamma_\mathrm{p}}. \tag{3.29}$$

For low intensities we can use Eqs. (3.22) to write $\Delta \sim \hbar\Omega_\mathrm{tot}/2 - \delta \sim \Omega^2/\delta$. Similarly, for $\delta > 0$ we can use Eqs. (3.21) to write the rate of type (a) transitions as $\Gamma_\mathrm{p} = \Gamma \sin^2\theta \sim \Gamma\Omega^2/\delta^2$. Now our estimate can be rewritten,

$$\alpha = \hbar k^2 \frac{\delta}{\Gamma}. \tag{3.30}$$

Our rough estimate demonstrates two important points. First, for large detunings, $\delta > \Gamma$, the friction coefficient can be much larger than the maximum possible from Doppler cooling, $\sim \hbar k^2$. Secondly, in this limit, the friction coefficient is independent of intensity whereas the heating terms will decrease when the intensity is lowered.

Our approach has been heuristic but a more in depth analysis confirms our conclusions that, for small velocities, the friction coefficient is independent of intensity [149]. For higher velocities the cooling becomes less effective because the atom begins to see some downhill as well as uphill during τ_p. Since τ_p scales inversely with intensity, this means the capture range of the polarisation gradient forces—the range of velocities over which they are effective—scales approximately linearly with the intensity.

Experimentally one can apply a large intensity to 'capture' the atoms in the high friction region and then lower the intensity to reduce the diffusion coefficient and hence the temperature. From our discussion so far, it would appear that arbitrarily low temperatures can be reached. This is of course unphysical and it turns out that the temperature is eventually limited by the breakdown of our semi-classical approximation. At sufficiently low velocity, the uncertainty principle dictates that the atoms position is no longer well-defined. This starts becoming a problem once the uncertainty in the position is of the order of a wavelength of the light. We can make an estimate for this lower limit on the velocity:

$$v \sim \Delta v \sim \frac{\hbar}{m\Delta r} \sim \frac{\hbar}{m\lambda} \sim \frac{\hbar k}{m}. \tag{3.31}$$

This is equal to the recoil velocity.

3.4.5 Application to molecules

Now we must consider how to apply this to a realisable transition in molecules. As discussed in Sec. 3.2.3, we must drive transitions of the type $F' \leq F$. In these systems, for any local polarisation, there exist dark ground-state superpositions which do not couple to the local light field, and bright states which do. The dark states have no mixing with the excited states and so no 'dressing' of their states occurs; their energy is identical to the bare ground state energy. The bright states are mixed with the excited state by the local light field.

In order to achieve a Sisyphus type effect, we need potential hills. This is possible, only in the bright states, by introducing intensity gradients. In this case optical pumping out of the bright states and into the dark state happens preferentially at field maxima. However, after transfer to a dark state, a molecule adiabatically following the local dark state of the system cannot leave this state; there is no admixture of excited states so spontaneous decays out of this state are not possible.

We can now return to an approximation we made before where we ignored the possibility of non-adiabatic transitions (see footnote 4). Since the dark states are only dark for a particular polarisation, it is possible for the system to make non-adiabatic transitions out of a dark state as it moves through a polarisation gradient. Although these transitions happen at a very low rate, for a system in a dark state they are the only mechanism affecting the dynamics and so they dominate. Non-adiabatic transfer happens preferentially at the field minima where the energy gap between the bright and dark states is minimum [155].

In contrast to the $F' = F + 1$ case illustrated above, in this case, the state to which the system is optically pumped has no light shift. To achieve cooling we must have positive light shift of the bright state, $\delta > 0$, so that the molecule moves up a potential hill as it enters the high intensity region where the optical pumping back to the dark state is most likely to take place.

We will take as a representative example a $F = 1 \rightarrow F' = 1$ transition. In order to have a light field with both intensity gradients and polarisation gradients, we will again consider two counter-propagating waves with linear polarisation, but this time their polarisations are separated by an angle $\phi = \pi/4$. This may seem a slightly contrived example in 1D but having both polarisation and intensity gradients is unavoidable in 3D. Figure 3.7 illustrates this process. A possible trajectory is shown to illustrate how the molecule may continually lose energy as it moves through the field. This mechanism has been demonstrated for atoms (see for example [156]) and is often referred to as a 'grey molasses' because the system spends time in both bright and dark states.

The opposite sign of the detuning for Doppler and grey-molasses cooling on $F' \leq F$ transitions presents a problem for molecular MOTs. Figure 3.8 (from [155]) shows the numerically calculated force in the direction of motion as a function of velocity for a model system. Red detuning is required to capture molecules from high velocities but the temperature will be limited by heating at low velocities from the polarisation gradient forces. In Sec. 5.2, we show that molecules can be transferred from such a MOT into a blue-detuned molasses to reduce the temperature to below the Doppler limit. This works due to the difference in the intensity dependence of the two mechanisms. The zero crossing of the force shown in Fig. 3.8 can be moved around by changing the intensity; at higher intensities it moves to higher velocities. We ramp down the intensity of the red-detuned MOT, moving the zero crossing to lower velocities and thereby decreasing the equilibrium temperature. We can then transfer

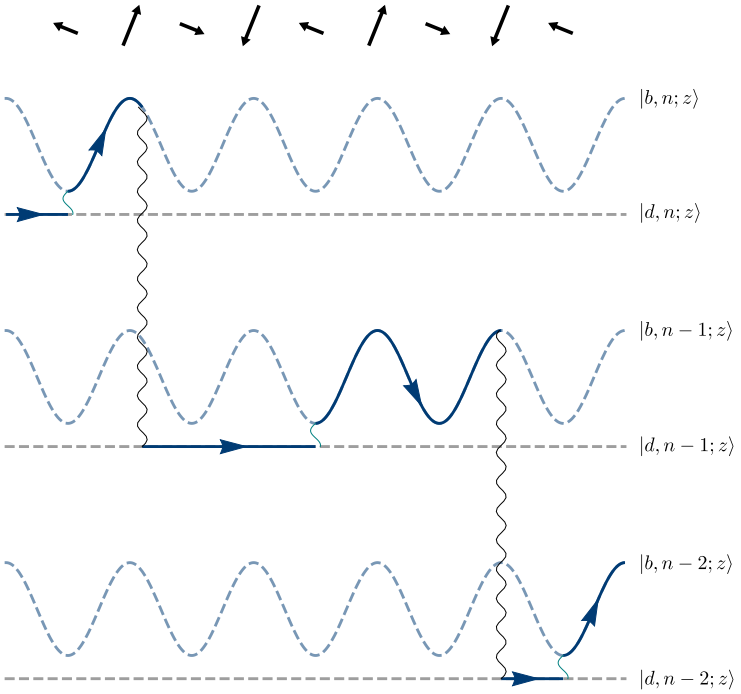

Figure 3.7: Illustration of Sisyphus mechanism for $F = 1 \rightarrow F' = 1$ system in a blue detuned standing wave composed of two counter-propagating laser beams, linearly polarised at 45 degrees to each other. Top line shows how polarisation varies with position along standing wave. Light blue dashed lines indicate how energy of dressed atomic ground states varies with position and dark blue arrows show a sample trajectory of the system. Black wavy lines show spontaneous emission events and green wavy lines show non-adiabatic transitions between states in the same manifold.

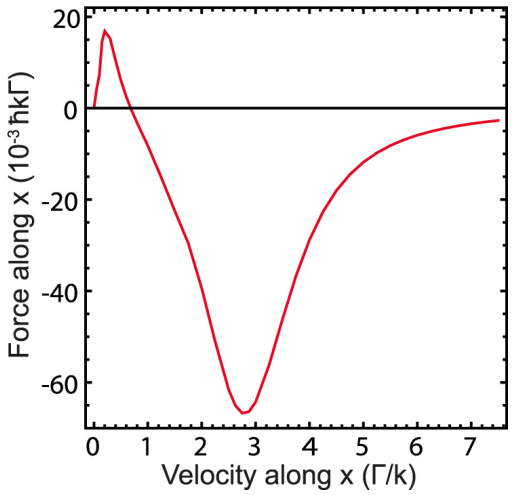

Figure 3.8: Steady-state force along x in an $F = F' = 1$ system moving in a 3D $\sigma^+\sigma^-$ light field as a function of velocity in x direction. The velocity along y is zero and along z is $0.1\Gamma/k$, the detuning $\delta = -2.5\Gamma$ and the intensity $I = 2I_s$ for each beam. Reproduced from [155].

to a higher-intensity blue-detuned molasses where all molecules see a cooling force. Transfer to a blue-detuned MOT has also been demonstrated for Rb atoms using the $F' \leq F$ components of the D2 line [157]. Combining cooling and confinement enables higher densities to be reached.

3.4.6 Velocity selective coherent population trapping

The 'grey molasses' technique introduces an interesting possibility. Because transitions out of the dark state are motion induced, a molecule that—by chance after a spontaneous emission event—happens to be in a very low velocity state can stay there for a long time. This is in contrast to the sub-Doppler cooling described in Sec. 3.4.4 where the molecule will quickly scatter more photons and heat out of the low velocity state.

To understand the limit of this type of scheme, we need to treat the motion of the molecule quantum mechanically. For simplicity, we will consider the $F' = 1$, $F = 1$ system again, but now in the presence of counter-propagating circularly polarised beams of the same handedness, σ^+ along the positive x direction and σ^- along the negative x direction. The interaction Hamiltonian is similar to that of Eq. (3.17) but now we include the molecule position operator,

$$\vec{E}^+ = \vec{E}^{-*} = \mathcal{E}\left(e^{i\vec{k}\cdot\vec{R}}\vec{e}_+ + e^{-i\vec{k}\cdot\vec{R}}\vec{e}_-\right)e^{-i\omega_F t}. \tag{3.32}$$

Here $\vec{e}_\pm = \mp(\vec{e}_x \pm i\vec{e}_y)/\sqrt{2}$ are the polarisation unit vectors. We can re-express this electric field operator in terms of eigenstates of the momentum operator,

$$\vec{E}^+ = \mathcal{E}\int \mathrm{d}p\left(|p+\hbar k\rangle\langle p|\,\vec{e}_+ + |p-\hbar k\rangle\langle p|\,\vec{e}_-\right)e^{-i\omega_F t}. \tag{3.33}$$

The eigenstates of the fully quantum mechanical interaction Hamiltonian are states where the internal and external degrees of freedom of the atom are entangled. We focus on the states involving only superpositions of the internal ground states $|g, m_F\rangle$, which are also resilient to spontaneous emission. These are

$$|\psi_{\mathrm{NC}}(p)\rangle = |g,-1\rangle\,|p-\hbar k\rangle + |g,+1\rangle\,|p+\hbar k\rangle\,. \tag{3.34}$$

The momentum parameter p can take any value and so Eq.(3.34) describes an infinite set of states. Each has a double-peaked momentum distribution with peaks separated by $2\hbar k$. However when we include the molecule kinetic energy operator, $\vec{P}^2/2m$, the only eigenstate of the full Hamiltonian is $|\psi_{\mathrm{NC}}(p=0)\rangle$, with its momentum distribution centred around zero. Molecules which end up in this state after a spontaneous emission event stay there indefinitely. Of course the probability of being scattered into $|\psi_{\mathrm{NC}}(p=0)\rangle$ is vanishingly small because the state is delocalised over all space. States with non-zero p evolve into bright states that contain some excited state admixture, which turns on the unwanted heating due to spontaneous emission. However, the rate for this evolution is $\sim 2pk/m$, which can be very small for small p. As a result, states with small p are dark for very long times and so population can still accumulate at small velocities, leading to velocity distributions with widths well below the recoil velocity.

This scheme is called velocity-selective coherent population trapping (VSCPT) and has been shown to cool meta-stable helium atoms below the recoil limit. The initial experimental demonstration was in 1D, relying only on the diffusive random walk in momentum space to populate the dark state [158]. In

three dimensions, a large fraction of the atoms will never pass near the zero-velocity state by random walk alone (see e.g. pp. 203–221 of [159]). By combining VSCPT with a grey molasses scheme which confines the atoms close to the origin of momentum space, Lawall et al. [160] demonstrated cooling below the recoil limit in three dimensions. In Sec. 5.3 we apply this technique to molecules, reaching temperatures corresponding to a few recoil energies.

In Chapter 8, another approach to cool atoms to temperatures below the recoil limit in tightly confining optical traps is explained, and its potential application to molecules explored in detail.

Chapter 4

Setup of the experiment

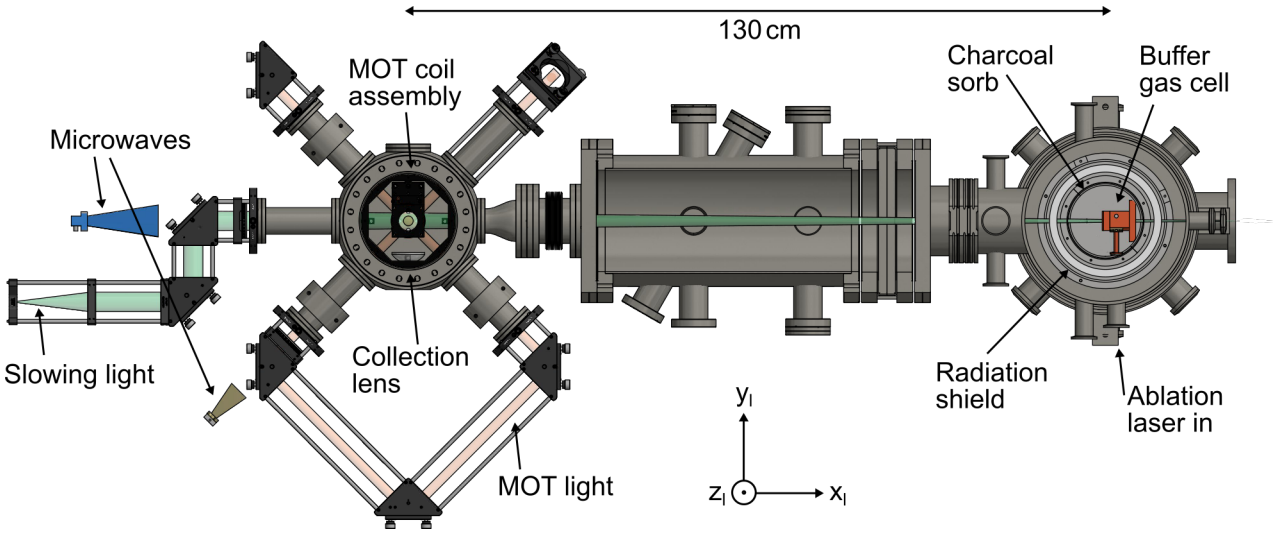

Figure 4.1: Schematic of the experiment. The lab fixed axes throughout this thesis will be defined as x_l, parallel to the slowing light, y_l parallel to the imaging axis and z_l vertical in the lab and perpendicular to the plane of this figure.

4.1 Introduction

This chapter presents the details of the apparatus used for all the experiments described in the later chapters. Figure 4.1 provides an overview of this setup. A beam of CaF molecules is produced by a cryogenic buffer-gas source on the left-hand side of the schematic. The molecules are slowed by frequency-chirped counter-propagating laser light, and then captured in the magneto-optical trap some 130 cm away. All subsequent experiments are done on this captured molecule sample.

4.2 Source

Each experiment described in this thesis begins with a pulse of CaF molecules created in a cryogenic buffer-gas source. The source is described in [161] and its development detailed in Moritz Hambach's thesis [162] so I will summarise it only briefly here.

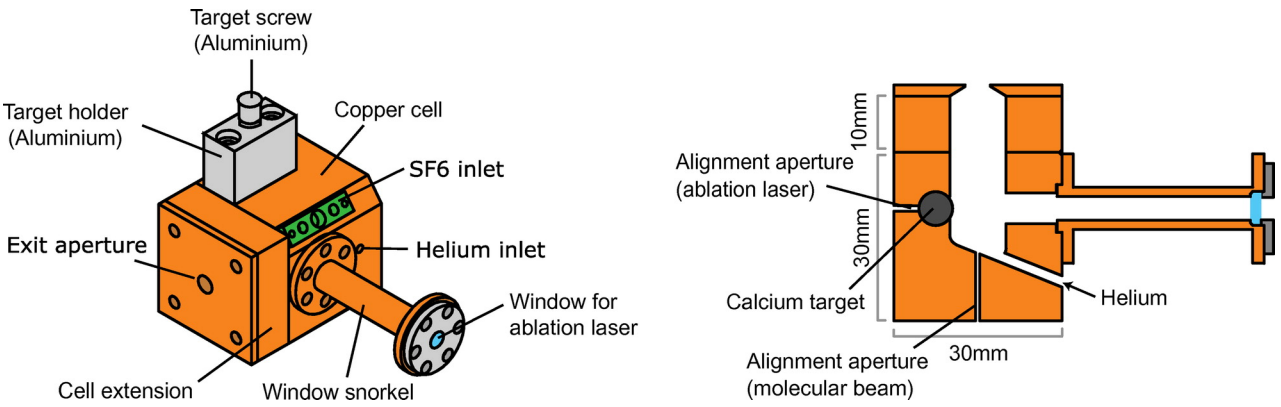

Figure 4.2: Schematic of buffer gas cell. Right side shows top view. Reproduced from [161].

A schematic of the buffer-gas cell is shown in Fig. 4.2. The cell consists of a Ca target mounted inside a copper cell which is cooled to 4 K by a cryocooler[1]. Cold helium gas and room temperature SF_6 gas are continually flowed into the cell at 0.3 sccm and 0.01 sccm respectively, with flows controlled by Alicat MCE series flow controllers. The Ca target is ablated by a pulse from a Nd:YAG laser which enters through a vacuum window and the released Ca atoms react with the SF_6 gas to produce CaF. The CaF molecules quickly thermalise with the helium through collisions and exit the cell through an aperture of 3.5 mm diameter. The source produces $\sim 5 \times 10^{10}$ molecules/steradian/pulse in the first rotationally excited and vibrational ground state ($v = 0, N = 1$) of the molecule. The average forward velocity of the pulse is around $150\,\mathrm{m\,s^{-1}}$.

Apart from a few centimeter exit aperture, the cell is completely enclosed by a charcoal sorb—a copper cylinder connected to the 4 K stage of the cryocooler and with its inner surface coated in charcoal. At temperatures less than 10 K, the charcoal acts as an effective pump for helium, reducing the gas load in the vacuum chamber. The charcoal sorb is in turn surrounded by an aluminium radiation shield that is connected to the 40 K stage of the cryocooler, thus reducing the radiative heat load on the 4 K stage of the cryocooler. The pressure in the source chamber, measured outside the radiation shields with the cold head at 4 K and the helium flow on, is typically $\sim 2 \times 10^{-7}$ mbar.

The molecules leave the source chamber, and pass into the slowing chamber, through an 8 mm diameter aperture, a distance of 35 cm from the cell exit aperture. In later experiments, described in Chapters 6 onwards, this aperture was replaced with an in-vacuum shutter (Uniblitz LS6S2Z0-EC-105 with VCM-D1 controller) to block the helium flow after the CaF pulse has passed through.

The source operates reliably on a single ablation spot for several hours ($\sim 10^4$ shots). When the signal starts to decay or become erratic we rotate the Ca target, exposing a new spot to the ablation pulse. Typically, after (very approximately) 8–10 hours of running the source signal decays in a way that cannot be improved by rotating the target. We find that we can recover the original signal by heating the source up close to room temperature and then cooling it back down again. Heaters mounted on the cold head allow us to increase its temperature to 40 °C in ~ 5 hours before cooling again. The high temperature required suggests the cause might be the absorption by the charcoal sorbs of a gas other than helium, which should be released at ~ 20 K. We perform this cycle each night to maintain consistent operation.

[1] Sumitomo RDK-415D

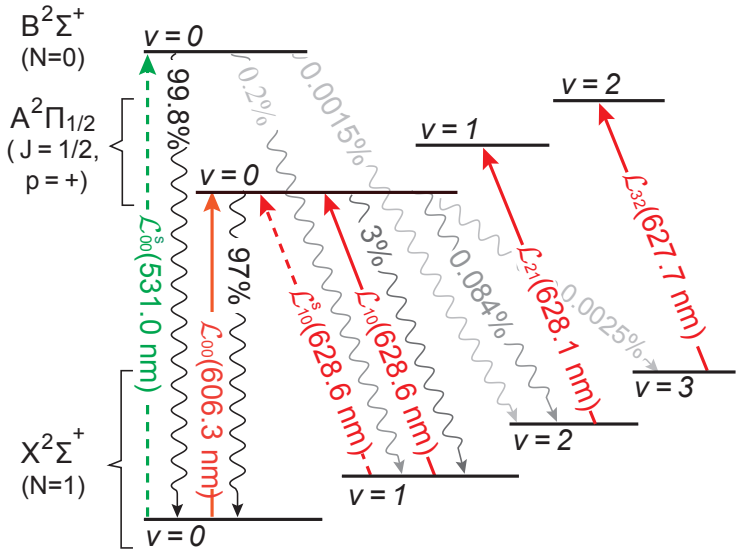

Figure 4.3: Transitions driven in the experiment, with wavelengths and branching ratios. Dashed lines are the transitions driven by the slowing lasers, while solid lines are those driven by the MOT lasers.

4.3 Lasers

The experiment uses five separate lasers to address different electronic and vibrational transitions in the molecule as shown in Fig. 4.3. In the MOT we drive the transitions $A^2\Pi_{1/2}(v = j, J = 1/2) \leftarrow X^2\Sigma^+(v = i, N = 1)$ using light which we denote $\mathcal{L}_{ij}$ with $ij \in \{00, 10, 21, 32\}$. To slow the molecular beam we drive the $B^2\Sigma^+(v = 0, N = 0) \leftarrow X^2\Sigma^+(v = 0, N = 1)$ transition using light $\mathcal{L}^{\mathrm{S}}_{00}$. The slowing also uses a single vibrational repump, $\mathcal{L}^{\mathrm{S}}_{10}$, which is derived from the same laser as $\mathcal{L}_{10}$. Figure 4.4 shows the optical setup used to prepare and control each light component. In the following section describes this setup in detail.

4.3.1 Preparation of light

To address the hyperfine components in the CaF ground state, we add sidebands to each laser. The sideband spectra are shown in Fig. 4.5. The centre frequencies of each laser, given in Table 4.1, are determined by using each as a transverse probe to the molecular beam and recording the fluorescence as we scan the frequency.

The 606 nm light used for $\mathcal{L}_{00}$ is derived from a 1212 nm Toptica DL Pro. The light from the DL Pro is amplified by an MPB Visible Raman fibre amplifier—pumped with a Yb fibre laser—and then frequency doubled by second-harmonic generation. After picking off a small amount of light to use for locking and monitoring, described later, the beam passes through a double pass AOM to allow for fast switching, frequency and amplitude control, before being split into two beams. Approximately one quarter of the light passes through a 48 MHz AOM to address the $F = 1^+$ hyperfine level and the remaining light passes through a 74 MHz EOM, driven so as to produce first order sidebands of roughly equal height to the carrier. The combined spectrum, shown in Fig. 4.5(a), matches very closely the hyperfine intervals of the $(v = 0, N = 1)$ state. At 600 mW output from the frequency doubling unit, the combined power of these two arms in the MOT chamber is ~ 80 mW. The two arms are delivered

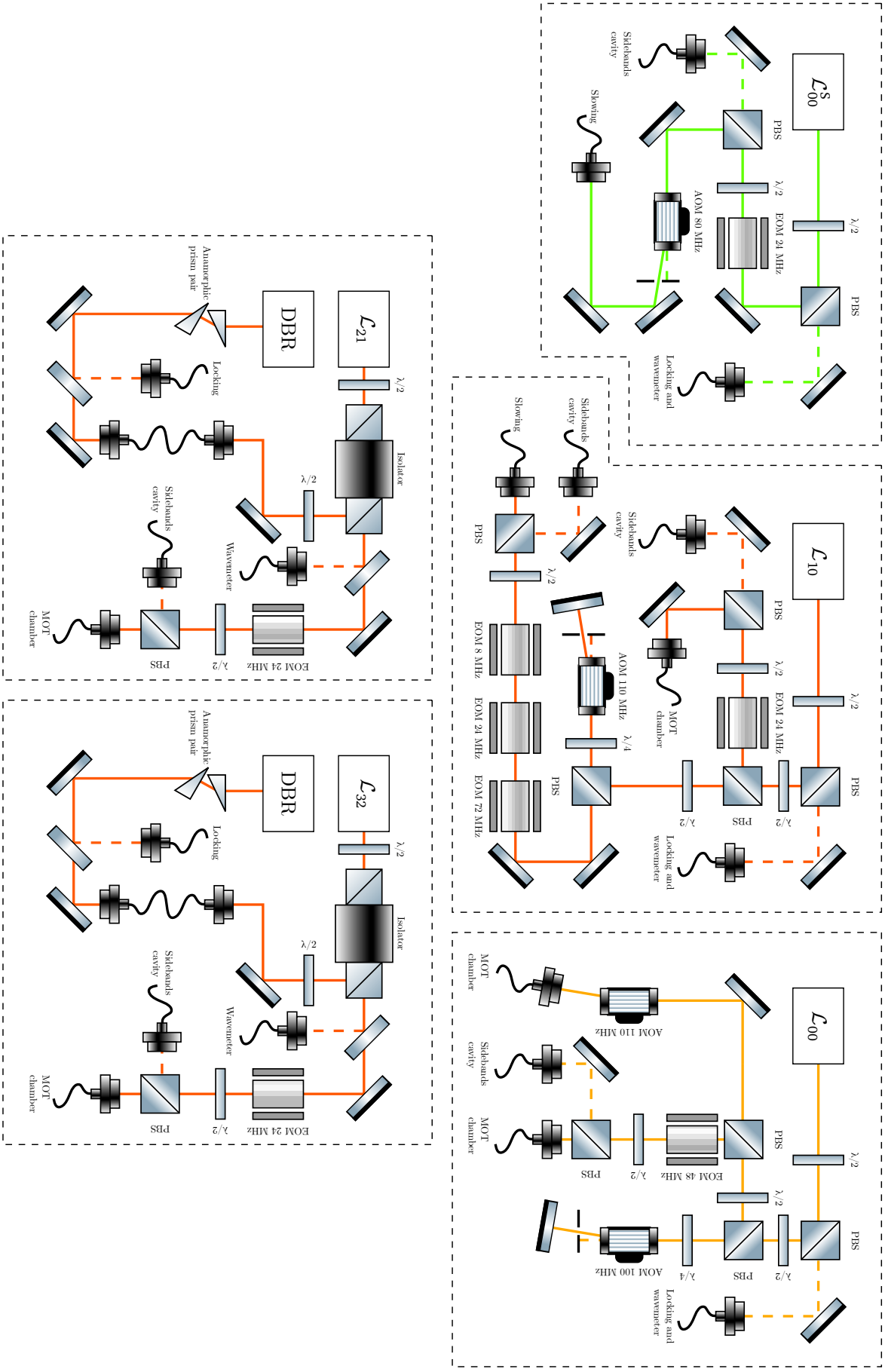

Figure 4.4: Schematic showing the optics used to prepare laser light for slowing and MOT.

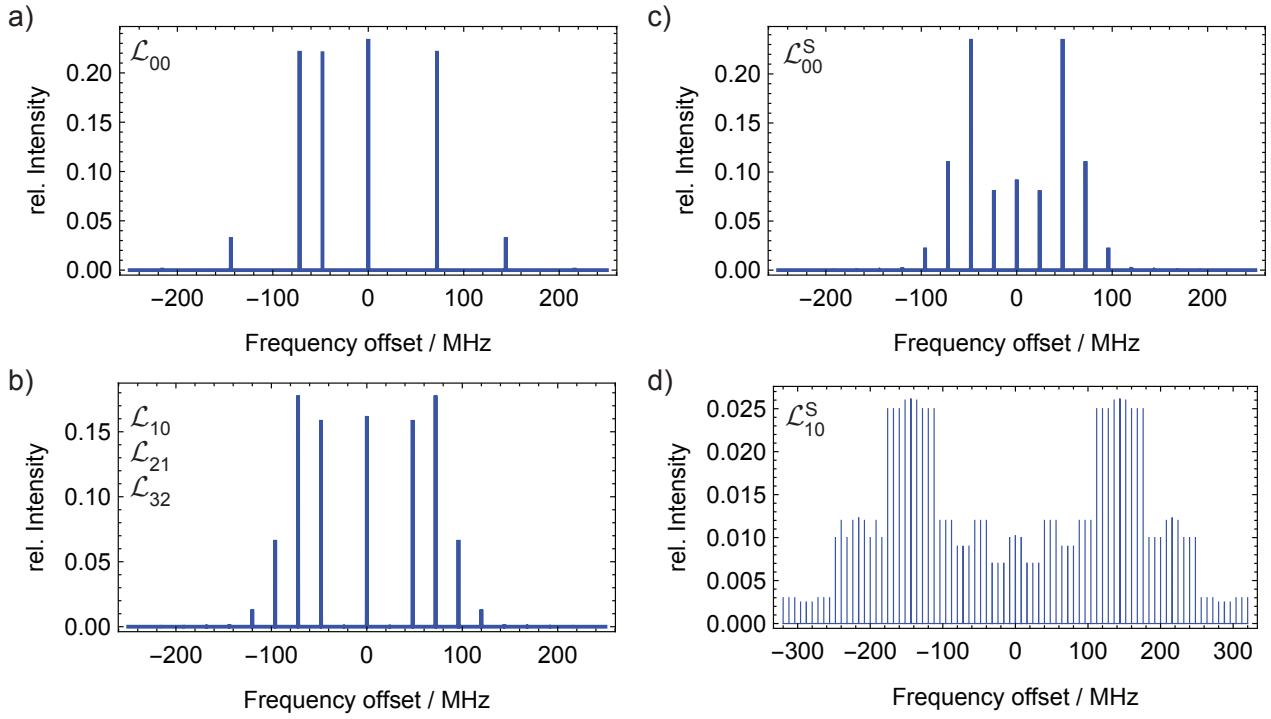

Figure 4.5: Frequency spectrum of each laser. a) $\mathcal{L}_{00}$. b) $\mathcal{L}_{10}$, $\mathcal{L}_{21}$, and $\mathcal{L}_{32}$. (c) $\mathcal{L}^{S}_{00}$. d) $\mathcal{L}^{S}_{10}$. The spectra were measured using a scanning cavity with a linewidth of about 7 MHz, and then converted into stick spectra

Table 4.1: Laser frequencies and powers used in the experiment. Frequencies are determined from a wavemeter and are accurate to $\sim 600\,\mathrm{MHz}$.

Laser	Frequency (GHz)	Power in chamber (mW)
$\mathcal{L}_{00}$	494431.3	80
$\mathcal{L}_{10}$	476958.0	80
$\mathcal{L}_{21}$	477298.7	10
$\mathcal{L}_{32}$	477627.6	0.5
$\mathcal{L}^{S}_{00}$	564581.3	120
$\mathcal{L}^{S}_{10}$	476958.0	120

to the MOT with orthogonal polarisations to realise the dual-freqeuncy MOT scheme described in Sec. 3.3.

The 531 nm light used for $\mathcal{L}_{00}^{\mathrm{S}}$ is derived from a 1062 nm Quantel Eylsa Yb fibre laser, frequency doubled by second-harmonic generation. The light passes through a 24 MHz EOM to generate the sideband structure shown in Fig. 4.5(b) and then through a single pass AOM to allow for fast switching.

The first vibrational repump light used in the MOT and the slowing, $\mathcal{L}_{10}$ and $\mathcal{L}_{10}^{\mathrm{S}}$, are derived from a laser setup very similar to that of $\mathcal{L}_{00}$. Light from a 1256 nm Toptica DL 100 is amplified by an MPB Visible Raman Fibre Amplifier, again pumped with a Yb fibre laser, and then frequency doubled by second harmonic generation. After picking off some light for locking, the light for the MOT passes through a 24 MHz EOM to create the sideband structure seen in Fig. 4.5(c). The light for $\mathcal{L}_{10}^{\mathrm{S}}$ passes through a double pass 110 MHz AOM to shift it into resonance with a molecule travelling at around $130\,\mathrm{m\,s^{-1}}$. The light then passes through a sequence of three EOMs driven at 72, 24 and 8 MHz respectively to create a near-continuous spectrum covering the Doppler shifts of molecules travelling at all velocities relevant to the experiment, as shown in Fig. 4.5(d).

The setups to generate $\mathcal{L}_{21}$ and $\mathcal{L}_{32}$ are identical and consist of a home-built leader–follower setup. The 'leader' laser is a frequency-stabilised distributed Bragg reflector (DBR) diode built by the Ferdinand-Braun Institute. The DBR diode is mounted in a hermetically sealed chamber which is water cooled to 15(1) °C. The diode is then further cooled close to its running temperature of $\sim 12\,^{\circ}\mathrm{C}$ by a peltier, regulated by a temperature controller (Wavelength Electronics MPT-2500) using feedback from a thermocouple mounted close to the diode. The diode has an internal temperature control system and is stabilised to $\pm 0.002\,^{\circ}\mathrm{C}$ by connecting to a Thorlabs TED200C temperature controller. The output frequency of the diode can be fine tuned with the current and we use this to lock the laser. We find the laser frequency to be extremely stable in this arrangement but the maximum output power is limited to 20 mW, insufficient for our needs. To realise higher power we use the light from the DBR to seed a higher powered 'follower' diode. The output mode from the DBR diode is extremely elongated and so we first pass it through an anamorphic prism pair to make it more circular. The light is then focused through an optical isolator (not shown in Fig. 4.4) and, after picking off a small amount to be used for frequency locking, coupled into an optical fibre. The output of this fibre is injected into the free running follower diode.

The follower diodes, either Thorlabs HL63163DG for $\mathcal{L}_{21}$ or HL63133DG for $\mathcal{L}_{32}$, emit at 637 nm and 633 nm respectively at room temperature, far above the wavelengths we require in the experiment. We bring them into the desired range by cooling them. The diode wavelengths change by $\sim 0.2\,\mathrm{nm\,^{\circ}C^{-1}}$ so require cooling to $-25\,^{\circ}\mathrm{C}$ and $-5\,^{\circ}\mathrm{C}$ respectively. We mount the follower diodes in the same water-cooled, hermetically sealed housing as used for the leader diodes but evacuate them to ~ 1 mbar to avoid condensation that would freeze at such low temperatures. Two stages of peltiers are used to reach the required temperatures. The lower stage runs at constant current and the top stage, closest to the diode, is stabilised by a temperature controller (Wavelength Electronics PTC5K-CH) with feedback from a thermocouple mounted close to the diode. The temperature is set, largely by trial and error, to give a free-running single-mode output which is closest to the target wavelength. The diode itself is held in an adjustable collimation tube (Thorlabs LTN330-A) and powered via a protection circuit which shields the diode from rapid power fluctuations.

After exiting the housing, the follower beam passes through a Faraday isolator. We use the rejection

port of the isolator to couple seed light in from the leader laser. By coupling light from the rejection port into the output of the optical fibre from the leader laser, we ensure maximum overlap of the spatial modes. A half-waveplate, placed between the fibre output and the rejection port, allows us to tune the power used to seed the follower laser. Following the isolator, the follower passes through a 24 MHz EOM to create the same sideband structure as the $\mathcal{L}_{10}$ light, shown in Fig. 4.5(c). The light from $\mathcal{L}_{21}$ and $\mathcal{L}_{32}$ is combined on a 90:10 beam splitter so that around 10 and 0.5 mW reaches the chamber from $\mathcal{L}_{21}$ and $\mathcal{L}_{32}$ respectively.

4.3.2 Delivery to chamber

All light for the MOT is combined in a Schäfter & Kirchoff fibre combiner which uses a combination of polarisation and dichroic optics to combine the different components into a single fibre. At the MOT chamber, the light is expanded into a beam with $1/e^2$ radius 8.1 mm, passed through a quarter waveplate and then passed through the centre of the MOT chamber six times. The first pass is vertical (along $-z_1$), then two orthogonal horizontal passes before the beam is retroreflected for the final three passes in the opposite direction. After each pass, a quarter waveplate transforms polarisation to linear for reflection off the mirrors before another returns it to circular for the pass through the chamber. This prevents distortion of the polarisation by the mirrors. We slightly focus the beam to compensate for losses through the optics although perfectly balancing the powers in each of the six passes is difficult to achieve.

The two components of the slowing light are combined on a PBS cube and also coupled into a single fibre to deliver the light to the experiment. The light is expanded to a beam which has a $1/e^2$ radius of 9 mm at the MOT and converges to 1.5 mm at the source. The polarisation of the light is linear along z_1.

4.3.3 Locking

We lock the various lasers for the experiment using a transfer cavity. A pickoff from each of the lasers is coupled into one of two scanning Fabry-Perot cavities. The outputs are separated using dichroic mirrors and the transmission of each laser continuously monitored on a photodiode. A 780 nm reference laser, locked to a Doppler-free saturated absorption signal in a Rb vapour, is also coupled into each cavity. A computer program TransferCavityLock, continuously scans the length of the cavities whilst monitoring the transmission signals. For each scan of the cavity, the program fits a Lorentzian to the transmission lineshape of each laser. The program feeds back to the offset voltage used to scan the cavity in order to stabilise the mean cavity length, and to each of the experiment lasers to stabilise its peak position relative to the reference peak. The program operates with a repetition rate of ~ 7 Hz and stabilises each laser to $\sim \pm 1$ MHz except $\mathcal{L}_{32}$ which is stabilised only to $\sim \pm 4$ MHz.

4.4 Magnetic field

4.4.1 Slowing coils

Two pairs of rectangular coils provide a roughly uniform magnetic field throughout the slowing chamber. The field is perpendicular to the axis of the molecular beam. The pair nearest to the source runs at a

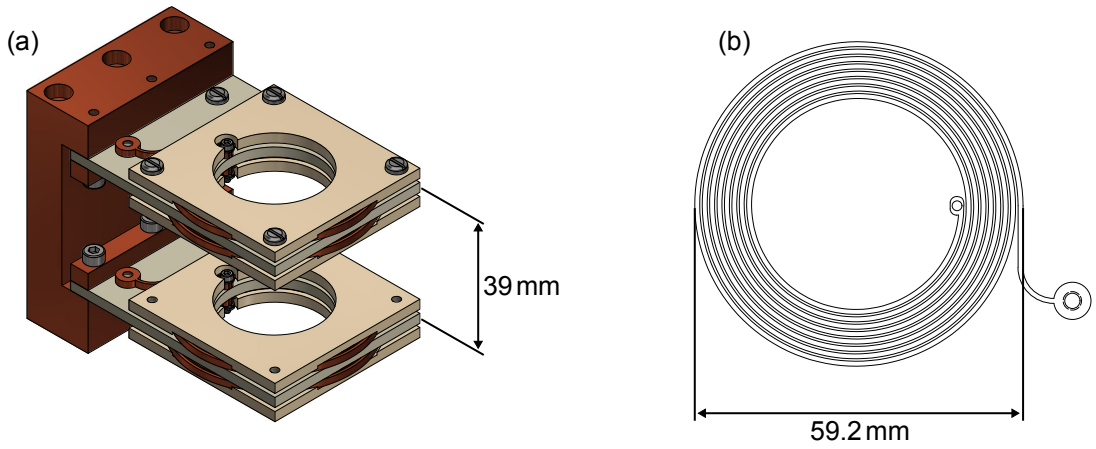

Figure 4.6: MOT coils. (a) Full MOT coil assembly. The copper spirals are sandwiched in pairs between three AlN plates. The centre plate is held in place by the copper heat sink. The distance between the centre of the plates is 39 mm. In the experiment, the entire assembly is painted black and the heatsink, which forms the background for fluorescence imaging of the molecules, is wrapped in black foil to reduce scattered light. (b) Drawing of single copper spiral.

constant current of 5 A. We find that the pair closest to the MOT chamber creates a significant fringe field at the position of the MOT which interferes with cooling. We use a FET circuit to switch them on, also at ~ 5 A, for the duration of the slowing and then off for the rest of the experiment sequence.

4.4.2 MOT coils

The MOT coils are illustrated in Fig. 4.6. They are positioned inside the vacuum chamber and consist of two pairs of laser-cut copper spirals. Each spiral is 2 mm thick and has 8 turns with an average radius of ~ 2 cm, and each pair is supported by a 2 mm thick AlN plate attached to a copper heatsink. The two pairs are separated by a distance of 38.3 mm. The design has very small inductance and so allows for fast switching of the current flowing in the coils (~ 1 ms). With a current of 10 A flowing in opposite directions through each pair, the coils produce an axial field gradient of $30\,\mathrm{G\,cm^{-1}}$.

Each pair of coils is connected in series to a vacuum feedthrough and the magnitude and direction of the current in each pair can be controlled independently using the H-bridge circuits shown in Fig. 4.7. The MOSFETs T1–4 and T6–9 can be switched to select the current direction through each pair of coils while the bypass circuit around the top coil (through T10) allows for higher current in the bottom coil than the top. The amount of current flowing around the bypass circuit is controlled by varying the gate voltage to T10 using feedback from the sense resistor R_S (Ohmite TGHGCR1000FE, 0.1 Ω 100 W). All 10 MOSFETs are IXYS IXFN180N15P (150 V, 150 A max) and are bolted to a copper heatsink. The power supply used is a Delta-Electronika SM 7.5-80 in constant current mode. The H-bridge control circuit was designed and built by Noah Fitch.

4.4.3 Shim coils

Three pairs of external shim coils positioned around the MOT chamber (not shown in Fig. 4.1) allow us to precisely control the magnetic field at the position of the molecules.

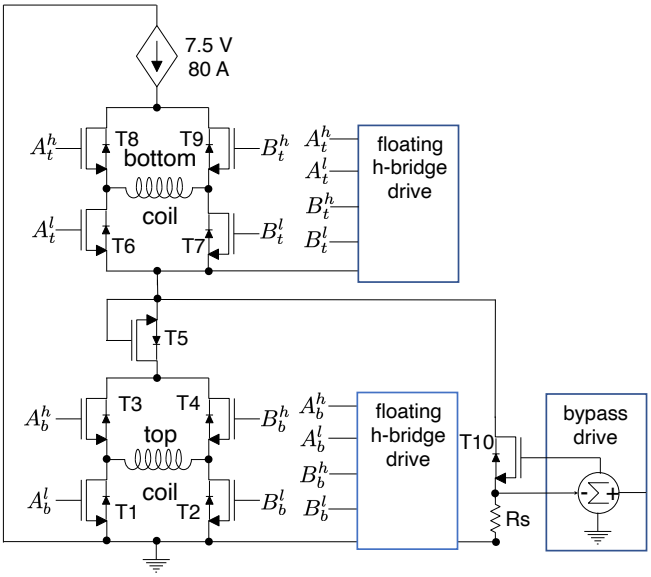

Figure 4.7: H-bridge circuit used to control the MOT coils.

4.5 Imaging

A collection lens of diameter $d = 60\,\text{mm}$ (Thorlabs LA1401-A) is positioned one back focal length ($f = 49.1\,\text{mm}$) from the centre of the MOT coils, inside the vacuum chamber. The lens collects the fluorescence light from the molecules and collimates it through an AR coated vacuum window. Outside the vacuum, a second lens (Comar 29 AF 40, $d = 40\,\text{mm}$, $f = 28.6\,\text{mm}$), images the fluorescence onto a CCD camera (Hammamatsu Orca R2).

The many high power laser beams circulating through the chamber mean that scattered light is a significant problem for imaging (an often small number of) molecules above the background. We take two principle measures to mitigate this:

(a) To minimise scattered light, the inside of the chamber is blackened. The copper heat sink for the MOT coils, which provides the backdrop against which the molecules are imaged, is wrapped in black foil (Acktar spectral black) which provides particularly low scatter at large angles of incidence. Both the MOT coils and a hexagonal insert inside the MOT chamber are painted with UHV compatible black paint (Alion MH2200) which we find provides lower scatter than the foil at small angles of incidence [162]. Soot coated baffels are inserted into each of the nipples of the MOT chamber to minimise the amount of scatter from the vacuum windows which reaches the imaging lens. Some of these additions have the potential to cause vacuum problems but after opening the chamber to air we bake our MOT chamber to $\sim 130\,^{\circ}\text{C}$ after which the pressure reaches the lower limit of our vacuum gauge at $5 \times 10^{-10}\,\text{mbar}$.

(b) A filter (fluorescence bandpass filter, Edmund Optics, $\lambda = 605\,\text{nm}$, FWHM $= 22\,\text{nm}$) positioned between the two lenses, blocks scattered light from the 628 nm repump lasers whilst allowing the 606 nm light to pass. For the scattering rate measurements described in Sec. 5.1.2 we swap this filter for a 652 nm filter (fluorescence bandpass filter, Edmund Optics, $\lambda = 648\,\text{nm}$,

FWHM = 20 nm).

4.6 Microwaves

The microwaves used in the experiments described in this thesis were generated using one of two synthesizers. Initially, for the experiments described in Sec. 6, we used a two-channel Windfreak SynthHD synthesizer (0.01–15 GHz, output power 20 dBm). The outputs from the synthesizer were connected to a four-to-one switch (Analog Devices HMC641ALC4) and then to a frequency doubler ~ 20.5 GHz (Pasternack PE8603, input range 9–13 GHz) and coupled into the chamber with a microwave horn (Pasternack PE9853/SF-15 15 dBi gain, 15–22 GHz). The horn is directed into the chamber through the back of one of the mirrors used for the MOT light as shown in Fig. 4.1. We find this arrangement to give sufficient microwave power at the position of the molecules provided the mirror is dielectric rather than metallic.

As detailed in Sec. 6.4.3.1, we found that the four-to-one switch (it is really designed as a one-to-four switch) resulted in chirping of the microwave frequency when switched. In addition we found that the Windfreak HD was unreliable in locking to our 10 MHz reference signal. For later experiments, from Sec. 6.7 onwards, we used two Gigatronics 7100 synthesizers (0.01–20 GHz, output power 10 dBm) to generate any frequency-sensitive microwaves and a two-to-one switch (Narda SP123DHTS) to connect to the frequency doubler.

Experiments driving $N = 1 \rightarrow N = 2$ transitions require frequencies ~ 41 GHz. To generate this frequency, the output of the synthesizer is fed into a frequency quadrupuler with built in amplifier (SAGE millimeter SFA-333473421-22SF-S1, 21 dBm gain, 33–47 GHz) which is then coupled into the chamber using a separate microwave horn (SAGE millimeter SAR-2013-222M-E2, 20 dBi gain, 33–50 GHz).

4.7 Computer control

The experiment is controlled using custom software written over many years by various members of our group working on a number of different experiments. Parts of the experiment which do not require rigourous timing are controlled by HardwareController. Examples of its responsibilities include changing the microwave synthesizer frequencies between experiments and controlling the cryocooler for overnight cycling. Timing-critical control during an experimental run is managed by MOTMaster. The software uses C# scripts to generate analogue and digital patterns which are then uploaded to National Instruments hardware to control the various components of the experiment. Both HardwareController and MOTMaster can be scripted using Python to allow for convenient scans over many experimental parameters.

Chapter 5

Sub-Doppler cooling

This chapter describes experiments to cool molecules to temperatures below the Doppler limit. The first step is to slow the molecular beam and capture the molecules in the MOT. These initial steps are described elsewhere [2, 135], but for completeness are also described briefly here before moving on to the main subject of the chapter. The results and analysis described in this chapter are also published in Refs. [1] and [5].

5.1 Slowing and the MOT

5.1.1 Introduction

All experiments described in this thesis begin by loading a single pulse of molecules into a magneto-optical trap (MOT). The pulse is produced at time $t = 0$ when the Nd:YAG laser ablates the calcium target and the freed calcium reacts with SF_6 gas flowing through the chamber to make CaF. The new molecules are entrained in the flow of helium gas which has thermalised with the cold head at 4 K. Collisions with the helium atoms quickly cool the molecules before they leave the cell through a 3.5 mm aperture travelling at $\sim 150\,\mathrm{m\,s^{-1}}$.

Each pulse of molecules is decelerated by frequency-chirped laser slowing. The technique is described in detail in Ref. [135] but summarised here. Light from $\mathcal{L}^{\mathrm{S}}_{00}$ is combined with $\mathcal{L}^{\mathrm{S}}_{10}$ repump light to form a single beam which counter propagates to the molecular beam and which is switched on at $t = 2.5\,\mathrm{ms}$. The frequency of the $\mathcal{L}^{\mathrm{S}}_{00}$ light, initially tuned to resonance with molecules travelling at $145\,\mathrm{m\,s^{-1}}$, is linearly chirped at $24.5\,\mathrm{MHz\,ms^{-1}}$ from $t = 3.4\,\mathrm{ms}$ to $t = 15\,\mathrm{ms}$, when the slowing light is switched off.

We load the MOT with $\mathcal{L}_{00}$ at a detuning of $\Delta = -0.75\Gamma$ and a total intensity (six times the single beam intensity) of $I_{00} = 500\,\mathrm{mW\,cm^{-2}}$. The axial magnetic field gradient is $\mathcal{B}' = 30\,\mathrm{G\,cm^{-1}}$. Molecules begin accumulating in the MOT as soon as the slowing light is switched off and the number of trapped molecules peaks at $t \sim 30\,\mathrm{ms}$. We have fully characterised the MOT and the results are detailed in Ref. [2] as well as in Hannah Williams' thesis [163]. Here I give only a summary of the key results.

5.1.2 Molecule number

The number of molecules in the MOT is determined by imaging the fluorescence from the molecules onto a CCD camera. The circulating laser light in the chamber means that we need to be careful to

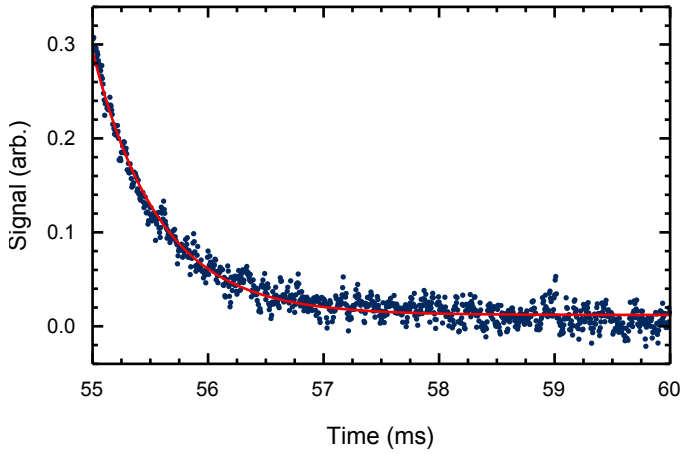

Figure 5.1: MOT fluorescence as a function of time after turning off $\mathcal{L}_{21}$ at $t = 55\,\text{ms}$. Dots show recorded fluorescence, line shows fit to single exponential decay giving time constant of $572(7)\,\mu\text{s}$.

avoid background light from scattering of the laser beams. We mitigate the effects of this by blackening the chamber and using a filter to block 628 nm light as described in Sec. 4.5. After these measures have been taken, the background count at full laser intensity is $8.5 \times 10^4\,\text{photons}\,\text{s}^{-1}\,\text{mm}^{-2}$. This background count is slightly non-uniform across the camera field of view and varies slowly with time so we record frequent background images—taken under the same conditions but with no molecules present—which we subtract from the MOT images so that only the fluorescence from the molecules remains. To translate the number of photons recorded in a given exposure time to a number of molecules we require: (i) The scattering rate of molecules in the MOT and (ii) the detection efficiency of our imaging system:

(i) We determine the scattering rate in the MOT by turning off $\mathcal{L}_{21}$ and using a PMT to measure τ_2, the time taken for the fluorescence to fall by $1/e$ as molecules are optically pumped to $v = 2$. The PMT is positioned at the normal position of the camera. Figure 5.1 shows an example scattering rate measurement with $\mathcal{L}_{21}$ turned off at $t = 55\,\text{ms}$ giving a time constant $\tau_2 = 572(7)\,\mu\text{s}$. The scattering rate is then $R_{\text{sc}} = 1/b_2\tau_2$, where b_2 is the branching ratio for the excited state to decay to $v = 2$. We determined b_2 by comparing the MOT fluorescence intensity on the $A(0) \to X(0)$ transition at 606 nm to that on the $A(0) \to X(2)$ transition at 652 nm. The two contributions were measured by swapping the bandpass filter placed between the two lenses of the imaging system. Each filter has a pass band of $\sim 20\,\text{nm}$ with transmission above 93 % at the wavelength of interest. The filter that transmits 652 nm has a transmission of less than 10^{-6} at 606 nm, small enough to neglect. We can express b_2 as

$$b_2 = b_0 \frac{I_2}{I_0} \frac{T_{\text{l1}}^{606}}{T_{\text{l1}}^{652}} \frac{T_{\text{l2}}^{606}}{T_{\text{l2}}^{652}} \frac{T_{\text{window}}^{606}}{T_{\text{window}}^{652}} \frac{T_{\text{f606}}^{606}}{T_{\text{f652}}^{652}} \frac{\epsilon_{\text{camera}}^{606}}{\epsilon_{\text{camera}}^{652}}. \tag{5.1}$$

Here, I_2/I_0 is the ratio of the detected fluorescence, $b_0 = 0.987^{+0.013}_{-0.019}$ is the branching ratio to $v = 0$ [138], T_{li}^{λ} is the transmission of lens i, $T_{\text{f}\lambda}^{\lambda}$ is the transmission of the filter that isolates wavelength λ at that wavelength and $\epsilon_{\text{camera}}^{\lambda}$ is the quantum efficiency of the camera at wavelength

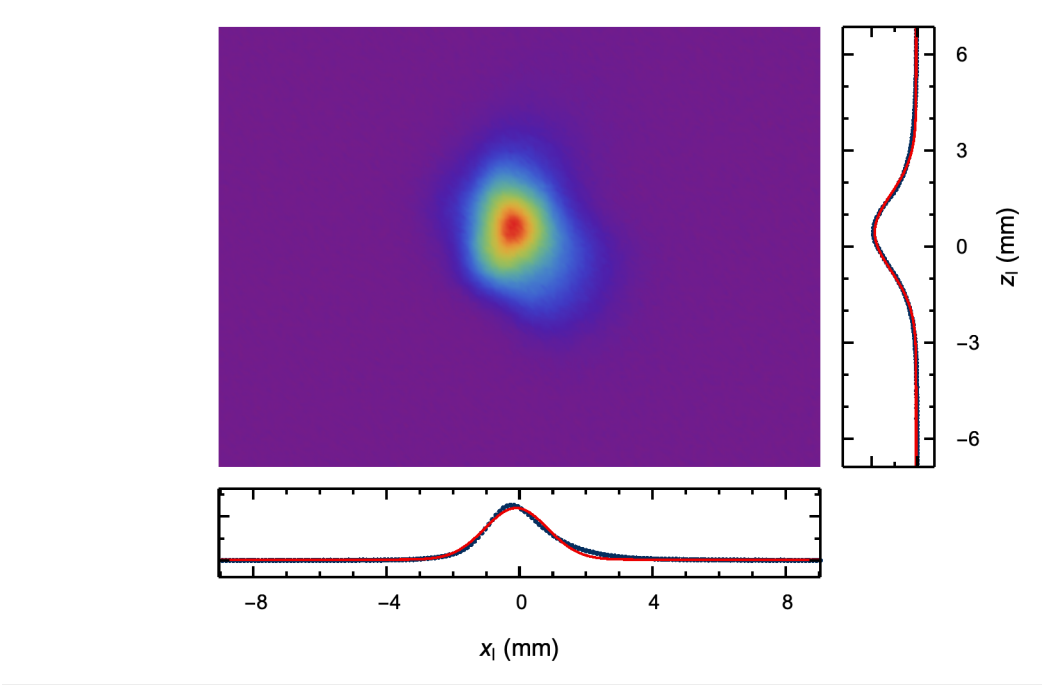

Figure 5.2: Single shot fluorescence image of MOT with an exposure time of 10 ms. Plots show profiles of the MOT in x_l (radial) and z_l (axial) directions. Red lines are Gaussian fits to data giving rms radii of 0.94 mm in the radial direction and 1.20 mm in the axial direction.

λ. All transmissions and quantum efficiencies are taken from data supplied by manufacturers. We measure $b_2 = 8.4(5) \times 10^{-4}$, 40 % smaller than the theoretical value of 1.2×10^{-3} given in [144]. The resulting scattering rate is $2.08(13) \times 10^6\,\mathrm{s}^{-1}$.

(ii) From numerical ray tracing, transmission measurements of the various components in the optical path, and the specified quantum efficiency of the camera, we calculate the detection efficiency to be 1.5(2) %.

Figure 5.2 shows an image of a typical MOT containing 2×10^4 molecules taken at $t = 40$ ms. Typically, fluctuations in the MOT number are around 20 % of the total. We believe these fluctuations are dominated by fluctuations in the number of molecules produced at the source.

5.1.3 Lifetime

We measure the lifetime of the MOT by recording the fluorescence on a PMT and fitting the decay to a single exponential. The lifetime of the MOT at full intensity is ~ 100 ms. Decreasing the power in the MOT beams increases the lifetime of the MOT with a lifetime in excess of 150 ms possible at low powers before the MOT starts to deteriorate.

The dependence of the loss rate on the scattering rate appears linear over the range of intensities measured. A possible interpretation is that the primary loss mechanism is optical pumping to a dark state not addressed by the lasers. However, we find that the absolute value of the lifetime is very sensitive to the alignment of the MOT beams, an observation which is difficult to explain if that is the main loss mechanism. An alternative hypothesis is that the loss comes from the hottest molecules in the cloud escaping from the trap. As the intensity is lowered, there is competition between the

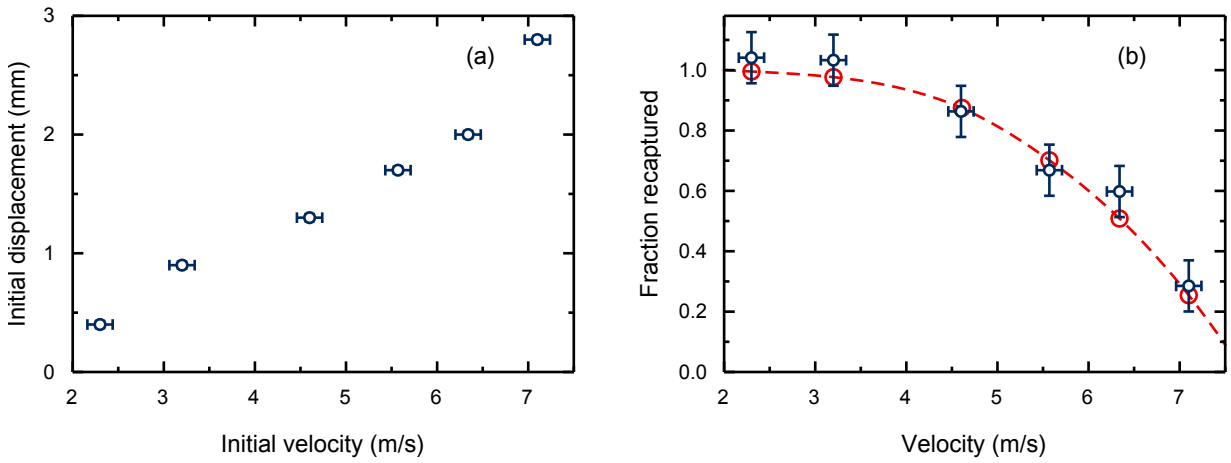

Figure 5.3: (a) Initial velocities and displacements used in measurements to determine the capture velocity. (b) Percentage of molecules recaptured into the MOT for each of the initial points in (a), indicated here by their velocities. Filled points: measurements. Open points: fit to the model described in the text. The dashed line is an interpolation between the open points.

decreasing trap frequency, meaning the minimum velocity required to leave the MOT is reduced, and decreasing temperature of the cloud (see Sec. 5.1.5), meaning there are fewer molecules at that velocity. The temperature of the MOT decreases faster than the trap frequency, resulting in a slight contraction of the cloud and an increase in the lifetime [2].

5.1.4 Capture velocity

Measuring the capture velocity of the MOT is challenging. Instead we measure the escape velocity by pushing the MOT and measuring the fraction of molecules that are lost as a function of their speed. We then infer the capture velocity from these results, with the help of a simple model. To apply an impulsive push, we turn off $\mathcal{L}_{00}$ and pulse on the slowing light, $\mathcal{L}_{00}^{\mathrm{S}}$, for a short time t_{push}.

Ideally we would apply an impulse to the molecules, imparting a velocity to them without displacing them from the centre of the trap. This requires a high scattering rate but molecules in the MOT are situated around zero magnetic field and so states which are dark to the polarisation of the $\mathcal{L}_{00}^{\mathrm{S}}$ light are not destabilised effectively. To improve the scattering rate, we found it necessary to modulate the polarisation of the slowing light. We used an EOM driven at 4 MHz and mounted at 45 degrees to the input polarisation of the light. We also decreased the size of the slowing beam to 3 mm $1/e^2$ radius, increasing the intensity at the position of the molecules. The polarisation modulation had no noticeable effect on the slowing efficiency while decreasing the beam size decreased the number of molecules captured slightly.

These measures improved our ability to impart a significant velocity to the cloud with a short pulse but displacement of the molecules during the push was still significant. Figure 5.3(a) shows the initial displacement x_i for various velocities v_i determined by imaging the cloud at a few different times after t_{push} with the magnetic field turned off. For each push we turn the MOT back on at $t = t_{\mathrm{push}}$ and measure the fraction of molecules recaptured by imaging the MOT at $t = t_{\mathrm{push}} + 20\,\mathrm{ms}$. The filled points of Fig. 5.3(b) show this fraction versus v_i where the v_i should be understood as $\{x_i, v_i\}$ pairs.

Table 5.1: Range of parameters used for capture velocity simulations.

Parameter	Value
Γ_{eff} (MHz)	2, 4, 6, 8, 10
$I_{\text{s,eff}}$ (mW cm^{-2})	20, 50, 80, 110, 140
g_{eff}	0.05, 0.25, 0.45, 0.65, 0.85

Were the initial displacements negligible, it would be simple to determine the capture velocity from these measurements. Since they are not, we use a model to interpret the results. In this model, the restoring force due to the MOT in the direction (x_{l}) of the slowing light is $F = \hbar k R_{\text{sc}}$ with R_{sc} given by Eq. (3.13). To account for the intensity distribution of the MOT beams we make the replacement $I \to I(\frac{x_{\text{l}}}{\sqrt{2}})$, where $I(r)$ has a Gaussian intensity distribution with a $1/e^2$ radius of 8.1 mm, truncated at a radius of $r_{\text{trunc}} = 15\,\text{mm}$. The detuning Δ includes both the velocity dependent Doppler shift and the position dependent Zeeman shift $g_{\text{eff}}\mu_B\mathcal{B}'x_{\text{l}}/2\hbar$ where g_{eff} is an effective g-factor and $\mathcal{B}'/2 = 15\,\text{G cm}^{-1}$ is the magnetic field gradient in the radial direction. Using this force, we solve the equations of motion for a distribution of initial coordinates in phase-space and for a time long enough that the distribution of final coordinates separates into two components, one with x_{l} close to zero and the other with $x_{\text{l}} \gg r_{\text{trunc}}$. This gives a contour in phase space, $v_{\text{sep}}(x_{\text{l}})$, which separates molecules that will be recaptured from those that escape. We then calculate the fraction of molecules from the initial phase-space distribution that lie inside this contour. We use a Gaussian spatial distribution centred at x_i with rms radius equal to the measured one, $s_0 = 2.0\,\text{mm}$, and a Gaussian velocity distribution centred at v_i and characterised by the measured temperature of 12 mK. This gives the simulated recapture fraction for each $\{x_i, v_i\}$ pair used for the measurement. In applying this procedure, it is not clear what values of Γ_{eff}, $I_{\text{s,eff}}$ and g_{eff} to use, so we keep them as free parameters. We calculated numerically the results of the model for all combinations of the parameters shown in Table 5.1 (125 different parameter sets). We then compared the results with the measured values and chose the parameter set that gives the smallest value of χ^2. The open circles in Fig. 5.3(b) show the results of that best fit with parameters $\Gamma_{\text{eff}} = 0.15\,\Gamma$, $I_{\text{s,eff}} = 50\,\text{mW cm}^{-2}$ and $g_{\text{eff}} = 0.25$, all reasonable values. The dashed line is an interpolation between these points.

The capture velocity v_{c} is the largest velocity a molecule that starts at the edge of the MOT can have if it is to be recaptured, $v_{\text{c}} = v_{\text{sep}}(-r_{\text{trunc}})$. The result, calculated from the model using the best fit parameters above, is $v_{\text{c}} = 11.2^{+1.2}_{-2.0}\,\text{m s}^{-1}$. The error bars are extracted from the fits by calculating v_{c} for all parameter sets with χ^2 within ± 1 of the minimum value and taking the maximum and minimum values. The rate model MOT simulations described in [147] predicted a capture velocity of $20\,\text{m s}^{-1}$ but used larger beams, higher power and a slightly different polarisation configuration. Repeating these simulations for the exact parameters used in the experiment we find a capture velocity of $14\,\text{m s}^{-1}$, closer to our measured value.

5.1.5 Temperature

We measure the temperature of the MOT using a ballistic expansion method. We turn off the MOT—both the light and magnetic field—to allow the molecular cloud to expand and then turn the light back

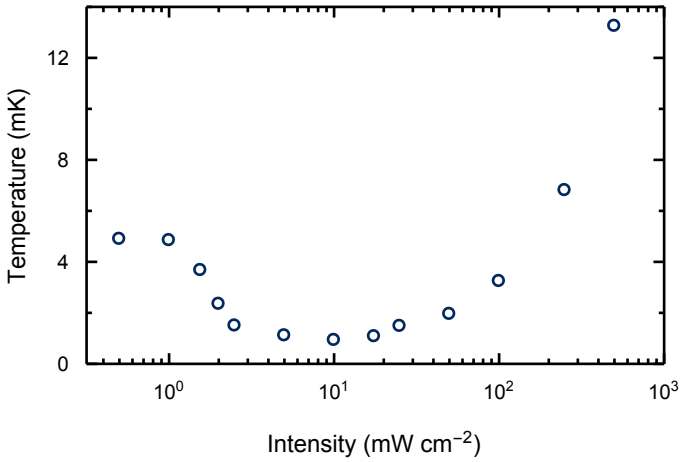

Figure 5.4: Temperature of the MOT versus I_{00}. Error bars, determined from fits similar to those shown in Fig. 5.6, are smaller than the points.

on after a delay $\tau_{\rm exp}$ to image the cloud for a short exposure time, typically 1 ms. For a thermal velocity distribution and an initial Gaussian density distribution with rms radius σ_0, the density distribution after a free expansion time $\tau_{\rm exp}$ is another Gaussian with rms radius σ given by

$$\sigma^2 = \sigma_0^2 + k_B T \tau_{\rm exp}^2 / M, \tag{5.2}$$

where M is the mass of the molecule. We measure σ for various values of $\tau_{\rm exp}$ and then fit a straight line to a plot of σ^2 against $\tau_{\rm exp}^2$. The gradient of this line gives the temperature. Figure 5.4 shows the measured temperature of the MOT as a function of $\mathcal{L}_{00}$ intensity. We see that, at full intensity where the capture velocity is largest, the temperature is 12 mK, but that by lowering the intensity to 9.2 mW cm^{-2} the temperature can be brought down to 960 µK. We find the temperature of the MOT is quite sensitive to alignment of the MOT beams and so can change significantly from day to day.

The ballistic expansion method for measuring the temperature is explored in more detail in the context of sub-Doppler cooling in Sec. 5.2. In particular, potential sources of systematic error in our measurements are discussed in Sec. 5.2.6.

5.1.6 Compressed MOT

The compressed MOT (CMOT) is a technique commonly used in atomic MOTs to increase the density of atoms in the trap and provides an important step on the way to evaporative cooling or other experiments that require high densities. We compress our molecular MOT by increasing the field gradient $\mathcal{B}'$ linearly between $t = 40$ and 50 ms and holding the higher $\mathcal{B}'$ until $t = 55$ ms, when we image the fluorescence from the cloud. Figure 5.5(a) shows how the axial and radial sizes of the MOT vary as a function of $\mathcal{B}'$ in the CMOT.

Figure 5.5(b) shows the peak number density n as a function of $\mathcal{B}'$ calculated assuming 2×10^4 molecules in the MOT and that the size of the cloud along the imaging axis ($y_{\rm l}$) is the same as that measured in the radial direction. Increasing $\mathcal{B}'$ from 30 to 113 G cm^{-1} increases n by a factor of 5.3 to 3.35×10^6 cm^{-3}. If $N_{\rm mol}$ and T are conserved in the compression, we expect $n \propto \mathcal{B}'^{3/2}$ [164]. Fitting our

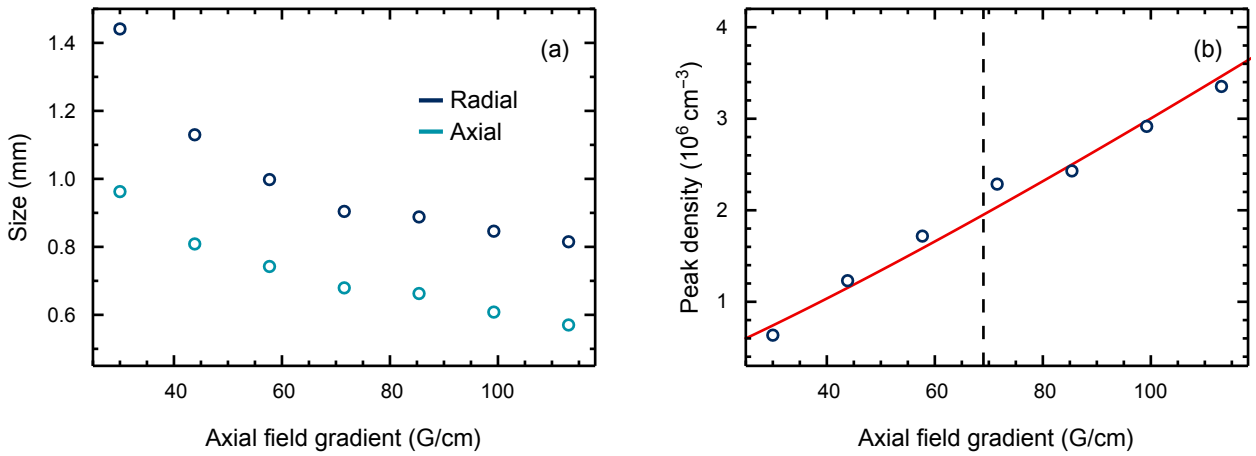

Figure 5.5: Compressed MOT. (a) rms radius of the MOT versus magnetic field gradient. (b) The density versus axial magnetic field gradient used for the compressed MOT. Solid line is a fit to $n = aA^b$. Dashed line indicates the field gradient used in later chapters of this thesis. Error bars throughout are smaller than the points.

data to the model $n = a\mathcal{B}'^b$ yields the less rapid scaling $b = 1.16(1)$. We attribute this to T increasing with $\mathcal{B}'$; we measure $T = 7.36(9)\,\mathrm{mK}$ at $\mathcal{B}' = 30\,\mathrm{G\,cm^{-1}}$, increasing to $8.75(5)\,\mathrm{mK}$ at $\mathcal{B}' = 69\,\mathrm{G\,cm^{-1}}$. For all experiments described in later chapters of this thesis we use $\mathcal{B}' = 69\,\mathrm{G\,cm^{-1}}$ in the CMOT, indicated by the dashed line in Fig. 5.5(b), giving $n \simeq 2 \times 10^6\,\mathrm{cm^{-3}}$. We use this field gradient because we find that holding the coils at higher currents for sustained periods causes them to heat up so that the paint begins to outgas.

5.2 Multi-frequency molasses

5.2.1 Introduction

As discussed in Sec. 3.4.5, the temperature in the MOT is limited by polarisation gradient forces present for molecules at low velocities. To cool the molecules further we exploit these forces by transferring the molecules into a three-dimensional blue-detuned optical molasses. Between $t = 50$ and $70\,\mathrm{ms}$, we ramp down the intensity of the $\mathcal{L}_{00}$ light by a factor of 100 to $4.6\,\mathrm{mW\,cm^{-2}}$ which brings the temperature of the MOT down to $\sim 1\,\mathrm{mK}$. At $t = 75\,\mathrm{ms}$, we switch off the MOT coils and $\mathcal{L}_{00}$. We then jump $\mathcal{L}_{00}$ to a detuning of $+2.5\,\Gamma$, and to a (variable) higher intensity to form the molasses. The light that forms the molasses has exactly the same sideband structure as for the MOT, and we call this the multi-frequency molasses to distinguish it from a second molasses described later in Sec. 5.3. After allowing the molasses to act for a variable time, we measure the temperature of the cloud in the same way as for the MOT, by ballistic expansion. $\mathcal{L}_{00}$ is turned off to allow the cloud to expand for a variable amount of time before it is imaged for 1 ms at full intensity and with the detuning returned to $\Delta = -0.75\,\Gamma$.

Figure 5.6 shows the free thermal expansion of a cloud after cooling for 5 ms in a $93\,\mathrm{mW\,cm^{-2}}$ molasses. After optimising all parameters, see below, the average of six such temperature measurements gives $T = 55(2)\,\mu\mathrm{K}$. This temperature is a factor of 4 below the Doppler limit of $199\,\mu\mathrm{K}$ and provides clear evidence for the presence of the sub-Doppler cooling mechanisms discussed in Sec. 3.4. To within

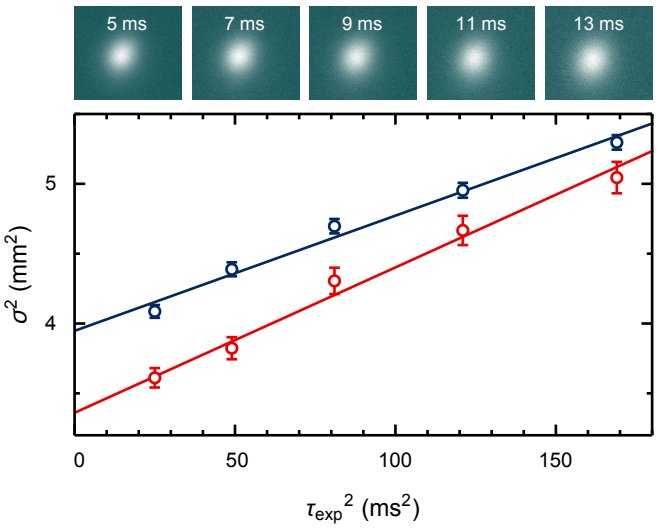

Figure 5.6: Temperature measurement in the multi-frequency molasses. Top row: sequence of fluorescence images of the cloud after various expansion times. Data points are extracted radial and axial sizes of the cloud.

our 5% uncertainty, no molecules are lost between the initial MOT and this ultracold cloud, excepting loss due to the MOT lifetime. The cloud now has $n = 0.8(2) \times 10^5\,\mathrm{cm}^{-3}$ and a phase space density $\rho = 2.4(6) \times 10^{-12}$, 1,500 times higher than in the initial MOT and 40 times higher than previously achieved for laser-cooled molecules. It also exceeds that obtained by other molecule cooling methods that have reached sub-millikelvin temperatures [119, 165]. The following sections detail the dependence of the temperature on a number of key parameters.

5.2.2 Cooling time

Figure 5.7 shows the temperature of the cloud as a function of hold time in the molasses at the maximum available intensity of $I_{00} = 460\,\mathrm{mW\,cm}^{-2}$, slightly lower than the $500\,\mathrm{mW\,cm}^{-2}$ in the MOT because of the reduced efficiency of the double pass AOM at this detuning. Our data are well described by a single exponential decay. The cloud cools towards a base value of $\sim 100\,\mu\mathrm{K}$ with a $1/e$ time of $361(2)\,\mu\mathrm{s}$, implying a damping constant of $1400\,\mathrm{s}^{-1}$.

5.2.3 Magnetic field

We find the temperature reached in the molasses is sensitive to all three components of the background magnetic field. Figure 5.8 shows the variation in the temperature of the molasses as a function of one component of the field, controlled with a pair of shim coils, after optimising the other two axes. The values of the applied magnetic field shown in the figure were determined when the chamber was open to air by measuring the field produced by the shim coil pair at the centre of the chamber with a Hall probe.

We can gain some insight into the dependence on magnetic field with a simple model. As discussed in Sec. 3.4.5, the sub-Doppler cooling mechanism relies on optical pumping into a dark state near the intensity maxima of the light field, and motion-induced non-adiabatic transitions back to a bright state

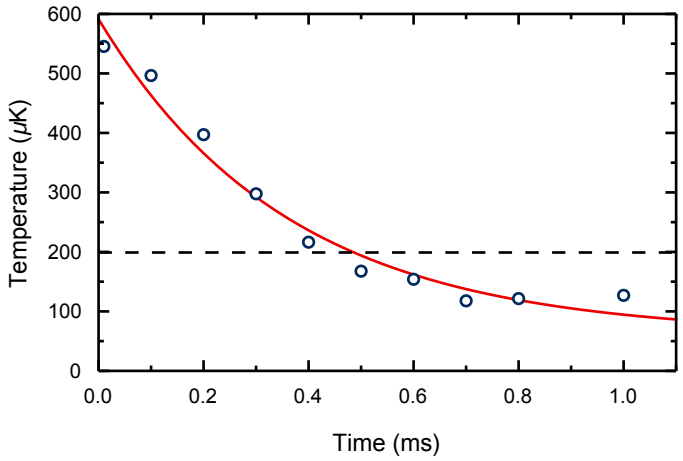

Figure 5.7: Temperature of molecules as a function of hold time in the multi-frequency molasses at $I_{00} = 460\,\mathrm{mW\,cm^{-2}}$ and $\delta = 2\pi \times 20\,\mathrm{MHz}$.

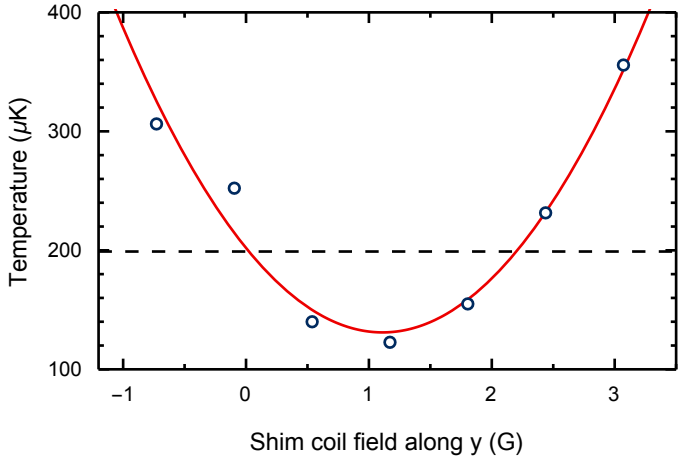

Figure 5.8: Temperature of molecules following the multi-frequency molasses as a function of magnetic field produced at the molecules by one of three shim coils during the molasses phase for $I_{00} = 460\,\mathrm{mW\,cm^{-2}}$, $\delta/2\pi = 20\,\mathrm{MHz}$ and a hold time of 5 ms. Solid line is a quadratic fit giving curvature of $57.4(3)\,\mu\mathrm{K\,G^{-2}}$. Dashed line is the minimum Doppler temperature.

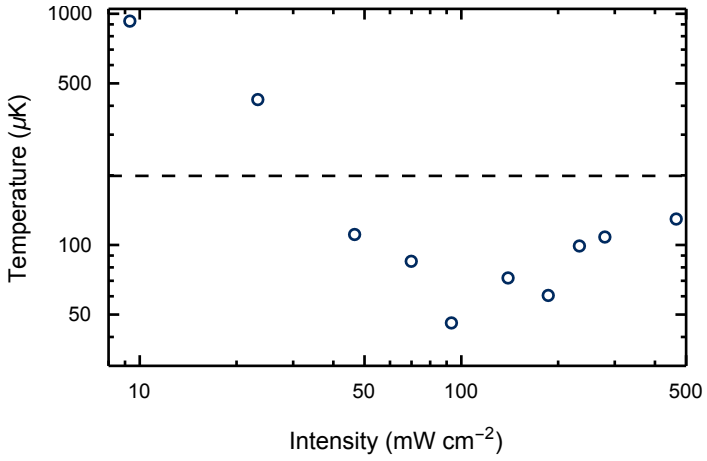

Figure 5.9: Temperature of molecules following the multi-frequency molasses as a function of intensity for $\delta = 2\pi \times 20\,\mathrm{MHz}$ and a hold time of 5 ms. Dashed line is the minimum Doppler temperature.

near the intensity minima. This process becomes ineffective if the Larmor precession time between bright and dark states is comparable to the time taken by a molecule to move from a minimum to a maximum. Therefore, in the presence of a magnetic field $\mathcal{B}$, the cooling will not reduce the mean velocity much below $v \approx \mu\lambda\mathcal{B}/(4h)$, where μ is the magnetic moment and λ is the wavelength. Converting from mean speed to temperature we find the relation $T \approx \frac{\pi M}{8k_\mathrm{B}}\left(\frac{\mu\lambda B}{4h}\right)^2$. Taking $\mu \approx \mu_\mathrm{B}$ we obtain $T = a\mathcal{B}^2$ with $a \approx 125\,\mu\mathrm{K\,G^{-2}}$. The solid line in Fig. 5.8 shows a quadratic fit to our data giving $a = 57.4(3)\,\mu\mathrm{K\,G^{-2}}$, consistent with our model, given its approximate nature. Later measurements using microwave spectroscopy (see Chapter 6) established that the absolute value of the field for which the temperature is minimised is consistent with zero, further supporting our model.

5.2.4 Intensity

Figure 5.9 shows the temperature of the molasses versus the laser intensity. The temperature has a minimum of 46 μK near 100 mW/cm^2, increases rapidly at lower intensities and more gradually at higher intensities. All these data used a initial MOT with temperature of $\sim 1\,\mathrm{mK}$. For experiments described later in this thesis, we used the compressed MOT technique described in Sec. 5.1.6 to maximise the density of molecules prior to the molasses. The parameters that give the highest density result in a slight increase in the temperature of the MOT (to roughly 2 mK). To ensure we capture all molecules from the MOT in the molasses, we found it necessary to step the intensity of the light. Typically we hold the molecules in the full intensity molasses at $I_{00} = I_\mathrm{max} = 460\,\mathrm{mW\,cm^{-2}}$ for 6.5 ms before holding at 50%, 30% and 20% of I_max for 0.5 ms each. The 6.5 ms hold time at I_max is much longer than required to cool the cloud but allows the eddy currents from the switching of the MOT coils to dissipate. Eddy currents are important in later experiments and are discussed in more detail in Chapter 6.

5.2.5 Beam alignment

Qualitatively, we find that the temperature of the molasses is sensitive to the alignment of the MOT beams. It seems to be particularly important to ensure that each pair of counter-propagating beams are as close to anti-parallel as possible. We found the most reliable and reproducible way to align the beams was to centre each outgoing beam on its vacuum window and then maximise the amount of the retro-reflected MOT light that is coupled back into the optical fibre. When light is successfully coupled back into the fibre, a small amount of $\mathcal{L}_{10}$ light (few µW) leaks back through the fibre cluster to the $\mathcal{L}_{21/32}$ port and this signal can be used to optimise the back reflection by adjusting the retro-reflection mirror. We normally carry out this procedure each morning.

5.2.6 Systematic error in ballistic expansion temperature measurements

There are several potential sources of systematic error when using the ballistic expansion method to measure the temperature which we address here.

(i) Finite exposure time. While the image is being taken using the MOT light, the magnetic quadrupole field is off. Thus, there is no trapping force, but there is a velocity-dependent force which, according to [155], may either accelerate or decelerate the molecules depending on whether their velocity is above or below some critical value, potentially distorting our temperature measurements. To quantify the effect, we made temperature measurements using the same molasses but with various exposure times. For a 12 mK cloud we estimate that the 1 ms exposure time results in an overestimate of the temperature by about 0.3(5) mK. For a 50 µK cloud, the overestimate is about 0.0(3) µK. These corrections are insignificant.

(ii) Intensity profile of MOT beams. With a MOT that is centred on the light beams, the intensity of the imaging light is higher in the middle of the cloud than it is in the wings, making the cloud look artificially small. This skews the temperature towards lower values because the effect is stronger for clouds that have expanded. The error is mitigated by using laser beams that are considerably larger than the cloud and that strongly saturate the rate of fluorescence. Using a three-dimensional model of the MOT beams and Eq. (3.13) for the dependence of the scattering rate on intensity, we have simulated the imaging to determine the functional form of $\sigma^2(\tau_{\mathrm{exp}}^2)$ expected in our experiment. The model suggests that a simple τ_{exp}^4 correction, $\sigma^2 = \sigma_0^2 + k_B T \tau_{\mathrm{exp}}^2/M + a_2 \tau_{\mathrm{exp}}^4$, will fit well to all our ballistic expansion data, will recover the correct temperature, and will give a significantly non-zero a_2 for our $T \sim 10$ mK data, but a negligible one for all our data where $T \leq 1$ mK. We have investigated this in detail using σ^2 versus τ_{exp}^2 data with a higher density of data points (12 points in each ballistic expansion measurement, instead of our standard 6). For a hot MOT ($T \sim 12$ mK), we see a nonlinear expansion and find that a fit to the above 'quadratic model' gives a temperature that is typically about 10 % higher than a linear fit. The quadratic model was used for the data presented in Sec. 5.1.5. For an ultracold molasses ($T \sim 100$ µK) linear fits to the earliest six points and the latest six points of the ballistic expansion give the same temperature to within the statistical uncertainty of 4 %.

(iii) Imaging imperfections. The magnification of the imaging system may not be perfectly uniform across the field of view. This can alter the apparent size of the cloud as it drops under gravity

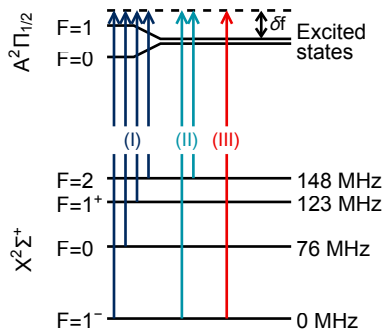

Figure 5.10: Schematic of molasses cooling schemes. Hyperfine components of the laser cooling transition in CaF, with three cooling schemes shown: (I) multi-frequency; (II) Λ-enhanced; (III) single-frequency.

and expands. We have measured the magnification across the whole field of view that is relevant to the data presented here and find that the uniformity is better than 3 %. At this level, the effect on the temperatures measured here is negligible. We will return to this in Sec. 5.3 where colder temperatures make this effect more problematic.

(iv) Magnetic field gradient. A non-uniform magnetic field can result in an expansion that does not accurately reflect the temperature. A magnetic field gradient accelerates the molecules, and since the magnetic moment depends on the hyperfine component and Zeeman sub-level, this acceleration is different for different molecules. We calculate that this effect contributes a velocity spread less than $0.5\,\mathrm{cm\,s^{-1}}$ after 10 ms of free expansion. This is negligible, even for a 50 µK cloud. The second derivative of the magnetic field causes a differential acceleration across the cloud, but this effect is even smaller.

5.3 Single-frequency molasses

5.3.1 Motivation

As noted earlier, the light used for the multi-frequency molasses contains the rf sidebands needed to address each of the hyperfine components. This is necessary in order to maintain a sufficiently high scattering rate to cool from the relatively high initial temperatures of the MOT. The frequency components used for the multi-frequency molasses, which we now call scheme (I), are illustrated in Fig. 5.10. With the molecules now cooled to 55 µK, other cooling schemes which may reach lower temperature become viable and we explore these here. The temperature of the multi-frequency molasses is limited by momentum diffusion from photon scattering; even for very slow molecules, the dark state is imperfect and so the molecules continue to scatter photons, preventing them from reaching lower temperatures. This photon scattering could be reduced by engineering a robust dark state for molecules at zero velocity as described in Sec. 3.4.6. This velocity-selective coherent population trapping turns off the heating for the slowest particles and has been used to cool atoms to below the recoil limit [158, 160].

In alkali atoms, the dark state is sometimes produced using a two-photon resonance between two different hyperfine states. This method, often called Λ-enhanced grey molasses, was recently used by Cheuk et al. [166] to cool CaF to 5 µK. As shown by scheme (II) of Fig. 5.10, they turned off two sidebands and tuned the remaining two into resonance with the Raman transition between $F = 1^-$

and $F = 2$, to engineer dark states that are superpositions of these levels. Nevertheless, a significant scattering rate remained and indeed they used the fluorescence to image their molecules. Their measured scattering rate corresponds to an excited-state fraction of $1.3(2) \times 10^{-3}$. The dark states in the system are de-stabilised by off-resonant excitation (the frequency and polarisation component targeting one hyperfine state may also excite the other), and by the $F = 0$ level in the excited state which couples to $F = 1^-$ but not to $F = 2$. These processes are illustrated in Fig. 5.11(a). Due to the close frequency spacing of the hyperfine levels in CaF, any scheme using multiple frequency components to address them will be limited by this off-resonant scattering.

The above considerations suggest that even lower temperatures might be reached by finding more robust velocity-selective dark states, while retaining a strong cooling force. In this section, I explain our approach to achieve this using a single frequency component, blue detuned from all hyperfine levels, as illustrated by scheme (III) in Fig. 5.10. For stationary molecules, and for any polarisation, there are two dark states that are superpositions of the $F = 2$ Zeeman sub-levels, shown in Fig. 5.11(b). One, shown in red, is an eigenstate of the full Hamiltonian, including the kinetic energy operator. Moving molecules spend some of their time in bright states, where the average light shift can be large because the light has high intensity and is not too far detuned from $F = 1^-$. Consequently, there can be a strong cooling force, but little scattering, for molecules at low speeds. These are the requirements for efficient 3D cooling to the recoil limit and below [160, 167].

5.3.2 Simulations

To explore these ideas, we simulated[1] all three schemes illustrated in Fig. 5.10. We use 3D optical Bloch equation simulations that include all relevant molecular levels and laser frequency components, and all six beams of the molasses [155, 168]. The motion of the molecules is treated classically. Results of these simulations are shown in Fig. 5.12(a,b). Figure 5.12(a) shows the acceleration as a function of speed for the three schemes. The gradient of the curve at low speeds gives the damping constant. We see that while scheme (I) gives the largest force over the widest range of speeds, scheme (III) provides just as high a damping constant at low speed. Figure 5.12(b) shows the excited state population as a function of speed for the three schemes. To minimize heating due to photon scattering, we would like this population to be as small as possible, especially at low speed. We see that, at all speeds, schemes (II) and (III) have lower excited-state population than scheme (I), and that in scheme (III) this drops to very low values at the lowest speeds, because the population is pumped into stable dark states at zero velocity[2]. This opens the possibility of cooling below the recoil limit, which would not be possible with the other schemes where a substantial scattering rate remains even at zero speed. The steady-state velocity distribution is determined by the balance of the cooling force as a function of the speed, and the heating due to the excited state fraction, also a function of speed. This velocity distribution, and the temperature that characterises it, is calculated by solving the Fokker-Planck-Kramers equation using the data given in Fig. 5.12, as described in Ref. [168]. Using this method, we estimate a lower temperature limit, T_{low}, for each scheme. For (I), we predict $T_{\mathrm{low}} = 11(1)\,\mu\mathrm{K}$, about 4 times lower than measured. The discrepancy arises because our method neglects heating due to fluctuations of the dipole

[1] These simulations were done by Jack Devlin

[2] In the simulations, the cooling time is 0.8 ms. In schemes (I) and (II) the populations have reached their steady-state values in this time, whereas in (III) the excited-state fraction continues to fall for longer cooling times.

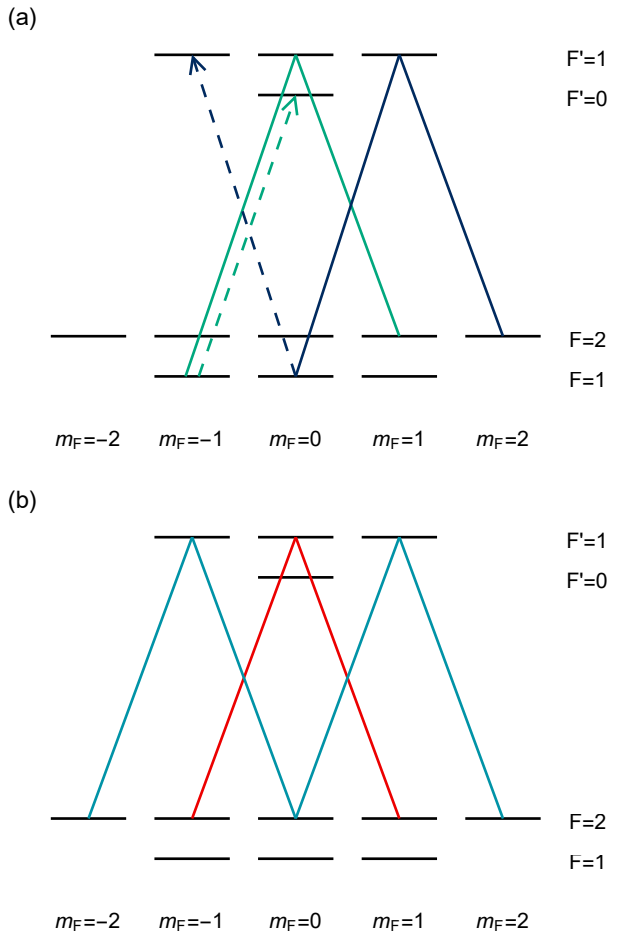

Figure 5.11: (a) Quasi-dark states in the Λ-enhanced cooling scheme. One frequency component drives σ^+ transitions from $F = 1$ while the other drives σ^- transitions from $F = 2$. The dark state shown in green is de-stabilized by excitation to the $F' = 0$ excited state (dotted green arrow). The dark state shown in blue is de-stabilized by off-resonant-excitation (dashed blue arrow). (b) Dark states in a single-frequency $\sigma^+\sigma^-$ molasses. They are stable.

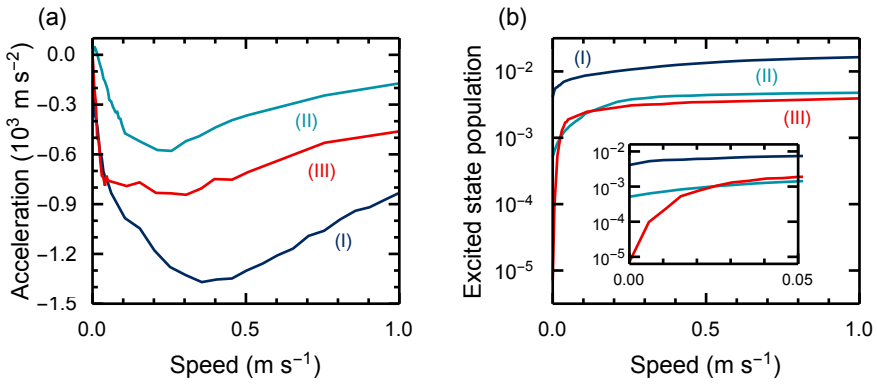

Figure 5.12: Simulations of the three cooling schemes. (a) Steady-state acceleration versus speed and (b) excited-state fraction versus speed, obtained from optical Bloch equation simulations of each scheme. The inset of (b) shows a zoom in for very low velocities. Simulation parameters are: (I) total intensity $I = 117$ mW/cm^2, detuning $\delta f = 20$ MHz; (II) $I = 50$ mW/cm^2, $\delta f = 30$ MHz; (III) $I = 340$ mW/cm^2, $\delta f = 8.3$ MHz. Parameters for (I) and (II) are close to those which give the lowest measured temperatures [1, 166].

force [168]. For (II), we predict $T_{\text{low}} = 5.4(8)$ µK, consistent with measurements [166]. For (III), the predicted temperature is below the recoil limit of 0.44 µK. In this regime a full quantum mechanical treatment of the motion is needed.

5.3.3 Experiment

We start from a cloud cooled to ~ 55 µK in the multi-frequency molasses. To implement the single-frequency molasses, we switch off $\mathcal{L}_{00}$, switch off the drive to the EOM and AOM that add sidebands to the laser (see Sec. 4.3) and step the laser frequency so that the detuning from $F = 1^-$ is δf. Finally, after a settling period, we turn the light back on with intensity I. The molecules are now in the single-frequency molasses.

Switching off the $\mathcal{L}_{00}$ EOM and AOM results in a single laser frequency with a single polarisation (per beam) but with around 3/4 of the total power because the power in the AOM arm is now lost. The frequency of this laser is initially close to resonance with the $F = 0$ hyperfine level and so to achieve a frequency blue of the $F = 1^-$ level requires a frequency jump of > 70 MHz, beyond the range of our double pass AOM. The frequency step is achieved by applying a 100 µs chirp directly to the laser piezo. We measured the response of the laser to this chirp using a low-finesse cavity (FWHM ~ 200 MHz). We tuned the laser such that its frequency sat on the side of the cavity transmission peak, where the response to any frequency change is greatest, and then monitored the transmission in response to the applied chirp. We found the laser frequency stabilises within ~ 500 µs and so we wait an additional 600 µs before turning the light back on with intensity I to be certain of the detuning applied. The laser-lock feedback will attempt to pull the frequency back to its previous value, so it is disabled until the laser is returned to its normal frequency.

5.3.4 Temperature measurement by ballistic expansion

After holding the molecules in the single-frequency molasses for time t_{sfm}, we measure the temperature, T. We first measured T using the standard ballistic expansion method described in Secs. 5.1 and

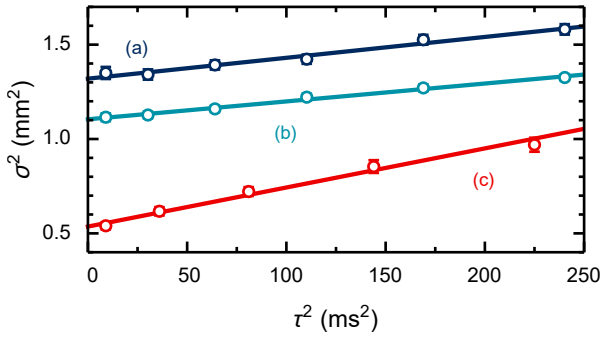

Figure 5.13: Temperature measurements of the single -frequency molasses by ballistic expansion. σ is rms width of cloud, τ is expansion time. (a) Axial and (b) radial measurements, after cooling in single-frequency molasses, but prior to compression. The axial and radial temperatures are 8(1) µK and 6.7(6) µK. (c) Axial measurement after compression and re-cooling. The compressed rms width is $\sigma_0 = 0.73(1)$ mm and the temperature is $T = 14(1)$ µK, Points: average and standard error of 20 experimental runs. Lines: fits to $\sigma^2 = \sigma_0^2 + k_B T\tau^2/M$.

5.2. Our results are shown in Fig. 5.13. Using optimised molasses parameters (see later), we measure axial and radial temperatures of 8(1) µK and 6.7(6) µK by this method, where we have given statistical uncertainties only. At these low temperatures, the cloud expands by less than 1 mm in the time taken to leave the field of view and the ballistic expansion method suffers from systematic errors which are difficult to control. Figure 5.14 shows a ballistic expansion dataset extended to longer expansion times, which clearly highlights the problem. At short times, the distribution is dominated by the initial spatial distribution, and deviations from a Gaussian shape (which are common, see for example the profiles in Fig. 5.2) can lead to systematic shifts in the measurement of the width that change as the cloud expands, potentially altering the gradient of the σ^2 vs τ^2 plot. Allowing the cloud to expand further reduces this problem, but brings the cloud towards the very edges of the field of view as it drops under gravity. Here, the imaging aberrations discussed in Sec. 5.2.6 are worsened, introducing significant systematic uncertainties in the measurement of the cloud size. These effects show up most strongly in the axial expansion data, where we tend to find that the gradient is systematically higher at late times than at early times, as can be seen in Fig. 5.14. For this dataset, the temperature determined by fitting to the first four points is 6(2) µK, whilst that found by fitting to the last four points is 14(1) µK. Because there are two potential sources of systematic error that are not easy to separate, and because they depend on the exact shape of the cloud, which is not easily controlled, it is difficult to estimate the size of the systematic correction needed, and the uncertainty on this correction.

The expansion time could be increased by magnetically levitating the cloud, but this introduces large systematic uncertainties due to the distribution of magnetic moments, even at large bias fields.

5.3.5 Temperature measurement by phase-space rotation

Because of the difficulties with the ballistic expansion method, we use a different approach to measure the temperature which we will refer to as phase-space rotation. The concept is to load the molecules into a harmonic trap. Here we implement it in one dimension although the technique generalises easily to 3D.

Suppose that our initial cloud has a 1D probability-density distribution $P_0(z_0, v_0)$ which we will

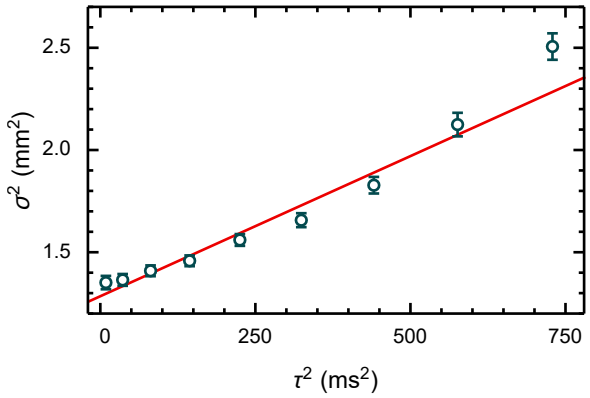

Figure 5.14: Temperature measurement by ballistic expansion, highlighting a difficulty of this method for large, cold clouds. σ is rms width of cloud in the axial direction, τ is expansion time. Points: average and standard error of 20 experimental runs. Line: fit to the model $\sigma^2 = \sigma_0^2 + k_B T \tau^2/m$. The data show a systematic deviation from this model, with a lower gradient at earlier times than at late times.

assume is separable such that we can write

$$P_0(z_0, v_0) = P_{0z}(z_0) P_{0v}(v_0). \tag{5.3}$$

We would like to know the probability-density distribution at a later time. Consider a molecule in the harmonic trap which, at $t = 0$, has position z_0 and velocity v_0. Its position z and velocity v at time t are given by

$$z = z_0 \cos\omega t + \frac{v_0}{\omega} \sin\omega t, \quad v = v_0 \cos\omega t - \omega z_0 \sin\omega t, \tag{5.4}$$

with ω the trap frequency. We can invert these functions to give

$$z_0 = z \cos\omega t - \frac{v_z}{\omega} \sin\omega t, \quad v_0 = v \cos\omega t + \omega z \sin\omega t. \tag{5.5}$$

To transform the probability density function P_0, we substitute in Eqs. (5.5) and multiply by the Jacobian of the coordinate transform,

$$\left| \frac{\mathrm{d}z_0}{\mathrm{d}z} \frac{\mathrm{d}v_0}{\mathrm{d}v} - \frac{\mathrm{d}z_0}{\mathrm{d}v} \frac{\mathrm{d}v_0}{\mathrm{d}z} \right| = \cos^2\omega t + \sin^2\omega t = 1. \tag{5.6}$$

We get

$$P(t; z, v) = P_{0z}(z \cos\omega t - \frac{v}{\omega} \sin\omega t) P_{0v}(v \cos\omega t + \omega z \sin\omega t). \tag{5.7}$$

Our expression for $P(t; z, v)$ shows that the phase space distribution rotates in the trap with a time period $2\pi/\omega$. We can obtain the position distribution by integrating over all molecule velocities,

$$P_z(t; z) = \int \mathrm{d}v P_{0z}(z \cos\omega t - \frac{v}{\omega} \sin\omega t) P_{0v}(v \cos\omega t + \omega z \sin\omega t) \tag{5.8}$$

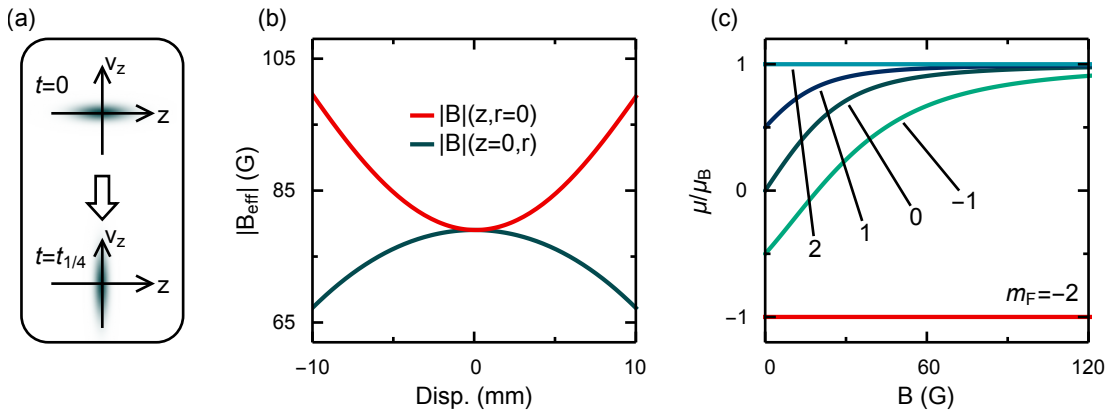

Figure 5.15: Phase space rotation in a 1D magnetic trap. (a) Phase space evolution in harmonic trap. After a quarter period, the position distribution is proportional to the initial velocity distribution. (b) Magnitude of effective magnetic field, $|B_{\text{eff}}| = |B| + mgz/\mu_{\text{B}}$, versus axial and radial displacements. Weak-field seeking molecules are trapped axially. (c) Magnetic moments, μ, of Zeeman sub-levels in the $X^2\Sigma^+(N = 1, F = 2)$ state, versus B. At large B, $\mu \approx \mu_{\text{B}}$ for $m_F \in \{-1, 0, 1, 2\}$.

At $t = t_{1/4} = \pi/2\omega$, a quarter of an oscillation period, this simplifies to

$$\begin{aligned} P_z(t; z) &= \left(\int \mathrm{d}v P_{0z}(-\frac{v}{\omega}) \right) P_{0v}(\omega z) \\ &= \omega P_{0v}(\omega z), \end{aligned} \tag{5.9}$$

As illustrated in Fig. 5.15, the phase-space distribution has rotated by $\pi/2$ and the molecules position distribution is now a direct mapping of their initial velocity distribution P_{0v}. By imaging the cloud at this time, we can directly measure the initial velocity distribution of the cloud. Note that so far we have made no assumptions about the phase-space distribution except that the velocities and positions are initially uncorrelated; a good approximation for almost all laser cooled samples. Now let's specialise to the case where the initial distribution is Gaussian in both z_0 and v_0,

$$P_{0z} = \sqrt{\frac{1}{2\pi\sigma_{0z}^2}} e^{-\frac{z_0^2}{2\sigma_{0z}^2}}, \tag{5.10a}$$

$$P_{0v} = \sqrt{\frac{M}{2\pi k_{\text{B}} T}} e^{-\frac{Mv^2}{2k_{\text{B}}T}}. \tag{5.10b}$$

Here M is the mass of the molecule. In this case the position distribution remains Gaussian at all times with an rms width of

$$\sigma(t) = \sqrt{\sigma_0^2 \cos^2 \omega t + \frac{k_{\text{B}} T}{M\omega^2} \sin^2 \omega t}, . \tag{5.11}$$

We implement the scheme, in the z_1 dimension only, as follows. After cooling, we turn off the light and use the H-bridge circuit (see Sec. 4.4.2) to switch the direction of the current in one of the MOT coils. In this configuration, with a current of 25 A (where our power supply hits its maximum voltage), the coils produce a large offset magnetic field in the z_1-direction with the required quadratic dependence on position along the z_1 axis. The red line in Fig. 5.15(b) show the field along the axial direction of the coils and the blue line shows the field in the radial direction where the field is anti-trapping for

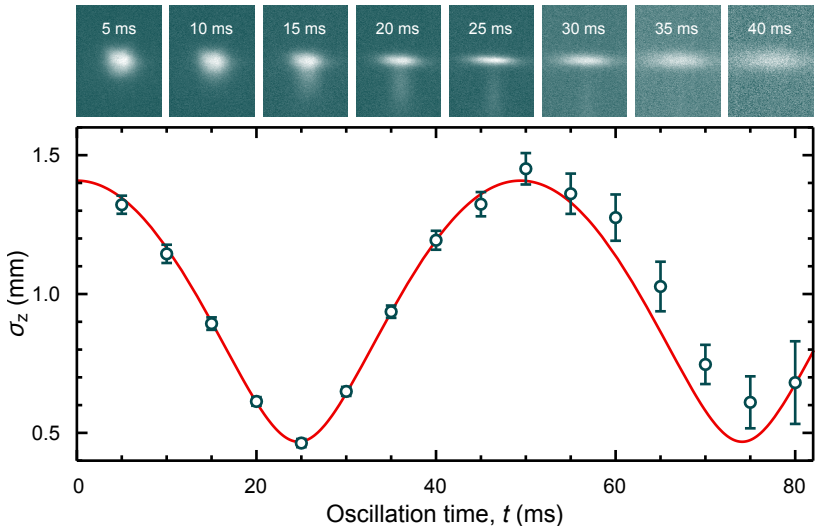

Figure 5.16: Molecule evolution in the 1D harmonic trap. Top row are fluorescence images of molecules at 5 ms intervals, averaged over 50 shots; z is vertical, and the field of view is 13.5 mm wide. Lower panel shows rms width in z direction versus time in trap, $\sigma_z(t)$. Error bars include systematic uncertainties. Line is a fit to Eq. (5.11).

weak-field seeking molecules. The field values shown come from a simple model of the coils where we treat each of the copper spirals as a sequence of 8 concentric current loops.

Our cooling simulations predict that, after cooling, the molecules are uniformly distributed amongst the m_F levels of $F = 2$, with no population in other states. The Zeeman shifts of each sub-level can be determined from Eqs. (2.1) and (2.35). Figure 5.15(c) shows μ, the magnetic moment of each of the $F = 2$ states as a function of $\mathcal{B}$. At $\mathcal{B} \approx \mathcal{B}_0$, molecules in $m_F = -2$ have $\mu = -\mu_B$ and are ejected, while all others have $\mu \approx \mu_B$ and are confined with almost equal trap frequencies. Our simple model of the coils predicts $\omega/2\pi = 11.1$ Hz.

By additionally shunting some of the current around the top coil, we add a small field gradient which cancels the force due to gravity, so that the minimum of the total potential experienced by the molecules coincides with the centre of the two coils and the position of the MOT. The coils provide a gradient of $50(3)\,\mathrm{G\,A^{-1}}$ when current is flowing in opposite directions and so shunting a current of 6.6 A is sufficient to cancel gravity for molecules with $\mu = \mu_B$. The magnetic field gradient was calibrated by preparing a cloud of molecules in a single Zeeman sub-level $X^2\Sigma(v = 0, N = 1, F = 2, m_F = 2)$ (see Chapter 6), and imaging the cloud after a number of free expansion times for various coil currents. We used a hall probe positioned at the centre of the chamber when it was open to air in order to measure the time taken for the magnetic field to switch on. We find that the field reaches within 5% of its final value in less than 1.4 ms.

To measure the position distribution, the magnetic field is turned off at time t, the cooling light (with sidebands) immediately turned back on at the detuning used for the MOT, and the fluorescence imaged onto a CCD camera for 750 µs. By measuring σ at various times t, and then fitting to Eq. (5.11), we determine ω and T.

The upper row of Fig. 5.16 shows images for various oscillation times t. As expected, $\sim 80\%$ of the molecules are trapped axially and slowly stretched radially. The remaining molecules are squeezed radially and accelerated downwards. They can be seen as a narrow vertical strip of fluorescence towards

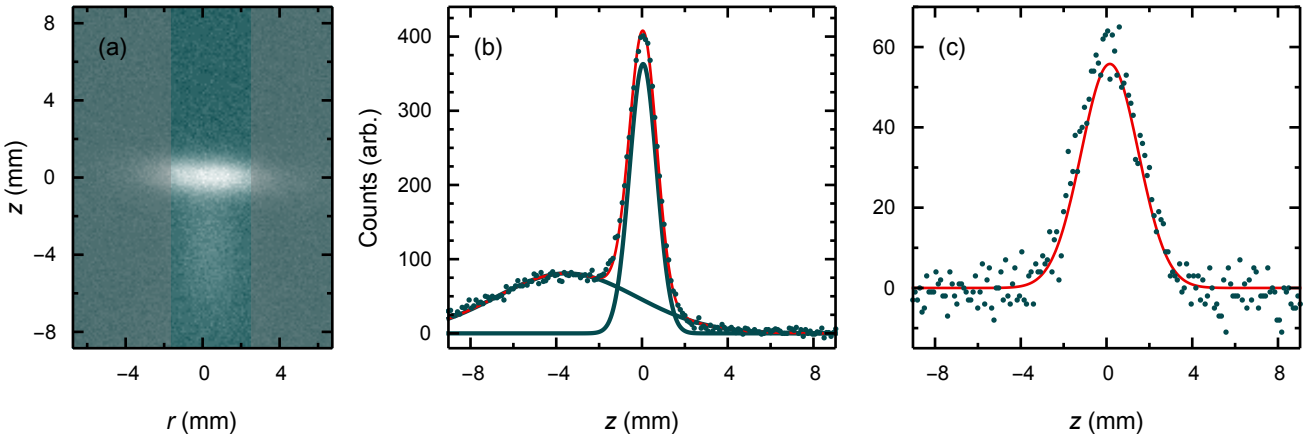

Figure 5.17: Image analysis for phase space rotation temperature measurements. (a) Fluorescence image (background subtracted) at $t = 20\,\mathrm{ms}$. Central region (not greyed out) shows region used for integration. (b) Integration over r of image shown in (a). Red line shows fit to sum of two Gaussians, green lines show individual Gaussians. (c) Same as (b) but for image taken at $t = 45\,\mathrm{ms}$. Red line shows fit to a single Gaussian.

the bottom of the images taken between 15 and 30 ms. Figure 5.17 shows the procedure we use for analysing the images. We determine the rms width in z of the trapped cloud, σ_z, by integrating the image along r over a region of width $w_{\mathrm{cut}} = 4.43\,\mathrm{mm}$ which is centred on the peak of the molecules position distribution, then fitting to the resulting distribution. Figure 5.17(a) shows an image taken at $t = 20\,\mathrm{ms}$ with the parts of the image we do not use for analysis greyed out. We find that using only this central region reduces the effects of imaging aberrations near the edges of the field of view. For $t \leq 30\,\mathrm{ms}$, when the ejected molecules are still visible, we fit to the sum of two Gaussians with the position and width of each as free parameters. Figure 5.17(b) shows such a fit to the image from Fig. 5.17(a). For later times, when the ejected molecules have left the field of view, a single Gaussian is sufficient. Figure 5.17(c) shows a fit to a single Gaussian for an image taken at $t = 45\,\mathrm{ms}$.

The lower panel of Fig. 5.16 shows σ_z versus t. The line is a fit to Eq. (5.11), giving $\omega/(2\pi) = 10.12(2)\,\mathrm{Hz}$ and $T = 5.6(6)\,\mu\mathrm{K}$. The model of Eq. (5.11) fits well, apart from at late times where the measured size is inflated, mainly by the effect of defocussing as the cloud expands radially out of the imaging plane. This effect is reproduced by numerical modelling, and has a negligible effect on our determinations of ω and T because these points have almost no weight in the fitting procedure (see the significantly lower signal-to-noise in Fig. 5.17(c) relative to Fig. 5.17(b)). The measured trap frequency is within 10% of that expected from the simple model described above. The discrepancy is likely due to treating the coils as concentric loops rather than spirals. The temperature is related to the minimum width, $\sigma_{z,\mathrm{min}}$, obtained at time $t_{1/4} = \pi/(2\omega)$, by $k_{\mathrm{B}}T = m\omega^2\sigma_{z,\mathrm{min}}^2$. All subsequent temperature data are obtained from images taken at $t_{1/4}$ and integrated over $w_{\mathrm{cut}}/2$. The statistical uncertainty in a single measurement made this way is $\sim 0.1\,\mu\mathrm{K}$, far smaller than when measured by ballistic expansion. We now consider the systematic shifts and uncertainties.

5.3.6 Systematic shifts and uncertainties in phase-space rotation method

There are a number of potential systematic shifts and uncertainties to consider in this new method for measuring temperature. I describe them here, and evaluate their typical sizes.

(i) Residual difference in magnetic moments. The first effect comes from the residual difference in the magnetic moments of the molecular states at the offset field used, $\sim 80\,\mathrm{G}$. As shown in Fig. 5.15(b)), for this B_0 the $(F = 2, m_F = -1)$ state has $\mu \approx 0.80\ \mu_B$, while the remaining weak-field seeking states of $F = 2$ all have $\mu > 0.94\ \mu_B$. The spread in magnetic moments causes a spread in trap oscillation frequencies which can inflate the minimum size of the cloud, making it appear hotter than it really is. We simulate the effect of this by fitting a single Gaussian to distributions made up of the sum of two Gaussians, one representing the distribution of molecules with $\mu = \mu_B$ in the harmonic trap, and the other, the fraction of molecules with $\mu = 0.8\ \mu_B$. The effect on the fitted size of the cloud at $t_{1/4}$ depends on the fraction of molecules that have the smaller magnetic moment. Our simulations predict that the molecules are equally distributed amongst the 5 m_F states of $F = 2$. This is supported by our observations that 20% of the molecules are ejected from the magnetic trap (see images in Fig. 5.16). Using this distribution, we find a temperature correction of $-0.7(5)\,\mu\mathrm{K}$ for the coldest clouds. The uncertainty on this correction has been assigned by considering the two extreme scenarios: (i) all molecules having the same magnetic moment, (ii) half the molecules in states of each magnetic moment. This is clearly not a 1σ bound, but to be conservative we treat it as such when combining with other sources of uncertainty in our analysis. This systematic correction and uncertainty can be reduced by increasing B_0.

(ii) Finite imaging resolution. The finite resolution of our imaging system can make the cloud appear larger than it is. We reduce the severity of aberrations and depth of field effects by aperturing down our imaging system to 20 mm diameter and using only the central 2.21 mm region when integrating over the radial dimension. We have measured the resolution of the imaging optics by imaging a wire of diameter 73 µm. The effect on the images is to convolve the true image with a Gaussian blur of rms radius 0.153(2) mm. This makes all clouds look hotter by 0.67(2) µK. Our optics were designed to collect the most light, not to be a good imaging system, and this systematic correction could be significantly reduced with an improved imaging setup.

(iii) Magnification. The magnification of the imaging system can introduce a systematic error if incorrectly calibrated. We determine the magnification to be 0.49(1) by fitting the acceleration of a falling cloud to the known acceleration due to gravity. The uncertainty in our calibration introduces a temperature uncertainty of 0.2 µK for the coldest clouds.

(iv) Oscillation frequency. Small errors in determination of the trap frequency have a negligible effect on the measured size of the cloud due to the flatness of $\sigma(t)$ in the vicinity of the minimum. However, an error in the trap frequency results in an error in conversion of the minimum size of the cloud to a temperature. From the oscillation fit in Fig. 5.16 we find this error to be less than 0.1 µK for the coldest clouds.

(v) Trap harmonicity. It is clear from Figure 5.16 that the simple model given by Eq. (5.11) does

not fit perfectly to the oscillation data at late times. The model will be incorrect if the trap is not harmonic. We find that the potential is harmonic to within 0.2% for $|z| < 5$ mm. The maximum rms width of the cloud is only 1.5 mm, so trap anharmonicity has a negligible effect. The trap oscillation frequency, ω, has a small dependence on the radial displacement, r. For all r within the selected central region of $w_{\mathrm{cut}} = 4.43$ mm, ω varies by less than 1%, and this variation has a negligible effect on the fitted model. We simulate the motion of a distribution of molecules using our calculation of the magnetic field due to the coils and the Zeeman shifts of the states, and analyse the change in the spatial distribution over time in the same way as the real data. These simulations show that the method accurately determines the temperature. Using these simulations, we have investigated the potential effect of coupling between the axial and radial motions, and find this has a negligible effect on the temperature measurement. We find that the small difference in magnetic moments of molecules in different states results in slightly different oscillation frequencies which then inflates the minimum size of the cloud, and this inflation increases at later times. Our modelling shows this to be a small, but noticeable, effect that makes a small contribution to the imperfect fit at late times. A larger effect is the defocussing of the cloud as it expands radially out of the imaging plane. We model this effect using data obtained on the resolution of the imaging optics as a function of object position (see above). We find that this defocussing effect is the main cause of the imperfect fit at late times. Because the data points at late times have so little weight in the fit, we did not find it useful to fit a more sophisticated model that includes these effects.

(vi) Heating during imaging. The red-detuned light used to image the molecules quickly heats the cloud resulting in expansion during the finite exposure time. The effect can be characterised by the size, σ_H, reached by an initial point-source distribution of molecules that is heated for the same amount of time. We find that imaging with blue-detuned light causes negligible expansion for short exposure times at the expense of lower fluorescence and utilise this to determine σ_H for different exposure times. Imaging at a detuning of $+3\Gamma/4$ for 750 µs, as done throughout this work, gives $\sigma_H = 0.06(8)$ mm. As a result, any cloud appears hotter by 0.1(3) µK.

(vii) Image integration. Integration of the images over the radial dimension to infer the size in the axial direction introduces the possibility of an error from misalignment of the camera axis relative to the axis of maximum compression. By fitting a two-dimensional Gaussian model with the angle between these axes as a free parameter, we determine this misalignment to be less than 40 mrad. This has a negligible effect on the measured sizes of our clouds when using only the central 2.21 mm region of each image in the radial direction, as we do in this work. The effect will be larger at lower temperatures or higher trap frequencies when the cloud is smaller.

Taken together, these systematic shifts in temperature amount to $-1.4(7)$ µK for the coldest clouds. In the next section, I present data that show how the temperature depends on various experimental parameters. All these data have been corrected for the systematic shifts discussed here, while the error bars include the systematic uncertainties discussed here.

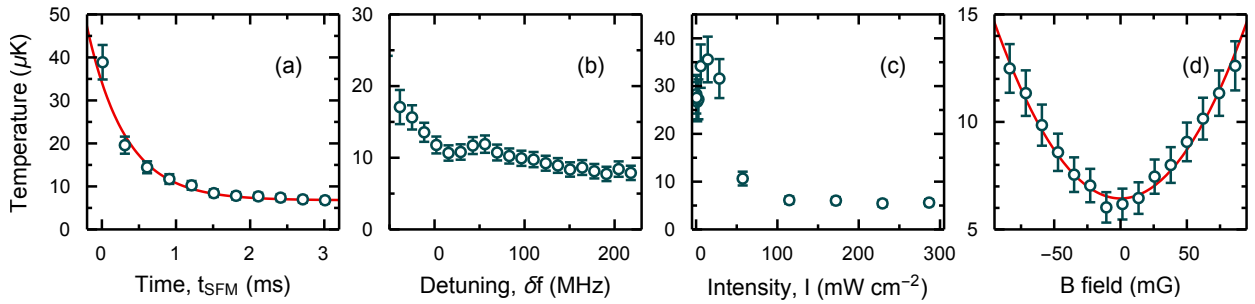

Figure 5.18: Temperature versus single-frequency molasses parameters. (a) T versus $t_{\rm sfm}$, when $I = 287\,\mathrm{mW\,cm^{-2}}$ and $\delta f = 164\,\mathrm{MHz}$. Line: fit to $T = T_0 + (T_{\rm i} - T_0)e^{-t_{\rm sfm}/\tau}$, giving $\tau = 0.52(6)\,\mathrm{ms}$. (b) T versus δf when $t_{\rm sfm} = 5\,\mathrm{ms}$ and $I = 287\,\mathrm{mW\,cm^{-2}}$. (c) T versus I when $t_{\rm sfm} = 5\,\mathrm{ms}$ and $\delta f = 164\,\mathrm{MHz}$. (d) T vs one component of $\mathcal{B}$, after optimisation of the other two components; $t_{\rm sfm} = 5\,\mathrm{ms}$, $I = 287\,\mathrm{mW\,cm^{-2}}$ and $\delta f = 164\,\mathrm{MHz}$. Line: fit to $T = T_0 + \alpha B^2$, giving $\alpha = 9(1) \times 10^{-4}\,\mu\mathrm{K\,mG^{-2}}$. Points give average and standard error of 50 experimental runs. Error bars are dominated by systematic uncertainties.

5.3.7 Dependence of temperature on cooling parameters

Figure 5.18(a) shows T versus $t_{\rm sfm}$ along with a fit to an exponential decay giving a $1/e$ time constant of 0.52(6) ms. This is almost as fast as that measured for the multi-frequency molasses. A similar thermalisation time constant of 0.41(7) ms is predicted by the simulations. The rapid thermalisation is a consequence of the high damping constant that can be seen in Fig. 5.12(a).

Figure 5.18(b) shows how T depends on δf. The temperature decreases as δf is tuned from negative to positive and reaches its lowest values for $\delta f > 180\,\mathrm{MHz}$. This is as expected from our approximate analysis in Chapter 3—Eq. 3.30 shows that the friction coefficient increases for larger detunings. The simulations show the same dependence of T on δf, including the mysterious dip near zero detuning, but at lower temperatures throughout. The temperature of the molecules is quite insensitive to δf at high-detunings, making the cooling robust to imperfect control of the detuning.

Figure 5.18(c) shows T as a function of the intensity I. We hold the molecules in the single frequency molasses at full intensity for 2 ms then step to another intensity and hold for a further 3 ms. We find that T is insensitive to I at high intensity, but increases at lower intensities which we attribute to a longer damping time at low I.

Figure 5.18(d) shows the variation in the temperature of the molasses as a function of one component of the magnetic field, controlled with a pair of shim coils, after optimising the other two axes. The line shows a fit to the model $T = a\mathcal{B}^2 + T_0$, with curvature $a = 9(1) \times 10^{-4}\,\mu\mathrm{K\,mG^{-2}}$. This is a factor of ~ 15 higher than the magnetic sensitivity of the multi-frequency molasses. Simulations also show a quadratic dependence, but with a curvature 4 times higher still. The lowest temperature is obtained when all three field components are zero (measured within 10 mG using microwave spectroscopy—see Sec. 6.4).

After optimising all parameters, we measure T =5.4(7) μK. This is consistent (within 2σ) with the value measured by ballistic expansion, but more reliable for the reasons discussed above. We observe no loss of molecules in the cooling step, other than the 20% lost when measuring T, and the data fit well to a single thermal distribution, so we conclude that all the molecules are cooled to the same low temperature. Our simulations suggest that considerably lower temperatures are feasible, so we

speculate that the temperature reached here may be limited by a time-varying magnetic field or laser polarisation, which could be improved. We have also found the success of the molasses to be very sensitive to leaking light at other frequencies. On one occasion, a small amount of light ($< 1\%$ of the total power) leaking through with frequency close to resonance with one of the transitions increased the temperature of the molasses to $> 40\,\mu\mathrm{K}$.

5.3.8 Magnetic compression

As seen in Fig. 5.16, the cloud is compressed by a factor 3 at time $t_{1/4}$. It is common to compress magnetically trapped atoms [169], and recently molecules [170], by adiabatically increasing the trap frequency, ω, or field gradient, $\mathcal{B}'$. Using this method, σ scales only as $\omega^{-1/2}$ in a harmonic trap or as $\mathcal{B}^{-1/3}$ in a quadrupole trap [169]. Thus, even modest reductions in cloud size require large field gradients, which must be maintained for long times to be adiabatic. The compression observed in Fig. 5.16 is not adiabatic; it is simply the natural motion of a sample of almost stationary molecules loaded into a harmonic trap. The compression is much faster than adiabatic compression and more effective because σ scales as ω^{-1}. The conservative trapping potential conserves the phase space density and so the compression heats the cloud, but it can be re-cooled by applying the molasses a second time. This sequence increases the phase-space density provided (i) the cooling is fast enough that re-expansion during the second cooling phase is small, (ii) the velocities after compression are within the capture velocity of the molasses, and (iii) the magnetic field used for compression can be turned off rapidly enough that the molasses is effective. The first two conditions are easily satisfied, but the third is difficult. Eddy currents make it difficult to turn off the magnetic field rapidly. This problem is much worse when the currents in the two coils flow in the same direction compared to when they are opposite because the fields seen at the edge of the chamber, where the eddy currents presumably flow, are much larger. To reduce the eddy currents, we apply the sequence illustrated in Fig. 5.19(a). The current in the bottom coil is switched from 25 A to zero at $t = 0$, then to $-25\,\mathrm{A}$ between $t = 0.5\,\mathrm{ms}$ and $t = 2.5\,\mathrm{ms}$, then back to zero. The short pulse of reverse current helps to reduce the eddy currents that are set up when the coil is switched off. The current in the top coil flows in the same direction as the bottom coil and is always proportional to it, though smaller because of the shunt. The cooling light is turned on between $t = 3$ and 8 ms for the second period of single-frequency molasses. Figure 5.19(b) shows the resulting magnetic field at the position of the molecules. We see that the magnetic field during the molasses period is about 3 times smaller when the reverse-current pulse is used.

After switching off the coils, we re-apply the single-frequency molasses for 5 ms, and finally measure T. Since the cloud is now much smaller, ballistic expansion measurements are reliable. A typical ballistic expansion measurement following compression is shown in Fig. 5.13(c). The short pulse of reverse current helps to reduce the eddy currents that are set up when the coil is switched off. Using this method, we measure $\sigma_0 = 0.73(1)\,\mathrm{mm}$ and $T = 14(1)\,\mu\mathrm{K}$, limited by the residual magnetic field. This could be reduced further by implementing a more complex eddy-current compensation sequence or taking measures to reduce the number of surrounding components which can support eddy-currents, in particular the copper gasket used to seal the chamber is situated only a few centimetres below the MOT coils. We find that a longer wait between turning off the trap and re-applying the cooling reduces T, because the magnetic field has more time to decay, but increases σ_0. The complete cycle of cooling, compressing, and re-cooling reduces the axial size by a factor 2, reduces the temperature by a factor 4,

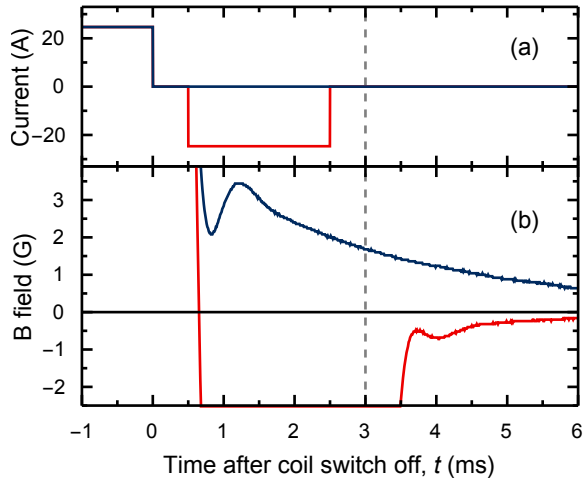

Figure 5.19: Sequence for reducing eddy-currents when switching off harmonic trap. (a) Commanded current profile as a function of time. (b) Magnetic field measured on a Hall probe placed at the position of the molecules as a function of time. Blue lines: Standard switching. Red lines: extra step to reduce eddy-currents. Where not visible, red line is below blue. To make the harmonic trap, each coil carries 25 A of current in the same direction. This current is turned off at $t = 0$ in the figure. To re-cool the molecules after compression, the single-frequency molasses light is turned on at $t = 3$ ms (indicated by the dashed grey line). The aim is to make the magnetic field as small as possible during the 5 ms-long molasses period. The brief reversal of the current direction (red line) helps to achieve this.

and retains 80% of the molecules.

There are several ways that this sequence could be improved. First, the trap frequency could be increased to give stronger compression. Second, any method that lowers T further will also improve the compression since $\sigma \propto T^{1/2}$. Finally, the method would be much better if implemented in three dimensions instead of just one. This could be done by using a magnetic trapping geometry which is harmonic in all three dimensions [171].

Chapter 6

Coherent control and magnetic trapping

6.1 Introduction

Almost all the applications of cold molecules outlined in Chapter 1 require control over the internal state of the molecules and rotational motion is particularly important. Polar molecules in superpositions of opposite-parity rotational states have large oscillating electric dipole moments, providing the long-range dipolar interactions required for quantum simulation or computation. Rotational transitions can be driven with easily generated microwave fields and, as discussed in Chapter 2, rotationally excited states have extremely long radiative lifetimes, potentially enabling long coherence times.

In this chapter and the next, I present our work on developing the tools and techniques for coherent control over the rotational degree of freedom. We will focus on the long-lived states within the electronic and vibrational ground state $X^2\Sigma^+(v=0)$, and label states within this manifold as $|N, F, m_F\rangle$ where N is the rotational quantum number, F is the total angular momentum and m_F its projection onto some laboratory axis, usually the local magnetic field direction.

In both chapters the experiments take place with a cloud prepared using the compressed MOT and then cooled in the multi-frequency molasses. The cloud has a temperature of $T = 55\,\mu\text{K}$ and a size $\sigma_0 = 1.4\,\text{mm}$. For reference, the full experimental sequence described in this Chapter is shown in Fig. 6.1.

6.2 Optical pumping

Following cooling in the optical molasses, the population is distributed amongst the 12 Zeeman sub-levels of $X^2\Sigma^+(v=0, N=1)$, and the corresponding 12 levels in $v=1$. To purify the state distribution, we optically pump into $|1,0,0\rangle$ by increasing the power of the rf driving field for the $\mathcal{L}_{00}$ EOM so that the carrier sideband—which addresses the $F=0$ hyperfine level—is extinguished. Figure 6.2(a) shows the usual $\mathcal{L}_{00}$ sideband structure we use for the MOT while Fig. 6.2(b) shows the sideband structure we use for the optical pumping step. We measure the efficiency of the optical pumping using an optimised microwave π-pulse which selectively transfers the molecules in $|1,0,0\rangle$ to $N=0$ (see Sec. 6.4). The molecules transferred to $N=0$ are decoupled from the MOT light and we measure the number remaining in $N=1$ by turning the MOT back on and imaging the fluorescence after a hold time, typically 30 ms. This number, divided by the initial number in the MOT, is the fraction

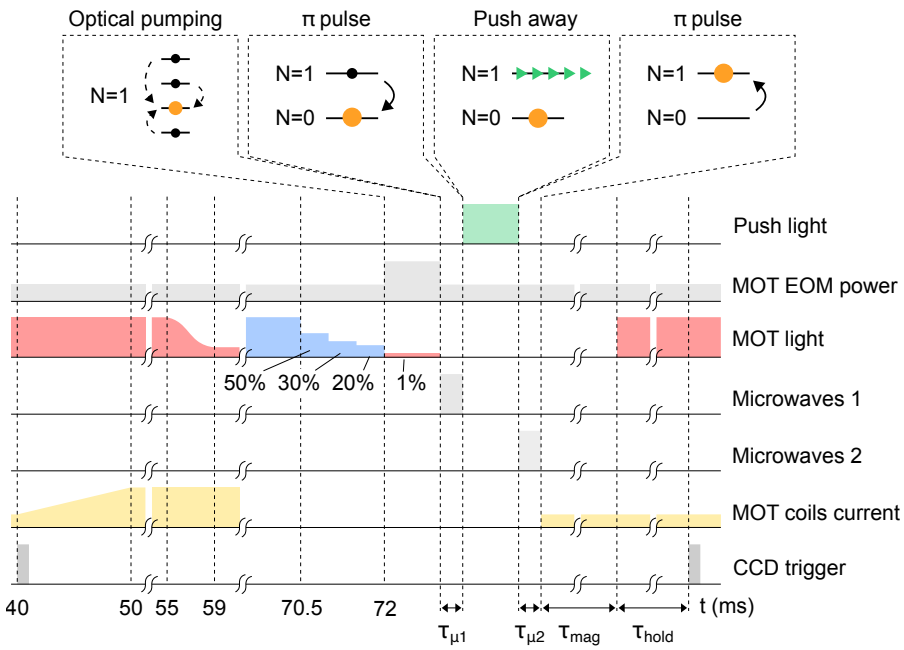

Figure 6.1: Timing sequence of the coherent control experiments (not to scale), starting from $t = 40\,\mathrm{ms}$ when the first fluorescence image is taken. The MOT light sequence is colour coded according to detuning. The MOT is first compressed by ramping up $\mathcal{B}'$. Then, the molecules are cooled in a blue-detuned molasses, optically pumped into $|1,0,0\rangle$, and transferred to $N = 0$ with a microwave pulse. A push pulse removes those remaining in $N = 1$, then (optionally) another microwave pulse transfers from $N = 0$ back to $N = 1$. Finally, the magnetic trap is turned on.

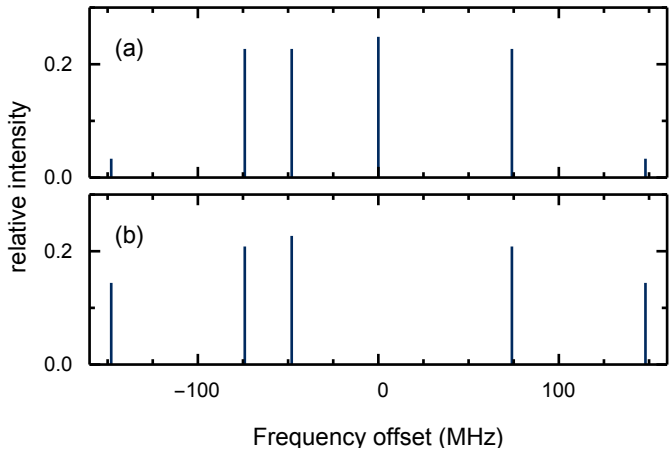

Figure 6.2: Stick spectra showing $\mathcal{L}_{00}$ sideband structure used for (a) the normal MOT and (b) the optical pumping step. Intensities are relative to the total intensity in $\mathcal{L}_{00}$.

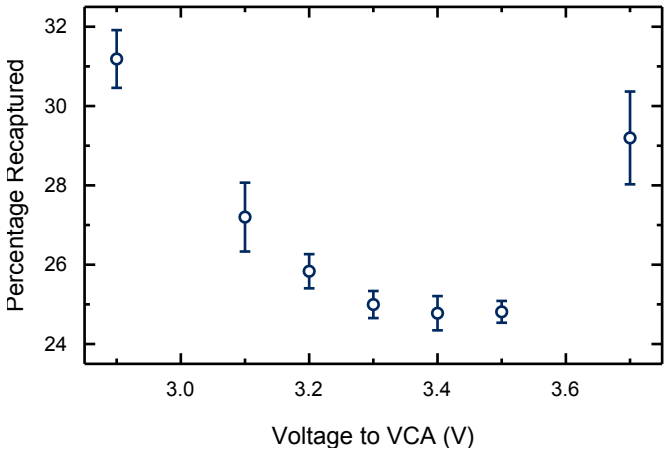

Figure 6.3: Optimising sideband extinction for optical pumping. Depletion from $N = 1$ after microwave π-pulse selectively transfers $|1, 0, 0\rangle$ population to $N = 0$, plotted against voltage applied to VCA which attenuates the rf driving $\mathcal{L}_{00}$ EOM. Points and error bars are mean and standard error of 9 experiments.

recaptured. We find the fraction recaptured is much less noisy than the absolute number because it is immune to fluctuations in the number of molecules produced in the source.

6.2.1 Sideband extinction

Any residual power in the $\mathcal{L}_{00}$ carrier sideband scatters molecules back out of the target state and so it is crucial to extinguish it as well as possible. We vary the power of the rf drive to the EOM using a voltage controlled attenuator (VCA) and minimise the power in the carrier sideband as observed in the transmission of a scanning cavity. The amplitude of the corresponding peak is reduced below the noise floor of the photodiode and from this we determine that the power in this sideband is reduced to $\leq 1\,\%$ of the total $\mathcal{L}_{00}$ power. The final optimisation is done using the signal from the molecules. Figure 6.3 shows the depletion of $N = 1$ molecules by the microwave pulse after optical pumping for 100 µs at $8\,\mathrm{mW\,cm^{-2}}$ with different control voltages to the VCA.

In a perfect EOM setup, the power in the carrier is expected to be proportional to $J_0(\beta_{\mathrm{rf}})^2$ where β_{rf} is the amplitude of the rf field used to drive the EOM and J_0 is the zeroth Bessel function. We find the optimum rf power to be fairly insensitive to the control voltage as expected since the optimum is at the minimum of a function where the first derivative is zero. The VCA voltage needs to be re-optimised occasionally as the resonant frequencies of our homemade EOM driving circuit, and hence the electric field across the crystal at our chosen driving frequency, vary slightly over time. Adding an elastic band to secure the inductor coil has greatly reduced this drift.

6.2.2 Intensity

The efficiency of the optical pumping step also depends on the intensity of the optical pumping light. At high powers off-resonant scattering from neighbouring sidebands limits the steady state population in $|1, 0, 0\rangle$, whilst at low powers the system takes too long to reach the steady state. Figure 6.4 shows the depletion from $N = 1$ after 100 µs of optical pumping at various $\mathcal{L}_{00}$ intensities. The maximum

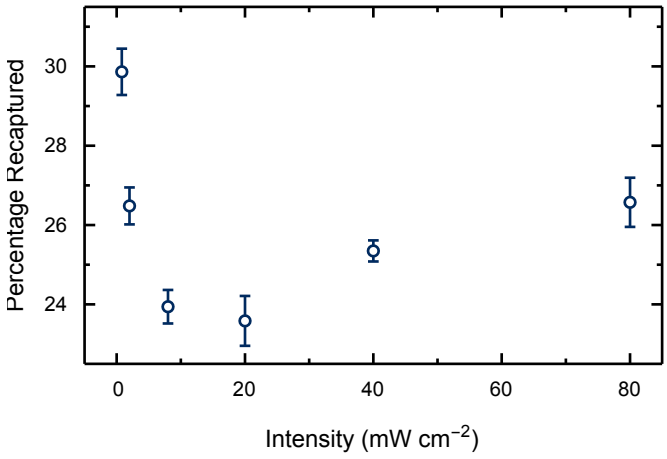

Figure 6.4: Effect of light intensity on optical pumping. Depletion from $N = 1$ after microwave π-pulse selectively transfers $|1, 0, 0\rangle$ population to $N = 0$, plotted against total intensity of $\mathcal{L}_{00}$ light during the optical pumping step. Points and error bars are mean and standard error or 9 experiments.

depletion is at around $10\,\mathrm{mW\,cm^{-2}}$, or $\sim 2\%$ of the $\mathcal{L}_{00}$ light intensity used in the MOT.

6.2.3 Duration

Figure 6.5 shows the depletion of the microwave pulse after optical pumping for various durations at $8\,\mathrm{mW\,cm^{-2}}$ intensity and after minimising the carrier intensity. The system reaches steady state after $\sim 40\,\mu\mathrm{s}$. We usually apply the pumping light for $100\,\mu\mathrm{s}$ to mitigate against small drifts from the optimum parameters.

6.2.4 Total efficiency and limitations

When optimised parameters are used, we transfer $\epsilon_{\mathrm{OP}} = 60\,\%$ of the molecules to $F = 0$. We determine the efficiency by measuring the number of molecules that are successfully trapped in the magnetic trap with and without optical pumping, with no microwave pulse. We assume that the reduction in trapping efficiency when the optical pumping is applied is due entirely to molecules being transferred to $|1, 0, 0\rangle$ which is not trapped. This gives us a number which is independent of the microwave transfer efficiency. The optical-pumping efficiency is likely limited by imperfect extinction of the carrier sideband. Even at the optimum rf drive amplitude, any polarisation components of the input light not parallel to the crystal axis are modulated differently and can result in non-zero carrier amplitude.

6.2.5 Alternative approach

An alternative optical pumping scheme is possible using polarisation rather than frequency to select a single state. Such an approach could be expected to produce a higher target state population in our setup due to the challenges in completely extinguishing the carrier sideband and the off-resonant excitation from nearby sidebands. If light is applied with two polarisation components—σ^+ and π—relative to a small quantising field, molecules will be optically pumped into $|1, 2, 2\rangle$, the only state

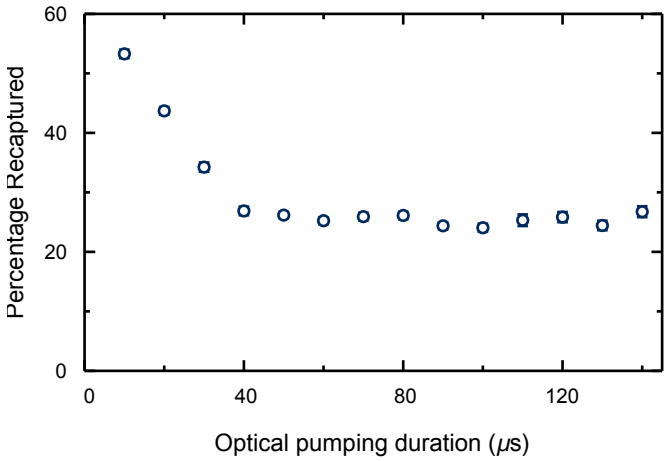

Figure 6.5: Effect of optical pumping duration on efficiency. Depletion from $N = 1$ after microwave π-pulse selectively transfers $|1, 0, 0\rangle$ population to $N = 0$, plotted against duration of optical pumping step. Points and error bars are mean and standard error of 9 experiments. Where not visible, error bars are smaller than the points.

completely dark to both components[1]. This could be achieved with two separate orthogonal beams or with a single beam of precisely chosen elliptical polarisation at an angle to the quantising field. The former has been demonstrated experimentally with SrF at Yale [170] albeit with similar efficiency to our current method.

6.3 Coherent microwave control

With the majority of molecules now in a single state, we can transfer them to a selected Zeeman sub-level by driving coherent microwave transitions. Consider a molecule subject to a microwave-frequency electric field $\vec{E} = \frac{1}{2}\mathcal{E}_0\vec{\epsilon}e^{-i(\omega t+\phi)} + \text{h.c.}$ with angular frequency ω close to resonance with a transition between two rotational levels at ω_0. Here $\mathcal{E}_0$ is the amplitude of the field, ϕ its phase and $\vec{\epsilon}$ the unit polarisation vector. If the two states in question are well separated from any others, we can restrict our Hilbert space to this two-level system—we label the two states $|\downarrow\rangle$ and $|\uparrow\rangle$. After transforming to the rotating frame and making the rotating wave approximation, the Schrödinger equation of the system can be written,

$$i\hbar\frac{\mathrm{d}\,|\psi(t)\rangle}{\mathrm{d}t} = H_{\mathrm{RF}}\,|\psi(t)\rangle\,. \tag{6.1}$$

Here H_{RF} is the Hamiltonian in the rotating frame,

$$H_{\mathrm{RF}} = -\frac{\hbar\Delta}{2}\sigma_z + \frac{\hbar\Omega}{2}(\cos\phi\sigma_x + \sin\phi\sigma_y), \tag{6.2}$$

where $\Omega = -\vec{d}\cdot\vec{\epsilon}\mathcal{E}_0$ is the Rabi frequency, $\Delta = \omega - \omega_0$ is the detuning from resonance, ϕ is the phase of the radiation and $\{\sigma_x, \sigma_y, \sigma_z\}$ are the normal two-by-two Pauli matrices. The general solution to

[1] Note that care must be taken to avoid creating any 'Λ dark states'—superpositions of two states which are dark to the pair of beams. This requires the difference in the detuning of the two beams to be non-coincident with the splitting between any two states that can be connected by the two photon transition.

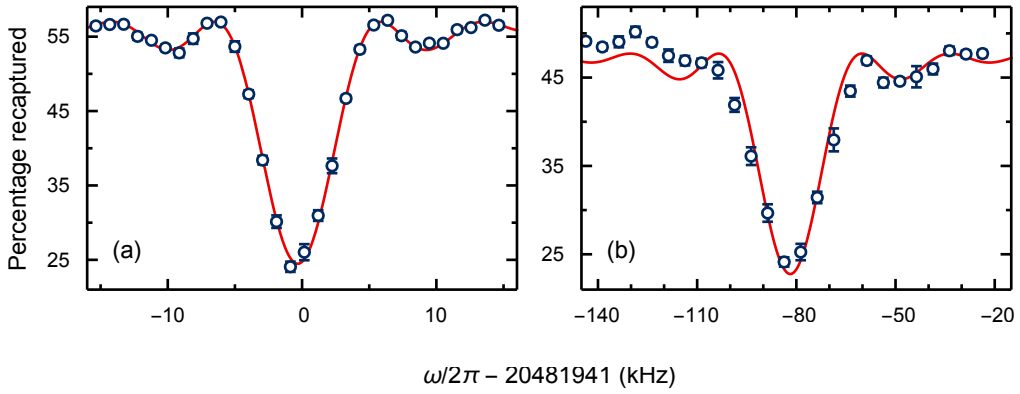

Figure 6.6: Single-pulse microwave spectroscopy – depletion of $N = 1$ population versus microwave frequency. (a) $|1,0,0\rangle \rightarrow |0,1,0\rangle$ transition driven by a 140 µs π-pulse; (b) $|1,0,0\rangle \rightarrow |0,1,1\rangle$ transition driven by a 40 µs π-pulse. Points and error bars are mean and standard error of 9 experiments. Where not visible, error bars are smaller than points. Lines are fits to the Rabi lineshape for a π-pulse of the known duration, with background, amplitude and central frequency as free parameters. The data have been corrected for a systematic frequency shift of 1.9 kHz in (a) and 4.7 kHz in (b), arising from a drift in microwave frequency when the pulse is applied (see Sec. 6.4.3.1).

Eq. (6.1) can be written

$$|\psi(t)\rangle = U_{\mathrm{RF}}(t,\Omega,\Delta,\phi)\,|\psi(0)\rangle\,. \tag{6.3}$$

The propagator is

$$U_{\mathrm{RF}}(t,\Omega,\Delta,\phi) = \cos\left(\frac{\Omega_{\mathrm{tot}}t}{2}\right)\mathbb{1} + i\sin\left(\frac{\Omega_{\mathrm{tot}}t}{2}\right)\left[-\frac{\Delta}{\Omega_{\mathrm{tot}}}\sigma_z + \frac{\Omega}{\Omega_{\mathrm{tot}}}\left(e^{-i\phi}\sigma_+ + e^{i\phi}\sigma_-\right)\right], \tag{6.4}$$

where $\Omega_{\mathrm{tot}} = \sqrt{\Omega^2+\Delta^2}$, $\mathbb{1}$ is the identity operator and $\sigma_\pm = (\sigma_x \pm i\sigma_y)/2$ are the raising and lowering operators of the subspace.

6.4 Single-pulse spectroscopy

We begin by driving transitions between $N = 0$ and $N = 1$ with $\omega_0 \sim 20.5$ GHz. The outputs of the two-channel Windfreak microwave synthesizer (see Sec. 4.6) are connected to a frequency doubler via a switch, and the doubled output is coupled to free space through a horn. The microwave field passes into the vacuum chamber along the same path as the slowing laser. Its polarisation at the molecules is poorly defined due to reflections inside the chamber, and we find that $\Delta m_F = -1, 0, 1$ transitions can all be driven. Bias coils cancel the background magnetic field (see Sec. 6.4.2.1) and apply a constant, uniform field of ~ 60 mG, sufficient to resolve the Zeeman sub-levels, but small enough not to disrupt the molasses cooling.

6.4.1 $|1,0,0\rangle \rightarrow |0,1,0\rangle$ transition

Figure 6.6(a) shows the depletion of the $N = 1$ population as a function of ω, as it is scanned through resonance with the $|1,0,0\rangle \rightarrow |0,1,0\rangle$ transition at ω_0. Because both states have $m_F = 0$, the transition between them is magnetically insensitive for low fields. The microwave pulse duration is $\tau_{\mu 1} = 140$ µs,

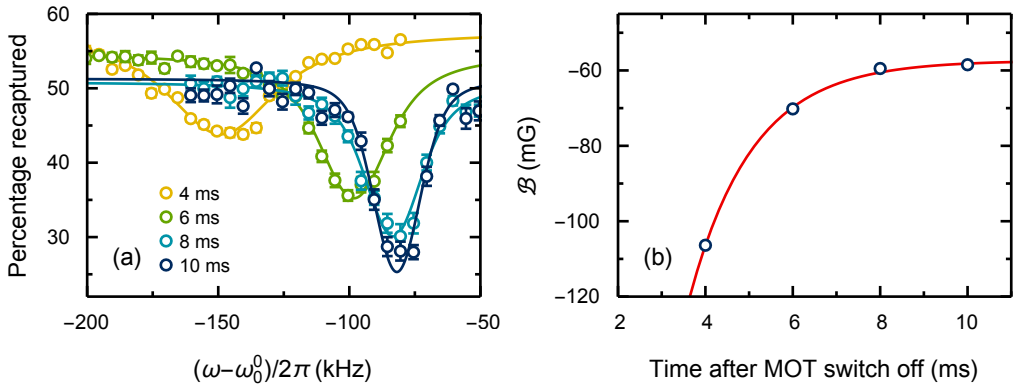

Figure 6.7: Exploring eddy currents from MOT coil switch off. (a) Lineshape of the magnetically sensitive $|1,0,0\rangle \rightarrow |0,1,1\rangle$ transition as a function of time after MOT coil switch off. Points and error bars are mean and standard error of 9 experiments. Lines are fits of each dataset to a Voigt profile. (b) Magnetic field at the position of the molecules as determined from the centre of fitted lineshapes from (a) vs time elapsed after MOT coil switch off. Error bars are smaller than points and line is fit to exponential decay.

and the Rabi frequency is $\Omega = \pi/\tau_{\mu 1}$. We measure the depletion from $N = 1$ as described above in Sec. 6.2.

For a perfectly initialised system with each molecule experiencing an identical microwave field, the fraction of molecules remaining in $N = 1$ is given by

$$\begin{aligned} f(\Delta, \tau_{\mu 1}) &= \left| \langle\uparrow| U_{\mathrm{RF}} \left(\tau_{\mu 1}, \frac{\pi}{\tau_{\mu 1}}, \Delta, \phi \right) |\uparrow\rangle \right|^2 , \\ &= 1 - \frac{1}{1 + \frac{\tau_{\mu 1}^2 \Delta^2}{\pi^2}} \sin^2 \left(\frac{\sqrt{\left(\frac{\pi}{\tau_{\mu 1}}\right)^2 + \Delta^2}}{2} \tau_{\mu 1} \right) . \end{aligned} \tag{6.5}$$

Note that the phase ϕ has no effect in this case. The line in Fig. 6.6(a) is a fit to the data using the model $y_0 + A f(\omega - \omega_0, \tau_{\mu 1})$, where y_0 is the fraction re-captured without the microwave pulse and A is an amplitude. We fix $\tau_{\mu 1}$, leaving y_0, A and ω_0 as free parameters. The fit gives $y_0 = 0.57$, consistent with the expected loss due to the MOT lifetime, and $A = -0.32$. The microwave transfer efficiency is $\epsilon_{\mathrm{MW}} = |A/(y_0 \epsilon_{\mathrm{OP}})| = 94\,\%$. We attribute this below-unit efficiency to reflections of the microwaves inside the chamber. The microwave wavelength is of comparable size to the chamber windows and so reflections from the inside walls of the chamber are inevitable. These reflections set up standing waves that create gradients of the intensity and polarisation of the microwave field across the cloud. From the duration of the π pulse we infer that, in the relevant polarisation, the average microwave intensity at the molecules is $64\,\mathrm{nW\,cm^{-2}}$.

6.4.2 $|1,0,0\rangle \rightarrow |0,1,1\rangle$ transition

Next we attempt to drive the nearby magnetically sensitive transition, $|1,0,0\rangle \rightarrow |0,1,1\rangle$. At low fields, the transition has a sensitivity of $\sim \mu_{\mathrm{B}}/h \simeq 1.4\,\mathrm{MHz\,G^{-1}}$. Our initial efforts discovered a dependence

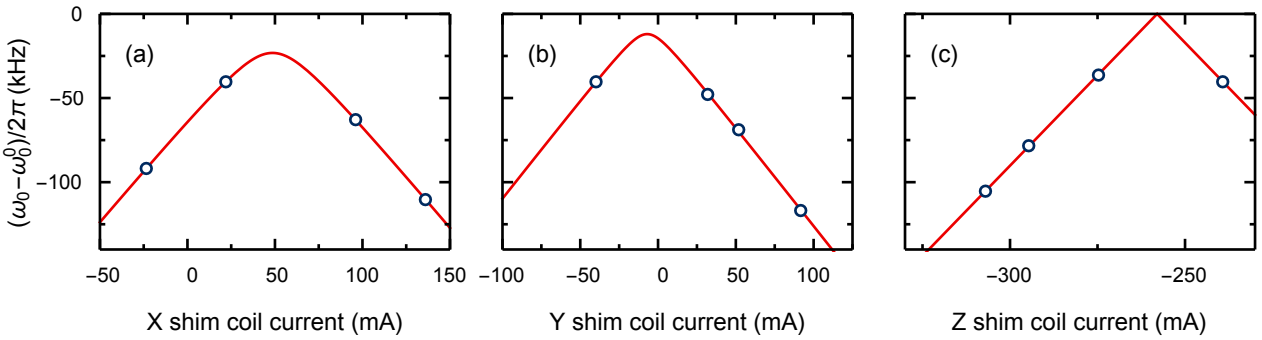

Figure 6.8: Shim coil calibration. Measured frequency shift of the $|1,0,0\rangle \rightarrow |0,1,1\rangle$ transition relative to the $|1,0,0\rangle \rightarrow |0,1,0\rangle$ transition as the current in each shim coil pair is varied: (a) x, (b) y and (c) z. Points are lineshape centres, estimated to an accuracy of $\sim \pm 1$ kHz. Line is a fit to model of Eq. (6.6).

on the time elapsed between switching off the MOT and the microwave pulse. Figure 6.7(a) shows the measured lineshape as a function of the hold time in the optical molasses before the microwave pulse. The pulse duration is $\tau_{\mu 1} = 40\,\mu$s. The lineshape shifts with time, becoming narrower at late times. We attribute this to a non-uniform magnetic field at the position of the molecules created by eddy currents when switching off the MOT coils. As mentioned in Sec. 5.3.8 the copper gasket sealing the large bottom flange of the chamber is relatively close to the coils and so is a likely candidate for contributing most of the eddy currents. Figure 6.7(b) shows the mean magnetic field across the cloud as a function of the time between when the MOT coils are switched off and the microwave pulse, inferred using the linshape centres from Fig. 6.7(a). The data are well described by an exponential decay with $1/e$ time of 1.4 ms. The magnetic field of -60 mG observed at long times is the field deliberately applied in the experiment

Figure 6.6(b) shows lineshape data for the $|1,0,0\rangle \rightarrow |0,1,1\rangle$ transition after increasing the hold time in the molasses to 8 ms to allow the eddy currents to die away. The shorter 40 µs π pulse—compared to that used in Fig. 6.6(a)—reduces the effects of any remaining magnetic field inhomogeneities and fluctuations, but their effects are still visible in the data, producing a slight broadening relative to the model, a poorer fit in the wings, and a lower efficiency of $\epsilon_{\mathrm{MW}} = 87\,\%$. The inferred microwave intensity in the relevant polarisation at the molecules is $780\,\mathrm{nW\,cm^{-2}}$.

6.4.2.1 Calibrating the shim coils

Spectroscopy of the magnetically sensitive $|1,0,0\rangle \rightarrow |0,1,1\rangle$ transition allows us to directly measure the magnetic field at the position of the molecules and we can use this to calibrate our shim coils. Figure 6.8 illustrates the process. For each shim coil in turn, we measure the transition probability as a function of microwave frequency for a number of shim-coil currents and extract the centre frequencies. Care must be taken to avoid the zero-field point where the three Zeeman sub-levels of $N = 0, F = 1$ are degenerate and the two-level approximation breaks down. Away from this region, and for small fields, the data are well described by the model

$$\omega_0 = \omega_0^0 - \frac{\mu_{\mathrm{B}}}{\hbar}\sqrt{(\alpha_i I_i + \mathcal{B}_i^0)^2 + \mathcal{B}_0^2}, \tag{6.6}$$

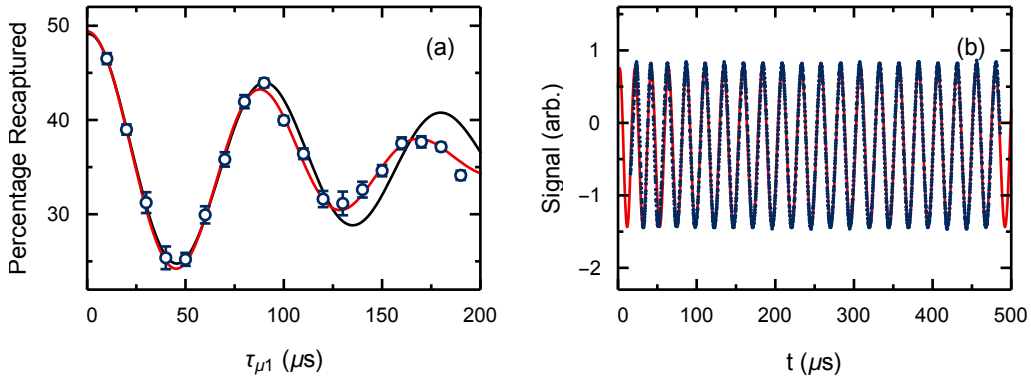

Figure 6.9: (a) Rabi flops on the $|1,0,0\rangle \rightarrow |0,1,1\rangle$ transition. Points and error bars are mean and standard error of 9 experiments. The black line is a fit to data with $\tau_{\mu 1} < 100\,\mu$s with simple exponential model. The data at late time appears to have a higher oscillation frequency. Red line is a fit of model including frequency chirp of microwave synthesizer. Both models are described in text. (b) Beat note of Windfreak synthesizer mixed with Gigatronics synthesizer tuned close to each other. The output of the Windfreak synthesizer passes through a microwave switch which is switched at t=0. Gigatronics is operated in dc. Line is a fit to sinusoid with exponentially decaying chirp as described in text.

where ω_0^0 is the zero field transition frequency, determined by measuring the magnetically insensitive $|1,0,0\rangle \rightarrow |0,1,0\rangle$ transition, I_i is the current in one of the three shim coil pairs with $i = \{x, y, z\}$, α_i is a calibration factor which determines the size of the field produced at the position of the molecules for a given current, $\mathcal{B}_i^0$ is the background field in the direction of the field produced by the shim coil in question and $\mathcal{B}_0$ is the residual field along axes orthogonal to the one being calibrated. The calibration gives $\alpha_x = 0.88(1)\,\mathrm{G\,A^{-1}}$, $\alpha_y = 0.84(1)\,\mathrm{G\,A^{-1}}$ and $\alpha_z = 1.53(1)\,\mathrm{G\,A^{-1}}$. The lab field is $\sim 400\,$mG and predominantly along z. After the field along each axis is zeroed, $|\mathcal{B}|$ is less than $2\,$mG and we can easily apply a small offset field to split the Zeeman levels. The field in the lab drifts slightly over time, requiring this process to be repeated whenever exact field values are required.

This spectroscopy has become an important tool in the lab and allowed us to verify that the magnetic fields which gave the lowest temperatures in both the multi- and single-frequency molasses in Chapter 5 were consistent with zero field.

6.4.3 Understanding experimental imperfections

Whilst the π pulses used for spectroscopy in the previous section are well described by the simple model of Eq. (6.5), we found that longer microwave pulses required additional consideration. Figure 6.9(a) shows Rabi oscillations on the $|1,0,0\rangle \rightarrow |0,1,1\rangle$ transition. We measure the percentage recaptured versus $\tau_{\mu 1}$, with ω on resonance and the power held constant. To model these results, we found it necessary to include the effects of two experimental imperfections.

6.4.3.1 Windfreak chirp

The black line in Fig. 6.9(a) shows the result of a fit of the $\tau_{\mu 1} < 100\,\mu$s data to a simple exponentially decaying sinusoid, $A_0 + Ae^{-t/\tau}\cos(\Omega\tau_{\mu 1} + \phi)$. The frequency of the Rabi oscillations slightly increases with time and so the fit is poor at late times. We found the cause is a transient frequency drift of

the Windfreak microwave synthesizer when switched. The microwave switch is positioned between the synthesizer and the frequency-doubler. When the switch is in the open position, the circuit is open causing reflections in the microwave line and when it closes there is a sudden change in the impedance driven by the synthesizer which seems to cause the chirp.

Figure 6.9(b) shows an oscilloscope trace of the beat note between the Windfreak synthesizer—operated through the switch which is closed at $\sim t = 0$—mixed with a second microwave synthesizer (Gigatronics) operated in dc and with frequency set a few kilohertz above that of the Windfreak. The red line in Fig. 6.9(b) is a fit to an exponentially decaying frequency chirp, $A_0 + A\sin\Big((\omega_\infty + \Delta\omega\, e^{-t'/\tau_\omega})t + \varphi\Big)$, where $\omega_\infty/(2\pi)$ is the frequency at late times, t' is the time since the start of the pulse, $\Delta\omega \approx 11\,\mathrm{kHz}$ is the total frequency change and $\tau_\omega \approx 120\,\mu\mathrm{s}$.

The drift has no observable effect on the lineshapes in Fig. 6.6, but causes a slight frequency shift in the line centres, accounted for in all the data presented in this chapter. In later experiments, from Sec. 6.7 onwards, we removed the effect by swapping the microwave switch for a non-reflective one; the switch terminates the open position at $50\,\Omega$, equal to the impedance of the microwave horn. We also replaced the Windfreak with the Gigatronics synthesizer which seems less susceptible to the effect and locks more reliably to the 10 MHz reference signal.

6.4.3.2 Polarisation and intensity gradients

The second imperfection is due to gradients of intensity and polarization produced by the standing wave component of the microwave field, and is the main reason for the gradual reduction in the contrast of the Rabi oscillations with increasing $\tau_{\mu 1}$. To model these effects, we solve the two-level Schrödinger equation of Eq. (6.1) with the measured frequency drift included, producing a function $y_0 + Ag(\Omega, \omega_\infty - \omega_0, \tau_{\mu 1})$. We average this over a Gaussian distribution of Rabi frequencies with a width of $\Delta\Omega$. The solid line in Fig. 6.9(b) is a fit to this model, with y_0, A, $\omega_\infty - \omega_0$, Ω and $\Delta\Omega$ as free parameters. We find that the fit is improved with the drift parameters tweaked slightly to $\Delta\omega = 7\,\mathrm{kHz}$ and $\tau_\omega = 105\,\mu\mathrm{s}$. In this case we find $\Delta\Omega/\Omega = 0.16$, which is reasonable since the distance from node to antinode of the standing wave is 3.5 mm, comparable to the size of the molecule cloud. We find that small movements of the microwave horn can change the contrast at late times substantially, presumably because it alters the standing wave produced at the position of the molecules.

6.5 Blow away

With most molecules now transferred to $N = 0$, we can push those remaining in $N = 1$ out of the trap region by turning back on $\mathcal{L}_{00}^S$ for a short period. For these experiments, we hold the frequency of $\mathcal{L}_{00}^S$ roughly resonant with molecules at zero velocity—where the slowing chirp finishes (see Sec. 5.1)—until after the 'blow away' pulse. This requires disabling the locking feedback to the slowing light for the duration of the MOT.

We would like to push the $N = 1$ molecules away in a time which is short compared to the time taken for the molecules to fall under gravity by more than a MOT radius, ideally a millisecond or less. We find that giving the molecules enough velocity to escape from the MOT in this time is challenging but it is relatively easy to give them enough of a push to escape from the magnetic trap (see Sec. 6.6). Following the microwave pulse that transfers population to $|0, 1, 1\rangle$, we apply a short pulse of slowing

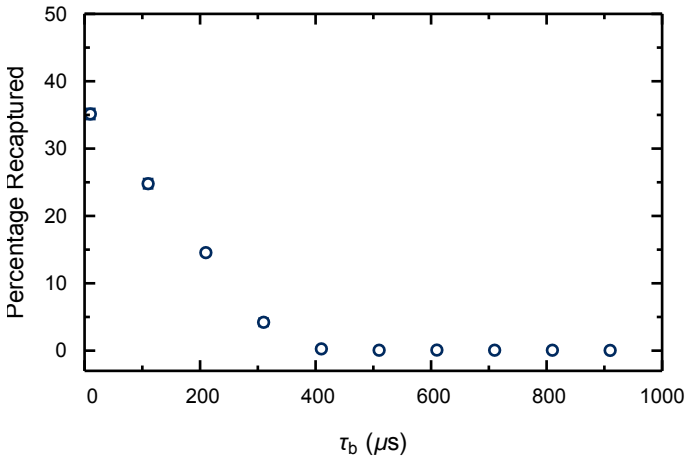

Figure 6.10: Blow away pulse. Percentage of molecules recaptured in MOT after blow away pulse of various durations followed by 20 ms magnetic trap. Points are mean of 9 repeat experiments. Error bars are smaller than points.

light, and then switch on the magnetic trap. The magnetic trap remains on for at least 20 ms which gives the pushed molecules sufficient time to leave the MOT capture region. We can image any molecules remaining in $N = 1$ by turning on the MOT and imaging the fluorescence as before. Figure 6.10 shows the fraction of molecules recaptured as a function of the duration of the blow away pulse. This experiment is done without optical pumping or microwave pulses and so the state distribution is the same as at the end of the MOT; only the molecules which are in weak field seeking states ($\sim 40\%$ of the total) can be captured. All molecules are removed after $\sim 400\,\mu$s but we normally apply a 1 ms pulse to be sure.

The blow away pulse leaves a pure sample of molecules in a single state of $N = 0$. We can image them by applying a second microwave pulse to transfer the molecules back to a selected sub-level of $N = 1$ where they can be imaged in the MOT. This second microwave pulse is applied after the blow away pulse and either before or after the magnetic trap. Figure 6.11 shows Rabi oscillations on the $|0, 1, 1\rangle \rightarrow |1, 2, 2\rangle$ transition as $\tau_{\mu 2}$, the duration of the second microwave pulse, is varied. The percentage recaptured is zero when $\tau_{\mu 2} = 0$, showing that we indeed have a pure sample. The line is a fit using the same model described above for the red line in Fig. 6.9. A π pulse has an efficiency of 75 % and takes 100 µs, implying a microwave intensity of $42\,\mathrm{nW\,cm^{-2}}$.

6.6 Magnetic trapping

With the procedures described above, we can trap molecules in any of the weak-field seeking states of $N = 0$ or $N = 1$. After preparing the molecules in a single state, we turn on the MOT coils to produce a quadrupole magnetic trap with axial field gradient $\mathcal{B}'$. The switch on time for the field is ~ 1 ms, sufficiently slow that the molecules are able to adiabatically follow the local field and remain in the state we prepare them in.

Here, we demonstrate trapping in the $|0, 1, 1\rangle$ and $|1, 1, 2\rangle$ states; these states have near equal magnetic moments of $\sim \mu_B$, as discussed in more detail in Chapter 7. We turn the trap on with

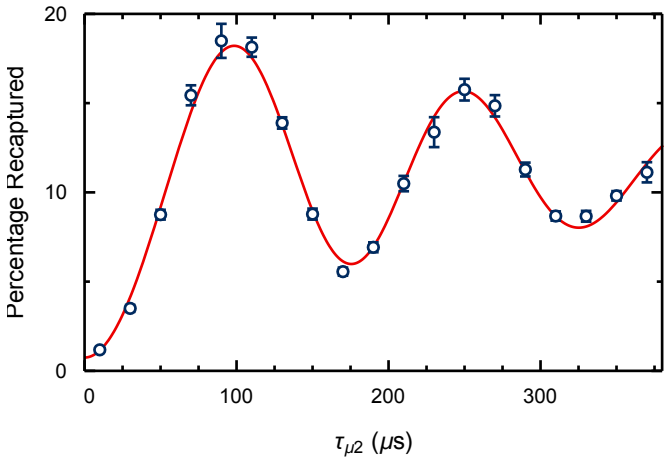

Figure 6.11: Rabi flops on the $|0,1,1\rangle \rightarrow |1,2,2\rangle$ transition. Molecules are first transferred to $|0,1,1\rangle$ with a microwave π pulse and then any remaining molecules in $N = 1$ removed with a blow away pulse. A second microwave pulse with duration $\tau_{\mu 2}$ transfers molecules to $|1,2,2\rangle$. Points and error bars are mean and standard error of 9 repeat experiments.

$\mathcal{B}' = 30\,\mathrm{G\,cm^{-1}}$ after the first or second microwave pulse, then detect the number remaining after a time τ_{mag} by turning the MOT light on and imaging the fluorescence. When trapping molecules in $N = 0$, which do not fluoresce in the MOT light, we transfer back to $N = 1$ using the $|0,1,1\rangle \rightarrow |1,2,2\rangle$ transition prior to detection. This magnetically insensitive transition can be driven while the molecules are magnetically trapped. Indeed, we observe Rabi oscillations on this transition, similar to those in Fig. 6.11, even when the molecules are trapped.

6.6.1 Lifetime

6.6.1.1 Leaking light

Our first experiments to measure the lifetime of the molecules in the magnetic trap found it to be limited to a few hundred milliseconds by scattering from light which leaks through the $\mathcal{L}_{00}$ and $\mathcal{L}_{00}^{S}$ AOMs which we use to turn off the light. Molecules can be transferred to untrapped states by scattering only one or two photons, so even a very small amount of leaking through the AOMs is sufficient to reduce the trap lifetime. Installing home-built shutters, which close in a few tens of milliseconds, into each beam increased the lifetime to more than one second at our normal helium flow rate.

6.6.1.2 MOT coil heating

With the longer lifetimes enabled by the shutters, we found our lifetime data were initially extremely noisy. We eventually established the noise was correlated with the length of time the MOT coils had been on for in the immediately previous shots of the experiment. We hypothesise the cause is that the MOT coils heat up when operated at high duty cycles. At higher temperatures, the black paint on the MOT coils (see Sec. 4.4.2) outgasses[2], and the released particles knock the molecules out of the trap. We removed the effect by reducing our repetition rate to 0.1 Hz for these experiments, effectively

[2]We can see this effect directly on the pressure gauge when we leave the coils on in dc at high currents.

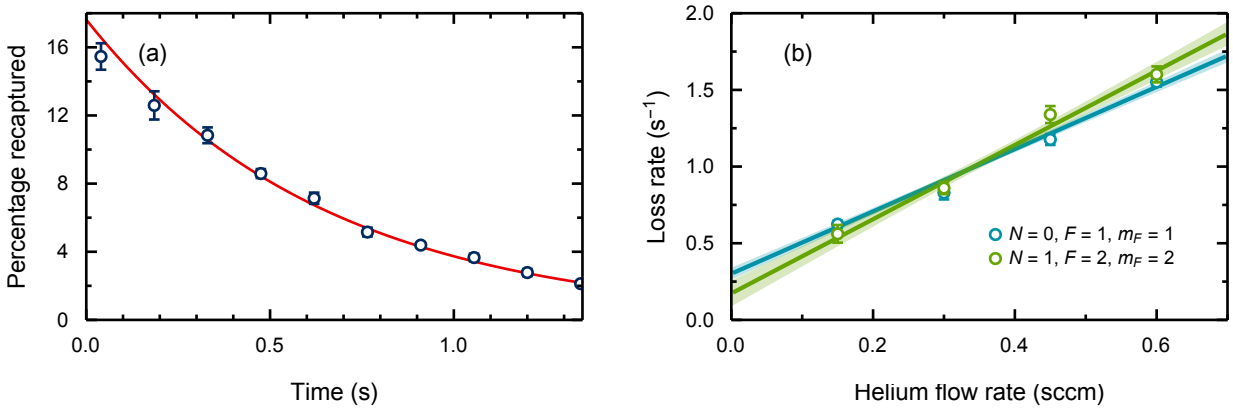

Figure 6.12: (a) Percentage recaptured versus time in magnetic trap for molecules in $|0,1,1\rangle$, when helium flow rate is 0.6 sccm. Points and error bars are mean and standard error of 19 repeat experiments. (b) Magnetic trap loss rate versus helium flow rate for molecules in states $|0,1,1\rangle$ (red) and $|1,2,2\rangle$ (blue). Error bars are statistical errors from fits. Lines are linear fits. Shaded regions are 68 % confidence bands.

adding a long pause at the end of each shot to allow the coils to cool. We found it necessary to run the ablation laser at the normal 2 Hz to avoid having significantly reduced signal from the source.

6.6.1.3 Helium flow

Figure 6.12(a) shows typical lifetime data after blocking the leaking light and adding in the extra wait time for coils to cool. The number of trapped molecules follows a single-exponential decay, $N_{\mathrm{mol}}(\tau_{\mathrm{mag}}) = N_{\mathrm{mol}}(0)\exp(-R_{\mathrm{loss}}\tau_{\mathrm{mag}})$, which we attribute mainly to collisions with helium from the buffer-gas source. Figure 6.12(b) shows the loss rate, R_{loss}, versus the helium flow rate from the source, for molecules in each of the two states, showing a linear dependence in both cases. The gradients are 2.03(8) and 2.42(16) $\mathrm{s}^{-1}\,\mathrm{sccm}^{-1}$ for the $|0,1,1\rangle$ and $|1,1,2\rangle$ states respectively, differing by $2.2\,\sigma$. At the lowest flow used, 0.15 sccm, the trap lifetimes are 1.60(6) s for $|0,1,1\rangle$ and 1.8(2) s for $|1,1,2\rangle$. Extrapolating to zero flow, the loss rates are 0.30(3) and 0.17(6) s^{-1}, differing by $1.9\,\sigma$. The small differences between the two gradients and the two intercepts are not significant, suggesting that there is no state-dependence to the loss rate at this level of precision. This is to be expected since the energy of the collisions with the helium is large compared to the rotational constant of the molecule. Later, we added an in-vacuum shutter (see Sec. 4.2) which closes after the pulse of molecules from the source has passed and blocks the helium flow during the magnetic trapping period. With this modification we measure a loss rate of 0.22(2) s^{-1}, close to our extrapolated values and corresponding to a lifetime of 4.5(4) s.

6.6.1.4 Blackbody radiation

The measured loss rate at zero flow is in excellent agreement with the loss rate due to vibrational excitation by room temperature blackbody radiation [172], which we calculate to be 0.22 s^{-1} for both states. The only way to extend the lifetime of the molecules in the magnetic trap beyond this point is to significantly cool the surrounding surfaces.

6.6.2 Heating rate

In our first experiments in the magnetic trap, we ran the two MOT coils with separate power supplies. In this configuration the molecules, which were initially prepared using the multi-frequency molasses at $\sim 55\,\mu\text{K}$, were heated to $> 1\,\text{mK}$ in 200 ms. This is a common problem in traps with separate supplies because uncorrelated current noise in the two coils causes the zero of the trap to move in time, heating the cloud. We switched to running both coils in series with a single supply which makes the current noise in each coil equal. In this configuration, although the gradient can fluctuate slightly, the trap centre does not.

Before turning on the trap, the radial, axial, and geometric mean temperatures of the molecules are $\{T_\rho, T_z, T\} = \{52(12), 69(12), 57(9)\}$ µK. After trapping for $\tau_{\text{mag}} = 40\,\text{ms}$ in the single supply configuration we measure {56(12), 131(12), 74(11)} µK, while at $\tau_{\text{mag}} = 500\,\text{ms}$ the values are {47(12), 123(12), 65(11)} µK. Each of these temperatures are measured by ballistic expansion which becomes more difficult as the number of molecules in the trap decreases. The measurements show that trap loading results in modest heating, though only in the axial direction. This is as expected because the trap is tighter along this axis and so the roughly symmetric cloud is loaded higher up the sides of the trap in this dimension, adding energy. The heating rate during trapping is consistent with zero and has an upper limit of $34\,\mu\text{K}\,\text{s}^{-1}$. Taking the mean of the two measurements gives a temperature for the trapped molecules of 70(8) µK. We load about 5×10^3 molecules into the trap, and the cloud has radial and axial rms radii of $\sigma_\rho = 1.37(1)\,\text{mm}$ and $\sigma_z = 1.44(2)\,\text{mm}$ respectively. The density is $1.2 \times 10^5\,\text{cm}^{-3}$, the phase-space density is 2.6×10^{-12}.

6.7 Ramsey spectroscopy

Precision metrology experiments and measurements of fundamental constants typically employ the Ramsey method for spectroscopy [73, 173]. The technique also forms the foundation of the coherent control needed for quantum simulation [174]. The highest precision measurements require long interrogation times, most easily realised for trapped samples. In this section we investigate Ramsey spectroscopy of the molecules in free space and in the magnetic trap.

In the Ramsey experiments detailed below, we apply microwave fields tuned close to resonance with a transition between the $|0,1,1\rangle$ and $|1,2,2\rangle$ states of the molecule. For brevity we will denote them as $|0\rangle$ and $|1\rangle$ respectively. In each experiment, the molecules are first prepared in $|0\rangle$, with the techniques described above, and then a $\pi/2$ microwave pulse of duration τ_{R} and detuning Δ creates a coherent superposition of $|0\rangle$ and $|1\rangle$. This state is allowed to evolve for a time T before a second identical $\pi/2$ pulse completes the sequence.

In order to model dephasing in our system it will be convenient to translate the two-level physics of Eqs. (6.1)-(6.4) into the density operator formalism. Rather than keeping track of the state vector $|\psi(t)\rangle$, we will follow the evolution of the density operator $\rho(t)$. In the absence of experimental imperfections, the density operator at the end of the sequence is

$$\rho^{\text{final}} = U_{\pi/2} \cdot U_{\text{free}} \cdot U_{\pi/2} \cdot \rho^{\text{initial}} \cdot U_{\pi/2}^\dagger \cdot U_{\text{free}}^\dagger \cdot U_{\pi/2}^\dagger, \tag{6.7}$$

with $\rho^{\text{initial}} = |0\rangle\langle 0|$ the initial density operator. The propagators for the $\pi/2$ pulse $U_{\pi/2}$, and for the

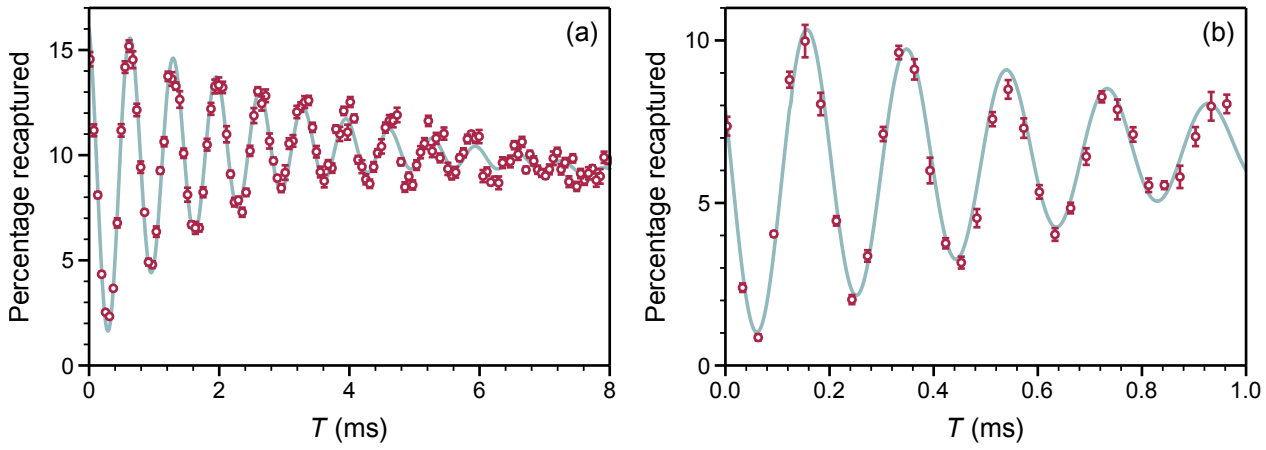

Figure 6.13: Ramsey fringes for CaF molecules prepared in a coherent superposition of states $|0\rangle = |N = 0, F = 1, M_F = 1\rangle$ and $|1\rangle = |N = 1, F = 2, M_F = 2\rangle$. The $\pi/2$ pulses have duration $\tau = 27$ μs, and the free evolution time T, is scanned. The plots show the fraction recaptured into the MOT, proportional to the number in $N = 1$, as a function of T. (a) Molecules in free space. The microwave frequency is 20,553,427.9 kHz, approximately 1.5 kHz above resonance. The main decoherence mechanism is scattering of residual laser light. (b) Molecules confined to a magnetic quadrupole trap with a radial magnetic field gradient of 15 G cm^{-1}. The microwave frequency is 20,553,431.2 kHz, approximately 5 kHz above resonance. The transition frequency is Zeeman shifted, and the main decoherence mechanism is dephasing due to the distribution of these Zeeman shifts. Points and error bars show the mean and standard error of 9 repeated experiments. Lines are fits to the models described in the text.

free evolution period U_{free}, are given in terms of U_{RF} (see Eq. (6.4)) by

$$U_{\pi/2} = U_{\text{RF}}\left(\tau_{\text{R}}, \frac{\pi}{2\tau_{\text{R}}}, \Delta, \phi\right) \tag{6.8}$$

$$U_{\text{free}} = U_{\text{RF}}\left(T, 0, \Delta\right) = \cos\left(\frac{T\Delta}{2}\right)\mathbb{1} + i\sin\left(\frac{T\Delta}{2}\right)\sigma_z. \tag{6.9}$$

The populations in $|0\rangle$ and $|1\rangle$ at the end of the sequence are $P_0 = \rho_{00}^{\text{final}}$ and $P_1 = \rho_{11}^{\text{final}}$.

When the molecules are confined in a trap to allow long interrogation times, dephasing can become an issue due to spatially varying transition-frequency shifts across the ensemble. The advantage of the density operator formalism is in considering the collective state of an ensemble of molecules in the presence of such dephasing.

6.7.1 Ramsey spectroscopy in free space

At the end of the sequence we again measure the number of molecules in $N = 1$ by turning on the MOT light, imaging the fluorescence and comparing with an image of the initial MOT. Figure 6.13(a) shows the percentage recaptured as a function of T for molecules that are freely expanding. Here, we have chosen $\Delta/(2\pi) \approx 1.5$ kHz, which is small compared to the Rabi frequency. The data show the beat note between the oscillations of the molecule and the microwave source. The coherence time, defined as the $1/e$ decay time of the oscillations, is 2.48(4) ms. Modelling these results required understanding a number of experimental imperfections and including them in the model of Eq. (6.7).

6.7.1.1 Switching time

We found that the new microwave switch, installed to avoid the issues described in Sec. 6.4.3.1, took substantially longer to turn off ($\sim 7.3\,\mu s$) in response to a falling edge than to turn on ($\sim 600\,ns$) in response to a rising edge[3]. As a result, our $\pi/2$ pulses of nominal length $20\,\mu s$ were actually $\tau_R = 27\,\mu s$ and the free evolution time was $\sim 7\,\mu s$ shorter than naively expected from the computer control signals sent. These turn-on and off times were measured using a fast microwave power detector and oscilloscope.

6.7.1.2 Leaking light

The second imperfection concerns leaked light. Although the slowing light is extinguished using an AOM, a small fraction of this light leaks through—the shutters added for the magnetic trapping experiments take a few tens of ms to close, too slow for these experiments. The leaked light excites molecules that are in state $|1\rangle$, and the excited molecules then decay back to one of the levels of $N = 1$. This effect limits the coherence time and pulls the steady-state population in $N = 1$ above 50%. The scattering rate is low enough that we can neglect events occurring during the $\pi/2$ pulses, and concentrate on the free-evolution period. Immediately after the first $\pi/2$ pulse, the density operator describing the molecules is

$$\rho^{\pi/2} = U_{\pi/2} \cdot \rho^{\text{initial}} \cdot U_{\pi/2}^{\dagger}. \tag{6.10}$$

We divide the molecules into two groups. The first contains those that have not scattered any photons. We define the density operator for this group $\rho^{(1)}$ and describe the evolution of its elements in turn. The element $\rho_{11}^{(1)}$ is the $N = 1$ population. Molecules in $N = 1$ scatter photons at a rate γ_{sc} and so the population which has scattered no photons decays as $\rho_{11}^{(1)}(T) = \rho_{11}^{\pi/2} e^{-\gamma_{sc}T}$. The elements $\rho_{10}^{(1)}$ and $\rho_{01}^{(1)}$ are the coherences and decay accordingly whilst evolving as normal due to the detuning of the microwave field $\rho_{10}^{(1)}(T) = \rho_{01}^{(1)\dagger}(T) = \rho_{10}^{\pi/2} e^{-\gamma_{sc}T/2 + i\Delta T}$. The element $\rho_{00}^{(1)}$, the population in $N = 0$, does not interact with the light and so remains constant in time $\rho_{00}^{(1)}(T) = \rho_{00}^{\pi/2}$.

The second group contains the growing fraction of molecules that have scattered a photon,

$$f_{\text{scat}} = \rho_{11}^{\pi/2}(1 - e^{-\gamma_{sc}T}). \tag{6.11}$$

These molecules are projected into the N=1 manifold, because photon scattering only occurs from those states. Of these molecules, a fraction b_r are returned to the subspace we are considering; they are in $|1\rangle$ with density operator $\rho^{(2)} = |1\rangle\langle 1|$ and are affected by the final $\pi/2$ pulse. The remainder are in other states of $N = 1$ and are unaffected by this pulse. Here, $b_r = 1/3$ is the probability that a molecule in $|1\rangle$ decays back to $|1\rangle$ after excitation by the slowing light. We can neglect multiple scattering events that further re-distribute the $N = 1$ population, since they are rare. The density operator at the end of the Ramsey sequence is now given by

$$\rho'^{\,\text{final}} = U_{\pi/2} \cdot \left[\rho^{(1)}(T) + b_r f_{\text{scat}} \rho^{(2)}\right] \cdot U_{\pi/2}^{\dagger}, \tag{6.12}$$

where $U_{\pi/2}$ is the propagator for a $\pi/2$ pulse. Note that this density operator is no longer normalised because of the loss to states outside our subspace. However the final population measured in the

[3]The more likely cause for this slow switching time is the home-built drive circuit since the datasheet for the switch itself specifies a much faster response.

experiment is the total population of $N = 1$, including those molecules lost from our subspace. It is given by

$$P_1'(\Delta, \tau, T) = \rho_{11}'^{\text{final}} + (1 - b_r) f_{\text{scat}}. \tag{6.13}$$

6.7.1.3 Expansion of the cloud beyond detection region

The last imperfection we consider is a reduction in P_1' with increasing T due to the free expansion of the cloud. We assume there is a cut-off radius, R, beyond which the molecules are not detected, and that the size of the cloud expands as $\sigma^2 = \sigma_0^2 + k_B T_{\text{mol}} T^2/M$. Here, M is the mass of a CaF molecule, and σ_0 and T_{mol} are fixed at 1.4 mm and 55 µK respectively. To find the proportion of molecules detected, we assume a spherically symmetric Gaussian spatial distribution and calculate the fraction of this distribution that lies inside a sphere of radius R. This fraction is

$$\beta(\zeta) = \text{erf}(\zeta) - \sqrt{4/\pi}\zeta e^{-\zeta^2}, \tag{6.14}$$

where $\zeta^2 = R^2/(2\sigma^2)$. This modifies the expression for the $N = 1$ population to

$$P_1''(\Delta, \tau, T) = \frac{\beta(\zeta)}{\beta(\zeta_0)} P_1'(\Delta, \tau, T), \tag{6.15}$$

where $\zeta_0^2 = R^2/(2\sigma_0^2)$.

The solid line in Fig. 6.13(a) shows a fit to the model AP_1'' with the amplitude A, the detuning Δ, the radius R, and the scattering rate γ_{sc} as free parameters. The fit has a reduced chi-squared $\chi^2_{\text{red}} = 7.0$, and gives $\Delta/(2\pi) = 1.5053(8)$ kHz, $R = 2.54(6)$ mm and $\gamma_{\text{sc}} = 890(10)$ s^{-1}. This value of R is surprisingly small, suggesting that our simple model may not fully describe the loss mechanism. We note that the statistical uncertainty in determining the transition frequency is less than 1 Hz. Correcting for a frequency shift of $-6(4)$ Hz due to the application of a 60 mG uniform magnetic field, we obtain a preliminary field-free transition frequency of $f_0 = 20,553,426,401(4)$ Hz. It should be emphasised that a precise measurement of the transition frequency was not the aim of this work, so we have not studied the systematic shifts and uncertainties present.

6.7.2 Ramsey spectroscopy in a trap

Figure 6.13(b) shows the same experiment for molecules confined in the quadrupole magnetic trap described in Sec 6.6. All other parameters are the same as above but with a larger detuning of $\Delta/(2\pi) \approx 5$ kHz. In the trap, the Zeeman shift of the transition frequency depends on position, so molecules at different positions fall out of phase, causing decoherence. The Zeeman shifts of states $|0\rangle$ and $|1\rangle$ are almost identical, so long coherence times are possible in the magnetic trap. Nevertheless, the observed coherence time of 0.61(3) ms is considerably shorter than in free space because of the residual difference between the magnetic moments of the two states, $\mu_{|1\rangle}$ and $\mu_{|0\rangle}$. This difference also shifts the transition frequency measured in the trap. Figure 6.14 shows another example of data taken using trapped molecules. Here, we fix $T = 493$ μs, and scan Δ. We observe the standard Ramsey lineshape, but with the contrast reduced, primarily due to the dephasing arising from the distribution of Zeeman shifts.

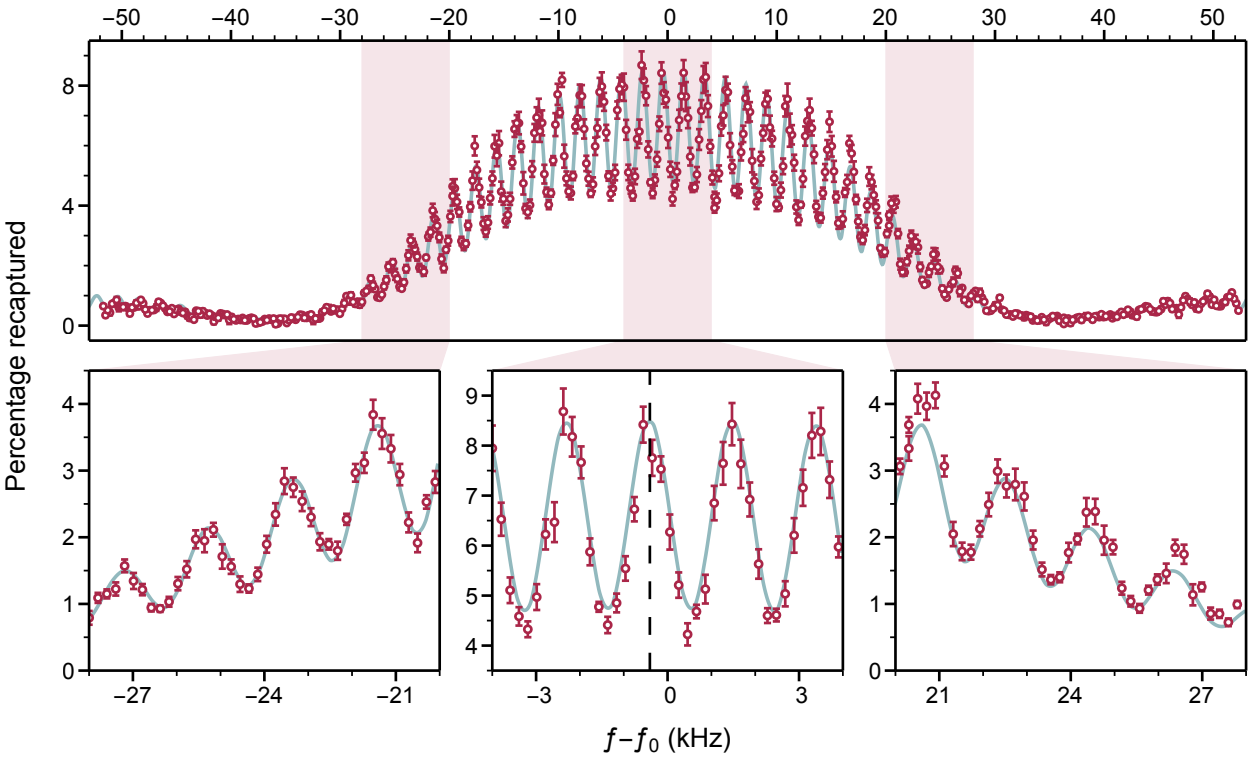

Figure 6.14: Ramsey data for CaF molecules prepared in a coherent superposition of states $|0\rangle = |N=0, F=1, M_F=1\rangle$ and $|1\rangle = |N=1, F=2, M_F=2\rangle$. Molecules are confined to a magnetic quadrupole trap with a radial magnetic field gradient of 15 G cm^{-1}. The $\pi/2$ pulses have duration $\tau = 27$ μs and the free evolution time is $T = 493$ μs. The plots show the percentage recaptured into the MOT, proportional to the number in $N = 1$, as a function of microwave frequency, f, relative to the transition frequency measured in free space, f_0. The lower row shows magnified regions of the data. The vertical dashed line in the central plot indicates the position of the central fringe; the transition frequency in the magnetic trap is shifted by $-404(1)$ Hz from f_0. Points and error bars show the mean and standard error of 9 repeated experiments. The line is a fit to the model described in the text.

To find the distribution of Zeeman shifts, we assume a Gaussian distribution of stationary molecules with standard deviations σ_ρ and σ_z in the radial and axial directions. The coherence time observed in Fig. 6.13(b) is about 50 times shorter than the typical oscillation period of a molecule in the trap[4], so the approximation of stationary molecules is a good one. In a quadrupole trap, the magnitude of the magnetic field at axial coordinate z and radial coordinate ρ is $|\vec{\mathcal{B}}| = \mathcal{B}'\sqrt{z^2 + \rho^2/4}$. Therefore, we can express the Zeeman shift of the transition $\delta_Z = \eta r$, where $r^2 = \rho^2 + 4z^2$ and $\eta = (\mu_{|1\rangle} - \mu_{|0\rangle})\mathcal{B}'/2\hbar$. We begin with the probability-density distribution for the position of the molecules,

$$f_{\rho Z}(\rho, z) = \frac{1}{\sigma_\rho^2}\rho e^{-\frac{\rho^2}{2\sigma_\rho^2}} \frac{1}{\sqrt{2\pi\sigma_z^2}} e^{-\frac{z^2}{2\sigma_z^2}}. \tag{6.16}$$

We need $f_r(r)$, the distribution for r, so we make the coordinate transformation $\rho = r\sin\theta$, $z = \frac{r}{2}\cos\theta$.

[4] A quadrupole trap does not have a single trap frequency but a reasonable estimate comes from time taken for a molecule at a distance σ_ρ from the centre to reach the centre and multiplying by four: $\tau \sim 4\sqrt{\frac{2m\sigma_\rho}{\mu_B \mathcal{B}'_\rho}} \sim 58$ ms.

We have

$$f_{r\theta}(r,\theta) = f_{\rho Z}\left(\frac{r}{2}\sin\theta, r\cos\theta\right)\left|\frac{\partial(\rho,z)}{\partial(r,\theta}\right|, \tag{6.17}$$

where $\left|\frac{\partial(\rho,z)}{\partial(r,\theta}\right| = \frac{r}{2}$ is the Jacobian determinant for the transformation. To obtain $f_r(r)$, we integrate out θ to give

$$\begin{aligned} f_r(r) &= \int_0^\pi \mathrm{d}\theta \frac{r^2}{2\sqrt{2\pi}}\frac{1}{\sigma_z\sigma_\rho^2}\sin\theta e^{-\frac{r^2}{2}\left(\frac{\sin^2\theta}{\sigma_\rho^2}+\frac{\cos^2\theta}{4\sigma_z^2}\right)}, \\ &= \frac{r}{\sigma'\sigma_\rho}e^{-r^2/(2\sigma_\rho^2)}\,\mathrm{erfi}\left(\frac{r\sigma'}{2\sqrt{2}\sigma_z\sigma_\rho}\right), \end{aligned} \tag{6.18}$$

where $\sigma' = \sqrt{4\sigma_z^2 - \sigma_\rho^2}$, and $\mathrm{erfi}(z) = \mathrm{erf}(iz)/i$. Finally we transform once more to obtain the pdf for the Zeeman shifts

$$f_{\delta_Z}(\delta_Z) = \frac{1}{\eta^2\sigma'\sigma_\rho}e^{-\delta_Z^2/(2\eta^2\sigma_\rho^2)}\delta_Z\,\mathrm{erfi}\left(\frac{\delta_Z\sigma'}{2\sqrt{2}\eta\sigma_z\sigma_\rho}\right). \tag{6.19}$$

The additional decoherence due to photon scattering is still present, just as in free space, but the loss due to cloud expansion is not present since the molecules are trapped. Therefore, we start with Eq. (6.13), make the replacement $\Delta \to \Delta + \delta_Z$, and then integrate over the distribution of δ_Z to yield a final expression for the population remaining in $N = 1$ after the Ramsey sequence,

$$P_1'''(\Delta,\tau,T) = \int_0^{\pm\infty} P_1'(\Delta+\delta_Z,\tau,T) f_{\delta_Z}(\delta_Z)\,d\delta_Z, \tag{6.20}$$

where the sign of the upper integration limit is the same as the sign of $\mu_{|1\rangle} - \mu_{|0\rangle}$.

We attempt a simultaneous fit of the two datasets shown in Figs. 6.13(b) and 6.14 to the model $y_0 + AP_1'''$ where y_0 is a background and A is an amplitude. In this fit, we fix $\tau = 27\,\mu\mathrm{s}$, the widths of the trapped distribution to their measured values, $\sigma_z = 1.44$ mm and $\sigma_\rho = 1.37$ mm, and the transition frequency to that measured in free space above. For the data in Fig. 6.14(b), we also fix $T = 493\,\mu\mathrm{s}$. We allow separate values of y_0, A and γ_{sc} for each dataset, but single values of the central frequency and of η that are common to both sets. The solid lines in Figs. 6.13(b) and 6.14 show the results of this simultaneous fit. The model fits well to both sets of data ($\chi^2_{\mathrm{red}} = 2.7$), finds values of γ_{sc} similar to the one found above, and gives $\eta = 8.54(7)\times10^5\,\mathrm{m^{-1}\,s^{-1}}$. This value of η is determined primarily from the shift in the transition frequency between the free-space measurement and the measurements in the trap. It is sensitive to a possible systematic shift between the position of the cloud loaded into the trap, and the magnetic minimum of the trap. If, instead, we allow the central frequency to float, the only information about η comes from the coherence time. In this case, the fit converges on a value of η that is 70% higher. We take the former fit to be most reliable and use the difference between the two fits as a measure of the uncertainty in η. We thus obtain a difference in magnetic moments of $\mu_{|1\rangle} - \mu_{|0\rangle} = -7(5)\times10^{-5}\,\mu_{\mathrm{B}}$. In the next chapter we will measure this value much more accurately.

Chapter 7

Extending rotational coherence times in a magnetic trap

7.1 Introduction

The application of ultracold molecules to quantum simulation and computation requires trapped samples and coherence times that are long compared to the characteristic interaction strength. To avoid the dephasing that arises from an inhomogeneous transition frequency, the trap potential should, ideally, be identical for the two rotational states. Most experimental realisations so far have focused exclusively on optical traps in the form of optical lattices or arrays of tweezer traps where inter-particle separations below 1 µm are possible, producing dipole-dipole couplings with energies $\sim 1\,\mathrm{kHz}$. Whilst second-long coherence times have been demonstrated for superpositions of hyperfine states [175], rotational coherence times longer than $\sim 1\,\mathrm{ms}$ are a challenge because of the dependence of the ac Stark shift on rotational state [176]. By using a dc electric field to uncouple the rotational angular momentum from the nuclear spin, and setting the polarization angle of the trapping light to equalize the Stark shifts of the chosen rotational states, Seeßelberg et al. [177] extended rotational coherence times to 8.7(6) ms in a sample of optically trapped NaK molecules. At the time of writing, this is the state-of-the-art for the coherence time of a sample of trapped molecules in rotational superposition. Long vibrational coherence times have also been demonstrated for Sr_2 molecules in a state-insensitive optical lattice [178].

In Chapter 6 we demonstrated magnetic trapping with $1/e$ lifetimes limited by black-body excitation at $\sim 5\,\mathrm{s}$. It is interesting to consider how one might approach the same quantum simulation and computation goals using magnetic trapping potentials. Two-dimensional arrays of magnetic traps have been demonstrated for atoms with spacings comparable to those achievable with optical arrays [179]. Molecules might also be held in magnetic chip traps close to superconducting microwave resonators [180], where the regime of strong coupling between molecules and microwave photons may be reached, and where molecules may be coupled via the resonator with interaction strengths of order 100 kHz.

To obtain long rotational coherence times in a magnetic trap, it is necessary to find states with large and nearly identical magnetic moments. At the end of Chapter 6 we demonstrated coherence times in a magnetic trap of $\sim 600\,\mu\mathrm{s}$ for a superposition of the $|0,1,1\rangle$ and $|1,2,2\rangle$ states. In this chapter we investigate ways to achieve longer rotational coherence times in the trap.

7.2 Theory

The interaction of a $^2\Sigma$ molecule with a magnetic field $\vec{\mathcal{B}}$ is described by the Zeeman Hamiltonian of Eq. (2.35), detailed in Chapter 2 but repeated here for convenience,

$$\begin{aligned} H_{\mathrm{Z}} &= H_{\mathrm{e}} + H_{\mathrm{n}} + H_{\mathrm{r}} + H_{\mathrm{a}} \\ &= g_S \mu_{\mathrm{B}} \vec{S}\cdot\vec{\mathcal{B}} - g_{\mathrm{N}}\mu_{\mathrm{N}}\vec{I}\cdot\vec{\mathcal{B}} - g_{\mathrm{r}}\mu_{\mathrm{B}}\vec{N}\cdot\vec{\mathcal{B}} + g_l\mu_{\mathrm{B}}(\vec{S}\cdot\vec{\mathcal{B}} - (\vec{S}\cdot\hat{\lambda})(\vec{\mathcal{B}}\cdot\hat{\lambda})). \end{aligned} \tag{7.1}$$

Each of the different angular momenta of the molecule make a contribution to the Zeeman interaction and the search for magnetically insensitive rotational transitions is hindered by the Hamiltonian for the fine and hyperfine structure, H_{fhf}, which couples the angular momenta in a way that depends on N [137]. This is solved by choosing a transition between a pair of stretched states $|N\rangle_{\mathrm{str}} = |N, m_N = N\rangle\,|S, m_S = S\rangle\,|I, m_I = I\rangle$ as we did in Sec. 6.7. These states are eigenstates of both H_{fhf} and H_{Z}. Their Zeeman shifts ΔE_N, are almost identical, because the large contribution from H_{e}, and the smaller one from H_{n}, are both independent of N. For the single-photon transitions $|N\rangle_{\mathrm{str}} \leftrightarrow |N+1\rangle_{\mathrm{str}}$, the residual magnetic sensitivity due to the two remaining terms is

$$\begin{aligned} \Delta\mu(N) &= (\Delta E_{N+1} - \Delta E_N)/B \\ &= \left(\frac{g_l}{(2N+4)^2 - 1} - g_{\mathrm{r}}\right)\mu_{\mathrm{B}}. \end{aligned} \tag{7.2}$$

If the ratio g_l/g_{r} is close to $(2N+4)^2 - 1$ for some N, the remaining two terms nearly cancel, giving the desired magnetic insensitivity.

Our colleagues Jeremy Hutson and Jesús Aldegunde have carried out calculations of this ratio for a variety of alkaline-earth fluorides, hydrides and hydroxides of interest for laser cooling. Further details of the calculation can be found in the Supplemental Material of Ref. [5]. The results obtained when the bond length for each molecule is fixed at its equilibrium value R_{e} are summarised in Table 7.1.

Figure 7.1 shows the resulting $\Delta\mu$ for transitions $|N\rangle_{\mathrm{str}} \leftrightarrow |N+1\rangle_{\mathrm{str}}$ up to $N = 6$. For $N = 0$, the sensitivities are dominated by g_l, and for large N they approach the value set by g_{r}. The hydrides generally have much larger values of both g_{r} and g_l and have no transitions with residual sensitivities on the scale shown. The remaining molecules each exhibit at least one transition with $|\Delta\mu/h| < 30\,\mathrm{Hz\,G^{-1}}$ and six of them have a transition with $|\Delta\mu/h| < 10\,\mathrm{Hz\,G^{-1}}$. These results suggest that convenient rotational transitions with extremely small magnetic sensitivities are a common feature of alkaline-earth fluorides and hydroxides.

7.3 Measurements of g_l and g_{r}

We determined g_l and g_{r} experimentally in CaF by measuring the magnetic sensitivity $\delta\mu$ of two of the stretched-state transitions. The two most easily accessible transitions are $|0\rangle_{\mathrm{str}} \leftrightarrow |1\rangle_{\mathrm{str}}$ and $|1\rangle_{\mathrm{str}} \leftrightarrow |2\rangle_{\mathrm{str}}$ with frequencies $f_{0\leftrightarrow1} = 20\,553.4\,\mathrm{MHz}$ and $f_{1\leftrightarrow2} = 41\,088.9\,\mathrm{MHz}$ respectively.

Table 7.1: Results of electronic structure calculations for g_l and g_r for a variety of potentially laser-coolable molecules at their equilibrium bond lengths R_e. Calculations by Jeremy Hutson and Jesús Aldegunde [6].

Molecule	BeF	MgF	CaF	SrF	BeH	MgH	CaH	SrH	BeOH	MgOH	CaOH	SrOH
R_e (M–X) (Å)	1.36	1.75	1.95	2.07	1.34	1.73	2.00	2.15	1.37	1.76	2.03	2.16
R_e (O–H) (Å)	—	—	—	—	—	—	—	—	0.94	0.94	0.95	0.97
$10^3 g_l$	−0.820	−1.74	−1.86	−4.97	−0.111	−2.18	−4.20	−15.1	−0.394	−1.26	−1.73	−5.24
$10^5 g_r$	−7.36	−3.73	−5.13	−4.77	−144	−88.5	−106	−111	−2.18	−1.48	−3.31	−3.17
g_l/g_r	11.1	46.6	36.3	104	0.077	2.46	3.95	13.6	18.0	85.0	52.3	165

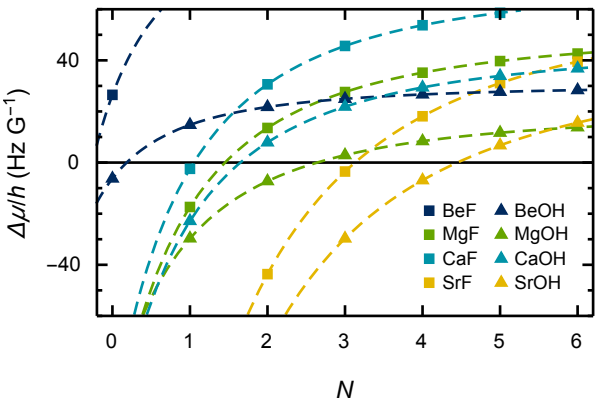

Figure 7.1: Calculated magnetic sensitivities of transitions $|N\rangle_{\mathrm{str}} \leftrightarrow |N+1\rangle_{\mathrm{str}}$ for a variety of alkaline-earth fluorides and hydroxides of interest for laser cooling.

7.3.1 Calibrating the $\mathcal{B}$ field

Rather than infer the sensitivity from measurements in an inhomogeneous trapping field as we did in Sec. 6.7, we want to directly measure the sensitivity here by doing spectroscopy of each transition at a variety of $\mathcal{B}$ fields. For this we need to be able to apply a known $\mathcal{B}$ field which can be switched on and off sufficiently quickly to allow for state preparation and detection. We do this by switching on the MOT coils in the same configuration used in 5.3.5; with the current in one of the coils reversed using the H-bridge circuit. This creates a field which is almost uniform across the $\sim 1.5\,\mathrm{mm}$ cloud (the spatial profile of the field is shown in Fig. 5.15(a)).

7.3.1.1 Current as a function of control voltage

A complication arises in determining the $\mathcal{B}$ field applied because we found that, for a given control voltage, the current from our voltage-controlled power supply can drift slightly. Figure 7.2 shows the voltage measured across the MOT coils 5 ms after the current is switched on as a function of the control voltage sent to the power supply. The 5 ms wait gives enough time for the transient effect of switching the current through the coils to die away so that the voltage is proportional to the applied current. It is also short enough to avoid any heating of the coils which would change their resistance. The three different colours of data points represent datasets taken on three different occasions over three days. Above $\sim 1.1\,\mathrm{V}$ the current supply hits a voltage rail and the current stops increasing. Below this value, the current for a given control voltage is proportional to the control voltage within a single dataset but with a constant of proportionality that varies between datasets. This behaviour suggests that the current drift is slow, occurring over a time that is long compared to the time needed for a typical dataset.

We calibrate the current for a given control voltage by performing a fit to the data. We are interested in knowing the uncertainty in the calibration as this will be important in our estimation of the uncertainty in g_l and g_{r}. The data show that the uncertainty in the current increases with increasing control voltage. We adopt the following model which includes a known offset of the zero current point

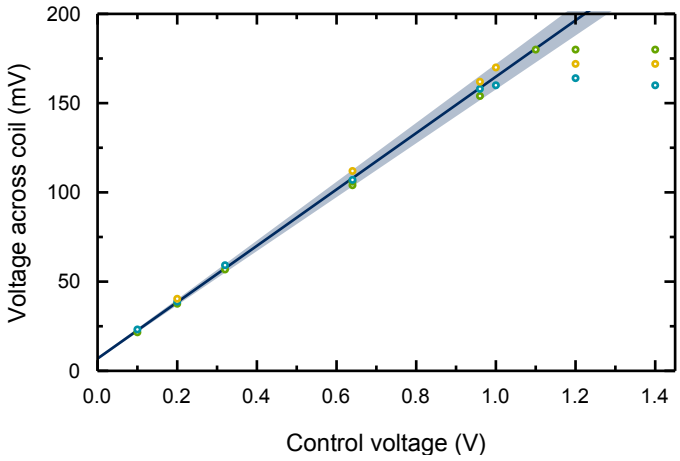

Figure 7.2: Calibration of current in MOT coils. Voltage measured across MOT coils 5 ms after switch on vs the control voltage sent from computer to voltage-controlled power supply. The three different colours of the data points represent measurements taken on three different occasions. Line is fit to data with control voltage less than 1.1 V as described in text.

and attempts to capture the slow variation in the response of the power supply to control voltage,

$$v_{ij} = (k + \beta_j)(V_i - V_0) + \epsilon_i. \tag{7.3}$$

Here v_{ij} is the voltage measured across the MOT coils and k and V_0 are parameters that define the behaviour of the power supply when connected to the MOT coils. β_j and ϵ_i are normally distributed random variables that represent the variation of the power supply response and our measurement uncertainty respectively. The index i is different for each data point whilst j changes only between datasets, representing the slow drift. The variances of β_j and ϵ_i are σ_β^2 and σ_ϵ^2 respectively. We will assume that the measurement uncertainty is small compared to the power supply drift, so that the probability of obtaining a particular set of measurements v_{ij} is given by the following product over $\{i, j\}$ pairs,

$$\text{MLE} = \prod_{i,j} \frac{1}{\sqrt{2\pi}\sigma_\beta(V - V_0)} e^{-\frac{(k(V_i - V_0) - v_{ij})^2}{2\sigma_\beta^2 (V_i - V_0)^2}}. \tag{7.4}$$

This quantity is the maximum likelihood estimator (MLE) and can be maximised with respect to k and V_0 to obtain best-fit values for these parameters.[1] To obtain the uncertainties on these best-fit values we can construct the covariance matrix,

$$\text{cov} = X^{\mathrm{T}} \cdot W \cdot X. \tag{7.5}$$

Here X is the design matrix,

$$X_{i,l} = \frac{\partial}{\partial \xi_l} k(V_i - V_0), \tag{7.6}$$

an $n \times m$ matrix where n is the number of data points, m is the number of unknown variables and

[1] In practice it is numerically easier to maximise log(MLE).

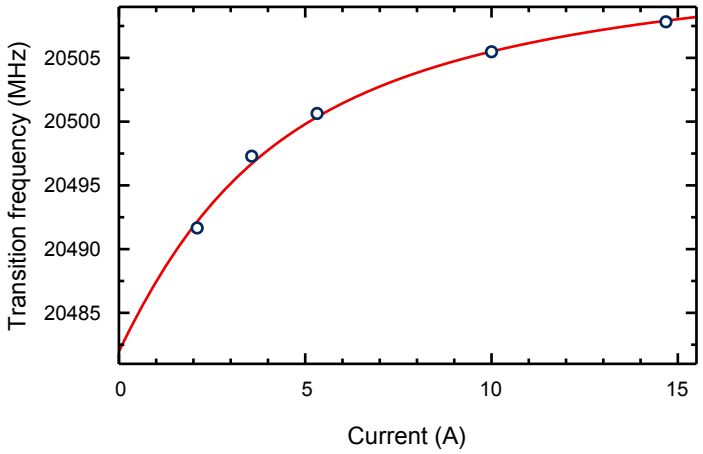

Figure 7.3: Calibration of the $\mathcal{B}$ field produced at molecules by MOT coils as a function of current. Data points show measured transition frequency of $|1,0,0\rangle \rightarrow |0,1,1\rangle$ transition for different applied currents. The uncertainty on each measurement is $< 10\,\mathrm{kHz}$, much smaller than the points. Line shows calculated transition frequency using fitted calibration factor as described in text.

$\xi_l = \{k, V_0\}$ is a vector of these unknown variables. W is the $n \times n$ diagonal weights matrix,

$$W_{i,i'} = \mathrm{diag}\left(\frac{n-2}{\sigma_\beta^2 (V_i - V_0)^2 n}\right). \tag{7.7}$$

The diagonal elements of this covariance matrix are the uncertainties in the fit parameters. A fit to our data, excluding data points with $V > 1.1\,\mathrm{V}$, gives best-fit values and associated uncertainties of $k = 0.158(3)$ and $V_0 = -43(5)\,\mathrm{mV}$. The line and shaded region in Fig. 7.2 show the best fit and 1σ confidence intervals. The resistance of the MOT coils through the region across which the voltages were measured is $0.011\,\Omega$ and can be used to convert these voltages into currents.

7.3.1.2 $\mathcal{B}$ field as a function of current

To calibrate the field at the position of the molecules for a given coil current, we performed single-pulse spectroscopy on the $|1,0,0\rangle \leftrightarrow |0,1,1\rangle$ transition, similar to that described in Sec. 6.4.2. The Zeeman shift of this transition can be calculated accurately because it is dominated by H_e, and because g_S and the hyperfine parameters are known to high precision [142]. Figure 7.3 shows the measured centre frequency of the transition vs the current in the MOT coils, calculated using the fit of the previous section. We use the transition frequencies to infer the $\mathcal{B}$ field at each current and then fit to $\mathcal{B} = aI$. The calibration measurements were recorded in a time short compared to the current supply drift and so the uncertainty in the current for each of the data points is correlated. Taking account of this correlation gives $a = 4.4(2)\,\mathrm{G\,A^{-1}}$. The line in Fig. 7.3 shows the numerical calculation of the transition frequency using this value of a.

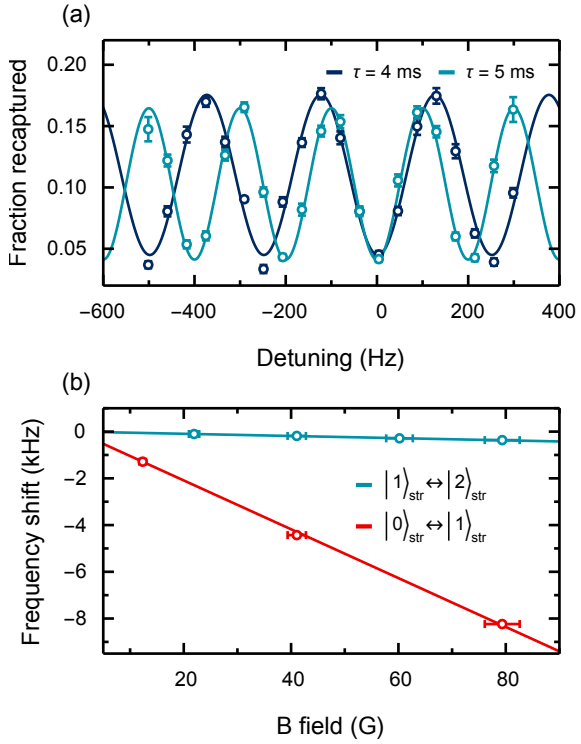

Figure 7.4: (a) Ramsey spectroscopy of the transition $|1\rangle_{\mathrm{str}} \leftrightarrow |2\rangle_{\mathrm{str}}$ in free space with $\tau = 4$ and 5 ms. Points and error bars show mean and standard error of 19 repeated experiments. Lines show sinusoidal fits to the data. (b) Magnetic sensitivity of the transitions $|0\rangle_{\mathrm{str}} \leftrightarrow |1\rangle_{\mathrm{str}}$ (red) and $|1\rangle_{\mathrm{str}} \leftrightarrow |2\rangle_{\mathrm{str}}$ (light blue). Lines show linear fits to the data. Vertical error bars are smaller than the points.

7.3.2 Ramsey spectroscopy

We used Ramsey spectroscopy to measure the frequency of each transition at a variety of applied fields. The Ramsey sequence uses a pair of nearly resonant $\pi/2$ pulses, each 20 µs long and separated by a free-evolution time τ. Following the second pulse, we measure the number of molecules in $N = 1$ as before, by recapturing them into the MOT and imaging their fluorescence.

Figure 7.4(a) shows Ramsey fringes for the transition $|1\rangle_{\mathrm{str}} \leftrightarrow |2\rangle_{\mathrm{str}}$, obtained by scanning the microwave frequency. The dark blue data are for $\tau = 4$ ms and the light blue for $\tau = 5$ ms. Repeating the measurement with different τ identifies the fringe corresponding to the centre frequency. Fitting to the fringes determines the transition frequency with statistical uncertainty below 1 Hz.

Figure 7.4(b) shows the change in transition frequency for both transitions as a function of $\mathcal{B}$. The solid lines show linear fits to the data that give residual magnetic sensitivities $\Delta\mu/h = -104(4)\,\mathrm{Hz\,G^{-1}}$ for the transition $|0\rangle_{\mathrm{str}} \leftrightarrow |1\rangle_{\mathrm{str}}$ and $-4.7(2)\,\mathrm{Hz\,G^{-1}}$ for $|1\rangle_{\mathrm{str}} \leftrightarrow |2\rangle_{\mathrm{str}}$. The uncertainties are dominated by the drift in $\mathcal{B}$ between measurements of the insensitive transition and the transition used for calibration, represented by the horizontal error bars. The error in magnetic field is correlated between different points, because the drift is again slow compared to the measurement time; this has been taken into account in the calculation of the uncertainties in $\Delta\mu$. From these measurements we determine $g_l = -1.87(8) \times 10^{-3}$ and $g_r = -5.0(2) \times 10^{-5}$, in excellent agreement with the calculated values. At $N = 1$ the two terms in Eq. 7.2 cancel to within 3%, resulting in cancellation of the magnetic moments of the two states to 3.3(1) parts per million. As expected from Fig. 7.1, the $|1\rangle_{\mathrm{str}} \leftrightarrow |2\rangle_{\mathrm{str}}$ transition

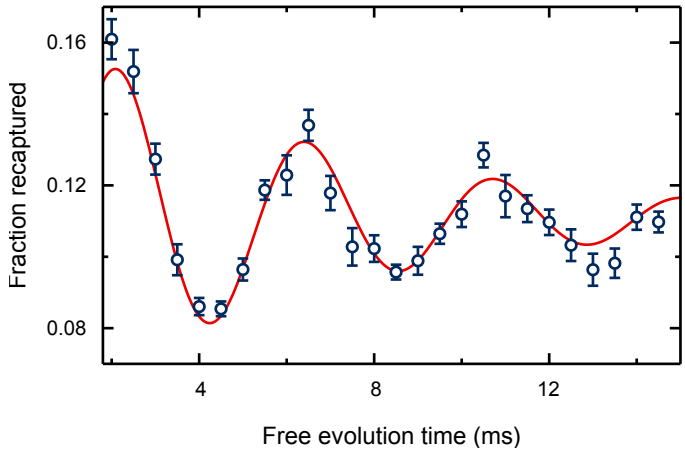

Figure 7.5: Ramsey fringes for molecules in the magnetic trap. Points and error bars throughout show mean and standard error of 19 repeated experiments. Line is a fit to $A + Be^{-\alpha t}\cos(\Delta t + \phi)$ giving a coherence time $1/\alpha = 6.4(8)$ ms.

has the smallest magnetic sensitivity.

7.4 Coherence times

7.4.1 Decoherence in magnetic trap

The very small magnetic sensitivity of the transition $|1\rangle_{\rm str} \leftrightarrow |2\rangle_{\rm str}$ suggests that long coherence times should be possible in a magnetic trap. To investigate this we measure the decay of the beat note between the oscillations of the rotational superposition and those of a slightly detuned microwave field. The first $\pi/2$ pulse is applied and then the quadrupole magnetic trap is immediately turned on with an axial field gradient of $\mathcal{B}' = 45\,\mathrm{G\,cm^{-1}}$. The second $\pi/2$ pulse is applied in the trap and the molecules are then held in the trap to allow the blown away molecules to leave before being recaptured and imaged in a MOT, as before. To remove the leaking light identified in Sec. 6.7, we added fast shutters to both $\mathcal{L}_{00}$ and $\mathcal{L}_{00}^{\rm S}$ that close shortly after the blow away pulse and reopen just before detection. Figure 7.5 shows the Ramsey fringes traced out by scanning the free evolution time τ. The solid line is a fit to a sinusoid with exponentially decaying amplitude, which gives a coherence time of 6.4(8) ms.

7.4.2 Understanding decoherence in the trap

To elucidate the sources of decoherence in the trap, we use a Monte-Carlo simulation of the motion of the molecules during the Ramsey experiment. The equations of motion for a molecule in the trap are,

$$\ddot{x} = -\mathrm{sgn}(x)\frac{\mu_{\rm B}\mathcal{B}'}{2m}, \tag{7.8a}$$

$$\ddot{y} = -\mathrm{sgn}(y)\frac{\mu_{\rm B}\mathcal{B}'}{2m}, \tag{7.8b}$$

$$\ddot{z} = -\mathrm{sgn}(z)\frac{\mu_{\rm B}\mathcal{B}'}{m} - g, \tag{7.8c}$$

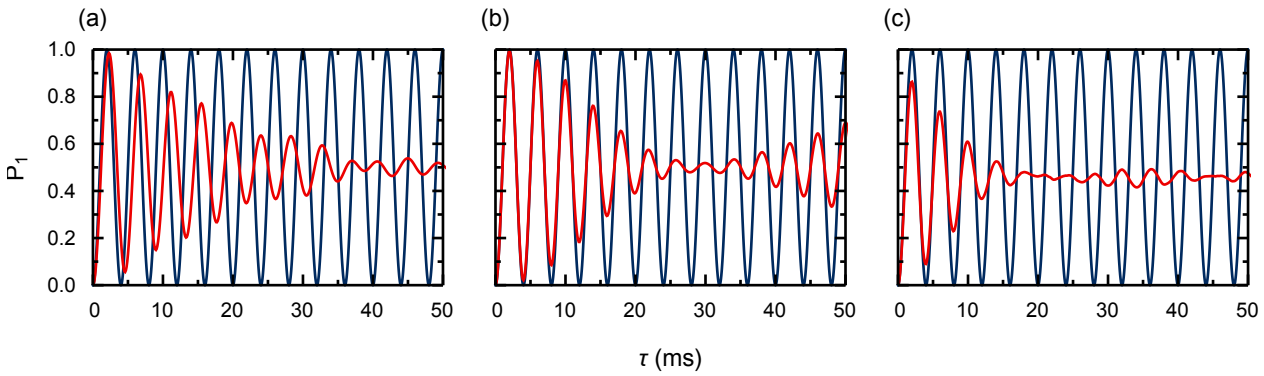

Figure 7.6: Simulations of the effect of each of the three decoherence mechanisms identified on Ramsey fringes for molecules in the trap. (a) Residual magnetic sensitivity. (b) Movement of molecules in the trap. (c) Rotation of local magnetic field in molecule frame. The red lines show the simulation results. The blue lines show the results in the absence of any imperfections for reference. In each plot, the effects of the other mechanisms have been artificially removed.

where g is the acceleration due to gravity, $\mathcal{B}'$ the axial field gradient and the extra factor of $1/2$ in the equations for x and y comes from the fact that the magnetic field gradient in those directions is half of that in the axial direction. We numerically solve the equations for 1000 different initial conditions to give 1000 trajectories $\vec{x}_i(t)$. The initial positions are drawn from a normal distribution with the clouds measured width of $\sigma_x = \sigma_y = \sigma_z = 1.5\,\mathrm{mm}$ and the initial velocities from a normal distribution of width $\sigma_v = \sqrt{k_\mathrm{B}T/m}$ with $T = 50\,\mu\mathrm{K}$.

We identify three decoherence mechanisms. To evaluate the contribution of each, we calculate the phase accumulated due to that mechanism only (see below) for every molecule trajectory $\vec{x}_i(t)$, artificially removing the effect of the other mechanisms. For each trajectory we then calculate P_1, the probability of detecting the molecule in $N = 1$ at the end of the Ramsey sequence[2], and then average over the 1000 trajectories. The results for each of the three mechanisms are shown in Fig. 7.6. The simulated fringes—calculated for a detuning of 250 Hz, chosen to clearly display the dephasing—decohere in a way which is not well described by an exponential decay. To quantify the decoherence rates we extract the peaks and troughs from the simulated fringes and interpolate between them to to give the envelope. We then find the time taken for the amplitude of this envelope to decay by a factor of e. The inverse of this is the decoherence rate for that mechanism.

7.4.2.1 Residual magnetic sensitivity

The residual difference in the magnetic moments of the $|1\rangle_{\mathrm{str}}$ and $|2\rangle_{\mathrm{str}}$ states causes a spread in the phases accumulated by different molecules in the trap. The additional phase acquired by each molecule is

$$\phi_i^{\Delta\mu} = \frac{\Delta\mu}{\hbar}\int_0^\tau |\vec{\mathcal{B}}(\vec{x}_i(t))|\mathrm{d}t. \tag{7.9}$$

[2]For the purposes of the simulation we assume that the molecules only move during the free evolution period and not during the microwave pulses. This is a very good approximation because the distance moved during the 20 µs pulses is very small.

The simulated effects of this mechanism are shown in Fig. 7.6(a). The additional phase always has the same sign—the same as that of $\Delta\mu$—and so there is a noticeable increase in the spacing of the fringes compared to the unperturbed data. The extracted $1/e$ decoherence rate is $50\,\mathrm{s}^{-1}$.

The decoherence rate from this mechanism scales linearly with the average field experienced by the molecules in the trap. In our experiment this is currently set almost entirely by the initial Gaussian width of 1.5 mm and so could be reduced by reducing the size of the cloud we load into the trap. In the limit of a small initial cloud, the sample explores a range of fields determined only by its temperature, T. The resulting spread of transition frequencies, $(k_\mathrm{B}T/h)(\Delta\mu/\mu_\mathrm{B})$, gives a decoherence rate of $0.14\,\mu\mathrm{K}^{-1}\,\mathrm{s}^{-1}$. This implies an achievable coherence time of 1.4 s at 5 µK, a temperature that has already been demonstrated for CaF, both in this thesis and elsewhere [166]. Such a small cloud could perhaps be loaded from an optical dipole trap where cloud sizes of a few tens of µm have already been demonstrated [181].

7.4.2.2 Movement of molecules

Movement along the k-vector of the microwaves, between the two $\pi/2$ pulses, causes a change of phase which is different for each molecule; this is a form of Doppler broadening. The additional phase acquired is

$$\phi_i^\mathrm{D} = \vec{k} \cdot (\vec{x}_i(\tau) - \vec{x}_i(0)), \tag{7.10}$$

where $\vec{k}$ is the wavevector of the microwaves – always in the xy plane in our experiments. The simulated effects of this mechanism are shown in Fig. 7.6(b). Accumulated phase shifts are equally likely with either sign and so the spacing of the fringes remains unchanged but their amplitude decays as the molecules move in different directions. There is a partial revival which peaks at ~ 70 ms and corresponds to the point at which the most molecules are closest to their original positions, an approximate trap period. The extracted $1/e$ decoherence rate—from the first time the envelope decays through $1/e$ of its original amplitude—is $60\,\mathrm{s}^{-1}$.

The decoherence rate from this mechanism is also related to the cloud size. When the maximum difference in the displacement of two molecules from their starting positions is less than the wavelength of the microwave field, the phase change due to motion is limited to less than 2π and the superposition never fully decoheres. The result is a fixed loss of contrast at late times. In our experiment, this maximum phase change is set by the initial cloud size; reducing the cloud size would again decrease the size of the effect.

7.4.2.3 Changing orientation of magnetic field

As the molecules move in the trap, their magnetic moments adiabatically follow the local magnetic field vector. The direction of the local magnetic field at any point can be mapped to the lab z_l axis by a rotation matrix $\mathfrak{R}_i(t)$,

$$\frac{\vec{\mathcal{B}}(\vec{x}_i(t))}{|\vec{\mathcal{B}}(\vec{x}_i(t))|} = \mathfrak{R}_i(t) \cdot \hat{z}_\mathrm{l}. \tag{7.11}$$

We choose to express $\mathfrak{R}$ using the Euler convention,

$$\mathfrak{R}_i(t) = E(\gamma_i(t), \beta_i(t), \alpha_i(t)), \tag{7.12}$$

where $E(\gamma, \beta, \alpha)$ is the 3D rotation matrix that corresponds to a rotation about z by γ, a rotation about the new y' axis by β, followed by a rotation around the new z'' axis by α. The microwave polarisation as seen by the molecule $\vec{\epsilon}'$, is then

$$\vec{\epsilon}' = \mathfrak{R}_i^{-1}(t) \cdot \vec{\epsilon} = E(-\alpha_i(t), -\beta_i(t), -\gamma_i(t)) \cdot \vec{\epsilon} \tag{7.13}$$

where $\vec{\epsilon} = \vec{e}_x$ is the polarisation in the lab frame—in our case linear along $\hat{x}$. We are interested in the change in the component of $\vec{\epsilon}'$ which can drive the σ^+ transition between $|1\rangle_{\text{str}}$ and $|2\rangle_{\text{str}}$ as the molecule moves around the trap. We define

$$\xi_i(t) = \sqrt{2}\vec{\epsilon}' \cdot \vec{e}^{\,+} = -e^{-i\alpha_i(t)} \left[\cos\beta_i(t)\cos\gamma_i(t) - i\sin\gamma_i(t)\right]. \tag{7.14}$$

Here the factor of $\sqrt{2}$ is to ensure that $\xi = 1$ for $\alpha_i(t) = \beta_i(t) = \gamma_i(t) = 0$ and we have used the fact that $\vec{e}^{\,+} = -(\vec{e}_x + i\vec{e}_y)/\sqrt{2}$. The magnitude of the quantity $\xi_i(t)$ is the relative amplitude of the electric field in the correct polarisation to drive the transition and is directly proportional to the Rabi frequency,

$$|\xi_i(t)| = \sqrt{\cos^2\beta_i(t)\cos^2\gamma_i(t) + \sin^2\gamma_i(t)}. \tag{7.15}$$

The effect is that the Ramsey pulses have different pulse areas for each molecule at each of the two pulses. The phase of $\xi_i(t)$ is the relative phase of the microwave field expressed in the molecule frame,

$$\arg(\xi_i(t)) = -\alpha_i(t) + \arctan\left(\frac{-\sin\gamma_i(t)}{\cos\beta_i(t)\cos\gamma_i(t)}\right). \tag{7.16}$$

To evaluate these quantities we need the Euler angles as a function of time. The angles $\beta_i(t)$ and $\gamma_i(t)$ are uniquely defined by the orientation of the local magnetic field at the position of the molecule $\vec{x}_i(t)$ but we are free to choose $\alpha_i(t)$. This is due to the cylindrical symmetry of the Zeeman interaction around the magnetic field axis. Our choice corresponds to a choice of gauge. At first glance this seems to suggest that the accumulated phase depends on the choice of gauge but this is a hint that this cannot be an observable quantity in isolation. We have so far considered the apparent rotation of the microwave field from an observer in the molecule frame but have not yet considered the effect on the molecule itself of being in a non-inertial frame. We will examine the fictitious forces in this moving frame next, loosely following the treatment of Ref. [182]. An alternative treatment from another perspective is given in Ref. [183].

If the Hamiltonian for the molecule in a static magnetic field is H_0, the Schrödinger equation of the molecule in the field which rotates in time is

$$i\hbar\frac{\partial\,|\psi_i(t)\rangle}{\partial t} = \mathcal{R}_i^{-1}(t)H_0\mathcal{R}_i(t)\,|\psi_i(t)\rangle\,. \tag{7.17}$$

Here $\mathcal{R}_i(t)$ is the rotation operator corresponding to our rotation matrix from Eq. (7.11),

$$\mathcal{R}_i(t) = e^{-i\alpha_i(t)J_z}e^{-i\beta_i(t)J_y}e^{-i\gamma_i(t)J_z}, \tag{7.18}$$

with $\{J_x, J_y, J_z\}$ the generators of rotation. If we express the molecules state in this rotating frame,

$|\psi_i(t)\rangle_{\mathrm{R}} = \mathcal{R}_i(t)\,|\psi_i(t)\rangle$, then the equation simplifies to

$$i\hbar\frac{\partial\,|\psi_i(t)\rangle_{\mathrm{R}}}{\partial t} = (H_0 + G_i(t))\,|\psi_i(t)\rangle_{\mathrm{R}}\,, \tag{7.19}$$

where $G_i(t) = -i\hbar\mathcal{R}_i(t)\frac{\partial}{\partial t}\mathcal{R}_i^{-1}(t)$. It will be useful to look at a specific example. Let's specialise for a moment to the case of an $F = 1$ state, in which case $\mathcal{R}_i$ can be written explicitly as

$$\mathcal{R}_i(t) = \begin{pmatrix} \frac{1}{2}e^{i(\alpha_i(t)+\gamma_i(t))}(\cos(\beta_i(t))+1) & \frac{e^{i\alpha_i(t)}\sin(\beta_i(t))}{\sqrt{2}} & e^{i(\alpha_i(t)-\gamma_i(t))}\sin^2\left(\frac{\beta_i(t)}{2}\right) \\ -\frac{e^{i\gamma_i(t)}\sin(\beta_i(t)_i(t))}{\sqrt{2}} & \cos(\beta_i(t)_i(t)) & \frac{e^{-i\gamma_i(t)}\sin(\beta_i(t))}{\sqrt{2}} \\ e^{-i(\alpha_i(t)-\gamma_i(t))}\sin^2\left(\frac{\beta_i(t)}{2}\right) & -\frac{e^{-i\alpha_i(t)}\sin(\beta_i(t))}{\sqrt{2}} & \frac{1}{2}e^{-i(\alpha_i(t)+\gamma_i(t))}(\cos(\beta_i(t))+1) \end{pmatrix}, \tag{7.20}$$

and $G_i(t)$ is

$$G_i(t) = \hbar\begin{pmatrix} -\dot{\alpha}_i(t) - \cos(\beta_i(t))\dot{\gamma}_i(t) & \frac{e^{i\alpha_i(t)}\left(\sin(\beta_i(t))\dot{\gamma}_i(t)+i\dot{\beta}_i(t)\right)}{\sqrt{2}} & 0 \\ \frac{e^{-i\alpha_i(t)}\left(\sin(\beta_i(t))\dot{\gamma}_i(t)-i\dot{\beta}_i(t)\right)}{\sqrt{2}} & 0 & \frac{e^{i\alpha_i(t)}\left(\sin(\beta_i(t))\dot{\gamma}_i(t)+i\dot{\beta}_i(t)\right)}{\sqrt{2}} \\ 0 & \frac{e^{-i\alpha_i(t)}\left(\sin(\beta_i(t))\dot{\gamma}_i(t)-i\dot{\beta}_i(t)\right)}{\sqrt{2}} & \dot{\alpha}_i(t) + \cos(\beta_i(t))\dot{\gamma}_i(t) \end{pmatrix}. \tag{7.21}$$

In the adiabatic limit, where the differences in the diagonal elements of H_0 are large compared to the off-diagonal elements of G_i which couple the corresponding states, we can disregard those off-diagonal elements of G_i. In our case we can disregard all off-diagonal elements of G_i provided that $\mu_{\mathrm{B}}\mathcal{B} \gg \hbar\{\dot{\alpha}_i(t), \dot{\beta}_i(t), \dot{\gamma}_i(t)\}$ for all t. This condition is satisfied for almost all trajectories in the trap[3] and so $G_i(t)$ can be reduced to

$$G_i(t) = \hbar\begin{pmatrix} -\dot{\alpha}_i(t) - \cos(\beta_i(t))\dot{\gamma}_i(t) & 0 & 0 \\ 0 & 0 & 0 \\ 0 & 0 & \dot{\alpha}_i(t) + \cos(\beta_i(t))\dot{\gamma}_i(t) \end{pmatrix}. \tag{7.22}$$

Thus the time dependent evolution of the system in the rotating frame—described by Eq. (7.19)—is identical to that in the static field, but with an additional contribution that has the form of a fictitious magnetic field oriented along the real one. By following the same procedure for higher values of angular momentum, we find that in general a molecule in a state with total angular momentum projection m_F will accumulate an additional phase,

$$-\,m_F\int_o^\tau \dot{\alpha}_i(t) + \cos(\beta_i(t))\dot{\gamma}_i(t)\mathrm{d}t. \tag{7.23}$$

The total additional phase accumulated will be the sum of the contributions from the rotation of the microwave field, given by Eq. (7.16), and this fictitious magnetic field that comes from the non-inertial

[3]The trajectories which do not satisfy the condition are those passing very close to the centre of the trap where $\mathcal{B}$ is very small. These trajectories make a up a vanishingly small proportion for our initial cloud size and so can be ignored.

reference frame. Our states have $m_F = 3$ and $m_F = 2$ so we have

$$\begin{aligned}\phi_i^{\mathrm{g}} &= \alpha_i(\tau) - \alpha_i(0) + \arctan\left(\frac{\sin\gamma_i(\tau)}{\cos\beta_i(\tau)\cos\gamma_i(\tau)}\right) - \arctan\left(\frac{\sin\gamma_i(0)}{\cos\beta_i(0)\cos\gamma_i(0)}\right) \\ &\quad - (3-2)\int_0^\tau \dot{\alpha}_i(t) + \cos(\beta_i(t))\dot{\gamma}_i(t)\mathrm{d}t \\ &= \arctan\left(\frac{\sin\gamma_i(\tau)}{\cos\beta_i(\tau)\cos\gamma_i(\tau)}\right) - \arctan\left(\frac{\sin\gamma_i(0)}{\cos\beta_i(0)\cos\gamma_i(0)}\right) - \int_0^\tau \cos(\beta_i(t))\dot{\gamma}_i(t)\mathrm{d}t.\end{aligned} \tag{7.24}$$

Note that the choice of gauge changes the relative contributions of the two components—indeed either can be made zero with a particular gauge choice—but not the overall result[4]. The first two terms in the final expression for ϕ_i^{g} depend only on the orientation of the field at the two $\pi/2$ pulses but the third term depends on the path taken between the two pulses; it is a type of geometric or Berry's phase. For a molecule whose local field traces out a closed loop during the free evolution time—i.e. the field orientation is the same at the beginning and end of the free evolution time—the phase ϕ_i^{g} is given by the third term only and is equal to the solid angle subtended by the loop.[5].

The simulated effects of this final mechanism are shown in Fig. 7.6(c). The change in Rabi frequency means the $\pi/2$ pulses are imperfect so that the sinusoidal oscillations are centred at a value below 0.5. The spread of ϕ_i^{g} across the ensemble of molecules causes the largest contribution to the dephasing of the three mechanisms. The extracted $1/e$ decoherence rate is $100\,\mathrm{s}^{-1}$. Its size could be greatly reduced by using a magnetic trap geometry with a large bias field [171] to ensure that there is little variation of the magnetic field direction in the region where the molecules are confined.

7.4.2.4 Full model

The result of the full simulation, with all mechanisms included is shown by the red line in Fig. 7.7. The blue line shows a fit of the simulated data to a sinusoid with exponentially decaying amplitude—the same model used to fit the experimental data in Fig. 7.5. The fit is reasonably good and gives a coherence time of 6.1 ms, in good agreement with our experimental data.

7.4.3 Decoherence in free space

To identify any decoherence mechanisms unrelated to the trap, we repeated the decoherence measurement in free space, as shown in Fig. 7.8(a). The data fit well to a model where the only source of decoherence is the expansion of the cloud along the k vector of the microwaves (the mechanism discussed in Sec. 7.4.2.2). In free space, the velocity of each molecule along the k vector is constant so the phase accumulated changes linearly with time. Consequently, this decoherence can be reversed by employing a spin-echo sequence in which a π pulse is applied mid-way between the two $\pi/2$ pulses. Figure 7.8(b) shows Ramsey fringes in free space with a π pulse applied 14.7 ms after the first $\pi/2$ pulse. Molecules

[4] At first glance, the cancellation seems somewhat strange; the part that depends on the rotation of the molecule is proportional to Δm_F, whilst the electric field part does not. What would happen if the states had the same m_F? Or were separated by $\Delta m_F = 2$? It turns out that the electric field operator operator relevant for our dipole-allowed transition has rank 1 and the k-th component picks up a phase proportional to k after rotation (so for a linearly polarised field appropriate to drive $\Delta m_F = 0$ transitions, no phase is accumulated). The operator relevant for an electric quadrupole transition will have rank 2 but its k-th component still acquires a phase proportional to k and so the cancellation is always complete.

[5] It is actually the solid angle subtended by the loop minus 2π but the 2π is, of course, physically meaningless.

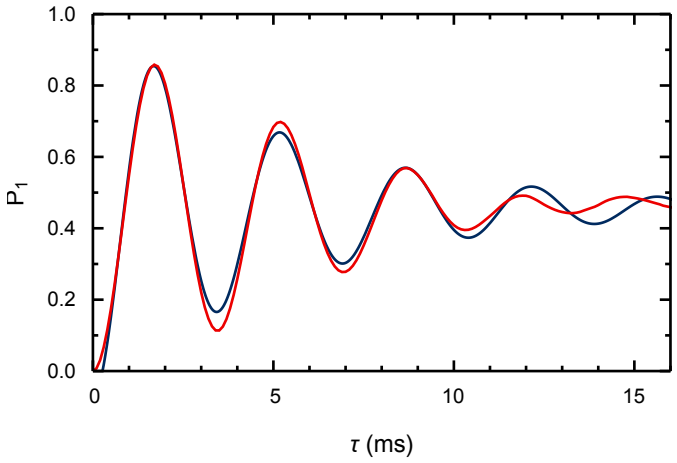

Figure 7.7: Simulation of Ramsey fringes in trap including all decoherence mechanisms. Red line is simulation results and blue line is a fit to an exponentially decaying sinusoid.

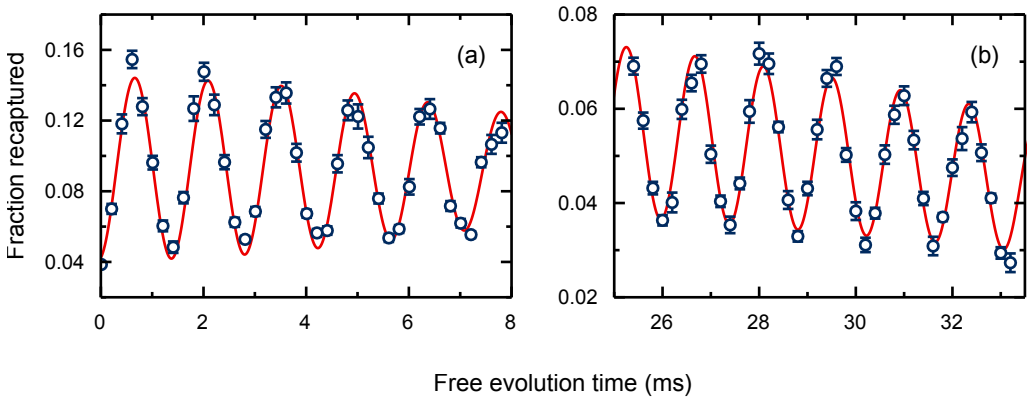

Figure 7.8: (a) Ramsey fringes for molecules in free space. Line shows fit to $A + Be^{-\alpha^2 t^2}\cos(\Delta t + \phi)$, with $1/\alpha = (\lambda/2\pi)\sqrt{m/2k_bT} = 11.4(6)$ ms, corresponding to $T = 37(4)$ µK. (b) As (a) but with a spin echo applied: an extra π pulse is applied, 14.7 ms after the first $\pi/2$ pulse. The x axis shows total free-evolution time between first and second $\pi/2$ pulses. Line shows fit to $(1 - Ct^2)(A + Be^{-\alpha t}\cos(\Delta t + \phi))$. The loss of fringe contrast is consistent with $\alpha = 0$. Points and error bars throughout show mean and standard error of 19 repeated experiments.

at different positions experience different microwave powers, so a π or $\pi/2$ pulse cannot be perfect for all molecules. The extra π pulse for the spin-echo technique thus causes an overall reduction in contrast. The signal also falls as the molecules expand and drop out of the detection region. However, we see no decoherence at all on this timescale and our data restrict the magnitude of any effect to less than 20 s^{-1} at the 95% confidence level.

7.5 Vibrational state dependence

The exceptionally small magnetic sensitivity of the transition $|1\rangle_{\rm str} \leftrightarrow |2\rangle_{\rm str}$ raises the question of whether the sensitivity might be even smaller in an excited vibrational state, $v > 0$. To consider this, we expand the calculated g_l and $g_{\rm r}$ for CaF as a Taylor series in the bond length R around the equilibrium value $R_{\rm e}$. For a harmonic oscillator, only even-order terms in this expansion contribute to expectation values. For a slightly anharmonic oscillator such as most chemically bound molecules, both the linear and quadratic terms contribute significantly to the dependence on v. Jeremy Hutson and Jesús Aldegunde calculated g_l and $g_{\rm r}$ at two additional bond lengths, close to the inner and outer turning points for the $v = 1$ state of CaF, to evaluate the coefficients linear and quadratic in $(R - R_{\rm e})$. Combining these with the expectation values of $(R - R_{\rm e})$ and $(R - R_{\rm e})^2$ for CaF yields

$$\begin{aligned} g_l(v) &= -1.86 \times 10^{-3} \left[1 + 6.20 \times 10^{-3} \left(v + \tfrac{1}{2}\right) + \ldots\right]; \\ g_{\rm r}(v) &= -5.13 \times 10^{-5} \left[1 - 5.77 \times 10^{-3} \left(v + \tfrac{1}{2}\right) + \ldots\right]; \\ g_l(v)/g_{\rm r}(v) &= 36.16 \left[1 + 0.0120 \left(v + \tfrac{1}{2}\right) + \ldots\right]. \end{aligned} \tag{7.25}$$

This indicates that the dependence on v is small, and that the magnetic sensitivity is lowest for $v = 0$. Nevertheless, the magnitude of the effect suggests that vibrational state dependence may be useful for fine-tuning magnetic sensitivity in other molecules.

7.6 Conclusions

In this chapter, we have shown that many laser-coolable molecules have pairs of states belonging to neighbouring rotational manifolds whose magnetic moments are large and identical to a few parts per million. In CaF, the transition between the stretched states of $N = 1$ and $N = 2$ has a magnetic sensitivity of only $-4.7(2)\,\mathrm{Hz\,G^{-1}}$ and we have demonstrated a coherence time of 6.4(8) ms for a magnetically trapped sample in a superposition of these states. Our analysis of the principal sources of decoherence suggests that using a biased magnetic trap and reducing the cloud size will yield considerable improvements, with the prospect of coherence times greater than 1 s for small clouds at 5 µK or below. These results open up potential new platforms for quantum simulation and computation with polar molecules in magnetic micro-traps [179] and provide a route to the regime of strong coupling between solid-state systems and molecules held in magnetic chip traps [180]. These magnetically insensitive transitions may also be valuable in precision measurement (see for example [184]) where sensitivity to magnetic fields is an important source of systematic error.

Chapter 8

Sideband cooling of molecules

8.1 Introduction

As discussed in Chapter 1, arrays of molecules interacting via the dipole-dipole interaction have been proposed as a platform to study many-body quantum physics [63, 185–187] or to implement two-qubit quantum gates [188]. Small arrays can be made using tweezer traps, and larger arrays using optical lattices. Molecules produced by association of ultracold atoms have been loaded into lattices at high enough filling factors to begin studying many-body effects [189]. Molecules have also been formed by associating pairs of atoms in tweezer traps [190].

From the perspective of a laser-cooled molecule experiment, tweezer arrays have the important advantage that the array can be rearranged to remove any defects created by imperfect filling [191]. This removes the requirement for extremely high initial phase-space densities. Very recently, laser-cooled molecules were captured in tweezer traps for the first time at Harvard [192]. At Imperial we are currently building an experiment to do the same. To fully exploit the potential of these low-entropy arrays it is necessary to initialise each molecule in a single quantum state. An important current challenge is how to cool these molecules to the ground state of motion in tweezer traps or lattices. This is frequently done for alkali atoms using Raman sideband cooling [193, 194], and these methods are now being extended to alkaline-earth atoms [195, 196]. Application of the same techniques to molecules is difficult because (i) the complex structure of the molecule tends to complicate all laser cooling methods and (ii) molecules have large tensor Stark shifts, resulting in state-dependent trapping potentials that, in most circumstances, make sideband cooling impossible.

Raman sideband cooling consists of a repeated two-step process illustrated in Fig. 8.1. The first step drives a stimulated two-photon transition between a pair of internal states, reducing the motional quantum number n. In order to selectively drive the red sideband of the transition, the linewidth must be narrow compared to the energy spacing of the motional levels of the trapped atom; typical trap frequencies are of order 100 kHz. The second step provides the dissipation necessary for cooling by optically pumping the atom back to its original internal state.

There are two key requirements for effective cooling. Both are challenging for molecules. First, in order to cool from a thermal state, the frequency required to drive the stimulated transition must be independent of the motional state of the molecule. In alkali atoms—which typically have very small

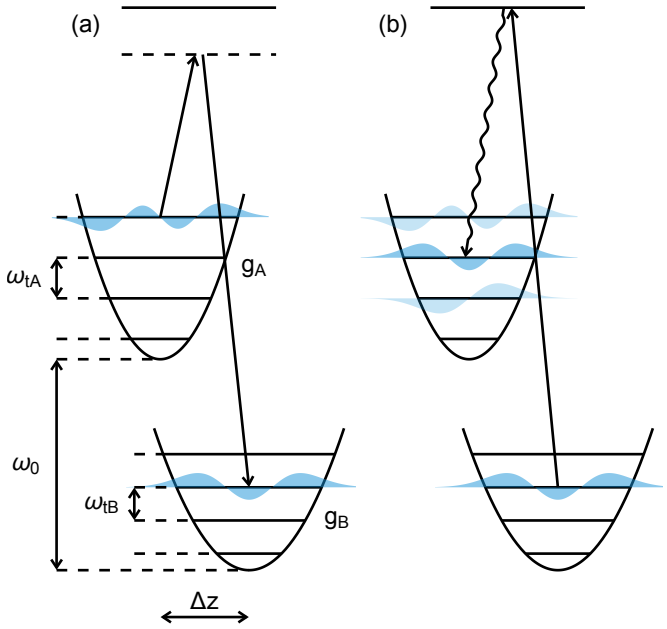

Figure 8.1: Schematic of the two steps of Raman sideband cooling. (a) Step 1: two-photon Raman transition with detuning set to change internal state from g_A to g_B whilst removing one quantum of motional energy. This step is forbidden when the molecule reaches the motional ground state. (b) Step 2: optical pumping via an electronic excited state returns the molecule to its original internal state. For cooling to work efficiently, the optical pumping should preserve the motional quantum number.

tensor Stark shifts[1] [197]—it is straightforward to find pairs of internal states for which the trapping potentials are nearly identical. Provided the potential is sufficiently harmonic, the transition frequency is then independent of the initial motional state. Because molecules have large tensor Stark shifts, the trap frequency depends strongly on internal state, so the two-photon transition frequency depends on the motional state.

The second requirement is that the optical pumping step must have a high probability of preserving the motional quantum number. When the potentials are identical, different motional states of the two potentials are orthogonal and the probability of changing n depends only on the Lamb-Dicke parameter, the square root of the ratio of the photon recoil energy to the level spacing of the traps. Provided this parameter is small, transitions that change the motional quantum number are strongly suppressed. However, for state-dependent potentials, the different motional states of the two traps are no longer orthogonal and the heating involved in scattering a photon has additional contributions associated with projection of the molecule from one potential to the other. Moreover, the additional complexity of a molecule compared to an atom means that optical pumping to a desired state often requires more photons to be scattered, each contributing to the heating.

A potential advantage of state-dependent potentials is that they could enable projection cooling schemes [198, 199]. For example, one could drive a rotational transition resonant only with molecules in the motional ground state followed by state-dependent detection to determine whether or not the molecule has made the transition. If it has, the molecule has been projected into the motional ground

[1] It is sometimes stated that the tensor Stark shift is zero for ground-state alkali atoms. This is only true in the absence of hyperfine structure.

state, if it has not we can reapply cooling light to scramble the motional state and try again. Whilst such schemes may be useful for a single molecule, they scale poorly and so are not suitable for arrays. An active cooling method is required.

This chapter is organised as follows. In Sec. 8.2 we outline the theory of sideband cooling in state-dependent harmonic potentials and establish a quantitative set of criteria for efficient cooling to take place. In Sec. 8.3 we outline the effective Stark shift operator for the interaction of molecules with the trapping light. The results are applied in Sec. 8.4 to determine the energy levels of a simplified molecule in an idealised tweezer trap and consider how they can be engineered to meet the requirements for sideband cooling. In Sec. 8.5 we consider complications that arise when we include the complex structure of real molecules — we use CaF as a case study, since it has already been loaded into a tweezer trap [192]. In Sec. 8.6 we discuss potential complications arising from the light field produced by a real tweezer trap. Finally, in Sec. 8.7, we propose a complete recipe for Raman sideband cooling of laser-cooled molecules. The coordinate system and set of angles that we use throughout the chapter are illustrated in Fig. 8.2.

8.2 Theory of sideband cooling in state-dependent potentials

In this section, we develop the general theory of sideband cooling in state-dependent potentials in order to derive expressions for the frequency and amplitude of the transitions, and the heating arising from the optical pumping step. The Hamiltonian H_0 describing a molecule with a pair of ground states $|g_A\rangle$ and $|g_B\rangle$ in a state-dependent harmonic trap is

$$\begin{aligned} H_{\text{2-level}} =& H_{\text{t}A} |g_A\rangle \langle g_A| + H_{\text{t}B} |g_B\rangle \langle g_B| \\ &+ \frac{\hbar\omega_0}{2}(|g_A\rangle \langle g_A| - |g_B\rangle \langle g_B|). \end{aligned} \tag{8.1}$$

Here $H_{\text{t}i}$ is the harmonic oscillator Hamiltonian associated with the external motion of a molecule in internal state $|g_i\rangle$, $i \in \{A, B\}$. The trap frequencies are $\omega_{\text{t}i}$ and the motional eigenstates are $|q\rangle_i$ such that $H_{\text{t}i}|q\rangle_i = \hbar\omega_{\text{t}i}(q + 1/2)|q\rangle_i$. $\hbar\omega_0$ is the energy difference between the minima of the two trapping potentials, shown in Fig. 8.1.

8.2.1 Raman step

In the first step of Raman sideband cooling, shown in Fig. 8.1(a), the two photon detuning required to coherently transfer the molecule from $|g_A\rangle |n\rangle_A$ to $|g_B\rangle |n-1\rangle_B$ is

$$\begin{aligned} \Delta_{\text{coh}} &= \omega_0 + (n + \frac{1}{2})\omega_{\text{t}A} - (n - 1 + \frac{1}{2})\omega_{\text{t}B}, \\ &= \omega_0 + n(\omega_{\text{t}A} - \omega_{\text{t}B}) + \frac{1}{2}(\omega_{\text{t}A} + \omega_{\text{t}B}), \end{aligned} \tag{8.2}$$

where we have assumed that the energy of $|g_A\rangle$ is above that of $|g_B\rangle$. We see that when the trap frequencies are different for the two internal states, Δ_{coh} depends on the motional quantum number n.

The matrix element for a transition between the two internal states via interaction with a light field is proportional to ${}_B\langle m|e^{i\Delta kz}|n\rangle_A$ where $\hbar\Delta k$ is the momentum kick imparted to the molecule from

absorption of the photon. For two-photon transitions, $\hbar\Delta k$ is the difference in momenta between the absorbed and emitted photons. We can re-express Δkz as

$$\begin{aligned}\Delta kz &= \Delta k\sqrt{\frac{\hbar}{2M\omega_{\mathrm{t}A}}}(a_A^\dagger + a_A),\\ &= \eta_A(a_A^\dagger + a_A),\end{aligned} \tag{8.3}$$

where $a_i^\dagger$, a_i are the harmonic oscillator raising and lowering operators associated with $H_{\mathrm{t}i}$ and M is the mass of the molecule. We have also introduced the Lamb-Dicke parameter $\eta_i = \sqrt{E_{\mathrm{rec}}/\hbar\omega_{\mathrm{t}i}}$, the square root of the ratio of the recoil energy along the trap axis $E_{\mathrm{rec}} = \hbar^2\Delta k^2/2M$, to the energy spacing of the motional states of the trap. When this ratio is small, commonly referred to as the Lamb-Dicke regime, we can expand the matrix element in powers of η_A,

$$\begin{aligned}{}_B\langle m|e^{i\Delta kz}|n\rangle_A &= \sum_{\ell=0}^{\infty}\frac{(i\eta_A)^\ell}{\ell!}\,{}_B\langle m|(a_A^\dagger + a_A)^\ell|n\rangle_A\\ &\simeq {}_B\langle m|n\rangle_A + i\eta_A(\sqrt{n}\,{}_B\langle m|n-1\rangle_A\\ &\quad + \sqrt{n+1}\,{}_B\langle m|n+1\rangle_A) + \mathcal{O}(\eta_A^2).\end{aligned} \tag{8.4}$$

When the potentials associated with the two states are identical we have ${}_B\langle m|n\rangle_A = \delta_{m,n}$ and the transition strength, $\left|{}_B\langle m|e^{i\Delta kz}|n\rangle_A\right|^2$, is proportional to $\eta_A^{2|m-n|}$. Under these conditions, transitions that change the motional quantum number are strongly suppressed. By using a two-photon Raman transition as shown in Fig. 8.1(a), Δk, and therefore η_i, can be varied by changing the relative directions of the two photons. Counter-propagating optical photons give sufficiently large Δk to allow higher order sidebands to be addressed. In general the two harmonic oscillator potentials will have different trap frequencies and different equilibrium positions; an explicit expression for the overlap integral in this case can be found in [200].

8.2.2 Optical pumping step

We now turn to the optical pumping step of the cooling cycle, which involves spontaneous emission. Consider the photon scattering event illustrated in Fig. 8.1(b). A particle in $|g_B\rangle|n\rangle_B$ absorbs a photon from the laser and then decays to $|g_A\rangle$ as it spontaneously emits a photon. The angles of the incoming and outgoing photons relative to the trap axis are labelled θ_{abs} and θ_{sp}, and are as shown in the inset of Fig. 8.2. The probability of ending up in state $|m\rangle_A$ is $\left|{}_A\langle m|e^{i\Delta kz}|n\rangle_B\right|^2$ where Δk depends implicitly on θ_{abs} and θ_{sp}.[2] For given directions of the incoming and outgoing photons, the mean change in motional quantum number is $\sum_m(m-n)\left|{}_A\langle m|e^{i\Delta kz}|n\rangle_B\right|^2$. Averaging over all possible directions of spontaneous emission gives

$$\begin{aligned}\overline{\Delta n_{B,A}^{\mathrm{sc}}} &= \frac{1}{2}\int_0^\pi \mathrm{d}\theta_{\mathrm{sp}}\mathcal{Y}(\theta_{\mathrm{sp}})\sin\theta_{\mathrm{sp}}\sum_m(m-n)\left|{}_A\langle m|e^{i\Delta kz}|n\rangle_B\right|^2\\ &= \frac{1}{2}\int_0^\pi \mathrm{d}\theta_{\mathrm{sp}}\mathcal{Y}(\theta_{\mathrm{sp}})\sin\theta_{\mathrm{sp}}\sum_m {}_A\langle m|\frac{1}{\hbar\omega_{\mathrm{t}A}}H_{\mathrm{t}A}e^{i\Delta kz} - \frac{1}{\hbar\omega_{\mathrm{t}B}}e^{i\Delta kz}H_{\mathrm{t}B}|n\rangle_B\,{}_B\langle n|e^{-i\Delta kz}|m\rangle_A,\end{aligned} \tag{8.5}$$

[2] The operator $e^{i\Delta kz}$ is unitary and so $\left|{}_A\langle m|e^{i\Delta kz}|n\rangle_B\right|^2$ gives a normalised probability: $\sum_m\left|{}_A\langle m|e^{i\Delta kz}|n\rangle_B\right|^2 = 1$.

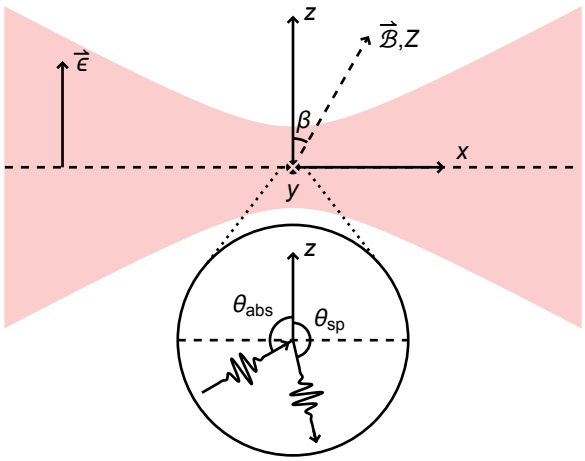

Figure 8.2: Schematic of the coordinate system used in this chapter. The tweezer light propagates along x and is (except where otherwise specified) linearly polarised along z. The y axis is into the page. The quantization axis of the molecule Z, taken along the $\mathcal{B}$ field in Sec. 8.5 onwards, makes an angle β to the z axis. Inset: For the optical pumping step we consider the angles $\theta_{\rm abs}$ and $\theta_{\rm sp}$ that the incoming and outgoing photons make with one of the three trap axes, chosen to be z in our illustration.

where $\mathcal{Y}(\theta_{\rm sp})$ is the probability density for the photon to be emitted at angle $\theta_{\rm sp}$ to the trap axis.[3] Using the completeness relation with respect to the set of $|m\rangle_A$ we have

$$\begin{aligned}\overline{\Delta n^{\rm sc}_{B,A}} &= \frac{1}{2}\int_0^\pi \mathrm{d}\theta_{\rm sp}\mathcal{Y}(\theta_{\rm sp})\, {}_B\langle n|\frac{1}{\hbar\omega_{{\rm t}A}}e^{-i\Delta kz}H_{{\rm t}A}e^{i\Delta kz} - \frac{1}{\hbar\omega_{{\rm t}B}}H_{{\rm t}B}|n\rangle_B \\ &= \frac{1}{2}\int_0^\pi \mathrm{d}\theta_{\rm sp}\mathcal{Y}(\theta_{\rm sp})\left[\frac{1}{\hbar\omega_{{\rm t}A}}\,{}_B\langle n|e^{-i\Delta kz}H_{{\rm t}A}e^{i\Delta kz}|n\rangle_B - (n+\frac{1}{2})\right].\end{aligned} \tag{8.6}$$

The remaining matrix element can be expanded as

$$\begin{aligned}&{}_B\langle n|e^{-i\Delta kz}H_{{\rm t}A}e^{i\Delta kz}|n\rangle_B \\ &= {}_B\langle n|\frac{(p+\hbar\Delta k)^2}{2M} + \frac{1}{2}M\omega_{{\rm t}A}^2(z-\Delta z)^2|n\rangle_B \\ &= \frac{\hbar\omega_{{\rm t}B}}{2}(n+\frac{1}{2}) + E_{\rm rec} + \frac{\hbar\omega_{{\rm t}A}^2}{2\omega_{{\rm t}B}}(n+\frac{1}{2}) + \frac{1}{2}M\omega_{{\rm t}A}^2\Delta z^2,\end{aligned} \tag{8.7}$$

where Δz is the displacement between the minima of the two potentials. In the first step we have used $e^{-i\Delta kz}pe^{i\Delta kz} = p + \hbar\Delta k$ and in the last step ${}_B\langle n|p^2|n\rangle_B = \hbar M\omega_{{\rm t}B}(n+1/2)$, ${}_B\langle n|z^2|n\rangle_B = (\hbar/M\omega_{{\rm t}B})(n+1/2)$ and ${}_B\langle n|p|n\rangle_B = {}_B\langle n|z|n\rangle_B = 0$.

The second term in the last line of Eq. (8.7), the recoil energy associated with the process, is the only part which depends on the directions of the absorbed and emitted photons. We define the average

[3] If $\mathcal{G}(\theta)$ is the angular distribution of photon emission relative to the quantization axis, then $\mathcal{Y}(\theta_{\rm sp}) = \int_0^{2\pi}\mathrm{d}\phi_{\rm sp}\left|\frac{\partial(\theta,\phi)}{\partial(\theta_{\rm sp},\phi_{\rm sp})}\right|\mathcal{G}(\theta(\theta_{\rm sp},\phi_{\rm sp}))$, with $\left|\frac{\partial(\theta,\phi)}{\partial(\theta_{\rm sp},\phi_{\rm sp})}\right|$ the Jacobian determinant for the coordinate transformation which rotates the quantisation axis on to the trap axis.

of this recoil energy over spontaneous emission directions,

$$\begin{aligned}\overline{E}_{\mathrm{rec}} =& \frac{1}{2}\frac{\hbar^2k^2}{2M}\int_0^{\pi}(\cos\theta_{\mathrm{abs}}-\cos\theta_{\mathrm{sp}})^2\,\mathcal{Y}(\theta_{\mathrm{sp}})\sin\theta_{\mathrm{sp}}\mathrm{d}\theta_{\mathrm{sp}}\\ =& \frac{\hbar^2k^2}{2M}(\cos^2\theta_{\mathrm{abs}}+\Upsilon),\end{aligned} \tag{8.8}$$

where $\hbar k$ is the single photon momentum, and

$$\Upsilon = \frac{1}{2}\int_0^{\pi}\cos^2\theta_{\mathrm{sp}}\mathcal{Y}(\theta_{\mathrm{sp}})\sin\theta_{\mathrm{sp}}\mathrm{d}\theta_{\mathrm{sp}} \tag{8.9}$$

is a geometric factor that depends only on the polarisation of the outgoing photon and the angle between the trap and quantisation axes. Its value lies in the range $1/5 \leq \Upsilon \leq 2/5$. In the second step of Eq. (8.8), we have used the fact that $\mathcal{Y}(\theta_{\mathrm{sp}})$ is symmetric about $\theta_{\mathrm{sp}} = \pi/2$ so that the integral over the term linear in $\cos\theta_{\mathrm{sp}}$ is zero. Finally we can write

$$\overline{\Delta n^{\mathrm{sc}}_{B,A}} = \Theta_{\mathrm{rec}} + \Theta_{\mathrm{disp}} + \Theta_{\mathrm{curv}}, \tag{8.10}$$

where

$$\Theta_{\mathrm{rec}} = \frac{\overline{E}_{\mathrm{rec}}}{\hbar\omega_{\mathrm{t}A}}, \tag{8.11a}$$

$$\Theta_{\mathrm{disp}} = \frac{1}{2}M\omega_{\mathrm{t}A}^2\Delta z^2/(\hbar\omega_{\mathrm{t}A}), \tag{8.11b}$$

$$\Theta_{\mathrm{curv}} = \frac{1}{2}\left(\frac{\omega_{\mathrm{t}A}}{\omega_{\mathrm{t}B}}+\frac{\omega_{\mathrm{t}B}}{\omega_{\mathrm{t}A}}-2\right)(n+\frac{1}{2}). \tag{8.11c}$$

The heating induced by the photon recoil, Θ_{rec}, is independent of n and equivalent to the heating in free space or in state-independent potentials. The expression for $\overline{E}_{\mathrm{rec}}$ in Eq. (8.8) shows that this contribution to the heating can be split into a part due to the momentum of the absorbed photon and a part due to that of the spontaneously emitted photon. The distribution of the former among the three trap axes can be controlled by choosing the direction of the optical pumping beam. We note that the sum of $\overline{E}_{\mathrm{rec}}$ evaluated for any three perpendicular axes is $2\frac{\hbar^2k^2}{2M}$. The second contribution, Θ_{disp}, is the additional heating associated with the displacement between the two potentials. The quantity $\hbar\omega_{\mathrm{t}A}\Theta_{\mathrm{disp}}$ is the gain in potential energy from moving the wavepacket a distance Δz up the side of the trap. Finally, Θ_{curv} is the heating resulting from the difference in curvature of the two trap potentials. This part depends linearly on n and is independent of the direction of the transition, $|g_A\rangle \leftrightarrow |g_B\rangle$.

In general several photons will be scattered in the optical pumping step. Each scattering event begins with the molecule in some state i and ends in some state j with the associated mean change in motional quantum number $\overline{\Delta n^{\mathrm{sc}}_{i,j}}$. We define the mean change in n for the complete process of optical pumping to the desired (dark) state, $\overline{\Delta n^{\mathrm{op}}}$, which is the sum of $\overline{\Delta n^{\mathrm{sc}}_{i,j}}$ for each step of the process. We will calculate $\overline{\Delta n^{\mathrm{op}}}$ for a realistic case in Sec. 8.4. For efficient cooling, the number of motional quanta removed during the coherent step Δn_{coh}, must be greater than $\overline{\Delta n^{\mathrm{op}}}$, remembering that the heating during optical pumping occurs for each axis regardless of which is being cooled during the coherent step. Whilst it is possible to use higher-order sidebands during the coherent step to satisfy this condition,

cooling to the motional ground state requires $\Delta n_{\mathrm{coh}} = 1$ since driving higher-order sidebands leaves population in other motional states.

8.3 Stark shift

To derive the potential for a molecule in a tweezer trap or an optical lattice, we need to understand its response to the trapping light. The interaction of a molecule with light is described by a term in the Hamiltonian $-\vec{d}\cdot\vec{E}$, where $\vec{d}$ is the dipole moment operator and $\vec{E} = \frac{1}{2}\mathcal{E}_0(\hat{\epsilon}e^{-i\omega_{\mathrm{L}}t} + \hat{\epsilon}^* e^{i\omega_{\mathrm{L}}t})$ is the electric field of the light. Here, $\mathcal{E}_0$ is the electric field amplitude, ω_{L} is the angular frequency of the light, and $\hat{\epsilon}$ is a unit polarisation vector. We divide the complete Hamiltonian into a zeroth-order part, H_0, that describes the energy level structure of the molecule down to the rotational structure, and a part H_1 that describes level shifts smaller than the rotational splitting. H_1 includes the spin-rotation interaction, the hyperfine interaction, and the Zeeman and Stark interactions. We are interested in the small degenerate subspace of H_0 corresponding to a single rotational state. The effective Stark Hamiltonian that operates within this subspace is developed in Appendix A. It is

$$H_{\mathrm{S}} = -\frac{\mathcal{E}_0^2}{4}\sum_{K=0}^{2}\sum_{P=-K}^{K}(-1)^P \mathcal{A}_P^K \mathcal{P}_{-P}^K. \tag{8.12}$$

Each of the three terms in the sum over K in Eq. (8.12) is the scalar product of two rank-K spherical tensors. The first, $\mathcal{A}^K$, is an operator related to the frequency-dependent polarisability of the molecule, and is given in terms of $\vec{d}$ and ω_{L} by Eq. (A.10). The second, $\mathcal{P}^K$, relates to the polarisation of the light, and is given in terms of $\hat{\epsilon}$ by Eq. (A.11). The matrix elements of $\mathcal{A}_P^K$ for $^1\Sigma$ and $^2\Sigma$ molecules are given in Sections A.2 and A.3 of the Appendix respectively. They are functions of the relevant angular momentum quantum numbers, and are proportional to the three molecular constants, α_K, given by Eq. (A.26). The α_K express the size of the scalar, vector and tensor polarisabilities, and their values depend on the frequency of the light. The scalar part shifts all the levels within the subspace equally. This shift is $W_0 = -\alpha_0\mathcal{E}_0^2/4 = -\alpha_0 I/(2c\epsilon_0)$, where I is the intensity of the light. It is convenient to define $\alpha'_K = \alpha_K/(2c\epsilon_0)$, so that the scalar Stark shift is simply $W_0 = -\alpha'_0 I$.

The vector and tensor polarisabilities produce different shifts for different states, leading to state-dependent trapping potentials. For an angular momentum eigenstate $|j, m_j\rangle$, the expectation value of $\mathcal{A}_0^1$ is proportional to m_j. The effect of this vector part can be large when the detuning of the light from a molecular transition is small, or comparable to, the fine-structure splitting of the transition. At larger detunings, the value of α_1 is proportional to the ratio of the fine-structure interval to the transition energy, as can be seen from Eq. (A.27). This ratio is normally small, so suppresses the vector part. The value of α_1 is also proportional to ω_{L}, so goes to zero when $\omega_{\mathrm{L}} = 0$. When the light is linearly polarised, all components of $\mathcal{P}^1$ are zero, so the vector polarisability contributes nothing to H_{S}. When the light is circularly polarised, the vector part has the same effect as a magnetic field applied along the axis of circular polarisation, so can be suppressed by applying a magnetic field orthogonal to that axis [193, 201]. As shown by Eq. (A.26c), the value of α_2 is proportional to the difference between the polarisabilities parallel and perpendicular to the molecular bond. These are typically very different, leading to a large value for α_2. This tensor part results in trap potentials that depend strongly on the

state of the molecule and on the polarisation of the light. In Sections 8.4 and 8.5, we show how to minimise the problems associated with these state-dependent potentials.

8.4 Simple molecule

We first consider a simple diatomic molecule that has no electronic or nuclear spin. We concentrate on the first rotationally excited state, $N = 1$, within the ground electronic state. Excitation from this state to an electronically excited state with $N = 0$ is rotationally closed, as needed for the optical pumping step of the sideband cooling. In this case, we are interested only in the three m_N states of $N = 1$, where m_N is the projection of the rotational angular momentum onto a laboratory-fixed Z axis. To make the link with the $^2\Sigma$ molecule considered later, we allow the states $m_N = -1, 0, 1$ to be non-degenerate at zero intensity, with energies $-w$, 0 and w respectively.

8.4.1 Linearly polarised light

Our coordinate system is shown in Fig. 8.2. The trapping light propagates along the x axis. We first assume the light is linearly polarised along the z axis, making an angle β to Z. The effective Hamiltonian for this system is

$$H_{\text{simple}} = \begin{pmatrix} -w & 0 & 0 \\ 0 & 0 & 0 \\ 0 & 0 & w \end{pmatrix} - \begin{pmatrix} 1 & 0 & 0 \\ 0 & 1 & 0 \\ 0 & 0 & 1 \end{pmatrix} \alpha_0' I - \begin{pmatrix} -\frac{1+3\cos 2\beta}{20} & \frac{3\sin 2\beta}{10\sqrt{2}} & -\frac{3\sin^2\beta}{10} \\ \frac{3\sin 2\beta}{10\sqrt{2}} & \frac{1+3\cos 2\beta}{10} & -\frac{3\sin 2\beta}{10\sqrt{2}} \\ -\frac{3\sin^2\beta}{10} & -\frac{3\sin 2\beta}{10\sqrt{2}} & -\frac{1+3\cos 2\beta}{20} \end{pmatrix} \alpha_2' I. \tag{8.13}$$

The first matrix gives the energies in the absence of the light, the second is the scalar Stark shift, and the third is the tensor part of the Stark interaction. There is no vector part because our model system has no spin, and because the light is linearly polarised. In terms of the eigenvalues of H_{simple}, which we may write as $E(\alpha_0' I, \alpha_2' I)$, the scalar Stark shift is $E(\alpha_0' I, 0) - E(0, 0)$ and the tensor Stark shift is $E(0, \alpha_2' I) - E(0, 0)$.

We can learn a great deal from this simple Hamiltonian. When $w = 0$ the Stark shifts are independent of β, and when $\beta = 0$ the Stark shifts are independent of w. In both cases, the $m_N = \pm 1$ states have equal Stark shifts of $\delta E_{\pm 1} = -(\alpha_0' - \alpha_2'/5)I$, while the $m_N = 0$ state shifts by $\delta E_0 = -(\alpha_0' + 2\alpha_2'/5)I$. When $\beta = 0$ and α_2'/w is positive (negative), the $m_N = -1(+1)$ and $m_N = 0$ states cross at the intensity where $3/5\alpha_2' I = w$ $(-w)$. This becomes an avoided crossing when $\beta \neq 0$, and the size of the gap at the avoided crossing is $w \sin(2\beta)/\sqrt{2}$. These features can be seen in Fig. 8.3, where we plot the energies of the three states as a function of $\alpha_2' I/w$ for the case where $\beta = \pi/24$, chosen here and later to clearly highlight the presence of the avoided crossings. We have removed the scalar Stark shift, since it shifts all states equally. We note that the Stark shifts cease to be linear in intensity near the avoided

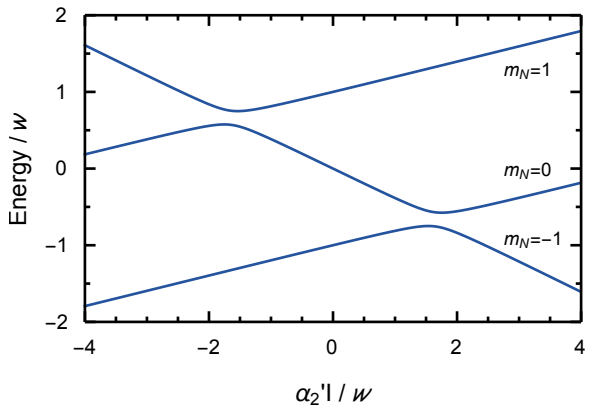

Figure 8.3: Energies (in units of w) of the $N = 1$ states of the model molecule as a function of $\alpha_2' I/w$, in the case where $\beta = \pi/24$. The horizontal axis is proportional to the intensity of the light and to the tensor polarisability of the molecule. The scalar Stark shift, which shifts all states equally, has been subtracted.

crossing, and that this non-linearity may translate into anharmonicity of the trapping potential if the trap intensity is in this range.

Figure 8.4 shows the ratio of the tensor Stark shift to the scalar Stark shift, as a function of the polarisation angle β. We have chosen $\alpha_2' = -0.6\alpha_0'$, and explore various values of w. The dashed lines show the limiting case where $|w/(\alpha_2' I)| \gg 1$. In this case, the eigenvalues of H_{simple} are very nearly equal to its diagonal elements. By inspection of these elements, we see that the $m_N = \pm 1$ states have identical tensor Stark shifts for all values of β, whereas the tensor Stark shift of $m_N = 0$ is twice as large and has the opposite sign. We also see that the tensor Stark shift is zero for all three states at the "magic angle" where $\beta = \beta_{\text{magic}} = \cos^{-1}(1/\sqrt{3})$. The solid lines in Fig. 8.4(a) show the case where $w/(\alpha_2' I) = 4$. The results follow the dashed lines closely, but the $m_N = \pm 1$ no longer have identical Stark shifts when $\beta \neq 0$. This difference increases as w decreases, as can be seen in Fig. 8.4(b) which shows the case of $w/(\alpha_2' I) = 1$. In particular, we note that there is no longer any angle where all three states have the same tensor shift.

8.4.2 Elliptically polarised light

Next we consider the case of elliptically polarised light. The light again propagates along x and Z is aligned with this axis also. The polarisation of the light is described by $\hat{\epsilon} = \cos(\xi)\hat{z} - i\sin(\xi)\hat{y}$. The tensor Stark part of H_{simple} now reads

$$\begin{pmatrix} -\frac{1}{10} & 0 & \frac{3}{10}\cos(2\xi) \\ 0 & \frac{1}{5} & 0 \\ \frac{3}{10}\cos(2\xi) & 0 & -\frac{1}{10} \end{pmatrix} \alpha_2' I. \tag{8.14}$$

When the light is circularly polarised ($\xi = \pm\pi/4$), this matrix is diagonal and the tensor Stark shifts are half the size and of opposite sign relative to the case of light linearly polarised along Z. Figure 8.5 shows the ratio of tensor to scalar Stark shifts as a function of ξ, with $\alpha_2' = -0.6\alpha_0'$. Once again,

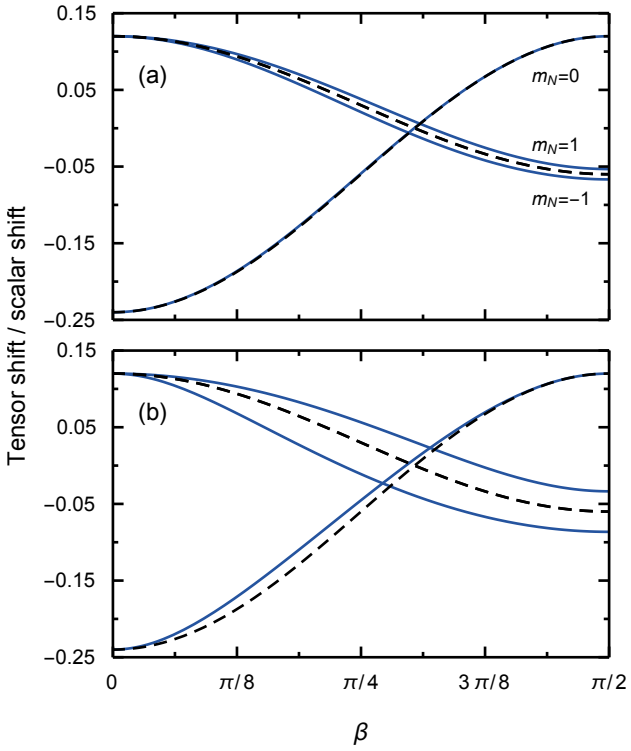

Figure 8.4: Ratio of tensor Stark shift to scalar Stark shift for the $N = 1$ states of the model molecule, as a function of polarisation angle β from the Z axis. In all cases, $\alpha_2' = -0.6\alpha_0'$. Dashed lines show the case where $|w/(\alpha_2' I)| \gg 1$. Solid, coloured lines are for (a) $w = 4\alpha_2' I$, (b) $w = \alpha_2' I$.

the dashed lines show the case where $|w/(\alpha_2' I)| \gg 1$. In this case, the shifts are independent of ξ and the $m_N = \pm 1$ states shift equally. The solid lines show the case where $w/(\alpha_2' I) = 1$. The shift of the $m_N = 0$ state has no dependence on ξ, while the shifts of the $m_N = \pm 1$ states depend on ξ and are different to one another. This difference is largest at $\xi = 0$ (linearly polarised along z), zero at $\xi = \pi/4$ (circularly polarised), and reduces as $|w/(\alpha_2' I)|$ increases.

8.4.3 Sideband cooling of simple molecule

For this simple molecule, sideband cooling could be done with any choice of polarisation where two of the three states have equal tensor shifts. This ensures that the Raman frequency for transitions between these two states is independent of the motional state, as required. Here, we consider the specific case where the Raman step is between the $m_N = -1$ and $m_N = +1$ states. The cooling proceeds as follows: (i) optically pump into $m_N = -1$, (ii) drive the Raman transition from $m_N = -1$ to $m_N = +1$ on a red motional sideband, (iii) repeat. The optical pumping should be on the rotationally closed transition, which excites the molecule to an $N = 0$ state. A pair of laser beams, one linearly polarised along Z and the other circularly polarised about Z achieves the desired optical pumping.

If it is possible to work in a regime where $|w/(\alpha_2' I)| \gg 1$, the polarisation of the tweezer is not important for the Raman step since the trapping potential is always the same for the $m_N = \pm 1$ states. The tweezer polarisation is relevant for the optical pumping step due to spontaneous emission to $m_N = 0$ for which the trapping potential is, in general, different. The extra heating this produces can be eliminated by choosing the polarisation at the magic angle where the trapping potential is identical

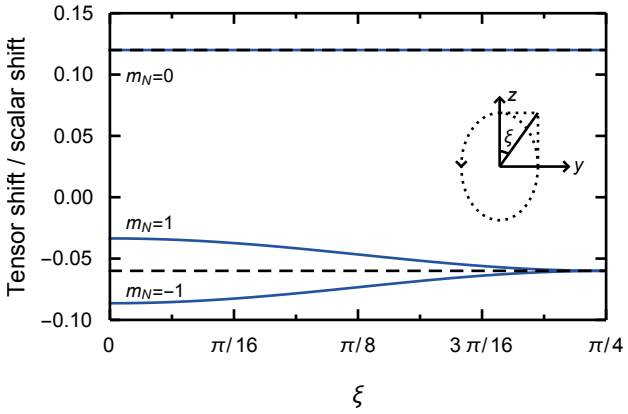

Figure 8.5: Ratio of tensor Stark shift to scalar Stark shift for the $N = 1$ states of the model molecule, as a function of ellipticity parameter ξ, defined in the text and shown schematically in inset. $\xi = 0$ corresponds to linear polarisation, and $\xi = \pi/4$ to circular polarisation. The light propagates along Z and we have chosen $\alpha_2' = -0.6\alpha_0'$. Dashed lines show the case where $|w/(\alpha_2' I)| \gg 1$. Solid, coloured lines are for $w = \alpha_2' I$.

for all three states. If it is not feasible to work in the regime where $|w/(\alpha_2' I)| \gg 1$, the tweezer should be linearly polarised along Z, or circularly polarised relative to Z, so that the trap potential is identical for the $m_N = \pm 1$ states. We emphasise that other configurations are possible using different pairs of states for the Raman step.

8.4.4 Heating during optical pumping

We now evaluate the extra heating that occurs during the optical pumping step when the third state—not used for the Raman transition—has a different ac Stark shift to the other two. We again focus on the case where the Raman step is between the $m_N = -1$ and $m_N = +1$ states and the third state is $m_N = 0$. The $N = 0$ excited state has equal branching ratios to each of the three ground states and so it takes, on average, three scattered photons for the molecule to reach the dark state; two of these leave the molecule in $|m_N| = 1$ and one in $m_N = 0$. The heating that each of these scattered photons produces is given by the three terms in Eq. (8.10). Let us consider each in turn. The recoil heating, Eq. (8.11a), depends on the direction of the absorbed photon and the angular distribution of the emitted photon. In our case, with a single excited state, specifying the initial and final value of $|m_N|$ is sufficient to uniquely define both the beam from which the photon is absorbed and the angular distribution of the emitted photon. By analogy with Eq. (8.8) we define $\overline{E}^{i,j}_{\mathrm{rec}}$, the average recoil energy for a scattering event which takes the molecule from a ground state with $|m_N| = i$ to a ground state with $|m_N| = j$. The circularly polarised beam which couples to $m_N = +1$—from which on average two photons are scattered—is necessarily parallel to the $\mathcal{B}$ field, but the linearly polarised beam which couples to the $m_N = 0$ state—from which on average one photon is scattered—can propagate along any direction perpendicular to that. We can control the heating along a particular trapping axis to some extent by choosing this angle appropriately. It is likely to be helpful to choose it orthogonal to the optical axis of the trapping light where, as we will see in Sec. 8.6, the confinement is weakest.

The contribution from Θ_{disp}, Eq. (8.11b), is zero because the potentials are not displaced with respect to one another. To understand the contribution of Θ_{curv}, given by Eq. (8.11c), we need to know

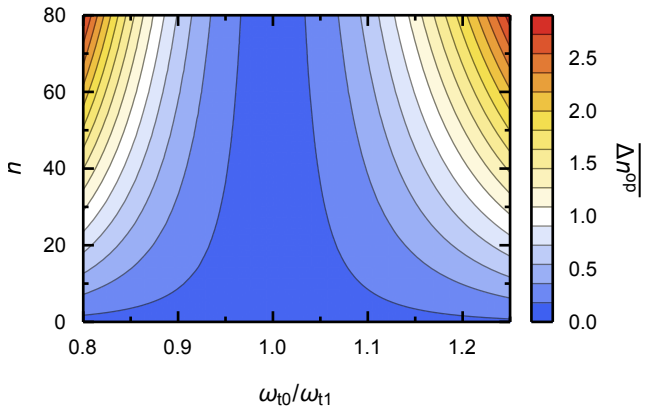

Figure 8.6: Mean change in n during optical pumping $\overline{\Delta n^{\mathrm{op}}}$ as a function of n and $\omega_{\mathrm{t}0}/\omega_{\mathrm{t}1}$ for $\eta_1 = 0.2$. The circularly polarised optical pumping beam is assumed parallel to the trap axis and the linearly polarised beam perpendicular.

how many of the scattering events change $|m_N|$. Let y_{m_N} be the mean number of $|m_N|$-changing events needed to reach the dark state, starting from state m_N. Consider a molecule initially in $m_N = -1$. If it scatters a photon and decays to $m_N = 1$, the dark state is reached with no $|m_N|$-changing events. If it decays to $m_N = 0$, there has been one $|m_N|$-changing event, and there are an average of y_0 more to come. If it decays back to $m_N = -1$, there are an average of y_{-1} events to come. Each outcome has a probability of $1/3$. Thus

$$y_{-1} = \frac{1}{3}y_{-1} + \frac{1}{3}(1 + y_0). \tag{8.15}$$

By a similar argument

$$y_0 = \frac{1}{3}(1 + y_{-1}) + \frac{1}{3}y_0 + \frac{1}{3}. \tag{8.16}$$

Together these equations give $y_{-1} = 4/3$ and $y_0 = 5/3$. Since the molecule begins and ends the optical pumping step in a state with $|m_N| = 1$, half of the $4/3$ events change $|m_N|$ from 1 to 0, and half the reverse.

We can now use Eq. (8.10) to estimate the mean change in motional quantum number during optical pumping, $\overline{\Delta n^{\mathrm{op}}}$. If $\overline{\Delta n^{\mathrm{sc}}_{i,j}} \ll 1$ for all $i, j \in \{-1, 0, 1\}$, so that we can assume a fixed n in Eq. (8.11c), then to a good approximation

$$\begin{aligned}\overline{\Delta n^{\mathrm{op}}} =& \frac{4}{3}\frac{\overline{E}^{1,1}_{\mathrm{rec}}}{\hbar\omega_{\mathrm{t}1}} + \frac{2}{3}\frac{\overline{E}^{1,0}_{\mathrm{rec}}}{\hbar\omega_{\mathrm{t}0}} + \frac{2}{3}\frac{\overline{E}^{0,1}_{\mathrm{rec}}}{\hbar\omega_{\mathrm{t}1}} + \frac{1}{3}\frac{\overline{E}^{0,0}_{\mathrm{rec}}}{\hbar\omega_{\mathrm{t}0}} \\ &+ \frac{2}{3}\left(\frac{\omega_{\mathrm{t}1}}{\omega_{\mathrm{t}0}} + \frac{\omega_{\mathrm{t}0}}{\omega_{\mathrm{t}1}} - 2\right)\left(n + \frac{1}{2}\right).\end{aligned} \tag{8.17}$$

Here, $\omega_{\mathrm{t}i}$ is the trap frequency corresponding to the ground states with $|m_N| = i$. Figure 8.6 shows how $\overline{\Delta n^{\mathrm{op}}}$ varies as a function of both n and the ratio of the trap frequencies, for $\eta_1 = 0.2$, which is a realistic Lamb-Dicke parameter for trap frequencies near 200 kHz. The blue areas of the plot show the parameter space where $\overline{\Delta n^{\mathrm{op}}} < 1$. This corresponds to net cooling along the axis being cooled when the coherent step drives the first-order red sideband. We will see later that $\omega_{\mathrm{t}1}/\omega_{\mathrm{t}0}$ is typically in the range 0.8–1.25. Throughout this range, $\overline{\Delta n^{\mathrm{op}}} < 1$ all the way up to $n \approx 25$.

8.5 Real molecule

Next, we consider a real molecule with a $^2\Sigma$ ground state and a nuclear spin. We will use CaF as an illustrative example, though our discussion will apply to other molecules of this type. For laser cooling, the electronic transition to either the $A^2\Pi_{1/2}$ state or the $B^2\Sigma$ state can be used. For sideband cooling, we choose to use the transition $B^2\Sigma(v=0, N=0) \leftarrow X^2\Sigma(v=0, N=1)$. Here, v and N refer to the vibrational and rotational quantum numbers respectively. With this choice of excited state, decay to any other rotational state of X is forbidden by the parity and angular momentum selection rules, so the transition is rotationally closed. The branching ratio for decays to other vibrational states depends on the choice of molecule. For CaF, it is particularly small, about 10^{-3}, so that for the purpose of sideband cooling we can consider the transition to be vibrationally closed. For other laser-coolable molecules with less favourable branching ratios, vibrational repump lasers can be used.

To understand how to apply sideband cooling, we need to consider the hyperfine interactions in the ground state. For CaF, and similar molecules, the Hamiltonian describing these interactions is

$$H_{\text{hfs}} = \gamma \vec{S}\cdot\vec{N} + \left(b + \frac{c}{3}\right)\vec{I}\cdot\vec{S} + \frac{c}{3}\sqrt{6}T^2(C)\cdot T^2(\vec{I},\vec{S}), \tag{8.18}$$

where $\vec{N}$, $\vec{S}$ and $\vec{I}$ are the dimensionless operators for the rotational angular momentum, electron spin and nuclear spin. The first term is the spin-rotation interaction, while the second and third represent the interaction between the electron and nuclear magnetic moments. Here, $T^2(\vec{I},\vec{S})$ is the rank-2 spherical tensor formed from $\vec{I}$ and $\vec{S}$, while $T^2(C)$ is a spherical tensor whose components are the spherical harmonics $C^2_q(\theta,\phi)$. We have neglected the nuclear-spin-rotation interaction which is much smaller than the other terms.

8.5.1 Reduction to the simplified molecule

The hyperfine interactions couple the angular momenta, and as a result the ac Stark shift is, in general, much more complicated than the simple picture described above. However, that simple picture can be recovered by applying a magnetic field, $\vec{\mathcal{B}}$, that is large enough to uncouple the angular momenta. The Zeeman Hamiltonian for a $^2\Sigma$ state is given in Eq. (2.35) but repeated again here for convenience,

$$\begin{aligned} H_{\text{Z}} = {} & g_S\mu_{\text{B}}\vec{S}\cdot\vec{\mathcal{B}} - g_{\text{N}}\mu_{\text{N}}\vec{I}\cdot\vec{\mathcal{B}} - g_{\text{r}}\mu_{\text{B}}\vec{N}\cdot\vec{\mathcal{B}} \\ & + g_l\mu_{\text{B}}(\vec{S}\cdot\vec{\mathcal{B}} - (\vec{S}\cdot\hat{\lambda})(\vec{\mathcal{B}}\cdot\hat{\lambda})). \end{aligned} \tag{8.19}$$

The first term is due to the unpaired electron spin and is typically 10^3 times larger than the other terms. We will often only need to consider this term. When $\vec{\mathcal{B}}$ is large, so that the Zeeman interaction is much larger than the hyperfine interaction, the eigenstates are well described by uncoupled angular momentum eigenstates, $|N, m_N\rangle|S, m_S\rangle|I, m_I\rangle$. Each rotational state splits into two manifolds with $m_S = \pm 1/2$, whose Zeeman shifts are $\Delta E_{\text{Z}} \approx g_S\mu_{\text{B}}m_S\mathcal{B} \approx \pm\mu_{\text{B}}\mathcal{B}$. Here, we have used $g_S \approx 2$ and have neglected the small terms. The hyperfine interaction lifts the degeneracy with respect to m_N and m_I within each of these manifolds. In the limit where the angular momenta are completely uncoupled, the ac Stark shift has no dependence on m_S and m_I. Furthermore, the values of m_S and m_I cannot

change in either the Raman step or the optical pumping step.[4] Having chosen a particular (m_S, m_I) pair, their values are fixed, so that (for $N = 1$) we are left with only three states, just as in Sec. 8.4.

Taking $N = 1$ and $S = I = 1/2$, the shifts due to $H_{\rm hfs}$ to first-order in perturbation theory are

$$\Delta E_{\rm hfs} \approx \gamma m_N m_S + \left(b + \frac{c}{3}\right) m_S m_I + (-1)^{m_N} \frac{4c}{15} \frac{m_S m_I}{m_N^2 + 1}. \tag{8.20}$$

Relative to $m_N = 0$, the energies of the $m_N = \pm 1$ states are

$$w_\pm = \pm\gamma m_S - \frac{2c}{5} m_I m_S. \tag{8.21}$$

In the limit where $c \ll \gamma$, the splitting is symmetric and the description is identical to that of Sec. 8.4. For CaF, γ and c are almost equal, so the splitting is not quite symmetric, though this makes little difference to the description.

In practice, the magnetic field is limited in strength. This has two important consequences. First, in the optical pumping step, the residual state mixing by $H_{\rm hfs}$ can result in decay to a different manifold of states from the one selected. Second, the ac Stark shifts deviate from the simple behaviour shown in Figs. 8.3, 8.4 and 8.5. Next, we work out the severity of these imperfections to our scheme.

8.5.2 Residual state mixing

Let us write the uncoupled states using the notation $|m_N, m_S, m_I\rangle$. All three terms in $H_{\rm hfs}$ result in mixing of these uncoupled states, and we can calculate the mixing amplitudes by perturbation theory (assuming that $\mu_{\rm B}\mathcal{B} \gg \gamma, b, c$). The spin-rotation interaction, $\gamma \vec{N} \cdot \vec{S}$, has no effect on the upper state of the transition which has $N = 0$, but it does change the lower states since they have $N = 1$. The state $|m_N, \pm 1/2, m_I\rangle$ obtains an admixture of $|m_N \pm 1, \mp 1/2, m_I\rangle$ (where that state exists), with amplitude $\pm\gamma/(2\sqrt{2}\mu_{\rm B}\mathcal{B})$. It follows that the excited state with $m_S = \pm 1/2$ can decay to the ground state with (nominally) $m_S = \mp 1/2$ with a branching ratio of

$$b_{\rm r,1} = \frac{2}{3}\left(\frac{\gamma}{2\sqrt{2}\mu_{\rm B}\mathcal{B}}\right)^2. \tag{8.22}$$

Importantly, this branching ratio is suppressed with increasing $\mathcal{B}$. For CaF at $\mathcal{B} = 300$ G, we find $b_{\rm r,1} = 7.4 \times 10^{-4}$. Similarly, due to the $\vec{I} \cdot \vec{S}$ term of Eq. (8.18), the state $|m_N, \pm 1/2, \mp 1/2\rangle$ obtains an admixture of $|m_N, \mp 1/2, \pm 1/2\rangle$ with an amplitude $(b + c/3)/(4\mu_{\rm B}\mathcal{B})$. This affects both the X and B states. The B state with $m_S = -m_I = \pm 1/2$ can decay to an X state with the opposite values of m_S and m_I with a branching ratio of

$$b_{\rm r,2} = (\epsilon_{\rm X} + \epsilon_{\rm B})^2, \tag{8.23}$$

where

$$\epsilon_{\rm X/B} = \left(\frac{b + c/3}{4\mu_{\rm B}\mathcal{B}}\right)_{\rm X/B}, \tag{8.24}$$

[4] Here, our choice of the $B^2\Sigma$ excited state is important: in strong magnetic field, m_S and m_I are good quantum numbers for both the ground and excited states. This would not be the case for the $A^2\Pi$ excited state because the fine-structure splitting is large compared to any reasonable Zeeman splitting.

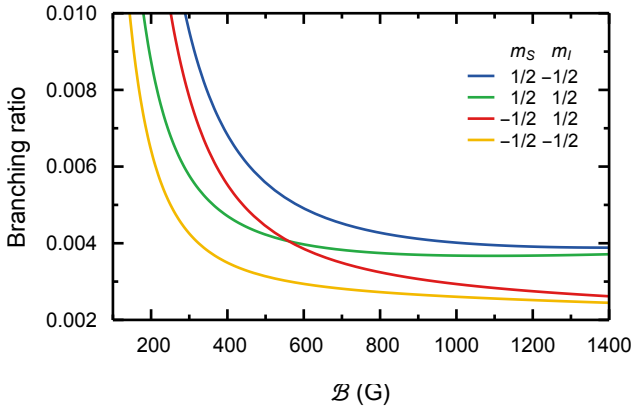

Figure 8.7: Branching ratio as a function of magnetic field for decay from each spin manifold of the $B^2\Sigma^+(N=0)$ states of CaF to a different spin manifold within $X^2\Sigma^+(N=1)$. In order of increasing branching ratio at $\mathcal{B} = 800\,\mathrm{G}$ the states have $(m_S, m_I) = (-1/2,-1/2)$, $(-1/2,1/2)$, $(1/2,1/2)$, $(1/2,-1/2)$. We have set the light intensity to zero.

and the subscript indicates which state the hyperfine coefficients belong to. For CaF at $\mathcal{B} = 300$ G, we find $b_{\mathrm{r},2} = 7.2\times10^{-3}$. This decay route can be eliminated by choosing to use a manifold with $m_S = m_I$.

Next, consider the last term of Eq. (8.18). In the uncoupled basis, it has non-zero matrix elements between all pairs of states with equal $m_F = m_N + m_S + m_I$. This means that as well as coupling states that differ in m_S, it couples states of the same m_S that differ in m_N and m_I. The former couplings are suppressed by the large Zeeman splitting between opposite m_S manifolds, in the same way as for the first two terms of Eq. (8.18) discussed above, but the latter couplings are not suppressed by the field because the terms in the Zeeman Hamiltonian that depend on m_N and m_I are very small. As an example, consider the nominal state $|-1,-1/2,1/2\rangle$. In perturbation theory, its admixture with $|-1,1/2,-1/2\rangle$ has amplitude $-c/(60\mu_{\mathrm{B}}\mathcal{B})$. This can cause m_S to change in the excited state decay. For CaF, the branching ratio is smaller than the terms already discussed above, because c and γ are approximately equal. Our chosen nominal state also has an admixture with $|0,-1/2,-1/2\rangle$. A rough estimate of its amplitude can be obtained by treating the last term in H_{hfs} as a perturbation to the other two terms, giving an amplitude

$$\zeta \approx -\frac{c}{\sqrt{2}(5\gamma - 5b - 5c/3)}.$$

Similarly, using the same approximation, the nominal state $|0,-1/2,1/2\rangle$ has an admixture with $|1,-1/2,-1/2\rangle$ with amplitude $-\zeta$. It follows that the $B^2\Sigma$ state with $m_S = m_I = -1/2$ can decay to the nominal X states $|m_N,-1/2,1/2\rangle$ with $m_N = -1, 0$, with a branching ratio of $b_{\mathrm{r},3} \approx 2/3\zeta^2$. The situation is the same for the other three states of $B^2\Sigma$—in each case there is a leak out of the chosen (m_S, m_I) manifold of approximate size $b_{\mathrm{r},3}$ which cannot be reduced by applying a magnetic field of any reasonable size. For CaF, $b_{\mathrm{r},3} \approx 3\times10^{-3}$.

Finally, we note that there is another mechanism for mixing states of different m_N and m_I but the same m_S. This is through the combination of the $\vec{S}\cdot\vec{N}$ and $\vec{I}\cdot\vec{S}$ terms. The amplitude for this is proportional to the product of two matrix elements, one for each term, but scales only as $1/\mathcal{B}$ because the mixing is with a state from the same m_S manifold through an intermediate state of opposite

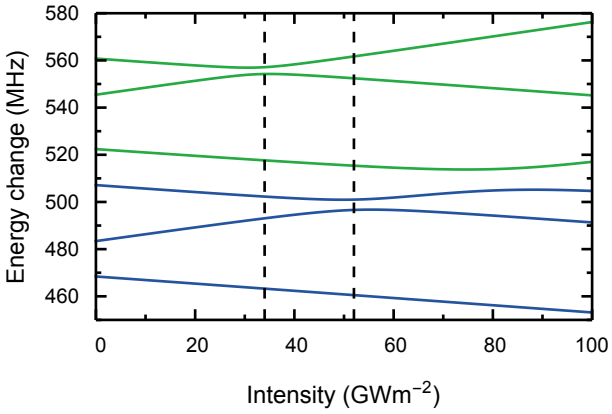

Figure 8.8: Energy levels of CaF as a function of light intensity, in a magnetic field of 300 G. All levels have $N = 1, m_S = 1/2$. For clarity, the rotational energy and the scalar Stark shift, which are common to all the levels, have been subtracted. The light is linearly polarised at an angle of $\pi/24$ to the magnetic field axis. In ascending order of energy, the states have $(m_N, m_I) = (-1, -1/2)$, $(0, -1/2)$, $(1, -1/2)$, $(-1, 1/2)$, $(0, 1/2)$, $(1, 1/2)$. The colour of the lines indicates (m_S, m_I) and follows the same scheme used in Fig. 8.7. Dashed lines show the intensities where the three-level model predicts avoided crossings between $m_N = 1$ and $m_N = 0$ levels. The pattern of levels with $m_S = -1/2$ is almost identical, but with states in the opposite order.

m_S. This mechanism affects 8 out of the 12 states of X and can be just as strong as the more direct mechanisms discussed above.

Figure 8.7 shows the exact branching ratio, calculated numerically, for each of the spin manifolds of the $B^2\Sigma^+(N = 0)$ state of CaF to decay to a different spin manifold of $X^2\Sigma^+(N = 1)$, as a function of $\mathcal{B}$. The behaviour is as discussed above—the branching ratios scale as $1/\mathcal{B}$ towards a constant value that is close to $b_{r,3}$. The branching ratios depend on the choice of spin manifold, and we see that using the $(m_S, m_I) = (-1/2, -1/2)$ manifold minimises the leak to other manifolds.

8.5.3 Tensor Stark shifts

Next, we calculate the tensor Stark shifts of CaF molecules in the presence of a strong magnetic field, and compare the results to those of the three-level model presented in Sec. 8.4. We calculate the eigenvalues of $H_{\rm tot} = H_{\rm Stark} + H_{\rm hfs} + H_{\rm Z}$ given by Eqs. (8.12), (8.18) and (8.19). We suppose the optical trap has a wavelength of 780 nm, and estimate the values of α_K by assuming that the $A^2\Pi$ and $B^2\Sigma^+$ states dominate the sums over states in Eq. (A.24). The energies of the states are calculated using the molecular constants given in [202], and the dipole moments using the data given in [138, 140, 143]. We find $\alpha'_0 \approx 1.4 \times 10^{-3}$ Hz/(W/m^2), $\alpha'_1 \approx 3 \times 10^{-5}$ Hz/(W/m^2) and $\alpha'_2 \approx -8 \times 10^{-4}$ Hz/(W/m^2).

Figure 8.8 shows the eigenvalues of $H_{\rm tot}$, focussing on the levels that have $N = 1$ and $m_S = 1/2$. We have chosen $\mathcal{B} = 300$ G and linearly polarised light at angle $\beta = \pi/24$, the same as used for Fig. 8.3. The upper three levels have $m_I = 1/2$, and their shifts with intensity are similar to those in Fig. 8.3 (remembering that $\alpha'_2 I/w$ is negative). The lower three levels have $m_I = -1/2$ and again show similar shifts with intensity. Our three-level model predicts an avoided crossing between $m_N = 1$ and $m_N = 0$ at an intensity $I_{\rm c} = -5/3 w_+/\alpha'_2$, where w_+ is given by Eq. (8.21). These values are $I_{\rm c} = 34$ and $52\,{\rm GW\,m^{-2}}$ for $m_I = 1/2$ and $-1/2$ respectively. These intensities are indicated by the

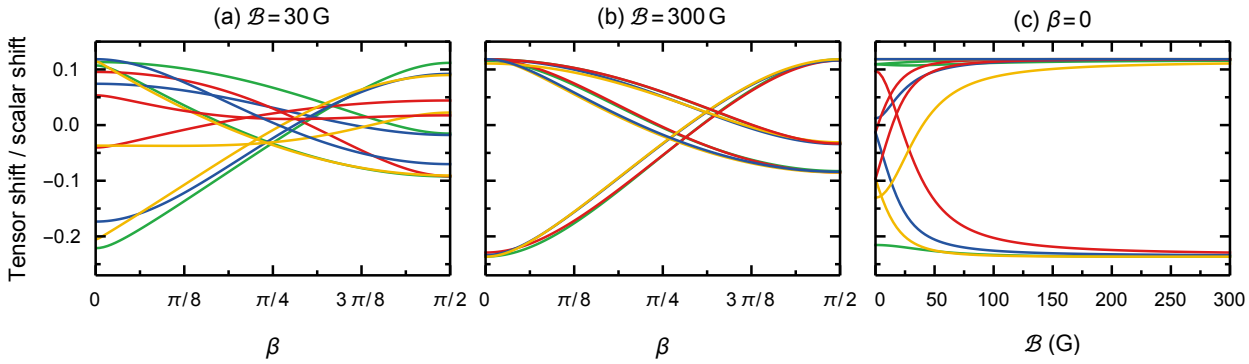

Figure 8.9: Ratio of tensor Stark shift to scalar Stark shift for the $N = 1$ states of CaF. (a,b) As a function of polarisation angle β with magnetic field of (a) 30 G (b) 300 G. (c) As a function of magnetic field with polarisation parallel to magnetic field. The light intensity is $I = 25$ GW/m^2 throughout. The colour of the lines indicates the value of (m_S, m_I) and follows the same scheme used in Fig. 8.7.

dashed lines in Fig. 8.8, and we see that the avoided crossings do indeed occur very close to these values. At intensities close to I_c the trapping potential will be distorted due to the non-linearity of the Stark shift with intensity around the avoided crossing. We note that, for CaF, with $m_S = m_I = 1/2$, $\alpha_0' I_c h/k_B = 2.1$ mK.

Figure 8.9(a) shows the ratio of the tensor Stark shift to the scalar Stark shift for the $N = 1$ levels of CaF, at an intensity of $I = 25\,\mathrm{GW\,m^{-2}}$, a magnetic field of $\mathcal{B} = 30$ G, and as a function of polarisation angle β. Every level has a different Stark shift and a different dependence on β. Figure 8.9(b) shows the same information for $\mathcal{B} = 300$ G, showing that at this higher field the levels group together and the pattern of shifts resembles the simple one shown in Fig. 8.4. Our chosen intensity gives $\alpha_2' I = -19.3$ MHz, which corresponds to $\alpha_2' I/w_+ = -1.22$ for positive $m_S m_I$, and $\alpha_2' I/w_+ = 0.81$ for negative $m_S m_I$, with w_+ given by Eq. (8.21). Thus, at high $\mathcal{B}$, we expect a close resemblance to Fig. 8.4(b), which is indeed what we see in Fig. 8.9(b). The small splitting of the three curves into closely spaced pairs is due to the different values of w_+ for opposite signs of $m_S m_I$. Figure 8.9(c) shows the ratio of the tensor Stark shift to the scalar Stark shift for $\beta = 0$ as a function of $\mathcal{B}$. At fields approaching 300 G the ac Stark shifts of the 12 states separate into two groups corresponding to states with $|m_N| = 1$ and $|m_N| = 0$ as expected.

8.6 Real light: a tweezer trap

Real tweezer traps are produced using a high numerical aperture (NA) lens to focus light down to a spot size comparable to the wavelength. To model a real trap, we use the vector Debye integral [203] to compute the distribution of intensity and polarisation close to the focus of a trap with parameters suitable for CaF. We then find the trap potential for all the $N = 1$ states of the molecule by calculating the eigenvalues of H_{tot} at each point in the distribution. The calculations are for a 780 nm input beam propagating along x and linearly polarised along z, focused through a lens of 0.55 NA. The $1/e^2$ diameter of the input beam is equal to the lens diameter and the total power is 20 mW. These parameters give a peak intensity at the centre of the tweezer of $25\,\mathrm{GW\,m^{-2}}$. For CaF molecules in the $N = 1$ manifold with a 300 G $\mathcal{B}$ field applied parallel to the incident polarisation vector, the trap

frequencies are nearly equal (less than 1 % difference) for states with the same value of $|m_N|$. For a molecule in $m_N = \pm 1(0)$, we calculate trap frequencies of 213(174) kHz parallel to the incident polarisation, 224(187) kHz perpendicular to both the incident polarisation and the optical axis, and 38(32) kHz parallel to the optical axis.

The intensity profile of the trap is not perfectly harmonic and the tight focusing gives rise to polarisation gradients close to the focus which can further distort the trap shape. Here, we consider the effects of these imperfections.

8.6.1 Anharmonicity

The tweezer trap potential is anharmonic away from the trap centre due to the approximately Gaussian intensity profile of the trap. Further distortions of the potential are introduced when the intensity is close to an avoided crossing between the internal states of the molecule (see Fig. 8.8). Any anharmonicity causes the sideband frequencies to depend on the motional state of the molecule.

At intensities far from any avoided crossings, we find the potential near the trap centre is approximately harmonic with a small, negative, quartic perturbation. The motional Hamiltonian is

$$H_{\mathrm{t}} = \frac{p^2}{2M} + \frac{1}{2}M\omega^2 z^2 - f z^4. \tag{8.25}$$

Working in the natural units of the system with $\tilde{z} = z\sqrt{M\omega/\hbar}$, $\tilde{p} = p/\sqrt{\hbar M\omega}$, the dimensionless motional Hamiltonian, $\tilde{H}_{\mathrm{t}} = H_{\mathrm{t}}/(\hbar\omega)$, can be written

$$\tilde{H}_{\mathrm{t}} = \frac{1}{2}\tilde{p}^2 + \frac{1}{2}\tilde{z}^2 - \tilde{f}\tilde{z}^4, \tag{8.26}$$

where $\tilde{f} = (\hbar/(M^2\omega^3))f \ll 1$. First order perturbation theory gives the dimensionless energy, $\tilde{E}_n = E_n/(\hbar\omega)$, of the n'th motional eigenstate as

$$\begin{aligned} \tilde{E}_n &\simeq n + \frac{1}{2} - \tilde{f}\,\langle n|\,\tilde{z}^4\,|n\rangle\,, \\ &= n + \frac{1}{2} - \frac{\tilde{f}}{4}(3 + 6n + 6n^2). \end{aligned} \tag{8.27}$$

The anharmonicity is apparent from the n dependence of the trap level spacing,

$$\tilde{E}_{n+1} - \tilde{E}_n = 1 - 3\tilde{f} - 3\tilde{f}n. \tag{8.28}$$

The $N = 1$ states of CaF in a 300 G field have $\tilde{f} \sim 7 \times 10^{-4}$ in the radial direction and $\sim 1 \times 10^{-4}$ in the axial direction, meaning the level spacing changes by less than 5 % for motional states up to $n \sim 25$ and $n \sim 170$ respectively. This effect is negligible, provided the effective Rabi frequency for the Raman process is not chosen too small compared to the trap frequency.

8.6.2 Polarisation gradients

Figure 8.10 shows example elements of the polarisation tensor at positions across the focal plane, multiplied by the ratio of the local intensity to the maximum intensity at the trap focus: $\mathcal{S} = (I/I_{\max})\mathcal{P}$.

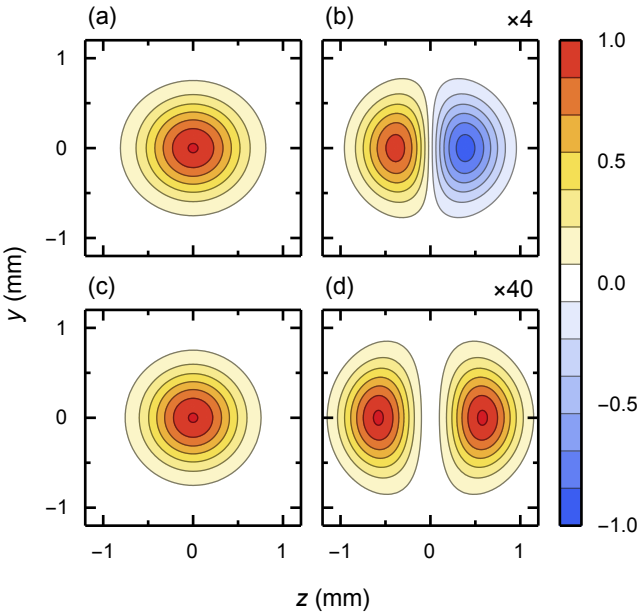

Figure 8.10: Calculated elements of the $\mathcal{S}$ tensor, defined in the text. (a) $\mathcal{S}_0^0$, (b) $\frac{1}{\sqrt{2}}\mathrm{Im}(\mathcal{S}_{-1}^1 + \mathcal{S}_1^1)$, (c) $\mathcal{S}_0^2$, (d) $\frac{1}{\sqrt{2}}\mathrm{Re}(\mathcal{S}_{-2}^2 + \mathcal{S}_2^2)$. The elements shown in (b) and (d) have been scaled by factors of 4 and 40 respectively in order to be shown on the same scale.

The elements are evaluated with respect to the incident polarisation vector. Figure 8.10(a) shows the scalar component $\mathcal{S}_0^0$. As shown in Eq. (A.13a), $\mathcal{P}_0^0$ is 1 everywhere and so the plot mirrors the Gaussian intensity profile of the light with a waist of 0.74 µm. Parts (b)-(d) of Fig. 8.10 illustrate how the non-paraxial focussing of the light creates polarisation gradients across the trapping volume. The polarisation tensor is, in general, complex, but useful real quantities can be obtained from linear superpositions of elements, as in Fig. 8.10.

For displacements away from the focus along the polarisation vector of the incident light, the local polarisation has a circular component with handedness along y, perpendicular to both the incident polarisation vector and the optical axis. The quantity $\frac{1}{\sqrt{2}}\mathrm{Im}(\mathcal{S}_{-1}^1 + \mathcal{S}_1^1)$, shown in Fig. 8.10(b), is proportional to the intensity of circularly polarised light along this axis. The component has opposite handedness on either side of the focus, reflected by the change of sign in the plot, and couples to the vector part of the polarisability. Within a given hyperfine level, the vector contribution to the Hamiltonian looks like a fictitious magnetic field along the axis of the circular component. The gradient of polarisation creates a gradient of this fictitious magnetic field that can shift the centre of the trap for different m_F states. The effect can be reduced to a negligible level by applying a large magnetic field orthogonal to the fictitious magnetic field, as previously demonstrated for atoms [193, 201]. Our method for sideband cooling of molecules already requires this large applied field, so the suppression will be automatic.

Figure 8.10(c) shows component $\mathcal{S}_0^2$. It is equal to 1 at the trap centre where the light field is linearly polarised. The structure is very similar to that of the intensity distribution in Fig. 8.10(a) with a slight and asymmetric narrowing caused by the polarisation gradient. The component couples to the tensor polarisability to provide a second mechanism by which the vector contribution is suppressed. To see this, choose a quantization axis for the molecule along z—the incident polarisation direction.

The effect of the vector Stark shift is that of a magnetic field orthogonal to this axis, introducing an off-diagonal matrix element—let's call it a_1—that couples $m_N = \pm 1$ to $m_N = 0$. The $\mathcal{P}_0^2$ component of the polarisation tensor, introduces diagonal matrix elements which shift the $m_N = \pm 1$ states relative to $m_N = 0$ by an amount a_2. When $a_2 \gg a_1$, as is often the case in molecules where the tensor polarisability is large compared to the vector polarisability, the coupling a_1 is ineffective because it couples states far apart in energy; the effect of the vector part is suppressed relative to a_1 by the factor a_1/a_2.

Figure 8.10(d) shows $\frac{1}{\sqrt{2}}\mathrm{Re}(\mathcal{S}^2_{-2} + \mathcal{S}^2_2)$. This part is zero for a light field linearly polarised with $\beta = 0$, as at the centre of the trap, but is not quite zero at other positions across the trap volume. The component can split the energies of the $m_N = \pm 1$ states but its size is comparatively small—note the $\times 40$ scaling—and so has no significant effect on the trapping potential. This is confirmed by the nearly identical trapping frequencies calculated for the two states at the beginning of this section.

8.7 Cooling recipe and conclusions

We have shown how to apply sideband cooling techniques to laser-coolable $^2\Sigma$ molecules in optical tweezer traps. The cooling must proceed from the $N = 1$ rotational level to avoid decays to other rotational levels, but the resulting state-dependent potentials introduce significant additional complexity. This complexity can be greatly reduced by applying a large magnetic field to decouple the nuclear and electron spins from the rotational angular momentum. Under these conditions, families of states can be found with three ground states coupled to a single excited state. For certain choices of laser polarisation, two of the three ground states have equal ac Stark shifts, so the frequency of the Raman transition between them is independent of the motional state. The reduction to only three ground states also greatly reduces the number of photons scattered during the optical pumping step, thereby reducing the heating. We have derived a formula for the additional heating caused by the different ac Stark shift of the third state, and have calculated the branching ratio out of this family of states as a function of applied magnetic field.

These considerations lead us to a recipe for Raman sideband cooling of laser-coolable molecules such as CaF. For trapping light with linear incident polarisation, the recipe is a straightforward extension of the scheme proposed for the simple molecule in Sec. 8.4: (i) Apply a weak magnetic field[5] along the incident polarisation vector of the trapping light. Apply π and σ^- polarised light relative to this axis to optically pump molecules into the stretched state $|N = 1, F = 2, m_F = -2\rangle = |m_N = -1, m_S = -1/2, m_I = -1/2\rangle$. According to Fig. 8.7, this state is part of the spin manifold with the smallest branching ratio to other spin manifolds. (ii) Increase the magnetic field to $\sim 300\,\mathrm{G}$ in order to decouple the angular momenta. (iii) Drive the Raman transition from $|m_N = -1, m_S = -1/2, m_I = -1/2\rangle \rightarrow |m_N = 1, m_S = -1/2, m_I = -1/2\rangle$ on the red motional sideband. (iv) Reapply optical pumping light from (i) to return molecules to $|m_N = -1, m_S = -1/2, m_I = -1/2\rangle$. (v) Repeat (iii) and (iv) until the molecule reaches the motional ground state.

The circularly polarised optical pumping beam must be orientated along the $\mathcal{B}$ field. The linearly polarised beam must be orthogonal to this and, as discussed in Sec. 8.4, to minimise heating should

[5]For this initial optical pumping, the magnetic field should be large enough that Zeeman splittings are large relative to any off-diagonal matrix elements of the tensor Stark interaction, but not large enough to uncouple the angular momenta.

also be perpendicular to the weakly confining optical axis of the trap. Using Eq. (8.17) and the trap frequencies for CaF in a real tweezer calculated in Sec. 8.6, the mean change in motional quantum number during the optical pumping step can be written

$$\overline{\Delta n^{\mathrm{op}}} = \kappa + \rho\, n. \tag{8.29}$$

Under these conditions, we find (κ, ρ) equal to $(0.17, 0.03)$ parallel to the incident polarisation vector, $(0.11, 0.02)$ perpendicular to both the incident polarisation and the optical axis, and $(0.29, 0.02)$ parallel to the optical axis. These calculations show sideband cooling should be effective on the first red sideband for small n. Driving higher-order sidebands may be helpful for initial cooling of hot clouds, particularly along the optical axis where the Lamb-Dicke parameter is much larger. As noted in Sec. 8.4, the cooling can also work for other polarisation choices—the main requirement is that two of the three states have equal tensor shifts. For example, choosing a linear polarisation at an angle close to β_{magic} can satisfy this requirement and also reduce the heating due to Θ_{curv}, which is useful at high n. We conclude that the heating due to state-dependent potentials is not a major obstacle for effective cooling.

Figure 8.7 shows that, at 300 G, the branching ratio to other spin manifolds is about 4×10^{-3}. Increasing the magnetic field reduces the branching ratio further, but only by a factor of 2 for realistic fields. Recalling that an average of 3 photons are scattered in the optical pumping step, we see that under these conditions, the cooling cycle can be applied 58 times before half the population is lost to a different spin manifold. For the tweezer parameters considered here, 58 cycles of sideband cooling on the first red sideband corresponds to an energy reduction of 600 µK in either of the radial directions, or 100 µK in the axial direction. It is straightforward to use higher-order sidebands, resulting in proportionally larger energy reductions. Considering that molecular samples with temperatures of 5 μK have already been demonstrated by free-space laser cooling [5, 166], we see that it is feasible to reach the ground state with little loss. We also note that loss to other spin manifolds is not fatal, since the cooling process could be applied to each spin manifold. Moreover, the entire cooling process—beginning with the optical pumping step at low magnetic field—can be applied multiple times if that proved necessary.

Our analysis here has focused on CaF, but the methods and conclusions also apply to other similar molecules amenable to laser cooling. The ability to cool these molecules to the ground-state of tweezer traps is a key advance that will open the door to molecules as processors of quantum information and simulators of many-body quantum systems.

Appendix A

Stark shift operator and its matrix elements

This text has previously appeared in the appendix of [7] and is reproduced here for ease of reference.

A.1 Operator

Consider a diatomic molecule interacting with light which has electric field amplitude $\mathcal{E}_0$, angular frequency ω_L, and unit polarization vector ϵ. The interaction Hamiltonian is $H' = -\vec{d}\cdot\vec{E}$, where $\vec{d}$ is the dipole moment operator of the molecule and $\vec{E} = \frac{1}{2}\mathcal{E}_0(\epsilon e^{-i\omega_\mathrm{L}t} + \epsilon^* e^{i\omega_\mathrm{L}t})$ is the electric field. We suppose that all effects much larger than this molecule-light interaction are included in a zeroth-order Hamiltonian, H_0, while the molecule-light interaction and all effects of a similar (or smaller) size are treated by perturbation theory. In second-order perturbation theory, the energy shift of a non-degenerate level i is

$$\Delta W_i = -\frac{1}{4}\mathcal{E}_0^2 \sum_{j\neq i}\left(\frac{\langle i|\,\vec{d}\cdot\epsilon^*\,|j\rangle\,\langle j|\,\vec{d}\cdot\epsilon\,|i\rangle}{\hbar\,(\omega_{ji}-\omega_\mathrm{L})} + \frac{\langle i|\,\vec{d}\cdot\epsilon\,|j\rangle\,\langle j|\,\vec{d}\cdot\epsilon^*\,|i\rangle}{\hbar\,(\omega_{ji}+\omega_\mathrm{L})}\right) \tag{A.1}$$

Here, ω_{ji} is the transition angular frequency between states j and i and the sum is over all states of the molecule. More generally, we may wish to know the energy shift of levels that are degenerate in the absence of the light, or handle cases where the ac Stark shifts are comparable to other level shifts and splittings, such as those arising from the hyperfine or Zeeman interactions. What is needed is an effective operator, which we will call H_S, that describes the effect of the light within a small subspace of levels, for example, a single rotational state. The matrix elements of the effective operator between states $|i\rangle$ and $|i'\rangle$ within the subspace are the generalization of Eq. (A.1):

$$\langle i|\,H_\mathrm{S}\,|i'\rangle = -\frac{1}{4}\mathcal{E}_0^2 \sum_{j}\left(\frac{\langle i|\,\vec{d}\cdot\epsilon^*\,|j\rangle\,\langle j|\,\vec{d}\cdot\epsilon\,|i'\rangle}{\hbar\,(\omega_{ji}-\omega_\mathrm{L})} + \frac{\langle i|\,\vec{d}\cdot\epsilon\,|j\rangle\,\langle j|\,\vec{d}\cdot\epsilon^*\,|i'\rangle}{\hbar\,(\omega_{ji}+\omega_\mathrm{L})}\right) \tag{A.2}$$

where the sum is over all states of H_0 that lie outside the subspace[1]. In spherical coordinates, this expression is

$$\langle i|\, H_{\rm S}\, |i'\rangle = -\frac{\mathcal{E}_0^2}{4}\sum_{p,q}(-1)^{p+q}\left(\langle i|\, d_p\mathcal{R}^- d_q\, |i'\rangle\,(\epsilon^*)_{-p}\epsilon_{-q} + \langle i|\, d_q\mathcal{R}^+ d_p\, |i'\rangle\,\epsilon_{-q}(\epsilon^*)_{-p}\right) \tag{A.3}$$

where we have defined the operator

$$\mathcal{R}^{\pm} = \sum_j \frac{1}{\hbar(\omega_{ji}\pm\omega_{\rm L})}|j\rangle\langle j|. \tag{A.4}$$

Provided H_0 does not include external fields, $\mathcal{R}^{\pm}$ is invariant under rotations.

The formula for building a spherical tensor of rank k_{12} from the product of two other spherical tensors of ranks k_1 and k_2 is

$$T^{k_{12}}_{p_{12}}(A,B) = \sum_{p_1}(-1)^{k_1+k_2-p_{12}}\sqrt{2k_{12}+1}\,T^{k_1}_{p_1}(A)\,T^{k_2}_{p_{12}-p_1}(B)\begin{pmatrix} k_1 & k_2 & k_{12}\\ p_1 & p_{12}-p_1 & -p_{12}\end{pmatrix}. \tag{A.5}$$

Applying this to the tensor product of two vectors, $\vec{u}$ and $\vec{v}$ gives

$$T^K_P(u,v) = (-1)^P\sqrt{2K+1}\sum_p T^1_p(u)T^1_{P-p}(v)\begin{pmatrix} 1 & 1 & K\\ p & P-p & -P\end{pmatrix}. \tag{A.6}$$

The inverse relation gives us the expansion of the product u_pv_q as

$$u_pv_q = \sum_{K=0}^{2}\sum_{P=-K}^{K}(-1)^P\sqrt{2K+1}\begin{pmatrix} 1 & 1 & K\\ p & q & -P\end{pmatrix}T^K_P(u,v). \tag{A.7}$$

Equation (A.3) contains two products of this form, one relating to the transition dipole moments of the molecule, and the other to the polarization of the light. Expanding each using Eq. (A.7), then evaluating the sums over p and q, we find that

$$\sum_{p,q}(-1)^{p+q}\left(d_p\mathcal{R}^{\pm}d_q\right)\left(\epsilon^*{}_{-p}\epsilon_{-q}\right) = \sum_{K=0}^{2}\sum_{P=-K}^{K}(-1)^P T^K_P(d,\mathcal{R}^{\pm}d)T^K_{-P}(\epsilon,\epsilon^*)\,. \tag{A.8}$$

Note that the transformation $d_p\mathcal{R}^{\pm}d_q \to d_q\mathcal{R}^{\pm}d_p$ on the left-hand side of this equation multiplies the terms in the sum over K on the right-hand side by $(-1)^K$. Applying these results to Eq. (A.3), we find that the effective Stark shift operator is

$$H_{\rm S} = -\frac{\mathcal{E}_0^2}{4}\sum_{K=0}^{2}\sum_{P=-K}^{K}(-1)^P\mathcal{A}^K_P\mathcal{P}^K_{-P} \tag{A.9}$$

[1] A derivation of this result can be found in, for example, Ref. [204]. See equation (26) of Complement B_I. Note that the zeroth-order energies include the energies of the photons in the light field, and that the perturbation couples states that change the photon number by ±1

where we have introduced the polarizability operators

$$\mathcal{A}_P^K = (\mathcal{A}^-)_P^K + (-1)^K (\mathcal{A}^+)_P^K, \tag{A.10a}$$

$$(\mathcal{A}^\pm)_P^K = \frac{1}{z_K} T_P^K(d, \mathcal{R}^\pm d), \tag{A.10b}$$

and the polarization tensors

$$\mathcal{P}_P^K = z_K T_P^K(\epsilon, \epsilon^*). \tag{A.11}$$

The z_K are numerical factors that can be chosen arbitrarily. We choose $z_0 = -\sqrt{3}$ so that $\mathcal{P}_0^0 = \epsilon \cdot \epsilon^* = 1$, $z_1 = -\sqrt{2}$ so that $\mathcal{P}^1 = -i(\epsilon \times \epsilon^*)$, and $z_2 = \sqrt{3/2}$, so that $\mathcal{P}_0^2 = 1$ for light that is linearly polarized along z.

The components of $\mathcal{A}^\pm$ are

$$(\mathcal{A}^\pm)_0^0 = \frac{1}{3}\left(-d_1 \mathcal{R}^\pm d_{-1} + d_0 \mathcal{R}^\pm d_0 - d_{-1}\mathcal{R}^\pm d_1\right), \tag{A.12a}$$

$$(\mathcal{A}^\pm)_0^1 = \frac{1}{2}\left(-d_1 \mathcal{R}^\pm d_{-1} + d_{-1}\mathcal{R}^\pm d_1\right), \tag{A.12b}$$

$$(\mathcal{A}^\pm)_{\pm 1}^1 = \pm\frac{1}{2}\left(d_0 \mathcal{R}^\pm d_{\pm 1} - d_{\pm 1}\mathcal{R}^\pm d_0\right), \tag{A.12c}$$

$$(\mathcal{A}^\pm)_0^2 = \frac{1}{3}\left(d_1 \mathcal{R}^\pm d_{-1} + 2d_0 \mathcal{R}^\pm d_0 + d_{-1}\mathcal{R}^\pm d_1\right), \tag{A.12d}$$

$$(\mathcal{A}^\pm)_{\pm 1}^2 = \frac{1}{\sqrt{3}}\left(d_0 \mathcal{R}^\pm d_{\pm 1} + d_{\pm 1}\mathcal{R}^\pm d_0\right), \tag{A.12e}$$

$$(\mathcal{A}^\pm)_{\pm 2}^2 = \sqrt{\frac{2}{3}} d_{\pm 1} \mathcal{R}^\pm d_{\pm 1}. \tag{A.12f}$$

The components of $\mathcal{P}$ are

$$\mathcal{P}_0^0 = \epsilon_{-1}{\epsilon_{-1}}^* + \epsilon_0{\epsilon_0}^* + \epsilon_1{\epsilon_1}^* = \epsilon \cdot \epsilon^* = 1, \tag{A.13a}$$

$$\mathcal{P}_0^1 = \epsilon_1{\epsilon_1}^* - \epsilon_{-1}{\epsilon_{-1}}^*, \tag{A.13b}$$

$$\mathcal{P}_{\pm 1}^1 = \mp\left(\epsilon_0{\epsilon_{\mp 1}}^* + {\epsilon_0}^*\epsilon_{\pm 1}\right), \tag{A.13c}$$

$$\mathcal{P}_0^2 = -\frac{1}{2}\left(\epsilon_{-1}{\epsilon_{-1}}^* - 2\epsilon_0{\epsilon_0}^* + \epsilon_1{\epsilon_1}^*\right) = -\frac{1}{2}\left(1 - 3\epsilon_0{\epsilon_0}^*\right), \tag{A.13d}$$

$$\mathcal{P}_{\pm 1}^2 = \frac{\sqrt{3}}{2}\left(-\epsilon_0{\epsilon_{\mp 1}}^* + {\epsilon_0}^*\epsilon_{\pm 1}\right), \tag{A.13e}$$

$$\mathcal{P}_{\pm 2}^2 = -\sqrt{\frac{3}{2}}{\epsilon_{\mp 1}}^*\epsilon_{\pm 1} \tag{A.13f}$$

Here, ${\epsilon_p}^*$ means $(\epsilon_p)^*$, and we have used the relation $(\epsilon^*)_q = (-1)^q(\epsilon_{-q})^*$.

A.2 Matrix elements for $^1\Sigma$ states

We consider a ground-state molecule with no orbital angular momentum, no electronic spin and no nuclear spin. In this simple case, the basis states are $|\Lambda, N, m_N\rangle$ with $\Lambda = 0$. Here, the quantum numbers are the projection of the orbital angular momentum onto the internuclear axis (Λ), the rotational angular momentum (N), and its projection onto the z-axis (m_N). The matrix elements of

the polarizability tensor are

$$\left\langle \Lambda, N', m'_N \left| \mathcal{A}^K_P \right| \Lambda, N, m_N \right\rangle = (-1)^{N'-m'_N} \begin{pmatrix} N' & K & N \\ -m'_N & P & m_N \end{pmatrix} \left\langle \Lambda, N' || \mathcal{A}^K || \Lambda, N \right\rangle \tag{A.14}$$

To evaluate the reduced matrix element, we rotate into the frame of the molecule using

$$\mathcal{A}^K_P = \sum_Q \left(\mathcal{D}^K_{PQ}\right)^* \mathcal{A}^K_Q. \tag{A.15}$$

Here, the index P is used for lab-frame components, and the index Q for molecule-frame components, and $\mathcal{D}^K$ is the rotation operator of rank K that transforms between them. This gives

$$\begin{aligned}
&\left\langle \Lambda, N', m'_N \left| \mathcal{A}^K_P \right| \Lambda, N, m_N \right\rangle \\
&= (-1)^{N'-m'_N} \begin{pmatrix} N' & K & N \\ -m'_N & P & m_N \end{pmatrix} \sum_Q \left\langle \Lambda \left| \mathcal{A}^K_Q \right| \Lambda \right\rangle \left\langle \Lambda, N' \left\| \left(\mathcal{D}_{\cdot Q}{}^K\right)^* \right\| \Lambda, N \right\rangle \\
&= (-1)^{N'-m'_N} \begin{pmatrix} N' & K & N \\ -m'_N & P & m_N \end{pmatrix} \sqrt{(2N+1)(2N'+1)} (-1)^{N'-\Lambda} \begin{pmatrix} N' & K & N \\ -\Lambda & 0 & \Lambda \end{pmatrix} \left\langle \Lambda \left| \mathcal{A}^K_{Q=0} \right| \Lambda \right\rangle.
\end{aligned}$$

In the first line, the dot in the subscript of the rotation operator indicates that the matrix element is reduced relative to the index P. In the last step, we've set $Q = 0$ since this is the only non-zero term in the sum over Q. Let us define the molecule-frame parallel and perpendicular polarizability components:

$$\alpha_\parallel = \sum_j \left(\frac{1}{\hbar(\omega_{ji} + \omega_\mathrm{L})} + \frac{1}{\hbar(\omega_{ji} - \omega_\mathrm{L})} \right) \left| \left\langle X \left| d_0 \right| j, \Sigma \right\rangle \right|^2 \tag{A.16a}$$

$$\alpha_\perp = \sum_k \left(\frac{1}{\hbar(\omega_{ki} + \omega_\mathrm{L})} + \frac{1}{\hbar(\omega_{ki} - \omega_\mathrm{L})} \right) \left| \left\langle X \left| d_1 \right| k, \Pi \right\rangle \right|^2 \tag{A.16b}$$

Here, X labels the $^1\Sigma$ ground state of interest, the index j labels the set of excited Σ states, k labels the set of excited Π states, and the dipole operators are acting in the molecule frame. We note that $\left|\left\langle X \left| d_{-1} \right| k, \Pi \right\rangle\right|^2 = \left|\left\langle X \left| d_1 \right| k, \Pi \right\rangle\right|^2$ because a Π state is an equal superposition of $\Lambda = \pm 1$. We introduce the molecular parameters $\alpha_K = \left\langle \Lambda = 0 \right| \mathcal{A}^K_{Q=0} \left| \Lambda = 0 \right\rangle$, which we can think of as the scalar, vector and tensor polarizabilities in the molecular frame. Using the definitions for the components of $\mathcal{A}$ given by Eq. (A.12), the definitions of $\alpha_\parallel$, $\alpha_\perp$ and α_K, and the relation $\left\langle i \right| d_q \left| j \right\rangle = (-1)^q \left\langle j \right| d_{-q} \left| i \right\rangle$, we find the complete expression for the matrix elements (for $\Lambda = 0, S = 0$):

$$\begin{aligned}
&\left\langle \Lambda, N', m'_N \left| \mathcal{A}^K_P \right| \Lambda, N, m_N \right\rangle \\
&\quad = (-1)^{m'_N} \begin{pmatrix} N' & K & N \\ -m'_N & P & m_N \end{pmatrix} \sqrt{(2N+1)(2N'+1)} \begin{pmatrix} N' & K & N \\ -\Lambda & 0 & \Lambda \end{pmatrix} \alpha_K,
\end{aligned} \tag{A.17}$$

where

$$\alpha_0 = \frac{1}{3}\left(\alpha_\parallel + 2\alpha_\perp\right), \tag{A.18a}$$

$$\alpha_1 = 0, \tag{A.18b}$$

$$\alpha_2 = \frac{2}{3}\left(\alpha_\parallel - \alpha_\perp\right). \tag{A.18c}$$

A.3 Matrix elements for $^2\Sigma$ states

Now we consider a more complicated case where the basis states are $|\Lambda, N, S, J, I, F, m_F\rangle$. In this order, the quantum numbers are the projection of the orbital angular momentum onto the internuclear axis, the rotational angular momentum, the total electronic spin, the total electronic angular momentum, the nuclear spin, the total angular momentum, and the projection of the total angular momentum onto the z-axis. Later, we shall also introduce the quantum numbers Σ and Ω, which are the projections of $\vec{S}$ and $\vec{J}$ onto the internuclear axis. Using the Wigner-Eckart theorem, and the fact that the operator acts in the space of the electronic coordinates, we have

$$\begin{aligned}
&\left\langle \Lambda, N', S, J', I, F', m'_F \left| \mathcal{A}^K_P \right| \Lambda, N, S, J, I, F, m_F \right\rangle \\
&\quad = (-1)^{F'-m'_F}(-1)^{F+J'+K+I}\sqrt{(2F+1)\,(2F'+1)}\begin{pmatrix} F' & K & F \\ -m'_F & P & m_F \end{pmatrix} \\
&\quad \times \begin{Bmatrix} J' & F' & I \\ F & J & K \end{Bmatrix} \left\langle \Lambda, N', S, J' \| \mathcal{A}^K \| \Lambda, N, S, J \right\rangle .
\end{aligned}$$

To help evaluate the remaining matrix element, we use the relation between Hund's case (b) and case (a) states:

$$|\Lambda, N, S, J\rangle = \sum_{\Sigma=-S}^{S} \sqrt{2N+1}(-1)^{N-S+\Omega}\begin{pmatrix} J & S & N \\ \Omega & -\Sigma & -\Lambda \end{pmatrix} |\Lambda, S, \Sigma, J, \Omega\rangle. \tag{A.19}$$

At this point, we specialize to $^2\Sigma$ states, which have $\Lambda = 0$ and $S = 1/2$. We also use the fact that our operator is built up from dipole moment operators that cannot change Σ. So, our reduced matrix element can be expressed as

$$\begin{aligned}
&\left\langle \Lambda, N', S, J' \| \mathcal{A}^K \| \Lambda, N, S, J \right\rangle \\
&\quad = (-1)^{N'+N}\sqrt{(2N+1)(2N'+1)}\begin{pmatrix} J & 1/2 & N \\ -1/2 & 1/2 & 0 \end{pmatrix}\begin{pmatrix} J' & 1/2 & N' \\ -1/2 & 1/2 & 0 \end{pmatrix} \\
&\qquad \times \left[\left\langle \Lambda = 0, \Sigma = -1/2, J' \| \mathcal{A}^K \| \Lambda = 0, \Sigma = -1/2, J \right\rangle \right. \\
&\qquad\quad \left. + (-1)^{J'+J+N'+N-1} \left\langle \Lambda = 0, \Sigma = 1/2, J' \left\| \mathcal{A}^K \right\| \Lambda = 0, \Sigma = 1/2, J \right\rangle \right]
\end{aligned} \tag{A.20}$$

This leaves us with reduced matrix elements of the general type $\langle \Lambda, \Sigma, J' \| \mathcal{A}^K \| \Lambda, \Sigma, J \rangle$. As before, we rotate into the molecule frame and factorize the result, to reach

$$\langle \Lambda, \Sigma, J' \| \mathcal{A}^K \| \Lambda, \Sigma, J \rangle = \sqrt{(2J+1)\,(2J'+1)}(-1)^{J'-\Sigma} \begin{pmatrix} J' & K & J \\ -\Sigma & 0 & \Sigma \end{pmatrix} \langle \Lambda, \Sigma \left| \mathcal{A}^K_{Q=0} \right| \Lambda, \Sigma \rangle . \quad \text{(A.21)}$$

We can use this result in Eq. (A.20), noting that the two matrix elements in the square brackets differ only in the sign of Σ, and that changing the sign of Σ in the 3j symbol of Eq.(A.21) introduces an extra phase factor of $(-1)^{J+J'+K}$. Thus we obtain

$$\begin{aligned} &\langle \Lambda, N', S, J' \| \mathcal{A}^K \| \Lambda, N, S, J \rangle = \\ &\quad (-1)^{N'+N+2J'+J+K+1/2} \sqrt{(2N+1)(2N'+1)(2J+1)(2J'+1)} \\ &\quad \times \begin{pmatrix} J & 1/2 & N \\ -1/2 & 1/2 & 0 \end{pmatrix} \begin{pmatrix} J' & 1/2 & N' \\ -1/2 & 1/2 & 0 \end{pmatrix} \begin{pmatrix} J' & K & J \\ -1/2 & 0 & 1/2 \end{pmatrix} \\ &\quad \times \left[\langle \Lambda = 0, \Sigma = -1/2 \left| \mathcal{A}^K_{Q=0} \right| \Lambda = 0, \Sigma = -1/2 \rangle \right. \\ &\qquad \left. + (-1)^{N'+N-K} \langle \Lambda = 0, \Sigma = 1/2 \left| \mathcal{A}^K_{Q=0} \right| \Lambda = 0, \Sigma = 1/2 \rangle \right] \end{aligned} \quad \text{(A.22)}$$

The molecule-frame matrix elements in square brackets can be evaluated using the definitions in Eq. (A.12). They involve terms of the type $|\langle \Lambda = 0, \Sigma = \pm 1/2 | d_q | \Lambda'', \Sigma'' \rangle|^2$, where the double-primes refer to excited electronic states, and the d_q operate in the molecule frame. The terms involving d_0 connect to the excited $^2\Sigma$ states, while the terms involving $d_{\pm 1}$ connect to the $^2\Pi_{1/2}$ and $^2\Pi_{3/2}$ states. For example

$$\langle \Lambda = 0, \Sigma = -1/2 | \, d_1 \mathcal{R}^{\pm} d_{-1} \, | \Lambda = 0, \Sigma = -1/2 \rangle = -\sum_k \frac{1}{\hbar\,(\omega_k \pm \omega_{\mathrm{L}})} | \langle X, ^2\Sigma_{-1/2} | \, d_1 \, | k, ^2\Pi_{-3/2} \rangle |^2, \quad \text{(A.23)}$$

where the sum is over all the Π states. We can write similar expressions for $\Sigma = 1/2$ and for the other operators appearing in the $\mathcal{A}^K_{Q=0}$. Using these expressions, the term in the square brackets can be written in terms of the following quantities:

$$\alpha_{\parallel} = \sum_j \left(\frac{1}{\hbar\,(\omega_j + \omega_{\mathrm{L}})} + \frac{1}{\hbar\,(\omega_j - \omega_{\mathrm{L}})} \right) | \langle X, ^2\Sigma | d_0 | j, ^2\Sigma \rangle |^2, \quad \text{(A.24a)}$$

$$\alpha_{\perp,\Omega} = \sum_k \left(\frac{1}{\hbar\,(\omega_{k,\Omega} + \omega_{\mathrm{L}})} + \frac{1}{\hbar\,(\omega_{k,\Omega} - \omega_{\mathrm{L}})} \right) | \langle X, ^2\Sigma | d_1 | k, ^2\Pi_{\Omega} \rangle |^2, \quad \text{(A.24b)}$$

$$\alpha_{\perp} = \frac{1}{2} \left(\alpha_{\perp,\frac{1}{2}} + \alpha_{\perp,\frac{3}{2}} \right) \quad \text{(A.24c)}$$

$$\begin{aligned} \beta_{\perp,\Omega} &= \sum_k \left(\frac{1}{\hbar\,(\omega_{k,\Omega} + \omega_{\mathrm{L}})} - \frac{1}{\hbar\,(\omega_{k,\Omega} - \omega_{\mathrm{L}})} \right) | \langle X, ^2\Sigma | d_1 | k, ^2\Pi_{\Omega} \rangle |^2 \\ &= \sum_k \left(\frac{1}{\hbar\,(\omega_{k,\Omega} + \omega_{\mathrm{L}})} + \frac{1}{\hbar\,(\omega_{k,\Omega} - \omega_{\mathrm{L}})} \right) \frac{\omega_{\mathrm{L}}}{\omega_{k,\Omega}} | \langle X, ^2\Sigma | d_1 | k, ^2\Pi_{\Omega} \rangle |^2. \end{aligned} \quad \text{(A.24d)}$$

After some algebra, we end up with a complete expression for the matrix elements (for $\Lambda = 0, S = 1/2$):

$$\begin{aligned}
&\left\langle \Lambda, N', S, J', I, F', m'_F \left| \mathcal{A}_P^K \right| \Lambda, N, S, J, I, F, m_F \right\rangle \\
&\quad = \left[(-1)^{N'+N} + 1 \right] (-1)^{F'-m'_F+F-J'+J+I+1/2} \sqrt{(2F+1)(2F'+1)} \\
&\qquad \times \sqrt{(2N+1)(2N'+1)(2J+1)(2J'+1)} \begin{Bmatrix} J' & F' & I \\ F & J & K \end{Bmatrix} \begin{pmatrix} F' & K & F \\ -m'_F & P & m_F \end{pmatrix} \\
&\qquad \times \begin{pmatrix} J & 1/2 & N \\ -1/2 & 1/2 & 0 \end{pmatrix} \begin{pmatrix} J' & 1/2 & N' \\ -1/2 & 1/2 & 0 \end{pmatrix} \begin{pmatrix} J' & K & J \\ -1/2 & 0 & 1/2 \end{pmatrix} \alpha_K,
\end{aligned} \tag{A.25}$$

where

$$\alpha_0 = \frac{1}{3}\left(\alpha_\parallel + \alpha_{\perp,\frac{1}{2}} + \alpha_{\perp,\frac{3}{2}}\right) = \frac{1}{3}\left(\alpha_\parallel + 2\alpha_\perp\right), \tag{A.26a}$$

$$\alpha_1 = \frac{1}{2}\left(\beta_{\perp,\frac{1}{2}} - \beta_{\perp,\frac{3}{2}}\right), \tag{A.26b}$$

$$\alpha_2 = \frac{1}{3}\left(2\alpha_\parallel - \alpha_{\perp,\frac{1}{2}} - \alpha_{\perp,\frac{3}{2}}\right) = \frac{2}{3}\left(\alpha_\parallel - \alpha_\perp\right). \tag{A.26c}$$

Note that in the particular case where only one Π state contributes to the sum, $\beta_{\perp,\Omega} = \frac{\omega}{\omega_{m,\Omega}}\alpha_{\perp,\Omega}$. In the special case where the detuning of the light is very large compared to the fine-structure interval of the excited state, $\alpha_{\perp,\frac{1}{2}} \approx \alpha_{\perp,\frac{3}{2}}$. When both of these special cases hold,

$$\alpha_1 \approx \frac{1}{2}\frac{\left(\omega_{3/2} - \omega_{1/2}\right)\omega}{\omega_{1/2}\omega_{3/2}}\alpha_\perp. \tag{A.27}$$

Bibliography

[1] S. Truppe, H. J. Williams, M. Hambach, L. Caldwell, N. J. Fitch, E. A. Hinds, B. E. Sauer, and M. R. Tarbutt. "Molecules cooled below the Doppler limit". *Nat. Phys.* 13.12 (2017), pp. 1173–1176.

[2] H. J. Williams, S. Truppe, M. Hambach, L. Caldwell, N. J. Fitch, E. A. Hinds, B. E. Sauer, and M. R. Tarbutt. "Characteristics of a magneto-optical trap of molecules". *New J. Phys.* 19.11 (2017), p. 113035.

[3] H. J. Williams, L. Caldwell, N. J. Fitch, S. Truppe, J. Rodewald, E. A. Hinds, B. E. Sauer, and M. R. Tarbutt. "Magnetic Trapping and Coherent Control of Laser-Cooled Molecules". *Phys. Rev. Lett.* 120.16 (2018), p. 163201.

[4] J. A. Blackmore, L. Caldwell, P. D. Gregory, E. M. Bridge, R. Sawant, J. Aldegunde, J. Mur-Petit, D. Jaksch, J. M. Hutson, B. E. Sauer, M. R. Tarbutt, and S. L. Cornish. "Ultracold molecules for quantum simulation: rotational coherences in CaF and RbCs". *Quantum Sci. Technol.* 4.1 (2018), p. 014010.

[5] L. Caldwell, J. A. Devlin, H. J. Williams, N. J. Fitch, E. A. Hinds, B. E. Sauer, and M. R. Tarbutt. "Deep Laser Cooling and Efficient Magnetic Compression of Molecules". *Phys. Rev. Lett.* 123.3 (2019), p. 033202.

[6] L. Caldwell, H. J. Williams, N. J. Fitch, J. Aldegunde, J. M. Hutson, B. E. Sauer, and M. R. Tarbutt. "Long Rotational Coherence Times of Molecules in a Magnetic Trap". *Phys. Rev. Lett.* 124.6 (2020), p. 063001.

[7] L. Caldwell and M. R. Tarbutt. "Sideband cooling of molecules in optical traps". *Phys. Rev. Res.* 2.1 (2020), p. 013251.

[8] M. Schioppo, R. C. Brown, W. F. McGrew, N. Hinkley, R. J. Fasano, K. Beloy, T. H. Yoon, G. Milani, D. Nicolodi, J. A. Sherman, N. B. Phillips, C. W. Oates, and A. D. Ludlow. "Ultrastable optical clock with two cold-atom ensembles". *Nat. Photonics* 11.1 (2016), pp. 48–52.

[9] T. L. Nicholson, S. L. Campbell, R. B. Hutson, G. E. Marti, B. J. Bloom, R. L. McNally, W. Zhang, M. D. Barrett, M. S. Safronova, G. F. Strouse, W. L. Tew, and J. Ye. "Systematic evaluation of an atomic clock at 2×10^{-18} total uncertainty". *Nat. Commun.* 6 (2015), p. 6896.

[10] S. M. Brewer, J. S. Chen, A. M. Hankin, E. R. Clements, C. W. Chou, D. J. Wineland, D. B. Hume, and D. R. Leibrandt. "$^{27}Al^{+}$ Quantum-Logic Clock with a Systematic Uncertainty below 10^{-18} ". *Phys. Rev. Lett.* 123.3 (2019), p. 033201.

[11] M. H. Anderson, J. R. Ensher, M. R. Matthews, C. E. Wieman, and E. A. Cornell. "Observation of Bose-Einstein Condensation in a Dilute Atomic Vapor". *Science* 269.5221 (1995), pp. 198–201.

[12] K. B. Davis, M.-O. Mewes, M. R. Andrews, N. J. van Druten, D. S. Durfee, D. M. Kurn, and W. Ketterle. "Bose-Einstein Condensation in a Gas of Sodium Atoms". *Phys. Rev. Lett.* 75 (22 1995), pp. 3969–3973.

[13] M. Greiner, O. Mandel, T. Esslinger, T. W. Hänsch, and I. Bloch. "Quantum phase transition from a superfluid to a Mott insulator in a gas of ultracold atoms". *Nature* 415.6867 (2002), pp. 39–44.

[14] Z. Hadzibabic, P. Krüger, M. Cheneau, B. Battelier, and J. Dalibard. "Berezinskii–Kosterlitz–Thouless crossover in a trapped atomic gas". *Nature* 441.7097 (2006), pp. 1118–1121.

[15] R. Bouchendira, P. Cladé, S. Guellati-Khélifa, F. Nez, and F. Biraben. "New Determination of the Fine Structure Constant and Test of the Quantum Electrodynamics". *Phys. Rev. Lett.* 106 (8 2011), p. 080801.

[16] N. Huntemann, B. Lipphardt, C. Tamm, V. Gerginov, S. Weyers, and E. Peik. "Improved limit on a temporal variation of m_p/m_e from comparisons of Yb^+ and Cs atomic clocks". *Phys. Rev. Lett.* 113.21 (2014), p. 210802.

[17] R. M. Godun, P. B. R. Nisbet-Jones, J. M. Jones, S. A. King, L. A. M. Johnson, H. S. Margolis, K. Szymaniec, S. N. Lea, K. Bongs, and P. Gill. "Frequency Ratio of Two Optical Clock Transitions in $^{171}Yb^+$ and Constraints on the Time Variation of Fundamental Constants". *Phys. Rev. Lett.* 113 (21 2014), p. 210801.

[18] H. Müller, A. Peters, and S. Chu. "A precision measurement of the gravitational redshift by the interference of matter waves". *Nature* 463.7283 (2010), pp. 926–929.

[19] R. H. Parker, C. Yu, W. Zhong, B. Estey, and H. Müller. "Measurement of the fine-structure constant as a test of the Standard Model". *Science* 360.6385 (2018), pp. 191–195.

[20] M. Jaffe, P. Haslinger, V. Xu, P. Hamilton, A. Upadhye, B. Elder, J. Khoury, and H. Müller. "Testing sub-gravitational forces on atoms from a miniature in-vacuum source mass". *Nat. Phys.* 13.10 (2017), pp. 938–942.

[21] P. Asenbaum, C. Overstreet, T. Kovachy, D. D. Brown, J. M. Hogan, and M. A. Kasevich. "Phase Shift in an Atom Interferometer due to Spacetime Curvature across its Wave Function". *Phys. Rev. Lett.* 118.18 (2017), p. 183602.

[22] N. Friis, O. Marty, C. Maier, C. Hempel, M. Holzäpfel, P. Jurcevic, M. B. Plenio, M. Huber, C. Roos, R. Blatt, and B. Lanyon. "Observation of Entangled States of a Fully Controlled 20-Qubit System". *Phys. Rev. X* 8.2 (2018), p. 021012.

[23] A. Omran, H. Levine, A. Keesling, G. Semeghini, T. T. Wang, S. Ebadi, H. Bernien, A. S. Zibrov, H. Pichler, S. Choi, J. Cui, M. Rossignolo, P. Rembold, S. Montangero, T. Calarco, M. Endres, M. Greiner, V. Vuletić, and M. D. Lukin. "Generation and manipulation of Schrödinger cat states in Rydberg atom arrays". *Science* 365.6453 (2019), pp. 570–574.

[24] M. T. Bell and T. P. Softley. "Ultracold molecules and ultracold chemistry". *Mol. Phys.* 107.2 (2009), pp. 99–132.

[25] J. L. Bohn, A. M. Rey, and J. Ye. "Cold molecules: Progress in quantum engineering of chemistry and quantum matter." *Science* 357.6355 (2017), pp. 1002–1010.

[26] N. Balakrishnan and A. Dalgarno. "Chemistry at ultracold temperatures". *Chem. Phys. Lett.* 341.5-6 (2001), pp. 652–656.

[27] D. J. Heinzen, R. Wynar, P. D. Drummond, and K. V. Kheruntsyan. "Superchemistry: Dynamics of Coupled Atomic and Molecular Bose-Einstein Condensates". *Phys. Rev. Lett.* 84.22 (2000), p. 5029.

[28] M. G. Moore and A. Vardi. "Bose-Enhanced Chemistry: Amplification of Selectivity in the Dissociation of Molecular Bose-Einstein Condensates". *Phys. Rev. Lett.* 88.16 (2002), p. 160402.

[29] V. V. Flambaum and J. S. M. Ginges. "Resonance reactions and enhancement of weak interactions in collisions of cold molecules". *Phys. Rev. A* 74.2 (2006), p. 025601.

[30] R. V. Krems. "Cold controlled chemistry". *Phys. Chem. Chem. Phys.* 10.28 (2008), pp. 4079–4092.

[31] R. V. Krems. "Molecules near absolute zero and external field control of atomic and molecular dynamics". *Int. Rev. Phys. Chem.* 24.1 (2005), pp. 99–118.

[32] I. Bloch, J. Dalibard, and W. Zwerger. "Many-body physics with ultracold gases". *Rev. Mod. Phys.* 80.3 (2008), pp. 885–964.

[33] T. Lahaye, C. Menotti, L. Santos, M. Lewenstein, and T. Pfau. "The physics of dipolar bosonic quantum gases". *Reports on Prog. Phys.* 72.12 (2009), p. 126401.

[34] R. Löw, H. Weimer, J. Nipper, J. B. Balewski, B. Butscher, H. P. Büchler, and T. Pfau. "An experimental and theoretical guide to strongly interacting Rydberg gases". *J. Phys. B: At. Mol. Opt. Phys.* 45.11 (2012), p. 113001.

[35] H. Bernien, S. Schwartz, A. Keesling, H. Levine, A. Omran, H. Pichler, S. Choi, A. S. Zibrov, M. Endres, M. Greiner, V. Vuletić, and M. D. Lukin. "Probing many-body dynamics on a 51-atom quantum simulator". *Nature* 551 (2017), pp. 579–584.

[36] A. Griesmaier, J. Werner, S. Hensler, J. Stuhler, and T. Pfau. "Bose-Einstein condensation of chromium". *Phys. Rev. Lett.* 94.16 (2005), p. 160401.

[37] M. Lu, S. H. Youn, and B. L. Lev. "Trapping Ultracold Dysprosium: A Highly Magnetic Gas for Dipolar Physics". *Phys. Rev. Lett.* 104.6 (2010), p. 063001.

[38] K. Aikawa, A. Frisch, M. Mark, S. Baier, A. Rietzler, R. Grimm, and F. Ferlaino. "Bose-Einstein Condensation of Erbium". *Phys. Rev. Lett.* 108.21 (2012), p. 210401.

[39] F. Böttcher, J. N. Schmidt, M. Wenzel, J. Hertkorn, M. Guo, T. Langen, and T. Pfau. "Transient Supersolid Properties in an Array of Dipolar Quantum Droplets". *Phys. Rev. X* 9.1 (2019), p. 011051.

[40] A. Micheli, G. Pupillo, H. P. Büchler, and P. Zoller. "Cold polar molecules in two-dimensional traps: Tailoring interactions with external fields for novel quantum phases". *Phys. Rev. A* 76.4 (2007), p. 043604.

[41] H. P. Büchler, E. Demler, M. Lukin, A. Micheli, N. Prokof'ev, G. Pupillo, and P. Zoller. "Strongly Correlated 2D Quantum Phases with Cold Polar Molecules: Controlling the Shape of the Interaction Potential". *Phys. Rev. Lett.* 98.6 (2007), p. 060404.

[42] K. Glaum, A. Pelster, H. Kleinert, and T. Pfau. "Critical Temperature of Weakly Interacting Dipolar Condensates". *Phys. Rev. Lett.* 98.8 (2007), p. 080407.

[43] K. Glaum and A. Pelster. "Bose-Einstein condensation temperature of dipolar gas in anisotropic harmonic trap". *Phys. Rev. A* 76.2 (2007), p. 023604.

[44] P. M. Lushnikov. "Collapse of Bose-Einstein condensates with dipole-dipole interactions". *Phys. Rev. A* 66.5 (2002), p. 051601.

[45] P. Pedri and L. Santos. "Two-Dimensional Bright Solitons in Dipolar Bose-Einstein Condensates". *Phys. Rev. Lett.* 95.20 (2005), p. 200404.

[46] N. R. Cooper, E. H. Rezayi, and S. H. Simon. "Vortex Lattices in Rotating Atomic Bose Gases with Dipolar Interactions". *Phys. Rev. Lett.* 95.20 (2005), p. 200402.

[47] J. Zhang and H. Zhai. "Vortex Lattices in Planar Bose-Einstein Condensates with Dipolar Interactions". *Phys. Rev. Lett.* 95.20 (2005), p. 200403.

[48] M. A. Baranov. "Theoretical progress in many-body physics with ultracold dipolar gases". *Phys. Reports* 464.3 (2008), pp. 71–111.

[49] K. Góral, L. Santos, and M. Lewenstein. "Quantum Phases of Dipolar Bosons in Optical Lattices". *Phys. Rev. Lett.* 88.17 (2002), p. 170406.

[50] M. Ortner, A. Micheli, G. Pupillo, and P. Zoller. "Quantum simulations of extended Hubbard models with dipolar crystals". *New J. Phys.* 11.5 (2009), p. 055045.

[51] M. L. Wall and L. D. Carr. "Hyperfine molecular Hubbard Hamiltonian". *Phys. Rev. A* 82.1 (2010), p. 013611.

[52] A. V. Gorshkov, K. R. Hazzard, and A. M. Rey. "Kitaev honeycomb and other exotic spin models with polar molecules". *Mol. Phys.* 111.12-13 (2013), pp. 1908–1916.

[53] M. Lemeshko, R. V. Krems, and H. Weimer. "Nonadiabatic Preparation of Spin Crystals with Ultracold Polar Molecules". *Phys. Rev. Lett.* 109.3 (2012), p. 035301.

[54] G. K. Brennen, A. Micheli, and P. Zoller. "Designing spin-1 lattice models using polar molecules". *New J. Phys.* 9.5 (2007), pp. 138–138.

[55] J. Schachenmayer, I. Lesanovsky, A. Micheli, and A. J. Daley. "Dynamical crystal creation with polar molecules or Rydberg atoms in optical lattices". *New J. Phys.* 12.10 (2010), p. 103044.

[56] J. Pérez-Ríos, F. Herrera, and R. V. Krems. "External field control of collective spin excitations in an optical lattice of $^2\Sigma$ molecules". *New J. Phys.* 12.10 (2010), p. 103007.

[57] F. Herrera, M. Litinskaya, and R. V. Krems. "Tunable disorder in a crystal of cold polar molecules". *Phys. Rev. A* 82.3 (2010), p. 033428.

[58] A. V. Gorshkov, S. R. Manmana, G. Chen, E. Demler, M. D. Lukin, and A. M. Rey. "Quantum magnetism with polar alkali-metal dimers". *Phys. Rev. A* 84.3 (2011), p. 033619.

[59] N. Y. Yao, C. R. Laumann, A. V. Gorshkov, S. D. Bennett, E. Demler, P. Zoller, and M. D. Lukin. "Topological Flat Bands from Dipolar Spin Systems". *Phys. Rev. Lett.* 109.26 (2012), p. 266804.

[60] N. Y. Yao, A. V. Gorshkov, C. R. Laumann, A. M. Läuchli, J. Ye, and M. D. Lukin. "Realizing Fractional Chern Insulators in Dipolar Spin Systems". *Phys. Rev. Lett.* 110.18 (2013), p. 185302.

[61] J. P. Kestner, B. Wang, J. D. Sau, and S. Das Sarma. "Prediction of a gapless topological Haldane liquid phase in a one-dimensional cold polar molecular lattice". *Phys. Rev. B* 83.17 (2011), p. 174409.

[62] S. R. Manmana, E. M. Stoudenmire, K. R. A. Hazzard, A. M. Rey, and A. V. Gorshkov. "Topological phases in ultracold polar-molecule quantum magnets". *Phys. Rev. B* 87.8 (2013), p. 081106.

[63] A. Micheli, G. K. Brennen, and P. Zoller. "A toolbox for lattice-spin models with polar molecules". *Nat. Phys.* 2.5 (2006), pp. 341–347.

[64] M. S. Safronova, D. Budker, D. DeMille, D. F. J. Kimball, A. Derevianko, and C. W. Clark. "Search for new physics with atoms and molecules". *Rev. Mod. Phys.* 90.2 (2018), p. 025008.

[65] M. G. Kozlov and L. N. Labzowsky. "Parity violation effects in diatomics". *J. Phys. B: At. Mol. Opt. Phys.* 28.10 (1995), pp. 1933–1961.

[66] D. DeMille, S. B. Cahn, D. Murphree, D. A. Rahmlow, and M. G. Kozlov. "Using Molecules to Measure Nuclear Spin-Dependent Parity Violation". *Phys. Rev. Lett.* 100.2 (2008), p. 023003.

[67] E. A. Hinds. "Testing time reversal symmetry using molecules". *Phys. Scripta* 70 (1997), pp. 34–41.

[68] ACME Collaboration. "Improved limit on the electric dipole moment of the electron". *Nature* 562.7727 (2018), pp. 355–360.

[69] W. B. Cairncross, D. N. Gresh, M. Grau, K. C. Cossel, T. S. Roussy, Y. Ni, Y. Zhou, J. Ye, and E. A. Cornell. "Precision Measurement of the Electron's Electric Dipole Moment Using Trapped Molecular Ions". *Phys. Rev. Lett.* 119.15 (2017), p. 153001.

[70] M. R. Tarbutt, B. E. Sauer, J. J. Hudson, and E. A. Hinds. "Design for a fountain of YbF molecules to measure the electron's electric dipole moment". *New J. Phys.* 15.5 (2013), p. 53034.

[71] E. R. Hudson, H. J. Lewandowski, B. C. Sawyer, and J. Ye. "Cold molecule spectroscopy for constraining the evolution of the fine structure constant". *Phys. Rev. Lett.* 96.14 (2006), p. 143004.

[72] A. Shelkovnikov, R. J. Butcher, C. Chardonnet, and A. Amy-Klein. "Stability of the proton-to-electron mass ratio". *Phys. Rev. Lett.* 100.15 (2008), p. 150801.

[73] S. Truppe, R. Hendricks, S. Tokunaga, H. Lewandowski, M. Kozlov, C. Henkel, E. Hinds, and M. Tarbutt. "A search for varying fundamental constants using hertz-level frequency measurements of cold CH molecules". *Nat. Commun.* 4 (2013), p. 2600.

[74] J. Kobayashi, A. Ogino, and S. Inouye. "Measurement of the variation of electron-to-proton mass ratio using ultracold molecules produced from laser-cooled atoms". *Nat. Commun.* 10.1 (2019), pp. 1–5.

[75] V. V. Flambaum and M. G. Kozlov. "Enhanced Sensitivity to the Time Variation of the Fine-Structure Constant and m_p/m_e in Diatomic Molecules". *Phys. Rev. Lett.* 99.15 (2007), p. 150801.

[76] C. Chin, V. V. Flambaum, and M. G. Kozlov. "Ultracold molecules: new probes on the variation of fundamental constants". *New J. Phys.* 11.5 (2009), p. 055048.

[77] D. Demille, S. Sainis, J. Sage, T. Bergeman, S. Kotochigova, and E. Tiesinga. "Enhanced Sensitivity to Variation of m_e/m_p in Molecular Spectra". *Phys. Rev. Lett.* 100.4 (2008), p. 043202.

[78] L. D. Carr, D. DeMille, R. V. Krems, and J. Ye. "Cold and ultracold molecules: Science, technology and applications". *New J. Phys.* 11 (2009), p. 055049.

[79] D. DeMille. "Quantum Computation with Trapped Polar Molecules". *Phys. Rev. Lett.* 88.6 (2002), p. 067901.

[80] U. Troppmann, C. M. Tesch, and R. de Vivie-Riedle. "Preparation and addressability of molecular vibrational qubit states in the presence of anharmonic resonance". *Chem. Phys. Lett.* 378.3-4 (2003), pp. 273–280.

[81] D. Babikov. "Accuracy of gates in a quantum computer based on vibrational eigenstates". *J. Chem. Phys.* 121.16 (2004), p. 7577.

[82] J. P. Palao and R. Kosloff. "Quantum Computing by an Optimal Control Algorithm for Unitary Transformations". *Phys. Rev. Lett.* 89.18 (2002), p. 188301.

[83] A. André, D. DeMille, J. M. Doyle, M. D. Lukin, S. E. Maxwell, P. Rabl, R. J. Schoelkopf, and P. Zoller. "A coherent all-electrical interface between polar molecules and mesoscopic superconducting resonators". *Nat. Phys.* 2.9 (2006), pp. 636–642.

[84] P. Rabl, D. DeMille, J. M. Doyle, M. D. Lukin, R. J. Schoelkopf, and P. Zoller. "Hybrid Quantum Processors: Molecular Ensembles as Quantum Memory for Solid State Circuits". *Phys. Rev. Lett.* 97.3 (2006), p. 033003.

[85] K.-K. Ni, S. Ospelkaus, M. H. G. de Miranda, A. Pe'er, B. Neyenhuis, J. J. Zirbel, S. Kotochigova, P. S. Julienne, D. S. Jin, and J. Ye. "A high phase-space-density gas of polar molecules." *Science* 322.5899 (2008), pp. 231–5.

[86] J. G. Danzl, M. J. Mark, E. Haller, M. Gustavsson, R. Hart, J. Aldegunde, J. M. Hutson, and H.-C. Nägerl. "An ultracold high-density sample of rovibronic ground-state molecules in an optical lattice". *Nat. Phys.* 6.4 (2010), pp. 265–270.

[87] T. Takekoshi, L. Reichsöllner, A. Schindewolf, J. M. Hutson, C. R. Le Sueur, O. Dulieu, F. Ferlaino, R. Grimm, and H.-C. Nägerl. "Ultracold Dense Samples of Dipolar RbCs Molecules in the Rovibrational and Hyperfine Ground State". *Phys. Rev. Lett.* 113.20 (2014), p. 205301.

[88] P. K. Molony, P. D. Gregory, Z. Ji, B. Lu, M. P. Köppinger, C. R. Le Sueur, C. L. Blackley, J. M. Hutson, and S. L. Cornish. "Creation of Ultracold $^{87}Rb^{133}Cs$ Molecules in the Rovibrational Ground State". *Phys. Rev. Lett.* 113.25 (2014), p. 255301.

[89] J. W. Park, S. A. Will, and M. W. Zwierlein. "Ultracold Dipolar Gas of Fermionic $^{23}Na^{40}K$ Molecules in Their Absolute Ground State". *Phys. Rev. Lett.* 114.20 (2015), p. 205302.

[90] M. Guo, B. Zhu, B. Lu, X. Ye, F. Wang, R. Vexiau, N. Bouloufa-Maafa, G. Quéméner, O. Dulieu, and D. Wang. "Creation of an Ultracold Gas of Ground-State Dipolar $^{23}Na^{87}Rb$ Molecules". *Phys. Rev. Lett.* 116.20 (2016), p. 205303.

[91] S. Ospelkaus, K.-K. Ni, G. Quéméner, B. Neyenhuis, D. Wang, M. H. G. de Miranda, J. L. Bohn, J. Ye, and D. S. Jin. "Controlling the Hyperfine State of Rovibronic Ground-State Polar Molecules". *Phys. Rev. Lett.* 104.3 (2010), p. 030402.

[92] S. A. Will, J. W. Park, Z. Z. Yan, H. Loh, and M. W. Zwierlein. "Coherent Microwave Control of Ultracold $^{23}Na^{40}K$ Molecules". *Phys. Rev. Lett.* 116.22 (2016), p. 225306.

[93] P. D. Gregory, J. Aldegunde, J. M. Hutson, and S. L. Cornish. "Controlling the rotational and hyperfine state of ultracold $^{87}Rb^{133}Cs$ molecules". *Phys. Rev. A* 94.4 (2016), p. 041403.

[94] L. De Marco, G. Valtolina, K. Matsuda, W. G. Tobias, J. P. Covey, and J. Ye. "A degenerate Fermi gas of polar molecules". *Science* 363.6429 (2019), pp. 853–856.

[95] S. A. Moses, J. P. Covey, M. T. Miecnikowski, D. S. Jin, and J. Ye. "New frontiers for quantum gases of polar molecules". *Nat. Phys.* 13.1 (2016), pp. 13–20.

[96] T. M. Rvachov, H. Son, A. T. Sommer, S. Ebadi, J. J. Park, M. W. Zwierlein, W. Ketterle, and A. O. Jamison. "Long-Lived Ultracold Molecules with Electric and Magnetic Dipole Moments". *Phys. Rev. Lett.* 119.14 (2017), p. 143001.

[97] A. Guttridge, S. A. Hopkins, M. D. Frye, J. J. McFerran, J. M. Hutson, and S. L. Cornish. "Production of ultracold Cs*Yb molecules by photoassociation". *Phys. Rev. A* 97.6 (2018), p. 063414.

[98] B. C. Yang, M. D. Frye, A. Guttridge, J. Aldegunde, P. S. Żuchowski, S. L. Cornish, and J. M. Hutson. "Magnetic Feshbach resonances in ultracold collisions between Cs and Yb atoms". *Phys. Rev. A* 100.2 (2019), p. 022704.

[99] J. M. Doyle, J. D. Weinstein, R. deCarvalho, T. Guillet, and B. Friedrich. "Magnetic trapping of calcium monohydride molecules at millikelvin temperatures". *Nature* 395.6698 (1998), pp. 148–150.

[100] J. G. E. Harris, R. A. Michniak, S. V. Nguyen, N. Brahms, W. Ketterle, and J. M. Doyle. "Buffer gas cooling and trapping of atoms with small effective magnetic moments". *Europhys. Lett. (EPL)* 67.2 (2004), pp. 198–204.

[101] A. B. Henson, S. Gersten, Y. Shagam, J. Narevicius, and E. Narevicius. "Observation of resonances in Penning ionization reactions at sub-kelvin temperatures in merged beams". *Science* 338.6104 (2012), pp. 234–8.

[102] S. Y. T. van de Meerakker, H. L. Bethlem, and G. Meijer. "Taming molecular beams". *Nat. Phys.* 4.8 (2008), pp. 595–602.

[103] J. J. Gilijamse, S. Hoekstra, S. Y. Van De Meerakker, G. C. Groenenboom, and G. Meijer. "Near-threshold inelastic collisions using molecular beams with a tunable velocity". *Science* 313.5793 (2006), pp. 1617–1620.

[104] M. I. Fabrikant, T. Li, N. J. Fitch, N. Farrow, J. D. Weinstein, and H. J. Lewandowski. "Method for traveling-wave deceleration of buffer-gas beams of CH". *Phys. Rev. A* 90.3 (2014), p. 033418.

[105] S. Hoekstra, M. Metsälä, P. C. Zieger, L. Scharfenberg, J. J. Gilijamse, G. Meijer, and S. Y. T. van de Meerakker. "Electrostatic trapping of metastable NH molecules". *Phys. Rev. A* 76.6 (2007), p. 063408.

[106] B. C. Sawyer, B. L. Lev, E. R. Hudson, B. K. Stuhl, M. Lara, J. L. Bohn, and J. Ye. "Magnetoelectrostatic Trapping of Ground State OH Molecules". *Phys. Rev. Lett.* 98.25 (2007), p. 253002.

[107] T. Rieger, T. Junglen, S. A. Rangwala, P. W. H. Pinkse, and G. Rempe. "Continuous Loading of an Electrostatic Trap for Polar Molecules". *Phys. Rev. Lett.* 95.17 (2005), p. 173002.

[108] S. Chervenkov, X. Wu, J. Bayerl, A. Rohlfes, T. Gantner, M. Zeppenfeld, and G. Rempe. "Continuous Centrifuge Decelerator for Polar Molecules". *Phys. Rev. Lett.* 112.1 (2014), p. 013001.

[109] N. Vanhaecke, U. Meier, M. Andrist, B. H. Meier, and F. Merkt. "Multistage Zeeman deceleration of hydrogen atoms". *Phys. Rev. A* 75.3 (2007), p. 031402.

[110] Y. Liu, M. Vashishta, P. Djuricanin, S. Zhou, W. Zhong, T. Mittertreiner, D. Carty, and T. Momose. "Magnetic Trapping of Cold Methyl Radicals". *Phys. Rev. Lett.* 118.9 (2017), p. 093201.

[111] N. Akerman, M. Karpov, Y. Segev, N. Bibelnik, J. Narevicius, and E. Narevicius. "Trapping of Molecular Oxygen together with Lithium Atoms". *Phys. Rev. Lett.* 119.7 (2017), p. 073204.

[112] R. Fulton, A. I. Bishop, and P. F. Barker. "Optical Stark Decelerator for Molecules". *Phys. Rev. Lett.* 93.24 (2004), p. 243004.

[113] A. Trottier, D. Carty, and E. Wrede. "Photostop: production of zero-velocity molecules by photodissociation in a molecular beam". *Mol. Phys.* 109.5 (2011), pp. 725–733.

[114] M. S. Elioff, J. J. Valentini, and D. W. Chandler. "Subkelvin cooling NO molecules via "billiard-like" collisions with argon." *Science* 302.5652 (2003), pp. 1940–3.

[115] K. Takase, L. A. Rahn, D. W. Chandler, and K. E. Strecker. "The kinematic cooling of molecules with laser-cooled atoms". *New J. Phys.* 11.5 (2009), p. 055033.

[116] G. Manish and D. Herschbach. "Slowing and Speeding Molecular Beams by Means of a Rapidly Rotating Source". *J. Phys. Chem. A* 105.9 (2001), pp. 1626–1637.

[117] M. Strebel, F. Stienkemeier, and M. Mudrich. "Improved setup for producing slow beams of cold molecules using a rotating nozzle". *Phys. Rev. A* 81.3 (2010), p. 033409.

[118] E. Narevicius, A. Libson, M. F. Riedel, C. G. Parthey, I. Chavez, U. Even, and M. G. Raizen. "Coherent Slowing of a Supersonic Beam with an Atomic Paddle". *Phys. Rev. Lett.* 98.10 (2007), p. 103201.

[119] A. Prehn, M. Ibrügger, R. Glöckner, G. Rempe, and M. Zeppenfeld. "Optoelectrical Cooling of Polar Molecules to Submillikelvin Temperatures". *Phys. Rev. Lett.* 116.6 (2016), p. 063005.

[120] E. Narevicius, S. T. Bannerman, and M. G. Raizen. "Single-photon molecular cooling". *New J. Phys.* 11.5 (2009), p. 055046.

[121] D. Reens, H. Wu, T. Langen, and J. Ye. "Controlling spin flips of molecules in an electromagnetic trap". *Phys. Rev. A* 96 (6 2017), p. 063420.

[122] Y. Segev, M. Pitzer, M. Karpov, N. Akerman, J. Narevicius, and E. Narevicius. "Collisions between cold molecules in a superconducting magnetic trap". *Nature* 572.7768 (2019), pp. 189–193.

[123] M. D. Di Rosa. "Laser-cooling molecules". *Eur. Phys. J. D* 31.2 (2004), pp. 395–402.

[124] B. K. Stuhl, B. C. Sawyer, D. Wang, and J. Ye. "Magneto-optical Trap for Polar Molecules". *Phys. Rev. Lett.* 101.24 (2008), p. 243002.

[125] E. S. Shuman, J. F. Barry, D. R. Glenn, and D. Demille. "Radiative force from optical cycling on a diatomic molecule". *Phys. Rev. Lett.* 103.22 (2009), p. 223001.

[126] E. S. Shuman, J. F. Barry, and D. Demille. "Laser cooling of a diatomic molecule". *Nature* 467.7317 (2010), pp. 820–823.

[127] J. F. Barry, E. S. Shuman, E. B. Norrgard, and D. Demille. "Laser radiation pressure slowing of a molecular beam". *Phys. Rev. Lett.* 108.10 (2012), p. 103002.

[128] M. T. Hummon, M. Yeo, B. K. Stuhl, A. L. Collopy, Y. Xia, and J. Ye. "2D Magneto-Optical Trapping of Diatomic Molecules". *Phys. Rev. Lett.* 110.14 (2013), p. 143001.

[129] J. F. Barry, D. J. McCarron, E. B. Norrgard, M. H. Steinecker, and D. DeMille. "Magneto-optical trapping of a diatomic molecule". *Nature* 512.7514 (2014), pp. 286–289.

[130] L. Anderegg, B. L. Augenbraun, E. Chae, B. Hemmerling, N. R. Hutzler, A. Ravi, A. Collopy, J. Ye, W. Ketterle, and J. M. Doyle. "Radio Frequency Magneto-Optical Trapping of CaF with High Density". *Phys. Rev. Lett.* 119.10 (2017), p. 103201.

[131] A. L. Collopy, S. Ding, Y. Wu, I. A. Finneran, L. Anderegg, B. L. Augenbraun, J. M. Doyle, and J. Ye. "3D Magneto-Optical Trap of Yttrium Monoxide". *Phys. Rev. Lett.* 121.21 (2018), p. 213201.

[132] I. Kozyryev, L. Baum, K. Matsuda, B. L. Augenbraun, L. Anderegg, A. P. Sedlack, and J. M. Doyle. "Sisyphus Laser Cooling of a Polyatomic Molecule". *Phys. Rev. Lett.* 118.17 (2017), p. 173201.

[133] J. Lim, J. R. Almond, M. A. Trigatzis, J. A. Devlin, N. J. Fitch, B. E. Sauer, M. R. Tarbutt, and E. A. Hinds. "Laser Cooled YbF Molecules for Measuring the Electron's Electric Dipole Moment". *Phys. Rev. Lett.* 120 (12 2018), p. 123201.

[134] V. Zhelyazkova, A. Cournol, T. E. Wall, A. Matsushima, J. J. Hudson, E. A. Hinds, M. R. Tarbutt, and B. E. Sauer. "Laser cooling and slowing of CaF molecules". *Phys. Rev. A* 89.5 (2014), p. 053416.

[135] S. Truppe, H. J. Williams, N. J. Fitch, M. Hambach, T. E. Wall, E. A. Hinds, B. E. Sauer, and M. R. Tarbutt. "An intense, cold, velocity-controlled molecular beam by frequency-chirped laser slowing". *New J. Phys.* 19.2 (2017), p. 022001.

[136] J. P. Dahl and M. Springborg. "The Morse oscillator in position space, momentum space, and phase space". *J. Chem. Phys.* 88.7 (1988), pp. 4535–4547.

[137] J. Brown and A. Carrington. *Rotational spectroscopy of diatomic molecules*. Cambridge University Press, 2003.

[138] T. E. Wall, J. F. Kanem, J. J. Hudson, B. E. Sauer, D. Cho, M. G. Boshier, E. A. Hinds, and M. R. Tarbutt. "Lifetime of the A ($v' = 0$) state and Franck-Condon factor of the A–X (0–0) transition of CaF measured by the saturation of laser-induced fluorescence". *Phys. Rev. A* 78.6 (2008), p. 062509.

[139] R. W. Field, D. O. Harris, and T. Tanaka. "Continuous wave dye laser excitation spectroscopy CaF $A^2\Pi_r - X^2\Sigma^+$". *J. Mol. Spectrosc.* 57.1 (1975), pp. 107–117.

[140] P. J. Dagdigian, H. W. Cruse, and R. N. Zare. "Radiative lifetimes of the alkaline earth monohalides". *J. Chem. Phys.* 60 (1974), pp. 2330–2339.

[141] M. A. Anderson, M. D. Allen, and L. M. Ziurys. "The Millimeter-Wave Spectrum of the CaF Radical ($X^2\Sigma^+$)". *Astrophys. J.* 424 (1994), p. 503.

[142] W. J. Childs, G. L. Goodman, and L. S. Goodman. "Precise determination of the v and N dependence of the spin-rotation and hyperfine interactions in the CaF $X^2\Sigma_{1/2}$ ground state". *J. Mol. Spectrosc.* 86.2 (1981), pp. 365–392.

[143] W. J. Childs, L. S. Goodman, U. Nielsen, and V. Pfeufer. "Electric-dipole moment of CaF ($X^2\Sigma^+$) by molecular beam, laser-rf, double-resonance study of Stark splittings". *J. Chem. Phys.* 80.6 (1984), pp. 2283–2287.

[144] M. Pelegrini, C. S. Vivacqua, O. Roberto-Neto, F. R. Ornellas, and F. B. Machado. "Radiative transition probabilities and lifetimes for the band systems $A^2\Pi$-$X^2\Sigma^+$ of the isovalent molecules BeF, MgF and CaF". *Braz. J. Phys.* 35.4 A (2005), pp. 950–956.

[145] M. Dulick, P. F. Bernath, and R. W. Field. "Rotational and vibrational analysis of the CaF $B^2\Sigma^+$–$X^2\Sigma^+$ system". *Can. J. Phys.* 58.5 (1980), pp. 703–712.

[146] M. R. Tarbutt. "Magneto-optical trapping forces for atoms and molecules with complex level structures". *New J. Phys.* 17 (2015), p. 015007.

[147] M. R. Tarbutt and T. C. Steimle. "Modeling magneto-optical trapping of CaF molecules". *Phys. Rev. A* 92.5 (2015), p. 053401.

[148] P. D. Lett, R. N. Watts, C. I. Westbrook, W. D. Phillips, P. L. Gould, and H. J. Metcalf. "Observation of atoms laser cooled below the doppler limit". *Phys. Rev. Lett.* 61.2 (1988), pp. 169–172.

[149] J. Dalibard and C. Cohen-Tannoudji. "Laser cooling below the Doppler limit by polarization gradients: simple theoretical models". *J. Opt. Soc. Am. B* 6.11 (1989), pp. 2023–2045.

[150] P. J. Ungar, D. S. Weiss, E. Riis, and S. Chu. "Optical molasses and multilevel atoms: theory". *J. Opt. Soc. Am. B* 6.11 (1989), p. 2058.

[151] G. Raithel, W. D. Phillips, and S. L. Rolston. "Collapse and revivals of wave packets in optical lattices". *Phys. Rev. Lett.* 81.17 (1998), pp. 3615–3618.

[152] J. Dalibard and C. Cohen-Tannoudji. "Atomic motion in laser light: connection between semi-classical and quantum descriptions". *J. Phys. B* 18.8 (1985), pp. 1661–1683.

[153] J. Dalibard and C. Cohen-Tannoudji. "Dressed-atom approach to atomic motion in laser light: the dipole force revisited". *J. Opt. Soc. Am. B* 2.11 (1985), pp. 1707–1720.

[154] A. Aspect, J. Dalibard, A. Heidmann, C. Salomon, and C. Cohen-Tannoudji. "Cooling Atoms with Stimulated Emission". *Phys. Rev. Lett.* 57.14 (1986), pp. 1688–1691.

[155] J. A. Devlin and M. R. Tarbutt. "Three-dimensional Doppler, polarization-gradient, and magneto-optical forces for atoms and molecules with dark states". *New J. Phys.* 18.12 (2016), p. 123017.

[156] G. Salomon, L. Fouché, P. Wang, A. Aspect, P. Bouyer, and T. Bourdel. "Gray-molasses cooling of ^{39}K to a high phase-space density". *EPL* 104.6 (2013), p. 63002.

[157] K. N. Jarvis, J. A. Devlin, T. E. Wall, B. E. Sauer, and M. R. Tarbutt. "Blue-Detuned Magneto-Optical Trap". *Phys. Rev. Lett.* 120.8 (2018), p. 083201.

[158] A. Aspect, E. Arimondo, R. Kaiser, N. Vansteenkiste, and C. Cohen-Tannoudji. "Laser Cooling below the One-Photon Recoil Energy by Velocity-Selective Coherent Population Trapping". *Phys. Rev. Lett.* 61.7 (1988), pp. 826–829.

[159] D. V. Lindley. *Introduction to Probability and Statistics from a Bayesian Viewpoint, Part 1*. Cambridge University Press, 1969.

[160] J. Lawall, S. Kulin, B. Saubamea, N. Bigelow, M. Leduc, and C. Cohen-Tannoudji. "Three-Dimensional Laser Cooling of Helium Beyond the Single-Photon Recoil Limit". *Phys. Rev. Lett.* 75.23 (1995), pp. 4194–4197.

[161] S. Truppe, M. Hambach, S. M. Skoff, N. E. Bulleid, J. S. Bumby, R. J. Hendricks, E. A. Hinds, B. E. Sauer, and M. R. Tarbutt. "A buffer gas beam source for short, intense and slow molecular pulses". *J. Mod. Opt.* 65.5-6 (2018), pp. 648–656.

[162] M. Hambach. "Development of a magneto-optical trap for CaF molecules". PhD thesis. Imperial College London, 2017.

[163] H. J. Williams. "Producing, trapping and controlling ultracold CaF molecules". PhD thesis. Imperial College London, 2018.

[164] W. Petrich, M. H. Anderson, J. R. Ensher, and E. A. Cornell. "Behavior of atoms in a compressed magneto-optical trap". *J. Opt. Soc. Am. B* 11.8 (1994), p. 1332.

[165] C. Cheng, A. P. Van Der Poel, P. Jansen, M. Quintero-Pérez, T. E. Wall, W. Ubachs, and H. L. Bethlem. "Molecular Fountain". *Phys. Rev. Lett.* 117.25 (2016), p. 253201.

[166] L. W. Cheuk, L. Anderegg, B. L. Augenbraun, Y. Bao, S. Burchesky, W. Ketterle, and J. M. Doyle. "Λ-Enhanced Imaging of Molecules in an Optical Trap". *Phys. Rev. Lett.* 121.8 (2018), p. 083201.

[167] F. Papoff, F. Mauri, and E. Arimondo. "Transient velocity-selective coherent population trapping in one dimension". *J. Opt. Soc. Am. B* 9.3 (1992), pp. 321–331.

[168] J. A. Devlin and M. R. Tarbutt. "Laser cooling and magneto-optical trapping of molecules analyzed using optical Bloch equations and the Fokker-Planck-Kramers equation". *Phys. Rev. A* 98.6 (2018), p. 063415.

[169] W. Ketterle, D. S. Durfee, and D. Stamper-Kurn. "Making, probing and understanding Bose-Einstein Condensates". In: *Proceedings of the International School of Physics "Enrico Fermi," Course CXL*. Ed. by M. Inguscio, S. Stringari, and C. Wieman. IOS Press, Amsterdam, 1999, pp. 67–176.

[170] D. J. McCarron, M. H. Steinecker, Y. Zhu, and D. DeMille. "Magnetic Trapping of an Ultracold Gas of Polar Molecules". *Phys. Rev. Lett.* 121.1 (2018), p. 013202.

[171] T. Bergeman, G. Erez, and H. J. Metcalf. "Magnetostatic trapping fields for neutral atoms". *Phys. Rev. A* 35.4 (1987), pp. 1535–1546.

[172] S. Y. Buhmann, M. R. Tarbutt, S. Scheel, and E. A. Hinds. "Surface-induced heating of cold polar molecules". *Phys. Rev. A* 78.5 (2008), p. 052901.

[173] J. J. Hudson, D. M. Kara, I. J. Smallman, B. E. Sauer, M. R. Tarbutt, and E. A. Hinds. "Improved measurement of the shape of the electron". *Nature* 473.7348 (2011), pp. 493–496.

[174] K. R. A. Hazzard, S. R. Manmana, M. Foss-Feig, and A. M. Rey. "Far-from-Equilibrium Quantum Magnetism with Ultracold Polar Molecules". *Phys. Rev. Lett.* 110.7 (2013), p. 075301.

[175] J. W. Park, Z. Z. Yan, H. Loh, S. A. Will, and M. W. Zwierlein. "Second-scale nuclear spin coherence time of ultracold $^{23}Na^{40}K$ molecules". *Science* 357.6349 (2017), pp. 372–375.

[176] S. Kotochigova and D. DeMille. "Electric-field-dependent dynamic polarizability and state-insensitive conditions for optical trapping of diatomic polar molecules". *Phys. Rev. A* 82 (6 2010), p. 063421.

[177] F. Seeßelberg, X.-Y. Luo, M. Li, R. Bause, S. Kotochigova, I. Bloch, and C. Gohle. "Extending Rotational Coherence of Interacting Polar Molecules in a Spin-Decoupled Magic Trap". *Phys. Rev. Lett.* 121 (25 2018), p. 253401.

[178] S. S. Kondov, C.-H. Lee, K. H. Leung, C. Liedl, I. Majewska, R. Moszynski, and T. Zelevinsky. "Molecular lattice clock with long vibrational coherence". *Nat. Phys.* (2019), pp. 1–5.

[179] Y. Wang, T. Tran, P. Surendran, I. Herrera, A. Balcytis, D. Nissen, M. Albrecht, A. Sidorov, and P. Hannaford. "Trapping ultracold atoms in a sub-micron-period triangular magnetic lattice". *Phys. Rev. A* 96.1 (2017), p. 013630.

[180] A. André, D. DeMille, J. M. Doyle, M. D. Lukin, S. E. Maxwell, P. Rabl, R. J. Schoelkopf, and P. Zoller. "A coherent all-electrical interface between polar molecules and mesoscopic superconducting resonators". *Nat. Phys.* 2.9 (2006), pp. 636–642.

[181] L. Anderegg, B. L. Augenbraun, Y. Bao, S. Burchesky, L. W. Cheuk, W. Ketterle, and J. M. Doyle. "Laser cooling of optically trapped molecules". *Nat. Phys.* 14.9 (2018), pp. 890–893.

[182] M. R. Tarbutt, J. J. Hudson, B. E. Sauer, and E. A. Hinds. "Prospects for measuring the electric dipole moment of the electron using electrically trapped polar molecules". *Faraday Discuss.* 142.0 (2009), p. 37.

[183] E. R. Meyer, A. E. Leanhardt, E. A. Cornell, and J. L. Bohn. "Berry-like phases in structured atoms and molecules". *Phys. Rev. A* 80.6 (2009), p. 062110.

[184] M. Kajita. "Prospects of detecting m_e/m_p variance using vibrational transition frequencies of $^2\Sigma$-state molecules". *Phys. Rev. A* 77.1 (2008), p. 012511.

[185] A. Micheli, G. Pupillo, H. P. Büchler, and P. Zoller. "Cold polar molecules in two-dimensional traps: Tailoring interactions with external fields for novel quantum phases". *Phys. Rev. A* 76.4 (2007), p. 043604.

[186] B. Capogrosso-Sansone, C. Trefzger, M. Lewenstein, P. Zoller, and G. Pupillo. "Quantum Phases of Cold Polar Molecules in 2D Optical Lattices". *Phys. Rev. Lett.* 104.12 (2010), p. 125301.

[187] T. Sowiński, O. Dutta, P. Hauke, L. Tagliacozzo, and M. Lewenstein. "Dipolar Molecules in Optical Lattices". *Phys. Rev. Lett.* 108.11 (2012), p. 115301.

[188] K.-K. Ni, T. Rosenband, and D. D. Grimes. "Dipolar exchange quantum logic gate with polar molecules". *Chem. Sci.* 9.33 (2018), pp. 6830–6838.

[189] B. Yan, S. A. Moses, B. Gadway, J. P. Covey, K. R. A. Hazzard, A. M. Rey, D. S. Jin, and J. Ye. "Observation of dipolar spin-exchange interactions with lattice-confined polar molecules". *Nature* 501.7468 (2013), pp. 521–525.

[190] L. R. Liu, J. D. Hood, Y. Yu, J. T. Zhang, N. R. Hutzler, T. Rosenband, and K.-K. Ni. "Building one molecule from a reservoir of two atoms." *Science* 360.6391 (2018), pp. 900–903.

[191] M. Endres, H. Bernien, A. Keesling, H. Levine, E. R. Anschuetz, A. Krajenbrink, C. Senko, V. Vuletic, M. Greiner, and M. D. Lukin. "Atom-by-atom assembly of defect-free one-dimensional cold atom arrays". *Science* 354.6315 (2016), pp. 1024–1027.

[192] L. Anderegg, L. W. Cheuk, Y. Bao, S. Burchesky, W. Ketterle, K.-K. Ni, and J. M. Doyle. "An optical tweezer array of ultracold molecules." *Science* 365.6458 (2019), pp. 1156–1158.

[193] A. M. Kaufman, B. J. Lester, and C. A. Regal. "Cooling a Single Atom in an Optical Tweezer to Its Quantum Ground State". *Phys. Rev. X* 2.4 (2012), p. 041014.

[194] Y. Yu, N. R. Hutzler, J. T. Zhang, L. R. Liu, J. D. Hood, T. Rosenband, and K.-K. Ni. "Motional-ground-state cooling outside the Lamb-Dicke regime". *Phys. Rev. A* 97.6 (2018), p. 063423.

[195] M. A. Norcia, A. W. Young, and A. M. Kaufman. "Microscopic Control and Detection of Ultracold Strontium in Optical-Tweezer Arrays". *Phys. Rev. X* 8.4 (2018), p. 041054.

[196] A. Cooper, J. P. Covey, I. S. Madjarov, S. G. Porsev, M. S. Safronova, and M. Endres. "Alkaline-Earth Atoms in Optical Tweezers". *Phys. Rev. X* 8.4 (2018), p. 041055.

[197] F. Le Kien, P. Schneeweiss, and A. Rauschenbeutel. "Dynamical polarizability of atoms in arbitrary light fields: general theory and application to cesium". *Eur. Phys. J. D* 67.5 (2013), p. 92.

[198] X. Li, T. A. Corcovilos, Y. Wang, and D. S. Weiss. "3D Projection Sideband Cooling". *Phys. Rev. Lett.* 108 (10 2012), p. 103001.

[199] D. S. Weiss, S. Lukman Winoto, and M. T. DePue. "Cooling atoms in a far-detuned optical lattice". *Proc. SPIE Int. Soc. Opt. Eng.* 2995 (1997), pp. 156–162.

[200] S. Waldenstrøm and K. Naqvi. "The overlap integrals of two harmonic-oscillator wavefunctions: some remarks on originals and reproductions". *Chem. Phys. Lett.* 85.5-6 (1982), pp. 581–584.

[201] J. D. Thompson, T. G. Tiecke, A. S. Zibrov, V. Vuletić, and M. D. Lukin. "Coherence and Raman Sideband Cooling of a Single Atom in an Optical Tweezer". *Phys. Rev. Lett.* 110.13 (2013), p. 133001.

[202] L. A. Kaledin, J. C. Bloch, M. C. McCarthy, and R. W. Field. "Analysis and deperturbation of the $A^2\Pi$ and $B^2\Sigma^+$ states of CaF". *J. Mol. Spectrosc.* 197 (1999), pp. 289–296.

[203] B. Richards and E. Wolf. "Electromagnetic diffraction in optical systems, II. Structure of the image field in an aplanatic system". *Proc. Royal Soc. A* 253.1274 (1959), pp. 358–379.

[204] C. Cohen-Tannoudji, J. Dupont-Roc, and G. Grynberg. *Atom-photon interactions*. 1992.